Improving computational methods for modeling reactivity

Esben Leonhard Kolsbjerg

. . .

Ph.D. Thesis

Interdisciplinary Nanoscience Center (iNANO)
Aarhus University

31th of July 2018.

The content of this thesis has been carried out under the exquisite supervision of Professor Bjørk Hammer at the Interdisciplinary Nanoscience Center (iNANO) and the Department of Physics and Astronomy. In agreement with the requirements for obtaining a Ph.D. degree in nanoscience the thesis has been submitted to the faculty of Science and Technology at Aarhus University.

Résumé in English

Catalysis is all around us, embodied in the growth of our society through technology, economics, and agriculture – it is even controlling the biological systems inside us. The importance of catalysis is without doubt tremendous and improving our catalyst know-how is a key component for a successful sustainable future. In this thesis different catalytic processes are investigated with density functional theory, some assisted by machine learning methods and others in collaboration with experimentalists. The main focus has been on developing strategies and algorithms to ease and improve how different catalytic systems are investigated.

The strategies and algorithms have been developed to ease systematic and automatic investigations of reaction processes as well as speeding up structure search algorithms. The newly established and more mature methods have been applied to different catalytic systems. One example is the study of adsorption and diffusion of aromatic molecules, which gave transferable insights into reaction mechanisms. Another study utilized several techniques to explain the driving force of self-assembled molecular corrals, while a third study of small metal clusters revealed new exciting structures.

Resume på dansk

Overalt omkring os er katalyse integreret i vores samfund, både teknologisk, økonomisk og i vores landbrug – det er endda essentiel for vores biologiske cellulære processer. Betydningen af katalyse kan ikke overvurderes og forbedring af vores katalyseviden er fundamental for en bæredygtig fremtid. Det er i denne kontekst min afhandling opererer, hvori der er fokuseret på forskellige katalytiske processer studeret både med tæthedsfunktionsteori, maskinlæringsmetoder og i samarbejde eksperimentelle kollegaer. Det helt centrale for studierne har været udviklingen af strategier og algoritmer til at lette og forbedre, hvordan forskellige katalytiske systemer studeres.

Strategierne og algoritmerne er helt konkret udviklet med fokus på systematik og automatik til brug i studier af reaktionsprocesser, samt hvordan man kan effektivisere struktursøgningsalgoritmer. De nyudviklede og etablerede metoder er blevet anvendt til at undersøge flere forskellige katalytiske systemer. Med hjælp fra en lang række af teknikker er alt fra reaktionsmekanismer i forbindelse med adsorption og diffusion af aromatiske molekyler til forståelse af hvorfor selvsamlende ringe dannes på overflader af kobber blevet belyst. De nyudviklede algoritmer er bl.a. også brugt til at finde og udforske nye stabile og katalytisk interessante metalklynger.

Contents

Preface **vii**
Acknowledgements . . . vii
List of publications . . . viii
Abbreviations . . . x

1 Introduction **1**
1.1 Catalysis and society . . . 1
1.2 Development of catalysis . . . 3
1.3 Thesis outline . . . 5

2 Computational methods **7**
2.1 Density functional theory . . . 7
2.2 Neural network modeled potential energy surface . . . 12

3 The "art" of locating transition states **17**
3.1 Challenges in the search for transition states . . . 18
3.2 Automating transition state search for efficiency . . . 25
3.3 Context . . . 27

4 Aromatic molecules adsorption and mobility on Pt(111) **31**
4.1 Surface interactions . . . 32
4.2 Context . . . 36

5 Modeling self-assembled molecular corrals **37**
5.1 Understanding the molecular arrangement . . . 38
5.2 Creating a molecular pair potential . . . 39
5.3 Modeling full sized corrals . . . 41
5.4 Context . . . 43

6 Structure search for small, supported Pt-nanoparticles **45**

6.1 A learning evolutionary algorithm 46
6.2 Benchmarking the algorithm 47
6.3 Using the LEA for finding supported Pt nanoparticles 48
6.4 Catalytic properties of the Pt_{13} nanoparticles 49
6.5 Pt_{13} isomer transformation 50
6.6 Context 52

7 Conclusion and outlook 55
7.1 A generic atomistic structure builder trained by reinforcement learning 57

Bibliography 59

Papers 69
Pyridine adsorption and diffusion on Pt(111) investigated with density functional theory 73
An automated nudged elastic band method 85
Supramolecular corrals on surfaces resulting from aromatic interactions of nonplanar triazoles 97
Exciting H_2 molecules for graphene functionalization 109
Rotation and diffusion of naphthalene on Pt(111) 119
NH_3 adsorption on anatase-TiO_2(101) 129
Neural-network-enhanced evolutionary algorithm applied to supported metal nanoparticles 137

Preface

Acknowledgements

For eight great years, Aarhus University has been the center of my study, work, and social life – the past five as a Ph.D. student. This thesis, the concluding remarks, would never have been possible without the help and support from a wide range of people I have come to learn.

First of all, I would like to thank my supervisor Bjørk Hammer who, concluding the second-year quantum mechanics course he taught, wrote me an email asking me if I would like to come by a for an informal chat concerning a potential bachelor project. Now six years later I stand at the brink of handing in my Ph.D. thesis. Bjørk's very direct dedicated engagement and involvement were the deciding factors for me in joining his group immediately concluding my bachelor project. The hands-on supervising strategy conducted by Bjørk is extremely appreciated. It has allowed me to grow tremendously, acquire a lot of knowledge, and learn many useful skills.

I would like to thank all current and previous members of Bjørk's research group whom all have helped me through thorough scientific discussions and provide concrete suggestions. I will especially like to thank the two previous post-docs Albert Bruix and Michael N. Groves as they have been willing to let me draw on their scientific expertise and answered my many questions. I would also like to extend my sincere appreciativeness to my friend and colleague Mathias Siggaard Jørgensen whom I for the most part have shared an office with. I have daily benefited greatly from Mathias input to all of my projects. I would also use the opportunity to acknowledge the great collaborations I have been so lucky to be a part of – a notably "thank you" goes to Line, Liv, Stig, Kræn, Stefan, Jeppe, Peter, Guillaume, Siddarth, Trolle, and Andrew. A distinct thank you to Andrew A. Peterson and the rest of his research group, which I had the unmistakable pleasure of visiting in Providence, Rhode Island in the spring 2017. It allowed me to see and learn in a different research environment. As a theoretician who

heavenly rely on well-functioning high-performance computers a pronounced thanks is extended to the CSCAA system administrator Niels Carl whom have helped me tremendously with many technical details. I know I have caused countless off-hours of headache.

Last but not least I would like to thank the members of my "study group" who all have become great friends. They have been indispensable for a smooth transition into the university world. As most of them have also pursued a Ph.D. degree I have had the pleasure of enjoying their company throughout the years on an everyday basis.

List of publications

Publications related to this Ph.D. thesis

I Pyridine adsorption and diffusion on Pt (111) investigated with density functional theory
E. L. Kolsbjerg, M. N. Groves, and B. Hammer
The Journal of Chemical Physics, 144 (16), 164112 (2016)

II An automated nudged elastic band method
E. L. Kolsbjerg, M. N. Groves, and B. Hammer
The Journal of Chemical Physics, 145 (9), 094107 (2016)

III Supramolecular corrals on surfaces resulting from aromatic interactions of nonplanar triazoles
S. J. Jethwa, E. L. Kolsbjerg, S. R. Vadapoo, J. L. Cramer, L. Lammich, K. V. Gothelf, B. Hammer, and T. R. Linderoth
ACS Nano 11 (8), 8302, (2017)

IV Exciting H_2 molecules for graphene functionalization
L. Kyhl, R. Bisson, R. Balog, M. N. Groves, E. L. Kolsbjerg, A. M. Cassidy, J. H. Jørgensen, S. Halkjår, J. A. Miwa, A. G. Čabo, T. Angot, P. Hofmann, M. A. Arman, S. Urpelainen, P. Lacovig, L. Bignardi, H. Bluhm, J. Knudsen, B. Hammer, and L. Hornekaer
ACS Nano 12 (1), 513 (2018)

V Rotation and diffusion of naphthalene on Pt(111)
E. L. Kolsbjerg, G. Goubert, P. H. McBreen, and B. Hammer
The Journal of Chemical Physics, 148 (12), 124703 (2018)

VI NH_3 adsorption on anatase-TiO_2(101)
S. Koust, K. Adamsen, E. L. Kolsbjerg, Z. Li, B. Hammer, S. Wendt, and J. V. Lauritsen
The Journal of Chemical Physics, 148 (12), 124704 (2018)

VII Neural-network-enhanced evolutionary algorithm applied to supported metal nanoparticles
E. L. Kolsbjerg, A. A. Peterson, and B. Hammer
Physical Review B, 97, 195424 (2018)

VIII Diffusion phenomena of ammonia on anatase-TiO_2 (101)
K. Adamsen, E. L. Kolsbjerg, S. Koust, B. Hammer, S. Wendt, and J. V. Lauritsen
Manuscript in preparation

Other publications not included in the thesis

IX The Atomic Simulation Environment – A Python library for working with atoms
A. H. Larsen, J. J. Mortensen, J. Blomqvist, I. E. Castelli, R. Christensen, M. Dulak, J. Friis, M. Groves, B. Hammer, C. Hargus, E. D. Hermes, P. C. Jennings, P. B. Jensen, J. Kermode, J. R. Kitchin, E. L. Kolsbjerg, J. Kubal, K. Kaasbjerg, S. Lysgaard, J. B. Maronsson, T. Maxson, T. Olsen, L. Pastewka, A. Peterson, C. Rostgaard, J. Schiøtz, O. Schütt, M. Strange, K. Thygesen, T. Vegge, L. Vilhelmsen, M. Walter, Z. Zeng, and K. W. Karsten
Journal of Physics: Condensed Matter 29 (27), 273002 (2017)

X An introductory example of machine learning enhanced global optimization
S. Meldgaard, E. L. Kolsbjerg, and B. Hammer
Submitted to The Journal of Chemical Physics

XI Reinforcement learned chemical intuition used to build atomistic structures from nothing
M. S. Jørgensen, E. L. Kolsbjerg, T. Jacobsen, H. L. Mortensen, S. A. Meldgaard K. H. Sørensen, and B. Hammer
Manuscript in preparation

Abbreviations

Notation	Description
Amp	Atomistic Machine-learning Package.
APE	adsorption potential energy.
ASE	Atomic Simulation Environment.
AutoNEB	automated nudged elastic band.
CI-EB	climbing image elastic band.
CI-NEB	climbing image nudged elastic band.
DFT	density functional theory.
DFTB	density functional tight-binding.
EA	evolutionary algorithm.
EB	elastic band.
EMT	effective medium theory.
fd	finite difference.
GA	genetic algorithm.
GGA	generalized gradient approximations.
IDPP	image dependent pair potential.
LCAO	linear combination of atomic orbitals.
LDA	local density approximation.
LEA	learning evolutionary algorithm.
MEP	minimum energy path.
ML	machine learning.
NEB	nudged elastic band.
NN	neural network.
PAW	projector augmented wave.
PBE	Perdew-Burke-Ernzerhof.
PES	potential energy surfaces.
PW	plane wave.
RPA	random phase approximation.
STM	scanning tunnel microscope.
TPD	thermal desorption spectroscopy.
TS	transition state.
vdW	van der Waals.
XC	exchange-correlation.

CHAPTER 1

Introduction

I have had the privilege to be involved in a wide span of projects concerning heterogeneous catalysis. The projects include both small and large organic molecules on transition metal surfaces, functionalization of supported graphene, studies of ammonia on TiO_2, and examination of reactive metal nanoparticles. Even though the individual projects may be seen as disconnected at first there are several common themes embodied throughout; namely how several theoretical tasks in catalysis can be investigated effectively and systematically. Especially the challenge involved in locating the correct atomic arrangement of key participants, along studies of their mobility, and interactions on surfaces. Locating reaction barriers belong to the list of recurring exercises in catalysis and an exciting challenge touched upon in all my projects. First the scene is set with an introduction to the astronomical social benefits of catalysis advancement along with methods of how to study catalysis for further improvements. This is followed by an outline of the content included in the thesis.

1.1 Catalysis and society

One of the most prominent inventions of the twentieth century is arguably the production of ammonia via the Haber-Bosch process – a Nobel Prize winning accomplishment [1]. The capability of sustaining the rapidly grow-

ing world population relies on the proficiency of producing enough food, and ammonia is undeniably one of the most important fertilizers used for growing crops. On the upside it has "saved" millions of lives from starvation, but on the downside it has come with the cost massive amount of casualties from cheap efficient explosives produced from the easy accessible ammonia [2]. Despite its ambiguous use, it is a key example of a heterogeneous catalyzed reaction, which is the preferred type of catalyst in industry. The preference originates from the catalysts being separate from the product and reactants, which allow for easy reuse. In the case of the Haber-Bosch process, the catalysts are solid while the reactants and product are in the gas phase. The synthesis of ammonia can be catalyzed by a range of solid catalysts, but the most popular are based on iron oxides with some additional promoter material. This highlights the fact that there rarely is a single catalyst, which works for a specific reaction. Rather a series of catalyst systems can be used. Not all catalysts are equally efficient and the search for the "silver bullet" is exactly what drives the studies, discoveries, and designs of new catalysts. The world is always eager for new, better, and cheaper catalysts. The different ammonia catalyst systems are common examples obeying the Sabatier principle, where the combination of materials allow for the right binding strength of key reactants, not too strong nor too weak, while at the same time facilitating the chemical reaction by weakening intermolecular bonds [3]. Visualization of the adsorbate binding strength is usually done by so-called volcano plots where the reactivity of a given chemical reaction is plotted against the adsorption strength as shown in Figure 1.1 [4]. Generally, the most reactive catalysts adsorb molecules with a binding strength in the midrange of adsorption energies, but many additional material properties are important for the catalytic prowess.

Heterogeneous catalysis is a central part of many industrial processes. Examples include refinery of petroleum [5], fine chemical production in both the pharmaceutical and agrochemical industry [6], and hydrogen production by water splitting in steam reforming [7] just to name a few. Catalysis is across all applications a billion-dollar industry as 90% of all used chemicals are produced by the use of catalysis. Globally, an estimated 30% of all gross product depend on some type of catalyst [8]. The society's tremendous dependency on catalysis is the reason why studies in catalysis are extremely beneficial for the global development. Even minor advances can reduce energy consumption in chemical production or reduce pollution, which can have huge remedy. Catalysis can also be used to promote chemoselectivity by lowering the barrier for a specific reaction, hence reducing the production of unwanted side products [9–11]. They are even capable of promoting

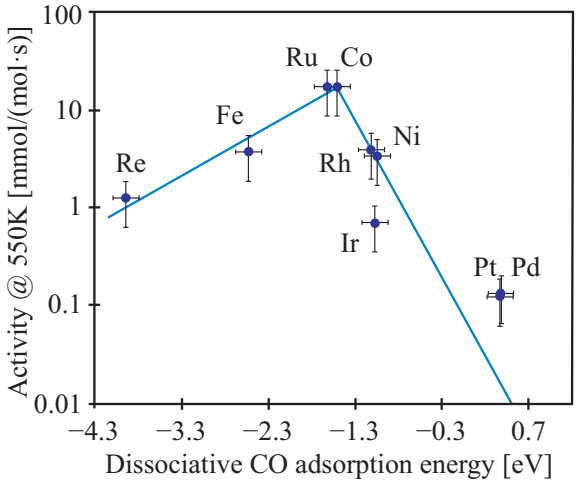

Figure 1.1 | Volcano graph of the activity of the methanation process as a function of dissociative CO chemisorption energy on different supported metals. The figure is adapted from [4].

a desired chirality, which is tremendously important for several pharmaceutical products [12–15]. The importance of the chirality in pharmaceutics derive from unique enantiomer specific interactions. This is a result of the natural evolution of biological systems, which has evolved to prefer one enantiomeric handedness over the other [16]. In best case, only one of the enantiomers is the active compound of a pharmaceutical application while the other is harmless, yet in the worst case the wrong enantiomer can inflict tremendous harm best exemplified with the previous use of thalidomide [17, 18]. Thalidomide was in the late fifties and early sixties considered a wonder drug alleviating nausea and morning sickness experienced by pregnant women. While both enantiomers work as a sedative, the *S*-enantiomer had severe side effects on the fetus development. A large number of affected infants were born with malformed limbs and many even died at a young age [19, 20].

1.2 Development of catalysis

The advancement of catalysts has over the last century been dominated by trial-and-error approaches, as the basic understanding of how and why the specific catalysts work have been lacking. With the development of surface science techniques such as X-ray photoelectron spectroscopy, low-energy electron diffraction, thermal desorption spectroscopy (TPD), and

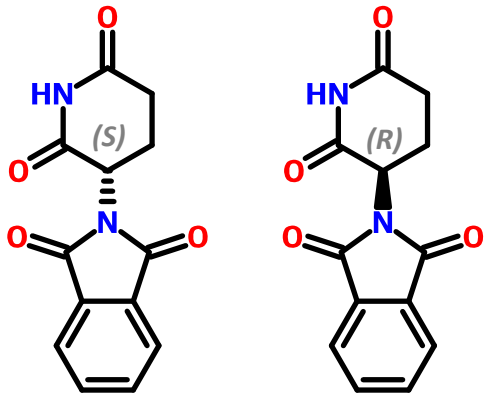

Figure 1.2 | Thalidomide has one chiral center and hence exist as both a *R*- and a *S*-enantiomer. Both works equally well as a sedative but the *S*-enantiomer has severe teratogenic side effects [19].

scanning tunnel microscope (STM) combined with the advances in theoretical calculations, the field has now moved into an era based on increased understanding. Advances of catalysts can now be guided by knowledge gained from these techniques and not only by random discovery. Today, the acquired knowledge of catalysts is not only used for explaining the observed properties but have opened the door for making qualified predictions. This is truly exciting, a trend that will only continue to develop with the potential of enabling tailor made catalyst systems designed from scratch.

When designing new catalysts, it requires an initial idea of a possible synthesis scheme through which an intermediate reaction is going to proceed [21]. From the designed virtual reaction mechanism, key rate determining steps must be isolated. It is in each of these decisive steps a catalyst must be designed to facilitate. Picking the right material to aid the desired mechanism can be heavily accelerated by profound understanding of the specific processes. Theoretical models shine in this regard, providing a method to model and understand the small individual steps. By understanding the driving mechanisms, it is possible to suggest further improvements to the catalyst system. It is exactly in this domain my contributions reside as my work covers a wide spectrum of theoretical heterogeneous catalysis systems. The work touches on some of the many computationally challenging subjects within the field. The main focus is turned towards resolving the reaction barriers of different recurring catalytic processes. This includes, but are not limited to, construction of reliable model systems to locate reaction paths and in particular transition states (TSs) by thorough and systematic navigation of the convoluted energy surfaces. The method for narrowing

down a minimum energy path (MEP) in a complex energy landscape and finding its corresponding TS has been dominated by the nudged elastic band (NEB) [22, 23] method and its deviates [24–29] for the last couple of decades although several other accomplished alternatives do exist [30]. By simply browsing through the thesis it should be clear that the NEB framework is also the choice for this endeavor.

To describe theoretic catalytic model systems the standard method is undoubtedly density functional theory (DFT), which is also the method of choice for this thesis. From the DFT calculations, the total energy and atomic forces are among other available, which is used to describe the potential energy surface of the studied systems and reactions. It has without doubt been the most popular electronic structure method for the last fifty years [31]. This is emphasized by two DFT articles residing in the top-10 of most cited papers ever, otherwise dominated by biological lab techniques. Even though the success of DFT lies in its cost-efficient nature, it is still relative expensive for large system sizes. This is why calculation of large systems historically have been done using cheaper empirical model potentials, which comes at the cost of reduced precision. However, a new player, machine learning (ML), has emerged and entered the field to disrupt this – a new era is on the rising [32–35]. The different ML regression methods excel at fitting arbitrary functions like DFT potential energy surfaces, hence it is a great alternative to both pure DFT and empirical potentials when efficiency is demanded. It is an advancing field with tremendous prospects and hence my concluding efforts and the final part of the thesis has been focused on implementing ML into tasks previously monopolized by DFT.

1.3 Thesis outline

The thesis is composed of seven chapters each containing separate themes. As most of the material presented in this thesis is published, each chapter serve as an extended review of the different topics covered in the published material. Even though the included material originates from different distinct projects, additional unpublished material is included in all but chapter 5 in the attempt at creating a consistent thread throughout the thesis. The published material associated with this thesis is included in the appendix. As the chapters are condensed stories the reader is referred to the manuscripts for further details especially when concerning experimental collaborations.

Chapter 2: This chapter covers an introduction to DFT in a practical

computational setting as well as a short overview of a used and trained scheme for ML potentials.

Chapter 3: The pitfalls and difficulties of locating TSs are discussed as well as different systematic tricks, schemes, and algorithms I have developed and used throughout the different projects. Different examples of located barriers from collaborative works are shown for support.

Chapter 4: In this chapter two aromatic molecules, pyridine and naphthalene, are studied on Pt(111). The emphasis is on how to construct reliable theoretical model systems and using systematic approaches to build and cover diffusion reaction networks. These systematic searches unravel with confidence the adsorption and diffusion processes and barriers.

Chapter 5: I have contributed with the theoretical part of a paper concerning molecular self-assembled corrals on a range of transition metals, which is discussed in this chapter. The focus is to resolve the interactions driving the corral formation.

Chapter 6: The main topic of this chapter is to find the global minimum structures of different sized supported Pt nanoparticles. The structures are located with a ML enhanced evolutionary algorithm (EA) developed for these types of problems.

Chapter 7: Finally, the thesis is wrapped up with a conclusion and a look towards how the theoretical quantum chemistry is now heading in to a new era dominated by ML enhanced calculations and predictions.

CHAPTER 2

Computational methods

This chapter outlines the main theoretical methods utilized to obtain the results presented in this thesis. In particular the basics of the DFT framework and how it is used in practice is discussed, but also a neural network (NN) scheme used for atomic potential fitting is briefly reviewed.

2.1 Density functional theory

Modern days material and surface science studies have evolved to a state where electron structure calculations have almost become the *de facto* standard as either the means of deriving fundamental understanding by itself or as a key complementary to experimental observations. The go-to formalism for such electron structure calculations is the DFT method. It has emerged as a wide spread tool spanning many fields of natural science as visualized in Figure 2.1. The core strength of DFT is its efficiency while still delivering surprisingly accurate results. It might lack some of the finer precision of the Post-Hartree-Fock quantum chemistry methods like coupled cluster or Møller-Plesset, but for many applications the DFT precision is very good and more than enough to describe trends and differences [36–38].

Common for electron structure calculations are their aim at solving the N-electron Schrödinger equation. In DFT this is achieved not by directly solving the Schrödinger equation for the N-electron wave functions but in-

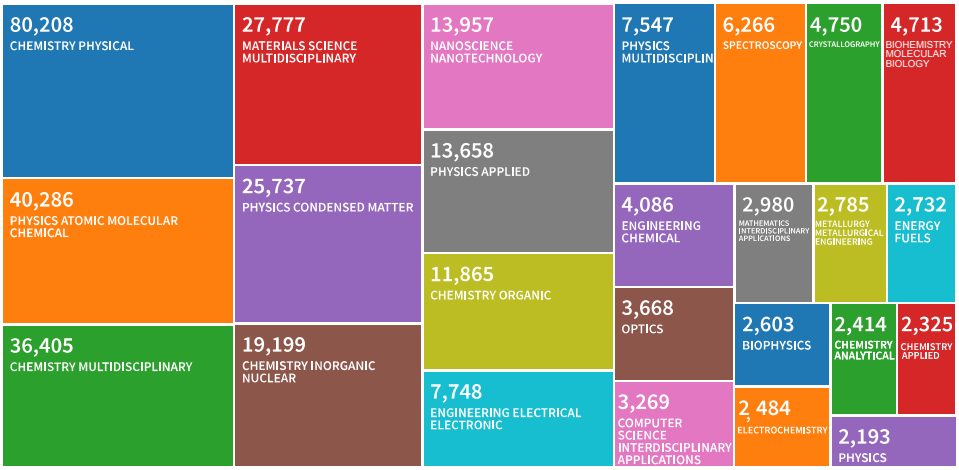

Figure 2.1 | The number of articles of all time including the words "density functional theory" or "DFT" categorized into different science fields (from Web of Science).

stead focusing on the density of said electrons. The foundation for this formalism was formulated by Hohenberg and Kohn in two theorems [39]. The first, in short, states how a system's ground state total energy can be formulated as a functional of the electron density. They showed, very elegantly, that this must be true by examining two external potentials that differ from each other by no more than a constant. They showed that these two potentials would give rise to a unique density to the ground state, and hence that all properties of the ground state must be contained in the density. The second Hohenberg-Kohn theorem states that the ground state energy, E_0, can be obtained via the variational principle by minimizing the total energy from a trial density. Thus, by treating electronic and atomic nuclei motion independently as suggested by Born and Oppenheimer [40] the electronic wavefunctions, and hence the density, will only depend on the electrons themselves. The ground state energy can then be written as:

$$E_0 = \min_{\rho(r)} \left\{ T[\rho] + V_{\text{ee}}[\rho] + V_{\text{ext}}[\rho] \right\}, \tag{2.1}$$

where ρ is the density, T the contribution from the kinetic energy, V_{ee} the electron-electron interaction, and V_{ext} representing the interaction with an external potential. Of the three terms, only the latter is trivial to evaluate. Historically, the next step towards practical use was achieved by Kohn and Sham [41] when they suggested to split the kinetic energy into two terms; one easily expressed by a fictitious term describing a system of non-interacting electrons, T_s, and a term containing the difference to the real

kinetic energy of interacting electrons. They further suggested to treat the electron-electron interaction much the same way by describing the majority of the interaction by a classic Coulomb repulsion term, V_H. They then grouped the non-classical part of the electron-electron interaction with the missing part of the real kinetic energy into the famous exchange-correlation (XC) functional, E_{XC}, leaving the final expression for the total energy as:

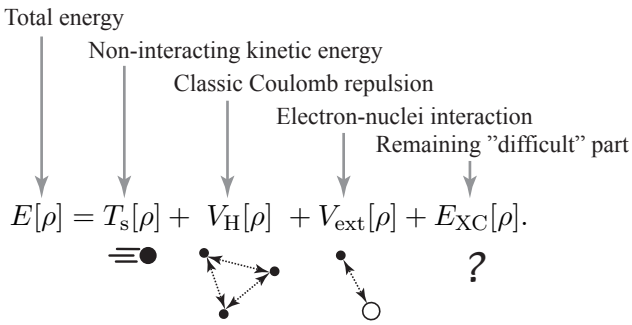

$$E[\rho] = T_{\mathrm{s}}[\rho] + V_{\mathrm{H}}[\rho] + V_{\mathrm{ext}}[\rho] + E_{\mathrm{XC}}[\rho]. \tag{2.2}$$

2.1.1 Choice of exchange correlation functional

In theory, every mathematical suggestion by Kohn and Sham has kept the DFT theory exact (within the Born-Oppenheimer approximation), but in practice the XC term containing all the unknown cannot be expressed analytically. A significant number of different approximations have been and still are derived to cater this rigorous problem, and even worse there is no systematic way of improving the methodology. The convention for distinguishing the different E_{XC} is instead a so-called Jacob's ladder as imaged in Figure 2.2. At the bottom at the first rung above the earthly level the family of local density approximation (LDA) functionals are located [42, 43], which include terms directly dependent on the density. Most LDA functionals are derived entirely from a homogeneous electron gas model and perform only well on solid-state problems [44]. Advancing a step up the ladder to the generalized gradient approximations (GGA) the XC functionals now also include terms dependent on the derivative of the density. One of the most applied functionals in physical surface science is the Perdew-Burke-Ernzerhof (PBE) functional [45], which reside this rung. It is used throughout the work contained in this thesis. Transforming the LDA approximation into the PBE functional is based entirely on fundamental constants, i.e. it includes no fitted hyperparameters, and hence the PBE functional behaves

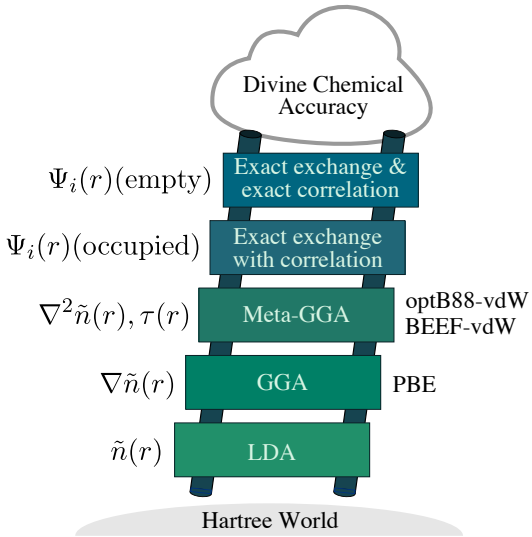

Figure 2.2 | A Jacob's ladder representation of the hierarchy of XC functionals as proposed by Perdew and Schmidt [46].

well for a wide variety of systems. The PBE functional was thus used for the published calculations in Paper II, VII, and X.

Some properties though, like the long-range van der Waals (vdW) interactions, are generally not described well with GGA functionals, and hence should be treated with at least functionals occupying the third rung – the rung containing META-GGA functionals. At this rung, the E_{XC} also involves the kinetic energy density, which can be expressed as

$$\tau = \frac{1}{2}\sum_n f_n \left|\nabla\psi_n(\mathbf{r})\right|^2, \tag{2.3}$$

with f_n representing the n'th orbital occupation number. For some systems, like aromatic molecule adsorption on transition metals, a good description of the vdW interactions is a requisite for capturing the right chemistry. The non-local optB88-vdW functional [47] is exactly designed for such systems and is shown to perform excellent for molecular adsorption on transition metals [48, 49]. Systems composed of molecules interacting with transition metal surfaces are well represented in the present work, which is why the optB88-vdW functional has been used for the final calculations in the projects documented in Paper I, III, IV, V, VI, and VIII. The optB88-vdW functional is constructed by a GGA exchange energy, namely the reoptimized B88 exchange, and a two-part correlation energy – one part from LDA and one "new" non-local vdW part as suggested by Dion *et al.* [50].

Returning to Jacob's ladder, the fourth rung is reserved for the so-called hyper-GGA functional. To live up to the criteria of this rung, the XC functionals need a portion of the exact exchange from Hartree-Fock theory incorporated. Of these functionals the B3LYP is by far the most used [51]. Moving to the fifth rung and beyond also part of the exact correlation is included, which is a field of study on its own but not discussed further here.

The consequence of climbing the ladder to gain accuracy is at the cost of computational time, which is the main reason for using functionals from the bottom rungs. Hence, "shopping" for a fitting functional for the precise study that describes the relevant physics/chemistry at a reasonable tariff is a common strategy, which is also used for this work.

2.1.2 GPAW

Even with the reference work of Hohenberg, Kohn, and Sham and the discussion of the E_{XC} there are several numerical challenges still to be confronted before any practical DFT calculations can be performed. Throughout this thesis, the DFT calculations presented are all conducted with the grid-based projector augmented wave (PAW) code, GPAW [52], which precisely handles these issues. As the name indicates the wavefunctions in GPAW are transformed into smooth wavefunctions within the PAW formalism as this is numerically convenient [53]. Furthermore, most modern electron structure codes greatly enhance the numerical efficiency by applying the frozen core approximation circumventing the need to treat relativistic, rapidly oscillating core states. Effectively, only the valence electrons participate in chemical reactions and bond formation, which justifies the approximation. The core states of the PAW setups are generated once for each species from an all-electron calculation from an isolated atom, and only the valence electrons are treated explicit in each calculation. GPAW provide various basis sets for the wave functions formally a linear combination of atomic orbitals (LCAO), a finite difference (fd), and a plane wave (PW) description. Of these, GPAW is famous for representing wave functions, densities, and potentials on real-space uniform grids as is utilized within the LCAO and fd frameworks. The LCAO method works by expanding the Kohn-Sham pseudo wave functions onto a set of atomic-like orbitals. Computationally, this is considerably cheaper than its two counterparts but its accuracy is limited by the quality of the chosen atomic basis, and it is extremely difficult to converge calculations in relation to said basis. Typically, the geometries obtained by structure optimization within the LCAO framework are of sufficient accuracy while the energy ordering of structures/adsorption

configurations can be wrongly sorted relative to the more precise fd and PW methods. Throughout this thesis, the LCAO method has been used for screening procedures and for testing general algorithms where the exact energy is of lesser importance as is the case for Paper II and X. The fd basis is the most used methodology in the present work as it has been applied in Paper I, III, IV, VIII, and VI where the wave functions are expanded onto a real space grid. The fd is competitive in accuracy with the very commonly used PW method but offer better scalability as it is possible to parallelize over bands, k-points, spins, as well as grid points. This allows calculations to be parallelized over ~200 CPUs on systems of up to 300 atoms as is for instance needed in Paper III for the studies of large organic molecules adsorbed on metal surfaces. The fd calculations converge well with decreasing grid spacing typically resulting in values ranging from 0.20 to 0.17 Å. However, there are drawbacks of the fd basis: namely a larger memory footprint and the so-called egg-box effect [54]. Especially the latter is problematic when trying to train a NN to mimic the DFT potential energy surface. Therefore, the PW method, which inherently has no egg-box error, is used exactly for training a NN in Paper VII.

To manage and visualize atomic simulations, the Atomic Simulation Environment (ASE) python package [55] has been extensively utilized. ASE offers an interface to a large number of electron structure codes, GPAW included, as well as a wide range of plug-and-play modules/implementations all very relevant in modern materials science studies. A range of these easy customizable methods, like the NEB (and AutoNEB), the Tersoff-Hamann STM topography, vibrational analysis, and the EA have all been applied in the work contained in this thesis.

2.2 Neural network modeled potential energy surface

As already touched upon there are several ML methods and strategies, which have been developed to describe potential energy surfaces for atomistic calculations. In this work (Paper VII) a NN atom-centered regression model formulated by Behler and Parrinello [33] has been used and is very briefly discussed in this section. The training and subsequent energy/force predictions are performed with the Atomistic Machine-learning Package (Amp) [56], which integrates closely with ASE making any calculator implemented in ASE a possible parent method for the trained ML method.

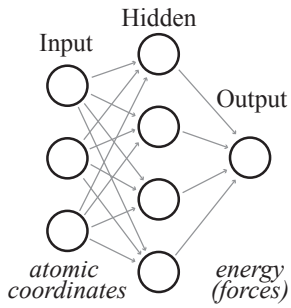

Figure 2.3 | A schematic representation of a simple feedforward NN. The input could for instance be the atomic features for a configuration of atoms and NN output could be the energy of the system.

In short, NNs are basically mathematical formulations heavily inspired by the biological NN in our brains [57]. In principle are NNs just very flexible mathematical functions that can be fitted to an arbitrary dataset. There are many variations of NNs, but in the most basic form they consist of an input layer, a number of hidden layers, and an output layer as imaged in Figure 2.3. The parameters used in the connections between the different neurons are optimized e.g. by backpropagation to fit a set of training data [58]. The trained NNs can afterwards be used to predict new values when presented with new data. It could be trained on a set of atomic structure energy relations building up a potential energy surfaces (PES) to be used to predict energies of new alike structures.

It is customary when fitting a PES, $E(\mathbf{R})$, to first map the M training data, whether it originates from DFT or some other quantum chemical method, from an internal coordinate space, $\mathbf{R}$, to some feature space with feature vectors, $\mathbf{G}$. The feature vector and energy pairs are then used to perform the regression (or optimizing the NN parameters) to construct the ML function $\bar{E}(\mathbf{R})$:

$$\begin{aligned}
&\{(\mathbf{R}_1, E_1), (\mathbf{R}_2, E_2), ..., (\mathbf{R}_M, E_M)\} \\
&\xrightarrow{\text{Feature map}} \{(\mathbf{G}(\mathbf{R}_1), E_1), (\mathbf{G}(\mathbf{R}_2), E_2), ..., (\mathbf{G}(\mathbf{R}_M), E_M)\}. \\
&\xrightarrow{\text{Regression}} E = \bar{E}(\mathbf{G}(\mathbf{R}_i))
\end{aligned} \tag{2.4}$$

It is well established that the transformation to an appropriate feature space is needed for ML methods designed for transferable systems. The feature representation of the atomic positions needs to be invariant to permutations of same-type atoms and translation/rotation of the whole system

– a specific atomic configuration should have the same energy no matter the ordering of atoms or orientation/location in a given super cell. Furthermore, a good descriptor should transfer the essential atomic environments, otherwise, important information will be extremely hard to capture during the regression. One choice, a set of well tested descriptors, are the so called Behler-Parrinello symmetry functions. These symmetry functions are in principle atom-centered meaning that a set of functions located on each atom describe the local chemical environment around said atom. By constructing a set of symmetry functions centered on each atom, i, the total energy, E, from the regression formulated in Equation 2.4 becomes a sum of atomic energy contributions, $\bar{E}_i$, given by the local environments as

$$E = \sum_{i=1}^{N_{\text{atoms}}} \bar{E}_i. \tag{2.5}$$

To confine the local environments around the atoms a cutoff function, R_c, is incorporated into the symmetry functions, which smoothly decreases to zero at some distance. In this work the cutoff function,

$$f_c(R_{ij}) = \begin{cases} \frac{1}{2}\left[\cos\left(\frac{\pi R_{ij}}{R_c}\right) + 1\right] & \text{, for } R_{ij} \leq R_c \\ 0 & \text{, for } R_{ij} > R_c \end{cases}, \tag{2.6}$$

takes a cosine form until R_c is reached from which it is zero. Two Behler-Parrinello symmetry functions with different properties have been used: one to catch the radial distribution of atoms, G^2, and one to describe the angular arrangement, G^4. The G^2 is, within the cutoff sphere, composed of a sum of products of the cutoff function and a set of Gaussians of varying width, η, and center, R_s,

$$G_i^2 = \sum_{j \neq i}^{N_{\text{atoms}}} e^{-\eta\left(R_{ij} - R_s^2\right)/R_c^2} \cdot f_c(R_{ij}). \tag{2.7}$$

Thus, different regions of radii and size are explored by a combination of diverse but appropriate η and R_s values. Probing the angular three body components centered on atom i is done for all possible triplets of atom i, j, and k through the G^4 symmetry function:

$$G_i^4 = 2^{1-\zeta} \sum_{\substack{j,k \neq i \\ (j \neq k)}}^{N_{\text{atoms}}} (1 + \lambda \cos\Theta_{ijk})^{\zeta}\, e^{-\eta\left(R_{ij}^2 - R_{ik}^2 + R_{jk}^2\right)/R_c^2} \cdot f_c(R_{ij}) f_c(R_{ik}) f_c(R_{jk}), \tag{2.8}$$

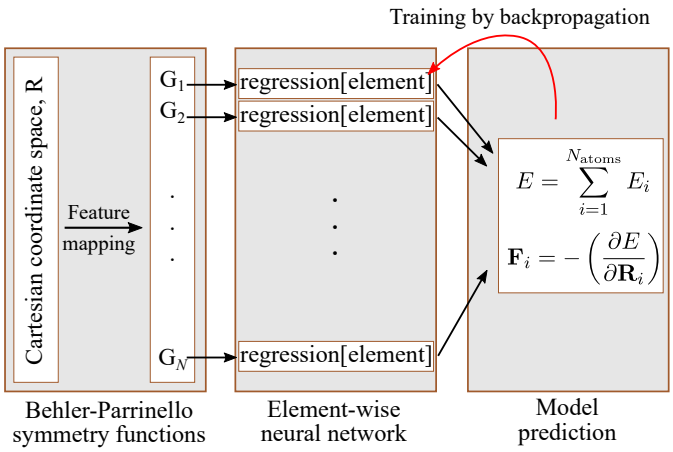

Figure 2.4 | The procedure of modeling energy predictions follows first a mapping of atomic positions into a feature space pursued by regression on a per atom basis.

where the hyperparameters ζ, λ, and η allows for different probing components of G_i^4.

As atoms of the same species are invariant to permutation, the same NN can be reused, and hence only one NN per atom type is constructed in the Behler-Parrinello framework. It is well known that the force is found as the gradient of the potential energy surface, and since the Behler-Parrinello symmetry functions are differentiable, the forces can be calculated in relations to the cartesian coordinates such as the ML model can be used as a regular force-field.

To have a working ML model it has to be trained. In the case of NNs there are several different ways to optimize the parameters for improved description of the training data. The most common choice is a backpropagation scheme where in this case a squared-error loss function is minimized. This is straight forward as the symmetry functions can be analytically differentiated. As a lot of information about the PES not only is located in the total energy but also in the forces experienced by the atoms, the forces are included in the model fitting through the loss function. The loss function hence takes the following form:

$$\Gamma = \frac{1}{2}\sum_{j=1}^{M}\left\{\left(\frac{\bar{E}}{N_j} - \frac{E_j}{N_j}\right)^2 + \frac{\alpha}{3N_j}\sum_{k=1}^{3}\sum_{i=1}^{N_j}\left(\bar{F}_{ik} - F_{ik}\right)^2\right\}, \tag{2.9}$$

where F_{ik} and $\bar{F}_{ik}$ are the parent and ML predicted forces on atom i in the kth direction. α is an adjustable parameter, which can be tuned such that the forces and energy prediction converge together.

A full description of the strategy is demonstrated in Figure 2.4: First, the structure coordinates are transformed into a feature space before each local feature vector enters an element-specific NN, which predicts the local energy and force. Finally, the total energy is calculated as a sum of the local energy contributions.

CHAPTER 3

The "art" of locating transition states

A common theme throughout the thesis is the aim of locating the lowest laying transition state whether it is for a diffusion process, a chemical reaction, or a configurational transformation. The "art" of how to effectively and systematically explore the immensely large configuration space of atomic systems is the topic of Paper II and this chapter. Some of the discussed technology is demonstrated on "real" examples from Paper IV, VI, and VIII.

A vital number in reaction chemistry is the height of the energy barrier, and hence the obsession of locating the right TSs between relevant transformations. As the TSs sit at the top of the MEP between two neighboring minima, the theoretical approaches are often centered around locating an approximate MEP before trailing it to a first order saddle-point. In principle it is possible to follow a minimum mode, an exact or approximate Hessian from an initial state to a final state as the path will naturally transition through a saddle-point. To follow the reaction path from an initial point is what is known as a single-ended search method, and it is the principle of the Lanczos [59] and the dimer methods [60]. Following the gradient of the energy landscape has some advantages but is in general expensive. More importantly the end point cannot be chosen manually, which is often desired.

Hence, a more feasible approach is to use a double-ended chain-of-state method like the NEB [22] method. Starting from an initial interpolated path, it is optimized towards the MEP before the TS is located with a gradient based method. The NEB method works by optimizing a path constructed by a set of images connected by nudged springs to a MEP in the immediate vicinity of the initial path. Throughout my projects, the above has been the schematic opting to use the climbing image nudged elastic band (CI-NEB) [23] method to locate the TS from a good initial guess. When the CI-NEB is invoked during the optimization the highest energy image do not experience the pull from the nudged springs. Instead it moves uphill parallel with the current path to the TS by inverting the forces parallel to the tangent of the path while keeping the real perpendicular forces.

This is mainly a methodology chapter where several pragmatic solutions developed in-house for effective TS "hunting" are discussed in the context of authentic obstacles met in real systems. Two of the examples shown arise from experimental collaborations. The first example originates from studies of graphene hydrogenation in collaboration with Line Kyhl in Liv Hornekær's lab. The second example stems from investigating ammonia diffusion on TiO_2 where the experimental part was mainly conducted by Kræn Adamsen in Jeppe Vang's lab.

3.1 Challenges in the search for transition states

As quickly touched upon, there are several obstacles when locating reaction barriers. First, how to locate the "right" in a multiple of TSs without knowing beforehand, hence searching through configuration space effectively. Secondly, highly dimensional energy landscapes offer many local minima and valleys, which can be tricky to navigate with an insufficient density of images. Last but not least, it can be computationally very expensive to fully converge pathways to the MEP and locate the TS. All three points are discussed in the following subsections.

3.1.1 Exploring several initial transition paths

Even though a TS is successfully obtained by the CI-NEB method, or some other method for that sake, it does not necessarily correspond to the TS of the lowest energy path between two minima. This exact issue is illustrated in Figure 3.1 for Pt diffusion on a stepped Pt(211) surface, with an almost fully Ag decorated edge. The model system is viewed from the side and top in Figure 3.1**a** and **b** respectively. The bare surface is fully constrained,

which allows a mapping of the potential energy surface as a function of the x-y coordinate using a Pt atom as a probe while only relaxing the z coordinate. The scan results are plotted in Figure 3.1**c**. On top of the energy landscape is a optimized NEB path (red) for diffusion of a Pt atom from one minima to another plotted. The path originated from the (white) linear interpolated path. It is evident that the path did not converge to the true MEP but passes through a higher laying TS. A path following the true MEP between the two minima can for instance be seen in Figure 3.1**i**.

How to construct the lowest energy path on this model surface is of course obvious as the whole energy surface is mapped, but such a surface is completely impossible both to map and illustrate for systems with more than a couple of degrees of freedom. As it is possible to plot the energy landscape for this system it is perfect for illustrating different strategies for exploring alternative paths, namely a method of jumping between adjacent minima and a scheme of mixing in neighboring minima in the initial guessed paths. Both strategies require knowledge of other minima on the potential energy surface, which can be found by numerous, preferably systematic, approaches.

With the knowledge of the local minima, a stepwise construction of a full pathway is possible as illustrated in Figure 3.1**e-i**. In the figure, increased numbers of minima are added to a full path down the column. Each interlinked minimum corresponds to a transformation, which is treated as a regular transition. In the end there will often be several unique routes from the initial to the final state and the problem boils down to picking the complete path with the lowest critical TS. The ”minima hopping” approach described here is applied in the search for diffusion pathways for pyridine and naphthalene on Pt(111) (Paper I and V) discussed in the following chapter.

An alternative or additive strategy to increase the search space, and hence the likelihood of finding the lowest possible TS, is to construct a subset of initial reasonable guessed paths. One way to do this is to mix in minima in the immediate neighborhood of the transition path as is illustrated in Figure 3.1**d**. First a projection of a neighboring minimum, $\mathbf{R}_{L,i}$, onto the line that directly connects the initial, $\mathbf{R}_I$, and final, $\mathbf{R}_F$, images defines the ”support” image,

$$\mathbf{R}_s = \mathbf{R}_I + \gamma_i(\mathbf{R}_F - \mathbf{R}_I), \tag{3.1}$$

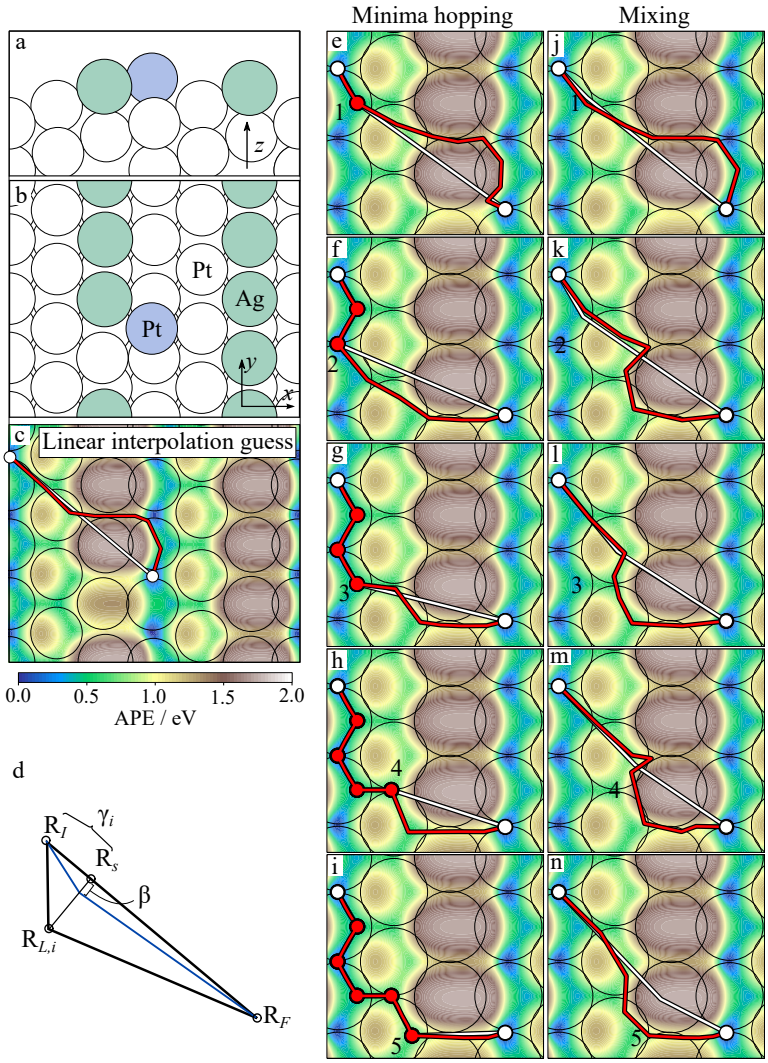

Figure 3.1 | **a** and **b** shows a model composed of a Ag decorated Pt(211) surface. The diffusing Pt atom is colored light blue while the stationary Ag edge atoms are painted green. The energy landscape experienced by a Pt atom is plotted in **c** with a converged NEB path (red) starting from an initial linear interpolation (white). The mixing scheme is sketched in **d**. **e-i** shows the gained detail of adding intermediate stepping stones that allows the "minima hopping" strategy to complete a path, which is the true MEP. **j-n** shows that when the initial interpolated path includes mixing in neighboring minima other pathways emerges. Some of these paths also passes the lowest critical TS.

where γ is the size of the projection given by:

$$\gamma_i = \frac{(\mathbf{R}_{L,i} - \mathbf{R}_I) \cdot (\mathbf{R}_F - \mathbf{R}_I)}{|\mathbf{R}_F - \mathbf{R}_I|^2}. \tag{3.2}$$

Each image, $\mathbf{R}_i(\alpha)$, on the modified interpolated path can thus be constructed as a point on the linear interpolation path with an added contribution from the supporting minima as:

$$\mathbf{R}_i(\alpha) = \mathbf{R}_I + \alpha(\mathbf{R}_F - \mathbf{R}_I) + f(\alpha, \gamma_i)\beta(\mathbf{R}_{L,i} - \mathbf{R}_s). \tag{3.3}$$

For a rational behavior of images, which projection lies outside a direct line between the initial and final image a switching function, $f(\alpha, \gamma_i)$, is introduced. $f(\alpha, \gamma_i)$ depends on γ_i and takes the following form:

$$f(\alpha, \gamma_i) = \begin{cases} \frac{\alpha}{\gamma_i} & \text{for} \quad \min(0, \gamma_i) \leq \alpha \leq \max(0, \gamma_i) \\ \frac{1-\alpha}{1-\gamma_i} & \text{for} \quad \min(1, \gamma_i) \leq \alpha \leq \max(1, \gamma_i) \end{cases}. \tag{3.4}$$

Good results have been achieved with $\beta = 0.25$ a value also used in the construction of the initial paths in Figure 3.1**j-n**. As β approaches 1, the mixing instead transitions into a complete jump to the supporting minima like in the case of the "minima hopping" strategy.

It is possible to apply both strategies at once by constructing different variations of the small steps in the "minima hopping" scheme with the mixing strategy. This variation is used in the exhaustive search for diffusion paths for naphthalene on Pt(111) in Paper V.

The simplest form of the minima hopping approach was used in Paper IV. Here the reaction mechanism for hydrogenation of graphene sitting on an Ir(111) surface were studied. It is known for this system that the most stable configuration for two hydrogen atoms is when adsorbed in a so-called meta configuration (Figure 3.2) on the hcp region of the moiré pattern as the graphene is supported by the Ir surface [61]. Several routes besides a direct adsorption into the meta configuration are possible. It could be that H_2 adsorb into a different configuration before diffusion into the meta site as shown in Figure 3.2. It turns out that diffusion is relatively easy but the barrier for adsorption is large (in all cases) though smallest through a direct adsorption.

3.1.2 Dealing with complex energy surfaces

The two strategies described above are the first systematic steps to safely navigate complex energy landscapes. The origin of the many obstacles is extremely delusive but primarily caused by difficulties in visualizing the underlying energy landscape. In the case of the NEB method it is often expressed as obscurely hard convergence problems. Convergence of paths to the MEP and for climbing images to the saddle points are thus unnecessarily extended. The latter is usually the result of a poor guess of the

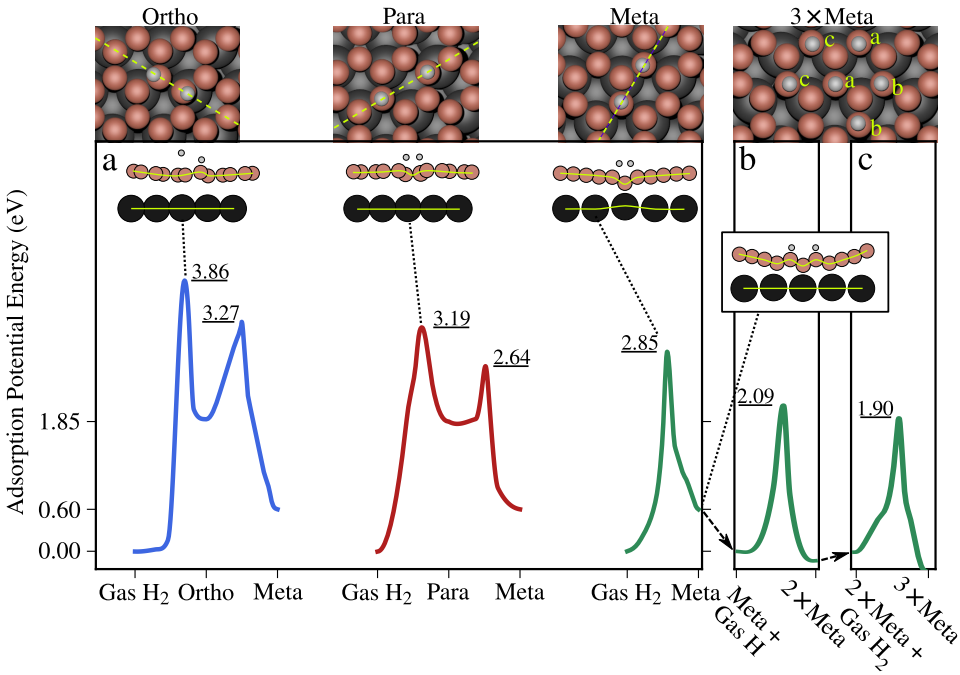

Figure 3.2 | **a** shows the different possible adsorption configurations of H_2 and the corresponding barriers. In a combination with experiments it is concluded that the relative high barrier makes the reaction only accessible for vibrationally excited H_2 molecules. **b** and **c** show that adsorbing more and more H_2 creates and avalanche effect that makes the adsorption process easier for subsequently molecules.

TS compared to the complexity of surrounding energy landscape when the climbing image method is invoked. It is usually an insufficient path resolution – too large configurational changes in between adjacent images – that drives the hardship when trying to converge the complete path. Even though smoother convergence is usually achieved by adding additional images each extra image increases the calculational needs, which especially for expensive *ab initio* calculations is undesirable.

One reason for slowly converging paths is an intrinsic instability within NEB formulation. During relaxation it can result in paths deviating from a more direct MEP. In the NEB formalism the forces acting on an image is split into two parts: the spring force parallel to the estimated tangent and the true perpendicular force from the energy landscape. If adjacent springs are of equal length, the spring force, Equation 3.5, will completely vanish, and the image is purely controlled by the perpendicular true force.

$$\mathbf{F}_i^s|_{\|} = \left(|\mathbf{R}_{i+1} - \mathbf{R}_i| k_i - |\mathbf{R}_i - \mathbf{R}_{i-1}| k_{i-1}\right) \hat{\boldsymbol{\tau}}_i. \tag{3.5}$$

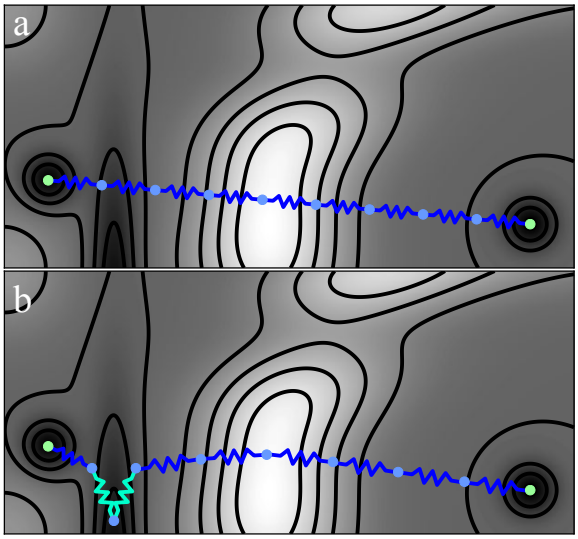

Figure 3.3 | A made up potential energy surface where in **a** an initial linear interpolated path is plotted. **b** shows how the path could look like after a few optimization steps where the intrinsic instability is occurred.

It can be difficult to grasp the consequences in a many dimensional energy landscape, but a designed 2D example is plotted in Figure 3.3**a** where also a linear interpolated path is illustrated. This path could after a few optimization steps be trapped in the state shown in Figure 3.3**b** where the instability is present. The two bright turquoise springs are of equal length and no springs holds the third image back from escaping out at the bottom of the picture along the valley in the potential energy surface.

One way to "cure" this undesired behavior is to introduce real springs, reverting to a slightly different definition of the tangent, while keeping the nudging of the true force. This formalism we refer to as the elastic band (EB) method. The parallel spring force is formulated as:

$$\mathbf{F}_i^s|_{\parallel} = (L_{eq} - |\boldsymbol{\tau}_1|)\frac{\boldsymbol{\tau}_1}{|\boldsymbol{\tau}_1|}k_{i-1} - (L_{eq} - |\boldsymbol{\tau}_2|)\frac{\boldsymbol{\tau}_2}{|\boldsymbol{\tau}_2|}k_i, \tag{3.6}$$

where,

$$\boldsymbol{\tau}_1 = \mathbf{R}_i - \mathbf{R}_{i-1}, \tag{3.7}$$

$$\boldsymbol{\tau}_2 = \mathbf{R}_{i+1} - \mathbf{R}_i, \tag{3.8}$$

$$L_{eq} = \frac{|\mathbf{R}_N - \mathbf{R}_0|}{N-1}, \tag{3.9}$$

and N is equal to the total number of images. In the case that i is adjacent to the highest energy image and the climbing image method is invoked the

formulation changes slightly for a smoother convergence:

$$\Delta V_i^{max} = \max(|V_{i+1} - V_i|, |V_{i-1} - V_i|) \tag{3.10}$$

$$\Delta V_i^{min} = \min(|V_{i+1} - V_i|, |V_{i-1} - V_i|) \tag{3.11}$$

$$\mathbf{F}_i^s|_{\parallel} = \left[(L_{eq} - |\boldsymbol{\tau}_1|)\frac{\boldsymbol{\tau}_1}{|\boldsymbol{\tau}_1|}k_{i-1} - (L_{eq} - |\boldsymbol{\tau}_2|)\frac{\boldsymbol{\tau}_2}{|\boldsymbol{\tau}_2|}k_i\right]\frac{\Delta V_i^{min}}{\Delta V_i^{max}} \tag{3.12}$$

The true force formalism is borrowed from the original NEB method such that the tangent of the path is estimated in the same manner when calculating the true and spring force contributions irrespectively:

$$\boldsymbol{\tau}_i = \frac{\mathbf{R}_i - \mathbf{R}_{i-1}}{|\mathbf{R}_i - \mathbf{R}_{i-1}|} + \frac{\mathbf{R}_{i+1} - \mathbf{R}_i}{|\mathbf{R}_{i+1} - \mathbf{R}_i|} \tag{3.13}$$

$$\nabla V(\mathbf{R}_i)|_{\perp} = \nabla V(\mathbf{R}_i) - \nabla V(\mathbf{R}_i) \cdot \hat{\boldsymbol{\tau}}_i, \tag{3.14}$$

where $\hat{\boldsymbol{\tau}} = \boldsymbol{\tau}/|\boldsymbol{\tau}|$. Each non-climbing image thus experience a total force given as:

$$\mathbf{F}_i = \mathbf{F}_i^s|_{\parallel} - \nabla V(\mathbf{R}_i)|_{\perp}. \tag{3.15}$$

One argument for the current NEB formalism is that it removes the tendency for a real elastic band to cut corners in the energy landscape where the curvature bends by nudging the spring force. The root of the corner cutting can be traced to the springs equilibrium length(s) as the springs are stretched beyond their natural length they will contract shortening the total path length. As real springs are used in the above described EB formalism, this issue is reintroduced and the path will not necessary converge completely to the MEP. The issue is effectively circumvented when searching for TSs as the climbing image method is applied where the highest energy image does not experience any spring forces, and hence do not cut any corners. Getting the remainder of the path *completely* right is of less importance, as it is the TS that holds all the important information – the barrier, the dominating reaction mechanism etc. Examples of CI-NEB and climbing image elastic band (CI-EB) optimized diffusion paths for oxygen on the Ag decorated Pt(211) surface is illustrated in Figure 3.4. When comparing the paths in Figure 3.4**b** with the paths in Figure 3.4**c** it is evident that the CI-NEB method may result in unwanted detours adding unnecessary complexity to the final path. The consequences of the unintended detour are clear when comparing the energy profiles for the 10 image CI-NEB and the 10 image CI-EB in **d** and **c** respectively. The CI-NEB path have an extra bump suggesting a more complex reaction mechanism. For this example,

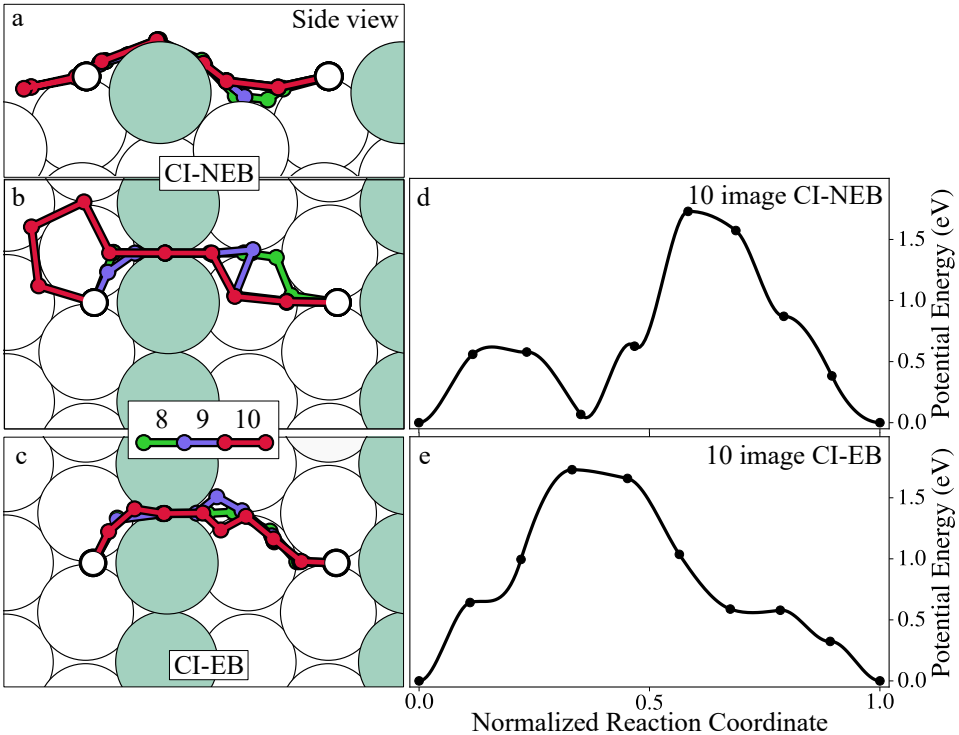

Figure 3.4 | **a** shows the side view and **b** the top view of the CI-NEB diffusion paths for oxygen on the Ag decorated Pt(211) surface. **c** shows a top view of the corresponding CI-EB diffusion paths on the same surface. In **d** and **e** the energy profiles are plotted respectively for the 10 image CI-NEB and the 10 image CI-EB.

it is clearly not a real feature of the natural MEP. Such detours in more advanced reactions might not be so easily spotted, hence why the more conservative EB method with a climbing image seems more pleasing.

3.2 Automating transition state search for efficiency

One of the reasons for not just resolving the path with a high number of images is the resulting computational cost. This is also why it is highly desirable to keep the number of images at a minimum while still being able to resolve the important parts of the path. One way to do this is described in Paper II where an automatic scheme, the automated nudged elastic band (AutoNEB), is outlined. The strategy revolves around how to dynamically add images to the path while converging it, such that the TS can be located

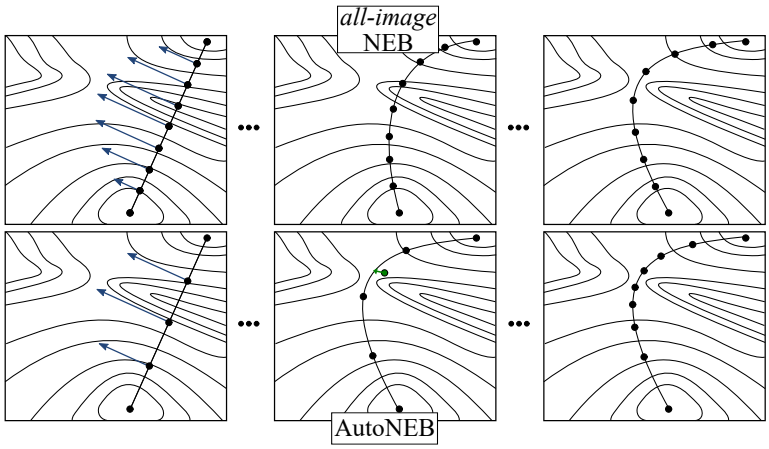

Figure 3.5 | The top panel shows snapshots of how an *all-image* NEB gradually converged to the MEP while optimized. The bottom panel illustrates snapshots of the AutoNEB scheme, where in this example three images are roughly optimized towards the MEP before a new image is added. Finally, the complete path is shown now with a higher density of images around the peak compared to the final *all-image* path above.

reliably and cost efficient. The idea is illustratively compared to the normal way of optimizing a NEB/EB path referred to as an *all-image* NEB in Figure 3.5. The concept is pretty straight forward: First, a rough path with few images is optimized towards the MEP. Afterwards, new images are added iteratively while the path surrounding the newly added image continues to be optimized. New images are added such that the final path does not include too large geometric changes between adjacent images while focusing on resolving the area around the apparent TS. This improve the TS guess before the highest energy image is converted to a climbing image, ensuring easier convergence. What is left is a roughly converged path far from the TS, while the area in the vicinity of the TS is well resolved and well converged. This approach hence reduces the amount of needed resources. For a test system of oxygen diffusion on a stepped Pt(211) surface the amount of force evaluations drop by a factor of ~4.

The AutoNEB has been a consistent technology throughout the various studies. In Paper VIII the scheme was for instance used to find the diffusion barrier for ammonia on anatase-TiO_2 (101). The possible paths were guided by STM movies and movement statistics. After trying different possible routes, the diffusion was finally found to by "catalyzed" by an adjacent ammonia molecule as visualized in Figure 3.6. The stationary molecule act as a hinge allowing a second ammonia molecule to move fairly easy around it on the left side while maintaining a hydrogen bond through the

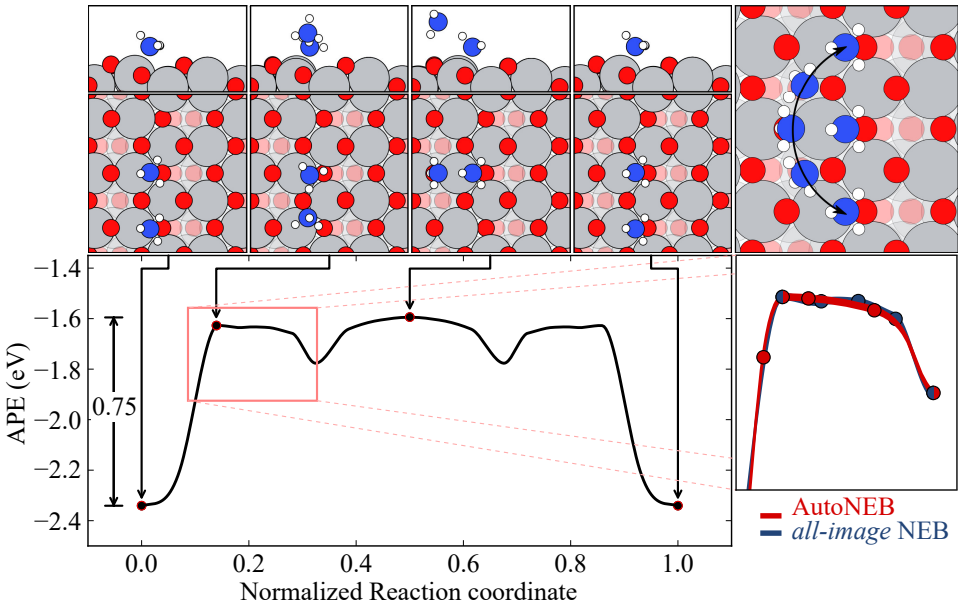

Figure 3.6 | The full diffusion path for NH_3 on anatase-TiO_2 (101) following a route left around a supporting NH_3 molecule. To the right of the supporting NH_3 is a path 0.07 eV higher than the left. Diffusion without any supporting NH_3 molecules is also possible but with a barrier 0.24 eV higher than the left path.

nitrogen to the stationary ammonia. In bottom right corner, a zoom-in on the path in the vicinity of the first saddle-point shows the difference between the AutoNEB scheme and the *all-image* NEB. This sub-part has been optimized with both approaches, and the AutoNEB scheme results in a higher image density close to the saddle-point, which is crucial for a smooth and effective TS convergence.

New images are added on-the-fly in the AutoNEB scheme, which immensely reduces the manpower and computer resources used. It is the combined effect with emphasis on the first that allows for the extensive searches for the most favored diffusion paths for pyridine and naphthalene on Pt(111), which are shown in the next chapter.

3.3 Context

It should be noted that large amount of resources also can be retained if the initial guess for the pathways are as close as possible to the converged paths. This can for instance be done by first minimizing a path with a computational cheap alternative to the final *ab initio* method. One pop-

ular potential is the image dependent pair potential (IDPP) [62], which is used to bring a linear interpolated path into a path that tries to maintain interatomic distances. The method is basically free of charge and is applied extensively in this work. A slightly different strategy is to train (and retrain) a ML potential to mimic the potential energy surface of the transition, which dramatically reduces the required *ab initio* calculations [63]. This idea is also applied in the search for Pt configurational transitions presented in Chapter 6 and Paper VII. All the above discussed strategies and methods can be (and is) rigorously used with the AutoNEB scheme.

There are several other attempts at making TS search algorithms that efficiently and reliably locates TSs. With the goal of stabilizing the optimization towards a MEP, like the present proposed EB method, Trygubenko *et al.* also modified the NEB method [25]. Instead of entirely removing the perpendicular part of the true force as in the NEB method, they reintroduced a portion of it via a double nudging formulation that resulted in more reliable TS guesses. Other pursuits of effective and stable strategies include Zhang and co-workers double-ended surface walking method [64]. It works by building up the reaction path by walking along the MEP from either side towards each other by modifying the PES with Gaussian functions within the Broyden framework. It also includes a radical different strategy suggest by Vaucher *et al.*, which do not try to optimize the geometry of distinct images along the path but optimizes the entire reaction path described by a continuous curve [65]. The reaction path is described by a set of parameters. They suggest two different designs to effectively optimize the parameters by applying a formalism relying on integrals: a cost-based and force-based with the latter closest related to the NEB formalism. It will be interesting to see whether this is a superior technique as the algorithm matures.

The development of multi-step schemes to map reaction networks and find TSs also includes several notable contributions like the ZStruct method [66–68] and a similar method by Suleimanov and Green [69]. Both methods aim at locating relevant intermediates and connecting them with graph techniques while resolving the elementary reaction steps with double-ended optimization methods. An alternative to systematically building up reaction networks to explore different reaction mechanism, as suggested in this work, is for instance Fournier and co-workers swarm intelligence scheme [70]. They allow different "climbers" to explore the PES, exchanging information to find different TSs. Future schemes like this could be very interesting when combined with ML potentials as it is inherently computationally expensive to utilize many workers as would be required for large complex reactions.

Interestingly, the AutoNEB algorithm has in addition been adopted by

the general ML community and has been used to find seamlessly barrier-less paths between distinct local minima in NN energy landscapes [71, 72]. This have changed the way one might interpret minima in the NN space from single points to connected valleys.

CHAPTER 4

Aromatic molecules adsorption and mobility on Pt(111)

This chapter summarizes the main results of Paper I and V in, which the two aromatic molecules pyridine and naphthalene are investigated interacting with a Pt(111) surface. In particular several of the strategies and schemes discussed in the previous chapter are applied in the search for reliable TS estimates.

Understanding the interplay between surfaces and small aromatic molecules is a key component in the field of heterogeneous catalysis, especially, when aiming at deriving models for complete reaction schemes. As a theoretician, several challenges are present when attempting to close the gap between computer simulations and real-world catalytic systems in the prospect of creating a *good model system*. The issues include finite temperature effects (DFT calculations are in principle performed at 0 K), how to include effects from contaminants, and the consequence of chemical pressure, just to mention a few. Even though huge advances have been achieved in this field, it is still by large only possible to construct semi ideal systems within the compromise of the desired complexity and reasonable simplicity.

To investigate the family of small aromatic systems on Pt(111) two key

members have been investigated: pyridine in a purely theoretical study, and naphthalene in a combined theoretical and experimental study where Guillaume Goubert in Peter McBreen's lab at Laval University imaged the molecules by STM.

4.1 Surface interactions

Even though the theoretical systems are models of the real systems, much fundamental knowledge can still be gained. This is also true when studying pyridine and naphthalene interacting with an ideal defect-free Pt(111) surface. One important challenge for a good model is to capture the correct chemistry in the molecule-surface interactions. Thus, the choice of an appropriate functional must be considered. This is evident when comparing adsorption energies for both pyridine and naphthalene. Important examples calculated with the PBE and optB88-vdW functionals are listed in Table 4.1 in relation to the adsorption sites illustrated in Figure 4.1. It is well known that the delocalized π-orbitals in aromatic molecules are prone to introduce important vdW interactions, both with neighboring molecules as well as the underlying surface. This is also revealed by the absorption energy calculations where the vdW corrected optB88-vdW functional estimates a higher adsorption energy than the PBE functional. Even though a comparison of the ideal conditioned calculated adsorption potential energies (APEs) to experimental values might shed light on the appropriate functional expression, it is not straightforward to compare them directly. In the case of pyridine, TPD experiments from 1986 imply that the PBE energies fits better [73]. Contrarily, a more recent experiment from 2016 suggest different pyridine species to leave the surface at increased temperatures. This directly points towards higher binding energies in alignment with the optB88-vdW predictions [74]. As for naphthalene, a 2006 experiment measured the APE to fit perfectly with optB88-vdW calculated APE at the same apparent coverage [75]. Several benchmark studies support the requirement of vdW aware functionals for a good description of similar systems [49, 76–78]. As a result, the detailed diffusion studies are done with the optB88-vdW functional.

Additionally, the APE is dependent on several other parameters such as the coverage of the adsorbates and the thickness of the model slab. The latter is depicted in Figure 4.2 where the APE for both pyridine in site **a** and naphthalene in site **g** are plotted with increasing number of Pt layers. Investigation of the convergence of the APE as a function of the number of Pt layers in the slab shows that the adsorption energy is indeed dependent

Table 4.1 | Adsorption energies in eV for pyridine and naphthalene in selected adsorption configurations.

Site	PBE	optB88-vdW	Site	PBE	optB88-vdW
a	−0.96	−1.58	g	−2.00	−2.81
b	−0.63	−1.26	h	−1.88	−2.45
c	−0.41	−1.06	i	−1.31	−2.10
d	−0.47	−1.11	j	−1.40	−1.99
e	−1.26	−1.66			
f	−0.94	−1.40			

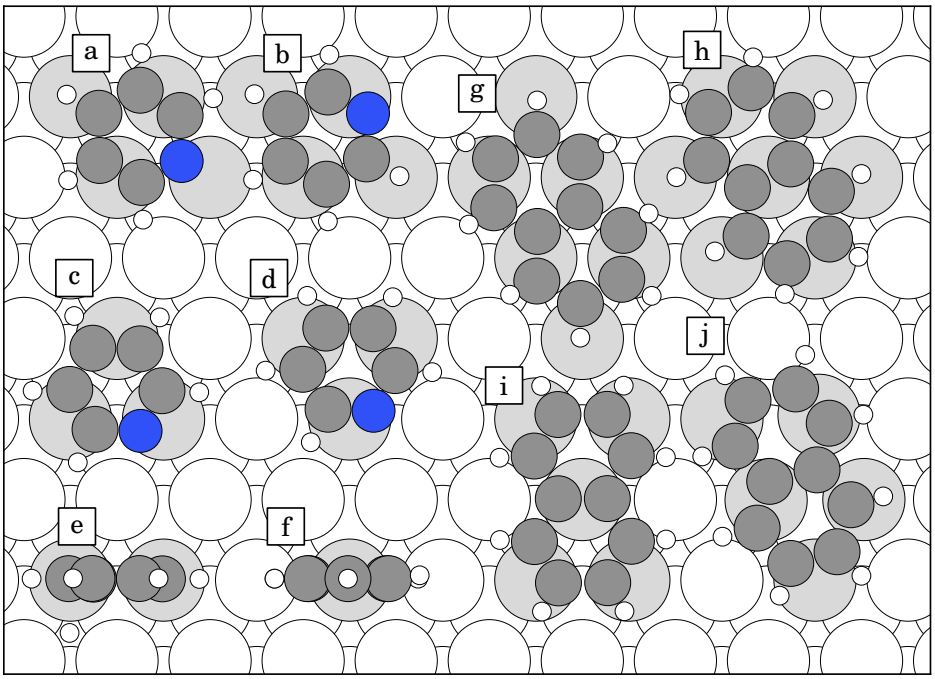

Figure 4.1 | Top view of selected adsorption sites for pyridine and naphthalene on Pt(111). Atoms colored dark grey, blue, and white are carbon nitrogen, and hydrogen respectively. Pt atoms are colored white or otherwise light grey if they are within 2.5 Å of any pyridine/naphthalene heavy atom.

on the number of layers. As a compromise between computational resources and accuracy, the extended number of calculations have been performed

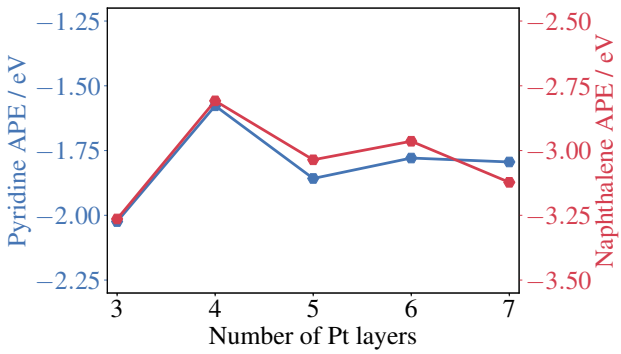

Figure 4.2 | The APE of pyridine and naphthalene (site **a** and **g** respectively) on top of Pt(111) slabs with different thickness (3-7 layers). APEs are calculated with the optB88-vdW functional.

with a four-layer slab. In fact, molecules adsorbed on a four-layer slab looks to be underbound relatively to the thinker slabs. It is evident that a seven-layer slab would provide a better description but the relative poor scaling of DFT with respect to the size of the systems, effectively prohibit this due to the many structure optimizations required.

4.1.1 Constructing a reaction network

As discussed in the previous chapter, reactions usually proceed along several possible paths, but not all paths are associated with the same TS energy, hence not equally relevant. To explore the different diffusion possibilities, corresponding reaction networks are constructed for both pyridine and naphthalene. Both reaction networks are made of small transition steps. For pyridine, each of the meta-stable configurations are associated with a coordinate (x, y, θ) as defined in Figure 4.3**a**. To keep the network reasonable simple, one coordinate is fixed while varying the two others upon construction. This allows a 2D representation of the 3D coordinate space shown in Figure 4.3**b**. The most interesting part of the full reaction network is where the y coordinate is fixed. This facet, with all its stable and meta stable minima, is plotted in Figure 4.3**c**. The coloring of the arrows connecting two minima indicate the relative energy of the relevant TS. The green frames further highlight the complete diffusion path with the lowest critical barrier.

For naphthalene, the reaction network is constructed slightly different. All minima on the surface are plotted in Figure 4.3**e** as a function of the the

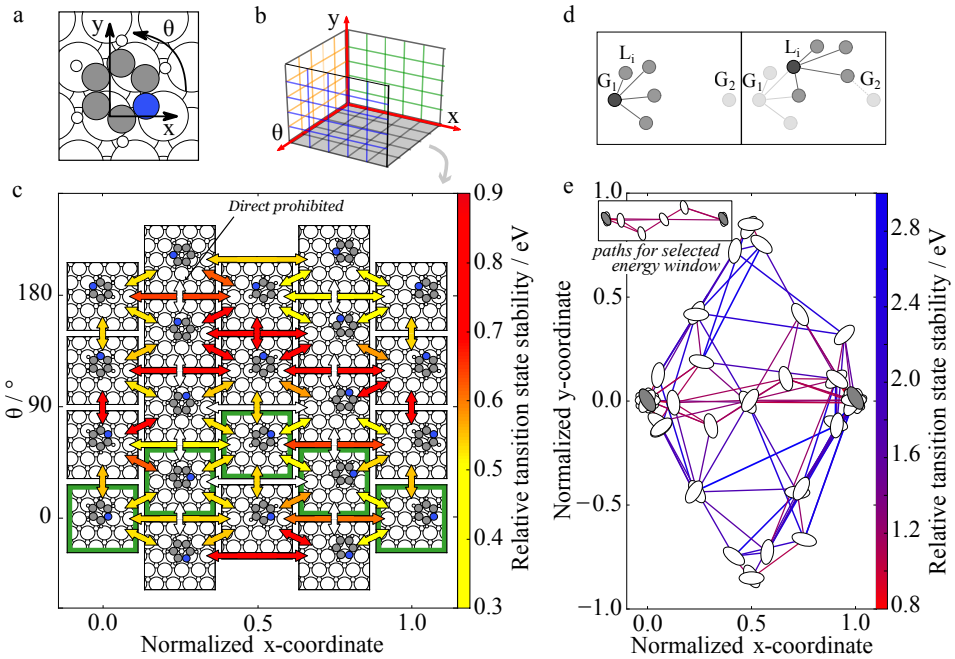

Figure 4.3 | **a** shows the chosen coordinate system for pyridine on the Pt(111) surface. Varying only two coordinates at a time allows for the four facets 3D plot shown in **b**. The grey θ-x facet is shown in **c** where the pyridine transitions are indicated with colored arrows depending on the TS energies – white arrows indicate prohibited direct transitions. A schematic of how the naphthalene reaction network is constructed is show in **d** while the full network is mapped in **e**. The insert shows the final paths examined with the full computational setup.

center of mass x-y coordinate. The relative rotation angle is indicated with the orientation of the ovals. To complete the reaction network, the minima are connected with neighboring minima as indicated in Figure 4.3**d**. Each minimum is connected to the four nearest minima starting from the global minimum moving towards the global minimum in an adjacent unit cell. To keep the calculations feasible, the reaction network is constructed in a size reduced super cell before a final window of promising paths (shown in the insert) are optimized in a $6 \times 6 \times 4$ Pt(111) super cell.

4.1.2 Resulting reactions

As the searches for TSs are based on systematic thorough approaches, the models of the reactions become more reliable and so does the resulting conclusions. The models indicate that both molecules move around the Pt(111) surface facilitated by anchored C-C double bonds on top of Pt

atoms. The anchors act as rotation centers much alike how benzene and benzaldehyde diffuse [79]. As a consequence, the nitrogen of the pyridine always moves as the nose or the tail. Inherently, naphthalene has more carbon atoms, and hence double bonds, causing the transition to be wigglier with shorter shifts between meta stable minima. The surface interactions are maximized by naphthalene pushing Pt atoms as it moves around. The critical TS for pyridine diffusion lies 0.53 eV above the global minima. This is significantly lower than the naphthalene counterpart at 0.78 eV, making pyridine mobile at much lower temperatures. As more bonds are broken for naphthalene to move on the surface it will inherently require more energy.

4.2 Context

It is known from several experiments that pyridine at elevated temperatures is also able to transition into a more stable upright dehydrogenated α-pyridyl species [74, 80, 81]. With the same minima jumping approach as described above, this barrier is found to be 0.71 eV. This fits well with the experimental observations where α-pyridyl is not observed before reaching temperatures of around 265 K [80].

In the case of naphthalene, the STM experiments revealed a rotation barrier of 0.67 ± 0.07 eV – a barrier lower than proper diffusion. This is also supported by the corresponding DFT calculations, which estimates the barrier to be 0.75 eV. The study of naphthalene on transition metals has recently been focused on processes involved in decomposition in relation to biomass gasification where naphthalene act as a representative molecule [82], but much is still to be learned in this specific sub field.

There is still plenty of knowledge to be gained from studying trends in DFT adsorption energies and reaction barriers. Especially combinations with experiments as for pyridine and naphthalene are highly effective. To elevate the studies, a demand for better theoretical models for improved predictability is still present. Within the DFT framework, the description of interactions of aromatic molecules with transition metals can of course be improved by moving up Jacobs ladder. Recently, the random phase approximation (RPA) correlation energy in combination with exact exchange have been used to study adsorption on different close packed transition metals. This have been highly successful with great accuracy compared to experimental measurements [83]. However, the computational cost of including RPA is ~50 times that of pure PBE. The computer resources of the future will though enable such theoretical studies to much greater extend [84].

CHAPTER 5

Modeling self-assembled molecular corrals

The current chapter covers a concise version of Paper III where the driving forces for experimental observed molecular self-assembled corrals are described. The corrals have been imaged with STM on (111) surfaces of Ag, Au, and Cu and subsequently modelled by constructing a molecular pair potential based on DFT calculations.

The prospects of increasing chemical selectivity in catalytically driven reactions are tremendous, and in the case of heterogeneous catalysis there are several directions to go in the aim of promoting selective reactions whether it is for chemoselectivity [11] and/or chirality. A heterogeneous chiral environment can for instance be constructed by cutting, cleaving, or growing the surface in a specific direction [85], introducing chiral modifiers [86], or creating chiral metal-organic frameworks [87]. All mentioned methods can all be used when producing chiral products. In this project we studied self-assembled molecular corrals, which led to small chiral pockets. These types of features have potential to be tailored to promote specific chiral reactions in the future.

The study came about as a collaborative project under the iNANO banner, where the molecules were synthesized in Kurt Gothelf's lab, the STM

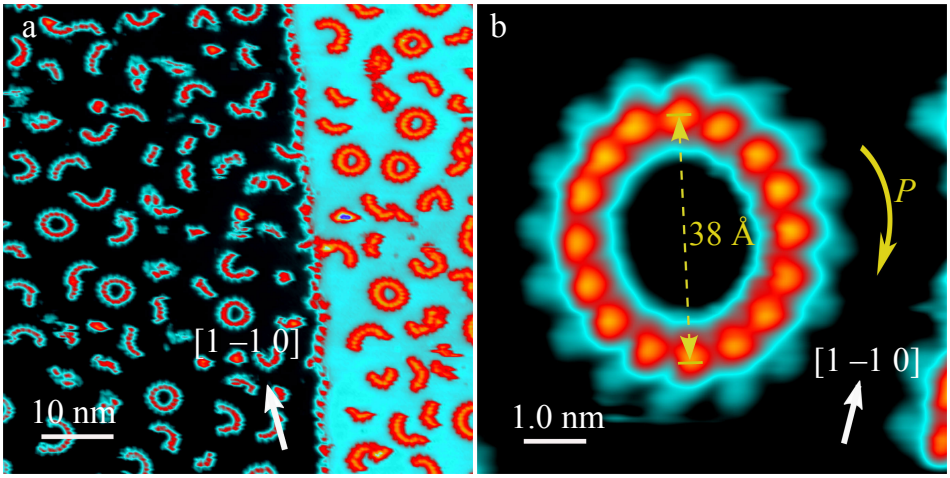

Figure 5.1 | **a** and **b** show STM images of the corrals formed by self-assembled 1,5-triazole molecules on a Cu(111) surface. A large overview is presented in **a** where different sized corrals and "half-corrals" are present while **b** shows a close-up of a *P*-orientated 16-monomer corral.

images were acquired in Trolle Linderoth's lab by Siddharth Jethwa, while the theoretical modeling were of my making.

5.1 Understanding the molecular arrangement

In this study a 1,5-triazole with a biphenyl group at the 1-position and a phenanthrene group at the 5-position were investigated. It was synthesized *ex situ* through a cycloaddition. When the 1,5-triazole molecules are deposited using thermal sublimation at medium coverage at ~388 K onto a Cu(111) surface and subsequently cooled to ~100 K a spontaneous self-assembly of supramolecular corrals emerged as imaged in Figure 5.1. During cooling both closed and partially closed chains are formed on the surface – the partially closed corrals are probably kinetically trapped during quenching, which prevents them from completing closed circles. The corrals, which are fully closed, come in different sizes ranging from 11 to 18 molecules per corral, but they all have similar features. Hence, all corrals are composed of an inner protruding ring that resemble beads on a string with each bead having a characteristic flat outer halo-feature pointing away from the ring giving the corrals a "cog-tooth" like look.

To understand the features of the corrals, the possible adsorption geometries were modelled by the means of DFT on Cu(111) in the search for the

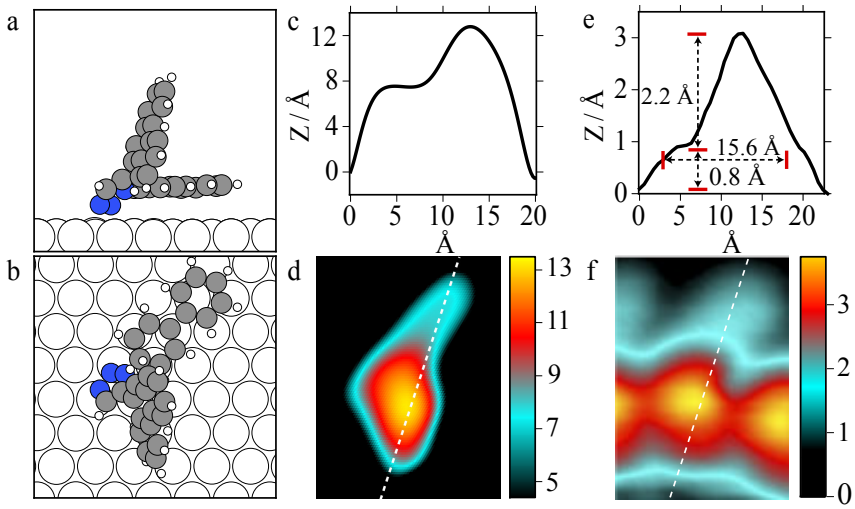

Figure 5.2 | The favored adsorption configuration is shown as a side and top view in **a** and **b** respectively. A complementary Tersoff-Hamann STM simulation of the favored adsorption configuration is shown in **d** with an associated line plot in **c**. **e** shows an experimental line plot of the single corral molecule shown in **f**.

optimal binding configuration. The found ideal P atropisomer configuration is visualized in Figure 5.2**a** and **b** and is associated with an adsorption energy of -2.04 eV. From the conformation it is apparent that the three aromatic groups do not organize in a coplanar arrangement as they are sterically hindered due to binding to adjacent sites on the triazole ring. The corresponding STM line profile and image simulated with the Tersoff-Hamann approximation are plotted in Figure 5.2**c** and **d**. The simulated data can be directly compared to the experimental imaged in Figure 5.2**e** and **f**. The two images show a line profile and STM image of a close-up of a single molecule sitting inside a corral. The compliance between the simulated and the experimental features are high, and hence it is concluded that the phenanthrene group accounts for the yellow protruding bead while the light blue "tooth" is accounted for by the biphenyl group. Unsurprisingly, further investigations revealed that the binding of the molecule is mainly dominated by the covalently bound triazole nitrogen and the physiosorbed biphenyl group.

5.2 Creating a molecular pair potential

Modeling full sized corrals with DFT is computationally very demanding. Just the smallest corral is made up of ~650 atoms not counting the surface

atoms, and hence excels the limit of what can be geometrically optimized with DFT. To simplify the problem a pairwise model potential is thus constructed reducing the DFT model system size to ~180 atoms including the Cu(111) slab. The smaller system is composed of two 1,5-triazole molecules adsorbed on Cu to form a dimer. The dominating adsorption configuration of a single 1,5-triazole combined with an experimentally determined molecule-molecule separation of 5-7 Å makes it possible to resolve the seven different viable dimer configurations, which are visualized in Figure 5.3**a**. The strength of the dimers interactions is dependent on their relative angle (θ_1 and θ_2) and their surface orientation. By mapping their interactions one combined pair potential were constructed by adding the seven dimer contributions. The potential was subsequently used for the full-sized corral studies. Much can though already be learned by studying the most favored dimer configuration, which is imaged in Figure 5.3**b**. In the optimal orientation, rotated ~35° apart, this dimer has an interaction strength of −0.27 eV per molecule. At first glance, the two molecules are non-aligned, which is a crucial criterion for forming closed circles when they are stacked. The driving force for the non-aligned stacking can be traced to a combination of effects visualized in Figure 5.3**c**. The "perfect" dimer is chopped into its three component: the phenanthrene (Figure 5.3**d**), the triazole (Figure 5.3**e**), and the biphenyl (Figure 5.3**f**). Their relative interactions are subsequently mapped as a function of a common rotation angle, ϕ, and plotted in Figure 5.3**c**.

From the plot it is clear that each group prefers a different rotation angle, but the interaction of the two phenanthrene groups are the most angle dependent in the vicinity of the global minima. The biphenyls are almost non-interacting around the global minima, while the triazoles pushes the global minima very slightly towards negative angles as they prefer to be perfectly aligned with the underlying substrate. Adding the three contributions together result in the dashed curve, which follows the global minima curve (full line) with an almost constant offset. This justifies subdividing the molecule into individual groups. The offset can be partly attributed to interactions missing in the summation, which originate from different groups of the two molecules like phenanthrene-biphenyl and phenanthrene-triazole interactions. These interactions are though not expected to have a high level of angle dependency due to the large spatial separation. The dominating driving force is hence safely assigned to the phenanthrene-phenanthrene aromatic interactions, which is optimal if the angle between the phenanthrene planes is ~30°.

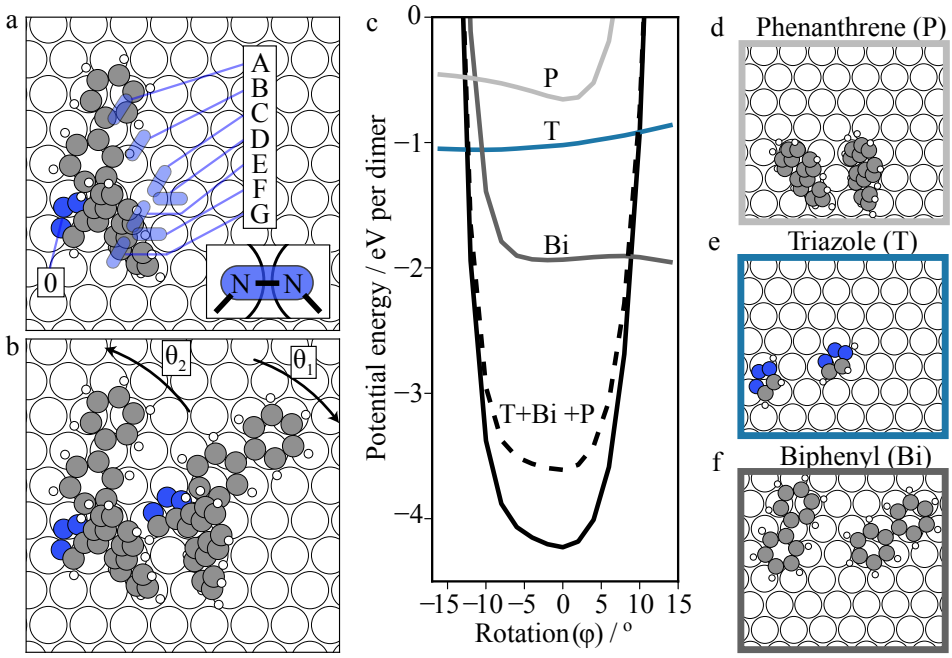

Figure 5.3 | The seven physically possible dimers are shown in **a**. The footprints of the two nitrogens binding to the surface for each additional molecule are marked with blue and assigned a letter while the stationary molecule is referred to as 0. **b** shows the favored interaction configuration, 0C, and the two mapped rotation angles, θ_1 and θ_2. In **c** the pairwise interactions of the three molecular fragments made from separating configuration 0C are plotted as a function of the angle $\phi = \theta_1 - \theta_1^{\text{opt}} = \theta_2 - \theta_2^{\text{opt}}$. The three fragments are shown in **d**, **e**, and **f**.

5.3 Modeling full sized corrals

By mapping the combined angle and site dependent interaction strength, full sized corrals can be evaluated by adding the contributions from the individual dimers in the aim of optimizing the full geometry in the pair potential. As there is no direct way of finding the global minimum configuration for each corral size, the optimizations are performed as random geometric displacements/rotation in a metropolis Monte Carlo scheme. As the energy evaluation is as fast as looking up a couple of numbers in a matrix and adding them together, it is remarkably quick and the optimizations can be run for thousands of iterations for all tried corral sizes. The optimizations are performed for corrals sized 10 to 20 and the stability per molecule of the most stable configurations are plotted as a function of the corral size in Figure 5.4**a**. From the plot, a minimum around 13 molecules

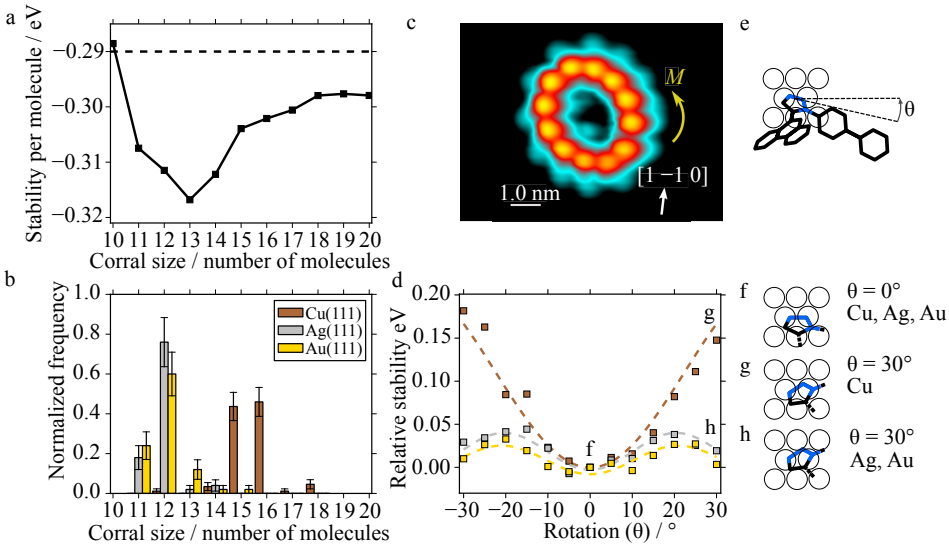

Figure 5.4 | In **a** the theoretical stability per molecule on Cu(111) is plotted against the size of the corrals. **b** shows the experimental size distribution on Cu, Ag, and Au. In **c** an STM example of a 12 membered corral on Ag is shown. **d** shows the relative penalty for rotating a single 1,5-triazole on the three surfaces with the rotation, ϕ, defined in **e**. **f-h** shows the different adsorption configurations depending on the substrate and the rotation angle.

per corral is present, and all corral sizes but the smallest are more stable than a theoretical infinite line (see dashed line in the plot). The experimental size distribution as plotted in Figure 5.4**b** reveals a slightly larger preferred size of 15-16 1,5-triazoles per corral on Cu. The underestimated corral size is probably due to the approximate pair potential, which is built entirely on dimer interactions and no extended information is included. It seems that the preference for a relatively large rotation angle of ~35° for the most stable dimer carries over from the mapping. Nevertheless, the model potential is sufficient to describe the corral formation, that is governed by a strong molecular adsorption in a specific configuration that guide the upright phenanthrene groups to interact favorably causing the 1,5-triazoles to stack non-aligned.

Interestingly the corrals formed on Ag(111) and Au(111) are smaller, usually with 12 molecules per corral. An example of a 12-membered corral on Ag is shown in 5.4**d**. The smaller corrals can be explained from a combination of effects. First, the lattice parameters of Ag and Au are about 10% larger than Cu naturally separating the individual molecules more. This require a larger rotation angle for the phenanthrenes to be in proximity

of each other resulting in smaller corrals. More importantly, the binding strength of the 1,5-triazole molecule is much weaker on Ag/Au and thus the penalty for rotating away from the optimal alignment with the surface is much lower than for Cu. This is shown in Figure 5.4**d** where the relative stability versus the rotation angle ϕ defined in Figure 5.4**e** is plotted. The behavior on the Ag/Au surfaces is also different where a second minimum is present at $\pm 30°$. On the Cu surface the 1,5-triazole is at all time pivoting around the N-N bond, while on Au/Ag it pivots around one of the N atoms that constantly binds to an Ag/Au atom. At the same time, the second N atom at $\theta = \pm 30°$ perfectly bridge two surface atoms. The discrepancy can be seen when comparing Figure 5.4**g** and **h**. The 30° separation of the minima allows the corrals to form with the molecules sitting in alternating sites (0° and 30°) completing a "perfect" 12-membered corral in agreement with the experiments.

5.4 Context

Usually when designing building blocks for supramolecular surface architectures, whether they are for extended networks or molecular clusters, they are fashioned to interact through directional bonds, in particular, hydrogen bonds in the surface plane [88–90]. The formation of non-covalently bound corrals found as discrete clusters, like those observed in this study, is thus very rare. The aromatic interactions acting as the driving force opens up for a different approach to design corrals with specific desired properties for instance to be used for chiral catalytic chemistry. Interestingly, the observed corrals occur in two chiral forms on the surface as there exist two mirror images of the 1,5-triazole molecule. For specific purposes only one chirality is usually desired, and the formation should be somehow controlled. For this specific 1,5-triazole molecule there is a barrier of only 0.41 eV (calculated with CI-EB method) for transforming between the two conformers, which is easily overcome at the deposited temperature. This is just one of the issues, which has to be overcome when approaching more tailored designs.

Concerning the simulation of the full corrals it would, in hindsight, be interesting to apply a more sophisticated ML approach. It is possible to train a model potential on the DFT energies and forces to learn the interactions of adjacent 1,5-triazoles. The corral geometries could subsequently be optimized within the model potential, not restricting the geometries to be composed of rigid molecules with a fixed angle orientation due to the coarseness of the dimer interaction scan. This might improve the accor-

dance between the optimal theoretically predicted size and real corral size. The next chapter demonstrate though in a different setting the prospects of applying ML methods to computationally expensive geometry optimization problems, which ideas also should be useful for the current discussed corral optimization problem.

CHAPTER 6

Structure search for small, supported Pt-nanoparticles

The current chapter outlines a computational enhancement for an evolutionary search algorithm used for structure optimization, which is described in detail in Paper VII. The algorithm is applied in the search for global optima structures of Pt_9, Pt_{10}, and Pt_{13} nanoparticles supported on a MgO(100) surface before their chemical properties are explored. Finally, the stability of different nanoparticles of 13 atoms are compared across different transition metals.

For reaction chemistry of nanoparticles, as for all other theoretical studies, a good model representing the real-world situation is highly valued. In this chapter we deal with the challenges of constructing well representative isomers of specific particle compositions and sizes. In the search for structure candidates there are several common approaches, but as the PES of a set of atoms is a nonlinear function with many local minima it quickly becomes impossible to explore every metastable atomic configuration as the studied systems increase in size. One practice is ”by hand” to evaluate different candidates inspired by chemical intuition and similar systems. There are several drawbacks with this strategy as important candidates might be ”forgotten” or never thought of, and thus it is highly preferred to use an

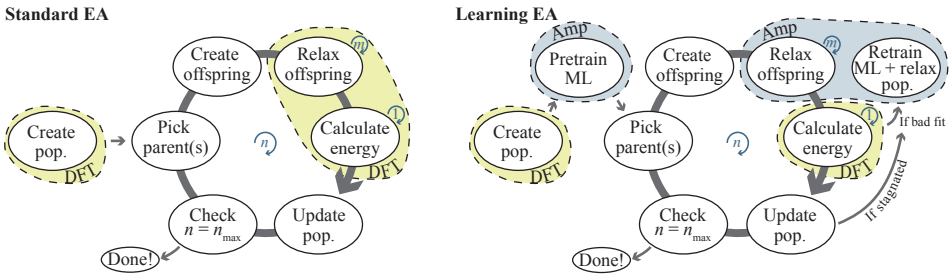

Figure 6.1 | The standard EA scheme is visualized in the left part of the figure while the full learning evolutionary algorithm (LEA) algorithm showing the addition of a trained ML model is illustrated to the right. It is important to have a decent ML potential before the main loop is initialized. In the case that the PES is initially hard to learn, the ML potential is iteratively retrained with additional single-point DFT data from relaxing the start population within the ML potential until its performance is satisfying.

unbiased global search algorithm to explore the PES.

As globally exploring the PES can be expensive, we turned to integrate ML potentials in the search algorithm. To smoothly incorporate the training and energy force evaluation we applied a ML package developed in Andrew Peterson's lab at Brown University whom I visited in the spring 2017.

6.1 A learning evolutionary algorithm

The consequences of applying global search algorithms are much higher computational demands, which can limit the possible search space. It is, however, still the much-preferred approach. The workhorse of this study is an EA [91] implemented in ASE. The idea is based on Darwin's theory of evolution, and in the context of a search algorithm, it works by searching configuration space by improving a pool of candidates called the population. The work flow is visualized in the left part of Figure 6.1. Each new candidate has to "grow up" to become an adult before being proved fit for breeding. It is precisely the process of "growing up", which in the framework of global structure optimization is the local geometric relaxation, that is the computationally demanding step as it is usually performed at the DFT level. To shepherd the population towards stable structures the population is composed of the most stable unique candidates found. It is from the population of stable structures the parents are drawn for pairing or mutation with the aim at producing new promising children. When the children are grown they can, if found fit, be used for breeding of even better structures.

The computational issue of relaxing the structures can though be ap-

proached with the recent advances in ML methods. When trained in a supervised learning scheme to mimic the DFT potential energy surface, ML potentials offer fast energy and force evaluations. This idea has been implemented as presented in the right part of Figure 6.1. The initial population is generated randomly as in the standard algorithm and then locally relaxed with the DFT energy description. The trajectories of the relaxed population are then used to pretrain a NN potential as described in Chapter 2. In principle is any ML method capable of describing energies and forces applicable. The DFT local relaxation step in the EA is thus replaced with the ML potential while a final single point calculation is performed at the DFT level. These single point calculations also serve as training points when the model is later improved. The DFT calculations ensure a maintenance of the correct energies for the candidate evaluation while serving as a safety net for the ML potential as the performance is continuously monitored. As the trained ML potential only works well within the interpolated part of the training data it will naturally perform worse as the population progresses to new parts of the PES. As this is caught by monitoring the ML potential, retraining can be initialized with the newly generated training data, updating the model to describe the relevant part of the PES well. As the algorithm is trained on-the-fly learning the PES, it is thus named a learning evolutionary algorithm (LEA).

6.2 Benchmarking the algorithm

Assessing the performance of the modified algorithm is crucial to validate the approach. For statistical purposes, the measurements are performed on a small system with the objective of locating the global minimum of a small Ag_3Pt_3 nanoparticle on top of a Pt(111) surface as visualized in Figure 6.2**a**. DFT has been swapped with the effective medium theory (EMT) as the parent calculator for this system, allowing for averaging the performance over 100 restarts. In Figure 6.2**b** the cumulative success of locating the global minimum is plotted as a function of the number of attempts (or children) produced for both the standard EA and for LEA. The performance only slightly decreases using the ML potential for the relaxation – from ~170 to ~260 attempts to locate the global minimum in 50% of the restarts. If the success is instead plotted as function of the number of parent calculations as in Figure 6.2**d** it is evident that the algorithm greatly reduces the expensive parent calculations before the global minimum is located. The average number of parent calculations needed is visualized in Figure 6.2**c**. As both

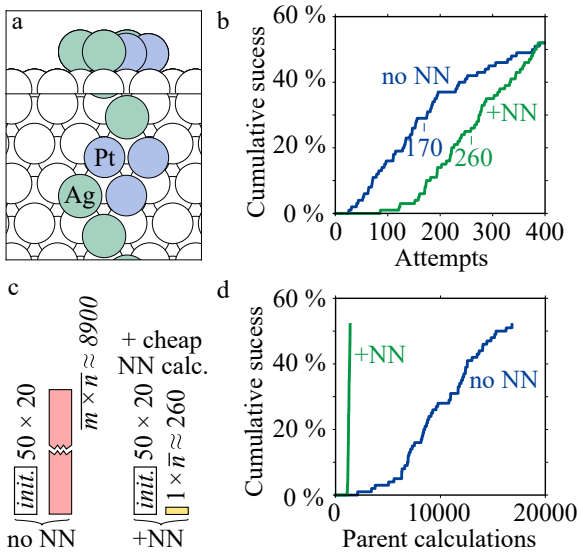

Figure 6.2 | The Ag_3Pt_3 model used for benchmarking the LEA algorithm is shown in **a**. Executing the EA and the LEA algorithms loops over 400 attempts result in the cumulative success plot in **b**. The same success plot is shown in **d** now as a function of the parent calculations needed. Finally, the significant reduction in parent calculations is visualized in **c**.

methods share the initial 1000 (50×20) relaxation steps, the computational gain originate from reducing the relaxation/energy evaluation steps from ~8900 to ~260. The gain has to be subtracted the training time of the ML potential and the cheap model potential calculations, which cost is negligible when compared to DFT calculations.

6.3 Using the LEA for finding supported Pt nanoparticles

With the performance boost of the EA we now move the focus to uncover the global optima structures of nanoparticles of 9, 10, and 13 Pt atoms supported on a MgO(100) slab. As is evident from the Figure 6.2**b** we cannot expect a success rate of 100% within a limited number of attempts, and thus the LEA algorithm is restarted three times for each stoichiometry. The same Pt_9 structure is found as the global minimum for all three searches while two out of three searches locate the same Pt_{10} and Pt_{13} global minimum. All three global minima can be found in Figure 6.3**a**, **c**, and **e**.

Interestingly the appearances of the three global minima are very dif-

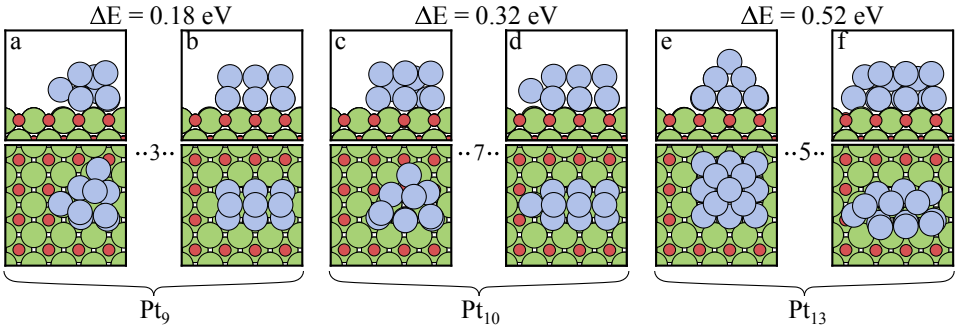

Figure 6.3 | The most stable isomer of each particle size and Crampton *et al.*'s previously suggested configurations shown as side and top views. The displayed energy differences are calculated with the PBE functional.

ferent with the Pt_{13} nanoparticle emerging as a hollow pyramid. Both the Pt_9 and Pt_{10} nanoparticles are much less symmetric making them hard to predict beforehand.

The alternative "by hand" approach to unbiased global minima structure search for predicting promising candidates has been shown several times to be insufficient [92–95], which is also the case for this system. Crampton *et al.* performed an extensive search inspired by cluster structural motifs collected for other similar systems resulting in the three suggested structures in Figure 6.3**b**, **d**, and **f** [96, 97], which are all significantly less stable than what was found with the global structure search presented here. The numbers in between the different isomers indicate how many other structures were discovered that are more stable than Crampton *et al.*'s. This revelation further advocates for the use of non-biased global search algorithms. Despite much effort from extensive human guided trial and error searches there is a limit to the creativity of the human brain, and even though chemical intuition is a good guideline it is certainly not enough for complex problems.

6.4 Catalytic properties of the Pt_{13} nanoparticles

It is interesting to assert the consequences of investigating the catalytic properties of a suboptimal model. For that purpose, a comparison between the best Pt_{13} isomers found by the LEA search and "by hand" is an obvious choice. To complete that objective, the adsorption energy of CO and ethylene has been thoroughly investigated and the preferred adsorption sites are visualized for each isomer-molecule combination in Figure 6.4. Following the Sabatier principle, the adsorption energy is a good catalytic descriptor

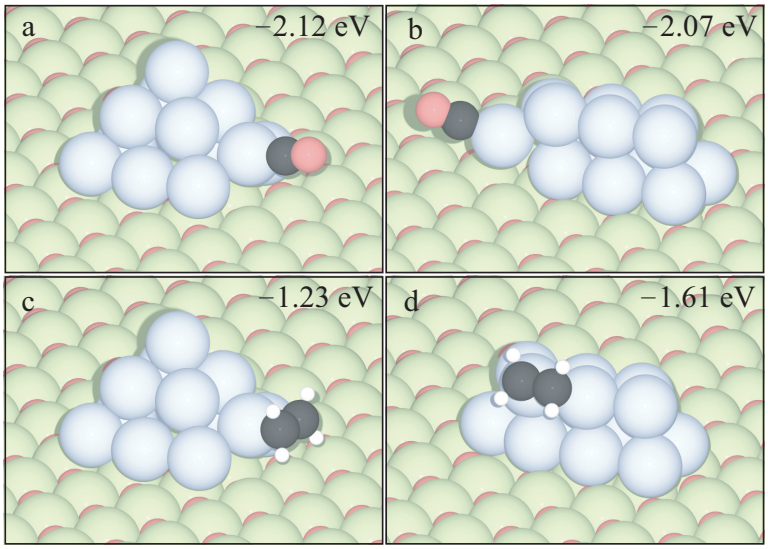

Figure 6.4 | **a** and **b** show the preferred adsorption configurations of CO on the hollow pyramid and elongated Pt_{13} isomers, while **c** and **d** show the corresponding sites for ethylene.

as adsorbate-substrate interaction has to be "just right" for the maximum turnover rate [3].

Investigating the preferred adsorption sites for CO on each isomer reveals two very comparable configurations. Both isomers adsorb CO pointing away from the nanoparticle at an easily accessible interface Pt-atom with comparable strength, indicating that they would act similarly in CO reactions. The two preferred ethylene adsorption configurations are very different, unlike CO. First of all, the hollow pyramid adsorbs ethylene at the same site as CO, binding it through the ethylene π-bond to a single Pt-atom. On the elongated isomer ethylene adsorb at the second layer of Pt-atoms binding through two σ-like bonds to two adjacent Pt-atoms. This binding site is also associated with significantly higher binding energy, which naturally would change the reaction mechanism and turnover rate. This just further strengthens the arguments for unbiased search methods as the particle geometry is certainly very important for its properties.

6.5 Pt_{13} isomer transformation

In the study of nanoparticles reactivity, it is also intriguing to get a grasp on the barriers for transforming between different isomers. This gives an

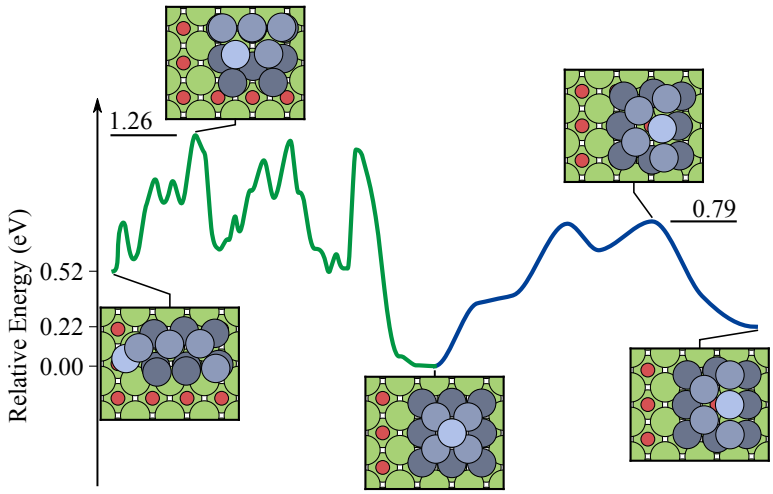

Figure 6.5 | To the left is the transformation barrier between the hollow pyramid and the elongated structure shown while the right part shows the transformation into the second most stable isomer.

idea of how large an ensemble of particle shapes one has to include in a detailed study. An analogue to the aromatic diffusion reaction networks discussed in Chapter 4 would require a way to connect the closest resembling isomers to circumvent calculating every single isomeric transformation. This could for instance be done via an isomerization graph constructed using a bipartite matching algorithm network as demonstrated by Zhai *et al.* [98], but we will, for now, ignore this challenge. We instead turn the focus to another problem: mapping of atomic indices. Since each Pt-atom can be permuted without changing the structure, the difficulties compared to aromatic diffusion now also lies in how to map the atomic indices of one isomer into another. The number of mapping combinations scale factorial with the number of atoms, and thus there are more than six billion ways to map two different 13 atom isomers, and this is only between two distinct isomers! For some transformations there are arguably only one or a few reasonable possibilities as is the case for the two most stable Pt_{13} isomers. The transformation is visualized in the right part of Figure 6.5, where the resulting NEB path is associated with a 0.79 eV barrier for escaping the global minimum.

For other transformations it is not straight forward to foresee how to create the ”best” mapping by purely inspecting the structure. An alternative to the ”by eye mapping” is to make an educated guess by for instance minimizing the 2-norm distance between the isomers (the Hungarian method)

and then subsequently optimize the resulting NEB pathway. This, however, only provide an upper bound for the barrier and a more satisfying approach would involve exploring other options. It is unfeasible to converge just a small fraction of the six billion combinations with pure DFT. To convert this impractical problem into a manageable one requires both a reduction in the number of possible pathways and a cheaper alternative energy and force description. One interesting transformation, where there is no logical mapping, is between the elongated structure and the hollow pyramid already investigated. To solve the first issue the number of pathways were reduced to 600 by manually pairing three atoms in five different ways while trying every other combination. The latter alternative energy description was borrowed from a previously trained ML potential from one of the finished LEA runs, which is exactly trained for these nanoparticles. To further improve the ML potential's performance when describing TS paths, the NN were retrained with the 600 intermediated converged pathways in an iterative and parallel fashion like what has been proven efficient for converging a single NEB path [63]. An energy window of plausible pathways was finally converged at the DFT level. From those the lowest barrier path has a 1.26 eV barrier, which is ~0.50 eV lower than the barrier found via the Hungarian method. This again shows that intuition might be insufficient. The most stable transformation is plotted to the left in Figure 6.5. Not surprisingly the relatively large geometric change between the hollow pyramid and the elongated structure, when compared to the two most stable isomers in the right part of the figure, is also associated with a much larger barrier. The relative high barrier also suggests that only at *very* high temperatures the elongated structure could take place in a catalytic reaction.

6.6 Context

Interestingly the hollow Pt_{13} pyramid nanoparticle is so structural "pleasing" that it could be guessed by a human. That is at least the case for the Au counterpart as it was discussed as a stable isomer on the same MgO surface in a previous study [100]. As the same hollow pyramid is found as the most stable isomer for Au, the question is raises whether this is the case for the other transition metals residing in the Pt and Au rows in the periodic table. This inquiry can at least be answered by just finding a more stable isomer (if possible) though leaving a proper EA search for the global minima for later studies. A large number of stable isomers were thus examined, and the most stable along a few selected can be seen in Figure 6.6.

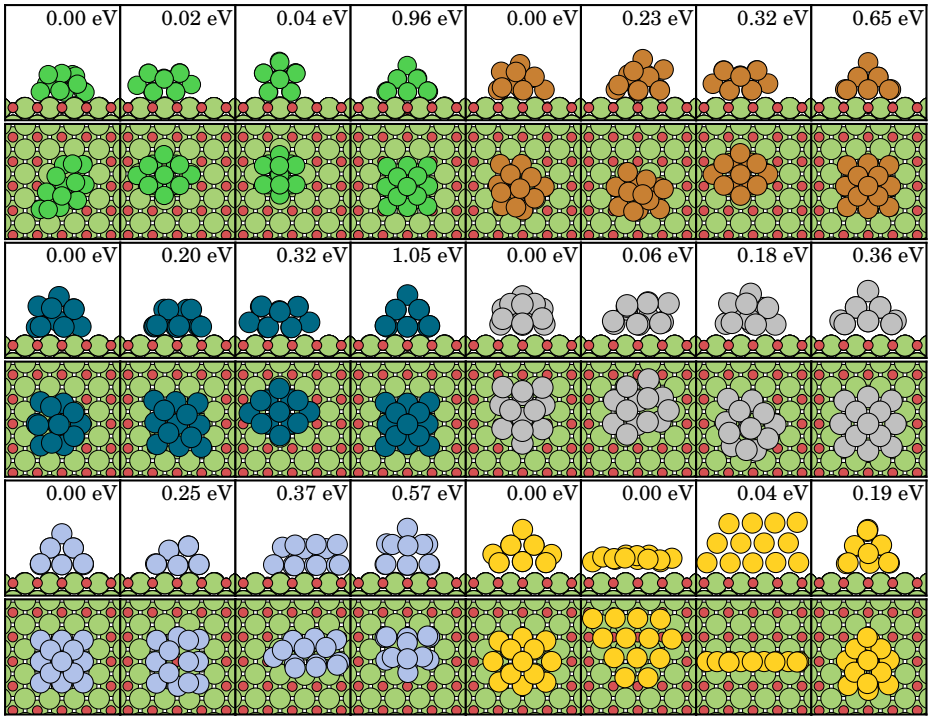

Figure 6.6 | Side and top view of the most stable and some selected 13 atom isomers found in an abbreviated search for Ni (green), Pd (dark blue), Pt (light blue), Cu (brown), Ag (gray), and Au (yellow) with the BEEF-vdW functional [99].

It is clear from the figure that it is indeed only Pt and Au which favor a hollow pyramid configuration. The preferred motifs are very different from metal to metal (except Cu and Ni), which is why a full global search is indeed needed for each individual case before any other kind of study can be performed. It is simply impossible to guess the right structure even with knowledge of stable structures of neighboring elements.

There are several ways one could introduce ML methods into global structure optimization, many of which have already been realized. In line with the just presented strategy, Patra *et al.* have also developed a "normal" genetic algorithm (GA) that operates in conjunction with a purely NN based GA [101]. The two GAs exchange favorable structures propelling the "normal" GA search forward. A very related approach to using ML for speeding up global optimization schemes is to refit parameters in model potentials on-the-fly. Wu *et al.* demonstrated on several crystal structures that classical interatomic potentials could be refitted during an EA search

to mimic the true DFT potential, and hence solve the complex crystal structures [102]. Likewise, Van den Bossche *et al.* showed a very comparable strategy for an EA based on a density functional tight-binding (DFTB) potential [103]. They successfully refitted the repulsive part of the DFTB potential to single-point DFT calculations, which they used to solve different crystal structures. It is not only EAs, which have had the ML treatment but also basin-hopping method [104] and particle swarm-intelligence based global optimizations schemes [105] just to name a few. It is clear that the many attempts of speeding up global optimization is a sign for the awareness of the need of efficient and reliable strategies.

CHAPTER 7

Conclusion and outlook

The material covered in this thesis addresses a diverse set of catalytic systems of which most have been published. Nevertheless, there are still several paths to continue investigating especially with the prospects of advancing ML techniques.

The first chapters lay out the technical groundwork where the methodology, systematic strategies, and the developed algorithms are presented. Each of the presented methods are justified by several examples including a diverse set of model systems. The strategies and algorithms consist of systematic ways of constructing reaction networks for diffusion processes as well as exploring a larger part of the relevant PES. Even though the developed strategies increase the likelihood of finding the right TS, it remains extremely hard for complex problems. There is certainly still room and need for expanding this area of expertise as the set of relevant systems are very diverse, and the possible solutions might not be applicable for all the different systems. One emerging strategy is to apply ML methods in various ways to speed up the calculations or cleverly reduce the problem size, as was also showcased in Chapter 6. This direction is without doubt one that should and will be pursued in the future. The whole field of modeling chemical reactions is very challenging and the tasks of mapping possible TSs is just one in many.

Throughout my work additional knowledge have been accumulated for many different molecule-surface systems significant in a variety of catalytic

designs. These systems include, but are not limited to, atoms and molecules such as hydrogen, pyridine, naphthalene, ammonia, and different transition metals on surfaces composed of either graphene, a metal, or an oxide. For these systems both adsorption energies, configurations, and trends have been established as well as a range of relevant system dependent properties. One of these peculiarities were the aromatic stacking of the phenanthrene subgroups that acted as the driving force for the corral formation. It will be exciting to see what tailored systems such as self-assembled corrals can bring to future chiral reaction chemistry.

Most of my efforts have been devoted to unravelling reaction, diffusion, and transformation mechanisms for the above-mentioned systems. For *every* single discussed system, some kind of barrier were found by applying the different developed methods. It is now clear how pyridine and naphthalene diffuse on Pt(111) surfaces by hinging double bonds on top of Pt-atoms, and how ammonia diffusion on anatase-TiO_2 can be catalyzed by adjacent molecules. Further details are as well added to the knowledge of (de)hydrogenation reactions of both pyridine on Pt(111) and graphene supported by an Ir(111) surface. The last type of barriers discussed in this thesis are for configurational transformations. As the molecular corrals investigated in Chapter 5 were composed of chiral molecules, the barrier for transforming from one chiral configuration to the other were examined. The transformation was found to be fairly easy for the individual molecules. In Chapter 6 a pretrained and on-the-fly adjusted ML potential was utilized to explore a large number of transformation barriers between two different Pt_{13} isomers to find the most probable one. This certainly highlighted how a tremendously challenging task it is to map just two isomers. The number of different mappings of atomic indices simply explode with the system size. This is a challenge that will persist for years to come.

The Pt nanoparticles study showed another intriguing use of ML with the integration into an evolutionary search scheme. Applying the ML potential to the local relaxation reduced the computational needs by at least a factor 10. This study made it clear that it is by large impossible to guess the global minimum configuration of a set of atoms – even for small nanoparticles – as new stable isomers were identified for all three sizes studied.

7.1 A generic atomistic structure builder trained by reinforcement learning

Techniques such as EAs are great for unbiased exploration of the PES when seeking a global minima configuration. This was for instance discussed in Chapter 6 in the search for stable Pt nanoparticles. There is, however, a couple of issues as for each new stoichiometry a completely new EA has to be initialized, and in the end ~99% of the produced candidates are thrown in the bin, and the information about previously visited part of the PES is not used for anything. Nevertheless, impartial algorithms are without doubt required to search for global minima structures.

The last six months I have been part of developing a completely new strategy to build stable atomic structures from nothing. The algorithm is heavily inspired by the advances in reinforcement learning applied to games like Go [106]. The project is by now fairly advanced and seems very promising. The strategy for building the different structures are stored in a NN. The NN is initiated with a random set of parameters and is trained on the structures it continuously builds, reinforcing its tendency to build highly stable structures. Ideally, at some point the ”perfect” NN and policy are achieved and the algorithm has learned to build the global minimum structure. A refined version of this algorithm could very likely in the future be the go-to method when searching for new structures.

No matter what, it is truly exciting what the future will bring as more and more ML techniques mature.

Bibliography

[1] *Fritz Haber – Biographical*. http://www.nobelprize.org/nobel_prizes/chemistry/laureates/1918/haber-bio.html. Nobelprize.org. Nobel Media AB 2014.

[2] J. W. Erisman, M. A. Sutton, J. Galloway, Z. Klimont, and W. Winiwarter. "How a century of ammonia synthesis changed the world". *Nature Geoscience* 1 (2008), pp. 636–639.

[3] P. Sabatier. *La catalyse en chimie organique*. Nouveau Monde éditions, 2014.

[4] T. Bligaard, J. K. Nørskov, S. Dahl, et al. "The Brønsted-Evans-Polanyi relation and the volcano curve in heterogeneous catalysis". *Journal of Catalysis* 224 (2004), pp. 206–217.

[5] G. A. Somorjai and Y. Li. *Introduction to surface chemistry and catalysis*. John Wiley & Sons, 1994.

[6] H.-U. Blaser, A. Baiker, and R. Prins. *Heterogeneous catalysis and fine chemicals IV*. Elsevier, 1997.

[7] J. M. Ogden. "Prospects for building a hydrogen energy infrastructure". *Annual Review of Energy and the Environment* 24 (1999), pp. 227–279.

[8] H. Toulhoat. "Heterogeneous Catalysis: Use of Density Functional Theory". *Encyclopedia of Materials: Science and Technology*. Ed. by K. H. J. Buschow, R. W. Cahn, M. C. Flemings, et al. Oxford: Elsevier, 2010, pp. 1–7.

[9] S. Diezi, D. Ferri, A. Vargas, T. Mallat, and A. Baiker. "The origin of chemo- and enantioselectivity in the hydrogenation of diketones on platinum". *Journal of the American Chemical Society* 128 (2006), pp. 4048–4057.

[10] X. Hong, Y. Liang, and K. N. Houk. "Mechanisms and Origins of Switchable Chemoselectivity of Ni-Catalyzed C(aryl)-O and C(acyl)-O Activation of Aryl Esters with Phosphine Ligands". *Journal of the American Chemical Society* 136 (2014), pp. 2017–2025.

[11] S. Tuokko, P. M. Pihko, and K. Honkala. "First Principles Calculations for Hydrogenation of Acrolein on Pd and Pt: Chemoselectivity Depends on Steric Effects on the Surface". *Angewandte Chemie International Edition* 55 (2016), pp. 1670–1674.

[12] H. U. Blaser. "The chiral pool as a source of enantioselective catalysts and auxiliaries". *Chemical Reviews* 92 (1992), pp. 935–952.

[13] R. Noyori and T. Ohkuma. "Asymmetric catalysis by architectural and functional molecular engineering: practical chemo-and stereoselective hydrogenation of ketones". *Angewandte Chemie International Edition* 40 (2001), pp. 40–73.

[14] I. Ojima. *Catalytic asymmetric synthesis.* John Wiley & Sons, 2004.

[15] M. Tada, N. Kojima, Y. Izumi, T. Taniike, and Y. Iwasawa. "Chiral self-dimerization of vanadium complexes on a SiO_2 surface for asymmetric catalytic coupling of 2-naphthol: Structure, performance, and mechanism". *Journal of Physical Chemistry B* 109 (2005), pp. 9905–9916.

[16] S. Mason. "The origin of chirality in nature". *Trends in Pharmacological Sciences* 7 (1986), pp. 20–23.

[17] S. Fabro, R. L. Smith, and R. T. Willaims. "Toxicity and teratogenicity of optical isomers of thalidomide". *Nature* 215 (1967), pp. 296+.

[18] W. H. Brooks, W. C. Guida, and K. G. Daniel. "The Significance of Chirality in Drug Design and Development". *Current Topics in Medicinal Chemistry* 11 (2011), pp. 760–770.

[19] J. H. Lin and A. Y. H. Lu. "Role of Pharmacokinetics and Metabolism in Drug Discovery and Development". *Pharmacological Reviews* 49 (1997), pp. 403–449.

[20] P. Hofland. "Reversal of Fortune: How a Vilified Drug Became a Life-saving Agent in the "War" Against Cancer". *Onco'Zine – The International Oncology Network* (2013).

[21] G. J. Hutchings. "Heterogeneous catalysts – discovery and design". *Journal of Materials Chemistry* 19 (2009), pp. 1222–1235.

[22] G. Henkelman and H. Jónsson. "Improved tangent estimate in the nudged elastic band method for finding minimum energy paths and saddle points". *The Journal of Chemical Physics* 113 (2000), pp. 9978–9985.

[23] G. Henkelman, B. P. Uberuaga, and H. Jónsson. "A climbing image nudged elastic band method for finding saddle points and minimum energy paths". *The Journal of Chemical Physics* 113 (2000), pp. 9901–9904.

[24] P. Maragakis, S. A. Andreev, Y. Brumer, D. R. Reichman, and E. Kaxiras. "Adaptive nudged elastic band approach for transition state calculation". *Journal of Chemical Physics* 117 (2002), pp. 4651–465.

[25] S. A. Trygubenko and D. J. Wales. "A doubly nudged elastic band method for finding transition states". *Journal of Chemical Physics* 120 (2004), pp. 2082–2094.

[26] N. Gonzalez-Garcia, J. Pu, A. Gonzalez-Lafont, J. M. Lluch, and D. G. Truhlar. "Searching for saddle points by using the nudged elastic band method: An implementation for gas-phase systems". *Journal of Chemical Theory and Computation* 2 (2006), pp. 895–904.

[27] I. F. Galvan and M. J. Field. "Improving the efficiency of the NEB reaction path finding algorithm". *Journal of Chemical Physics* 29 (2008), pp. 139–143.

[28] D. Sheppard, P. Xiao, W. Chemelewski, D. D. Johnson, and G. Henkelman. "A generalized solid-state nudged elastic band method". *Journal of Chemical Physics* 136 (2012), pp. 074103+.

[29] E. L. Kolsbjerg, M. N. Groves, and B. Hammer. "An automated nudged elastic band method". *The Journal of Chemical Physics* 145 (2016), pp. 094107+.

[30] J. Klimeš, D. R. Bowler, and A. Michaelides. "A critical assessment of theoretical methods for finding reaction pathways and transition states of surface processes". *Journal of Physics: Condensed Matter* 22 (2010), pp. 074203+.

[31] A. D. Becke. "Perspective: Fifty years of density-functional theory in chemical physics". *The Journal of Chemical Physics* 140 (2014), 18A301+.

[32] S. Lorenz, A. Groß, and M. Scheffler. "Representing high-dimensional potential-energy surfaces for reactions at surfaces by neural networks". *Chemical Physics Letters* 395 (2004), pp. 210–215.

[33] J. Behler and M. Parrinello. "Generalized Neural-Network Representation of High-Dimensional Potential-Energy Surfaces". *Physical Review Letter* 98 (2007), pp. 146401+.

[34] A. P. Bartok, M. C. Payne, R. Kondor, and G. Csanyi. "Gaussian Approximation Potentials: The Accuracy of Quantum Mechanics, without the Electrons". *Physical Review Letters* 104 (2010), pp. 136403+.

[35] F. Brockherde, L. Vogt, L. Li, et al. "Bypassing the Kohn-Sham equations with machine learning". *Nature Communications* 8 (2017), pp. 872+.

[36] J. E. Yazal and Y.-P. Pang. "Comparison of DFT, Møller-Plesset, and coupled cluster calculations of the proton dissociation energies of imidazole and N-methylacetamide in the presence of zibc(II)". *Journal of Molecular Structure: THEOCHEM* 545 (2001), pp. 271–274.

[37] A. Karton, A. Tarnopolsky, J.-F. Lamère, G. C. Schatz, and J. M. L. Martin. "Highly Accurate First-Principles Benchmark Data Sets for the Parametrization and Validation of Density Functional and Other Approximate Methods. Derivation of a Robust, Generally Applicable, Double-Hybrid Functional for Thermochemistry and Thermochemical Kinetics". *The Journal of Physical Chemistry A* 112 (2008), pp. 12868–12886.

[38] D. Hait and M. Head-Gordon. "How Accurate Is Density Functional Theory at Predicting Dipole Moments? An Assessment Using a New Database of 200 Benchmark Values". *Journal of Chemical Theory and Computation* 14 (2018), pp. 1969–1981.

[39] P. Hohenberg and W. Kohn. "Inhomogeneous Electron Gas". *Physical Review* 136 (1964), B864–B871.

[40] B. M. and O. R. "Zur Quantentheorie der Molekeln". *Annalen der Physik* 389 (1927), pp. 457+.

[41] W. Kohn and L. J. Sham. "Self-Consistent Equations Including Exchange and Correlation Effects". *Physical Review* 140 (1965), A1133.

[42] P. A. M. Dirac. "Note on Exchange Phenomena in the Thomas Atom". *Mathematical Proceedings of the Cambridge Philosophical Society* 26 (1930), pp. 376–385.

[43] S. H. Vosko, L. Wilk, and M. Nusair. "Accurate spin-dependent electron liquid correlation energies for local spin density calculations: a critical analysis". *Canadian Journal of Physics* 58 (1980), pp. 1200–1211.

[44] S. F. Sousa, P. A. Fernandes, and M. J. Ramos. "General Performance of Density Functionals". *The Journal of Physical Chemistry A* 111 (2007), pp. 10439–10452.

[45] J. P. Perdew, K. Burke, and M. Ernzerhof. "Generalized Gradient Approximation Made Simple". *Physical Review Letter* 77 (1996), pp. 3865–3868.

[46] J. P. Perdew and K. Schmidt. "Jacob's ladder of density functional approximations for the exchange-correlation energy". *AIP Conference Proceedings* 577 (2001), pp. 1+.

[47] J. Klimeš, D. R. Bowler, and A. Michaelides. "Van der Waals density functionals applied to solids". *Physical Review B* 83 (2011), pp. 195131+.

[48] J. Carrasco, W. Liu, A. Michaelides, and A. Tkatchenko. "Insight into the description of van der Waals forces for benzene adsorption on transition metal (111) surfaces". *The Journal of Chemical Physics* 140 (2014), pp. 084704+.

[49] S. Gautier, S. N. Steinmann, C. Michel, P. Fleurat-Lessard, and P. Sautet. "Molecular adsorption at Pt(111). How accurate are DFT functionals?" *Physical Chemistry Chemical Physics* 17 (2015), pp. 28921–28930.

[50] M. Dion, H. Rydberg, E. Schröder, D. C. Langreth, and B. I. Lundqvist. "Van der Waals Density Functional for General Geometries". *Physical Review Letter* 92 (2004), pp. 246401+.

[51] K. Kim and K. D. Jordan. "Comparison of Density Functional and MP2 Calculations on the Water Monomer and Dimer". *The Journal of Physical Chemistry* 98 (1994), pp. 10089–10094.

[52] J. Enkovaara, C. Rostgaard, J. J. Mortensen, et al. "Electronic structure calculations with GPAW: a real-space implementation of the projector augmented-wave method". *Journal of Physics: Condensed Matter* 22 (2010), pp. 253202+.

[53] P. E. Blöchl. "Projector augmented-wave method". *Physical Review B* 50 (1994), pp. 17953+.

[54] T. Ono, M. Heide, N. Atodiresei, et al. "Real-space electronic structure calculations with full-potential all-electron precision for transition metals". *Phys. Rev. B* 82 (2010), pp. 205115+.

[55] A. H. Larsen, J. J. Mortensen, J. Blomqvist, et al. "The atomic simulation environment – a Python library for working with atoms". *Journal of Physics: Condensed Matter* 29 (2017), pp. 273002+.

[56] A. Khorshidi and A. A. Peterson. "Amp: A modular approach to machine learning in atomistic simulations". *Computer Physics Communications* 207 (2016), pp. 310–324.

[57] M. van Gerven and S. Bohte. *Artificial neural networks as models of neural information processing.* Frontiers Media SA, 2018.

[58] P. J. Werbos. "Beyond Regression: New Tools for Prediction and Analysis in the Behavioral Sciences". PhD thesis. Harvard University, 1974.

[59] L. J. Munro and D. J. Wales. "Defect migration in crystalline silicon". *Physical Review B* 59 (1999), pp. 3969–3980.

[60] G. Henkelman and H. Jónsson. "A dimer method for finding saddle points on high dimensional potential surfaces using only first derivatives". *The Journal of Chemical Physics* 111 (1999), pp. 7010–7022.

[61] J. H. Jørgensen, A. G. Čabo, R. Balog, et al. "Symmetry-Driven Band Gap Engineering in Hydrogen Functionalized Graphene". English. *ACS Nano* 10 (2016), pp. 10798–10807.

[62] S. Smidstrup, A. Pedersen, K. Stokbro, and H. Jónsson. "Improved initial guess for minimum energy path calculations". *The Journal of Chemical Physics* 140 (2014), pp. 214106+.

[63] A. A. Peterson. "Acceleration of saddle-point searches with machine learning". *The Journal of Chemical Physics* 145 (2016), pp. 074106+.

[64] X.-J. Zhang, C. Shang, and Z.-P. Liu. "Double-Ended Surface Walking Method for Pathway Building and Transition State Location of Complex Reactions". *Journal of Chemical Theory and Computation* 9 (2013), pp. 5745–5753.

[65] A. C. Vaucher and M. Reiher. "Minimum Energy Paths and Transition States by Curve Optimization". *Journal of Chemical Theory and Computation* 14 (2018), pp. 3091–3099.

[66] P. M. Zimmerman. "Automated discovery of chemically reasonable elementary reaction steps". *Journal of Computational Chemistry* 34 (2013), pp. 1385–1392.

[67] P. M. Zimmerman. "Navigating molecular space for reaction mechanisms: an efficient, automated procedure". *Molecular Simulation* 41 (2015), pp. 43–54.

[68] M. Jafari and P. M. Zimmerman. "Uncovering reaction sequences on surfaces through graphical methods". *Phys. Chem. Chem. Phys.* 20 (2018), pp. 7721–7729.

[69] Y. V. Suleimanov and W. H. Green. "Automated Discovery of Elementary Chemical Reaction Steps Using Freezing String and Berny Optimization Methods". *Journal of Chemical Theory and Computation* 11 (2015), pp. 4248–4259.

[70] R. Fournier, S. Bulusu, S. Chen, and J. Tung. "Using swarm intelligence for finding transition states and reaction paths". *The Journal of Chemical Physics* 135 (2011), pp. 104117+.

[71] F. Draxler, K. Veschgini, M. Salmhofer, and F. A. Hamprecht. "Essentially No Barriers in Neural Network Energy Landscape". *ArXiv e-prints* (2018). arXiv: `1803.00885 [stat.ML]`.

[72] N. Rahaman, D. Arpit, A. Baratin, et al. "On the Spectral Bias of Deep Neural Networks". *ArXiv e-prints* (2018). arXiv: `1806.08734 [stat.ML]`.

[73] V. H. Grassian and E. L. Muetterties. "Electron energy loss and thermal desorption spectroscopy of pyridine adsorbed on platinum(111)". *The Journal of Physical Chemistry* 90 (1986), pp. 5900–5907.

[74] C. Wöckel, A. Eilert, M. Welke, et al. "Pyridine on flat Pt(111) and stepped Pt(355)-An *in situ* HRXPS investigation of adsorption and thermal evolution". *The Journal of Chemical Physics* 144 (2016), pp. 014702+.

[75] J. M. Gottfried, E. K. Vestergaard, P. Bera, and C. T. Campbell. "Heat of Adsorption of Naphthalene on Pt(111) Measured by Adsorption Calorimetry". *The Journal of Physical Chemistry B* 110 (2006), pp. 17539–17545.

[76] W. Liu, J. Carrasco, B. Santra, et al. "Benzene adsorbed on metals: Concerted effect of covalency and van der Waals bonding". *Physical Review B* 86 (2012), pp. 245405+.

[77] K. Berland, V. R. Cooper, K. Lee, et al. "van der Waals forces in density functional theory: a review of the vdW-DF method". *Reports on Progress in Physics* 78 (2015), pp. 066501+.

[78] R. J. Maurer, V. G. Ruiz, J. Camarillo-Cisneros, et al. "Adsorption structures and energetics of molecules on metal surfaces: Bridging experiment and theory". *Progress in Surface Science* 91 (2016), pp. 72–100.

[79] A. M. H. Rasmussen and B. Hammer. "Adsorption, mobility, and dimerization of benzaldehyde on Pt(111)". *The Journal of Chemical Physics* 136 (2012), pp. 174706+.

[80] S. Haq and D. A. King. "Configurational Transitions of Benzene and Pyridine Adsorbed on Pt111 and Cu110 Surfaces: An Infrared Study". *The Journal of Physical Chemistry* 100 (1996), pp. 16957–16965.

[81] C. Zuo and P. W. Jagodzinski. "Surface-Enhanced Raman Scattering of Pyridine Using Different Metals: Differences and Explanation Based on the Selective Formation of α-Pyridyl on Metal Surfaces". *The Journal of Physical Chemistry B* 109 (2005), pp. 1788–1793.

[82] M. Ghadami Yazdi, P. H. Moud, K. Marks, et al. "Naphthalene on Ni(111): Experimental and Theoretical Insights into Adsorption, Dehydrogenation, and Carbon Passivation". *The Journal of Physical Chemistry C* 121 (2017), pp. 22199–22207.

[83] J. A. Garrido Torres, B. Ramberger, H. A. Früchtl, R. Schaub, and G. Kresse. "Adsorption energies of benzene on close packed transition metal surfaces using the random phase approximation". *Physical Review Materials* 1 (2017), pp. 060803+.

[84] S. Grimme and P. R. Schreiner. "Computational Chemistry: The Fate of Current Methods and Future Challenges". *Angewandte Chemie International Edition* 57 (2018), pp. 4170–4176.

[85] S. M. Barlow and R. Raval. "Complex organic molecules at metal surfaces: bonding, organisation and chirality". *Surface Science Reports* 50 (2003), pp. 201–341.

[86] M. O. Lorenzo, S. Haq, T. Bertrams, et al. "Creating Chiral Surfaces for Enantioselective Heterogeneous Catalysis: R,R-Tartaric Acid on Cu(110)". *The Journal of Physical Chemistry B* 103 (1999), pp. 10661–10669.

[87] N. Georg, H. Antje, G. Ronny, G. Kristina, and K. Stefan. "Chiral Metal-Organic Frameworks and Their Application in Asymmetric Catalysis and Stereoselective Separation". *Chemie Ingenieur Technik* 83 (2011), pp. 90–103.

[88] T. Yokoyama, S. Yokoyama, T. Kamikado, Y. Okuno, and S. Mashiko. "Selective assembly on a surface of supramolecular aggregates with controlled size and shape". *Nature* 413 (2001), pp. 619–621.

[89] B. Davide, M. Stefan, and L.-P. Anna. "Supramolecular Chemistry at Interfaces: Molecular Recognition on Nanopatterned Porous Surfaces". *Chemistry – A European Journal* 15 (2009), pp. 7004–7025.

[90] S. Karan, Y. Wang, R. Robles, N. Lorente, and R. Berndt. "Surface-Supported Supramolecular Pentamers". *Journal of the American Chemical Society* 135 (2013), pp. 14004–14007.

[91] L. B. Vilhelmsen and B. Hammer. "A genetic algorithm for first principles global structure optimization of supported nano structures". *The Journal of Chemical Physics* 141 (2014), pp. 044711+.

[92] L. B. Vilhelmsen and B. Hammer. "Systematic Study of Au_6 to Au_{12} Gold Clusters on MgO(100) F Centers Using Density-Functional Theory". *Physical Review Letters* 108 (2012), pp. 126101+.

[93] W. Luo, Y. Ma, X. Gong, and H. Xiang. "Prediction of Silicon-Based Layered Structures for Optoelectronic Applications". *Journal of the American Chemical Society* 136 (2014), pp. 15992–15997.

[94] Z. Wang, X.-F. Zhou, X. Zhang, et al. "Phagraphene: A Low-Energy Graphene Allotrope Composed of 5-6-7 Carbon Rings with Distorted Dirac Cones". *Nano Letters* 15 (2015), pp. 6182–6186.

[95] F. Ma, G. Gao, Y. Jiao, et al. "Predicting a new phase (T″) of two-dimensional transition metal di-chalcogenides and strain-controlled topological phase transition". *Nanoscale* 8 (2016), pp. 4969–4975.

[96] A. S. Crampton, M. D. Rötzer, C. J. Ridge, et al. "Structure sensitivity in the nonscalable regime explored via catalysed ethylene hydrogenation on supported platinum nanoclusters". *Nature Communications* 7 (2016), pp. 10389+.

[97] A. S. Crampton, M. D. Rötzer, C. J. Ridge, et al. "Assessing the concept of structure sensitivity or insensitivity for sub-nanometer catalyst materials". *Surface Science* 652 (2016), pp. 7–19.

[98] H. Zhai and A. N. Alexandrova. "Local Fluxionality of Surface-Deposited Cluster Catalysts: The Case of Pt_7 on Al_2O_3". *The Journal of Physical Chemistry Letters* 9 (2018), pp. 1696–1702.

[99] J. Wellendorff, K. T. Lundgaard, A. Møgelhøj, et al. "Density functionals for surface science: Exchange-correlation model development with Bayesian error estimation". *Physical Review B* 85 (2012), pp. 235149+.

[100] R. Ferrando, G. Barcaro, and A. Fortunelli. "Structures of small Au clusters on MgO(001) studied by density-functional calculations". *Physical Review B* 83 (2011), pp. 045418+.

[101] T. K. Patra, V. Meenakshisundaram, J.-H. Hung, and D. S. Simmons. "Neural-Network-Biased Genetic Algorithms for Materials Design: Evolutionary Algorithms That Learn". *ACS Combinatorial Science* 19 (2017), pp. 96–107.

[102] S. Q. Wu, M. Ji, C. Z. Wang, et al. "An adaptive genetic algorithm for crystal structure prediction". *Journal of Physics: Condensed Matter* 26 (2014), pp. 035402+.

[103] M. Van den Bossche, H. Grönbeck, and B. Hammer. "Tight-Binding Approximation-Enhanced Global Optimization". *Journal of Chemical Theory and Computation* 14 (2018), pp. 2797–2807.

[104] R. Ouyang, Y. Xie, and D.-e. Jiang. "Global minimization of gold clusters by combining neural network potentials and the basin-hopping method". *Nanoscale* 7 (36 2015), pp. 14817–14821.

[105] Q. Tong, L. Xue, J. Lv, Y. Wang, and Y. Ma. "Accelerating CALYPSO structure prediction by data-driven learning of a potential energy surface". *Faraday Discussions* (2018).

[106] D. Silver, J. Schrittwieser, K. Simonyan, et al. "Mastering the game of Go without human knowledge". *Nature* 550 (2017), pp. 354–359.

Papers

All peer-reviewed published or submitted publications discussed in the thesis, to which I have contributed, are attached on the following pages. The publications are listed in the same order as in the "List of Publications" on page viii.

Paper I

THE JOURNAL OF CHEMICAL PHYSICS **144**, 164112 (2016)

Pyridine adsorption and diffusion on Pt(111) investigated with density functional theory

Esben L. Kolsbjerg, Michael N. Groves, and Bjørk Hammer[a)]
Interdisciplinary Nanoscience Center (iNANO), Department of Physics and Astronomy, Aarhus University, Aarhus, Denmark

(Received 8 January 2016; accepted 8 April 2016; published online 26 April 2016)

The adsorption, diffusion, and dissociation of pyridine, C_5H_5N, on Pt(111) are investigated with van der Waals-corrected density functional theory. An elaborate search for local minima in the adsorption potential energy landscape reveals that the intact pyridine adsorbs with the aromatic ring parallel to the surface. Piecewise interconnections of the local minima in the energy landscape reveal that the most favourable diffusion path for pyridine has a barrier of 0.53 eV. In the preferred path, the pyridine remains parallel to the surface while performing small single rotational steps with a carbon-carbon double bond hinged above a single Pt atom. The origin of the diffusion pathway is discussed in terms of the C_2–Pt π-bond being stronger than the corresponding CN–Pt π-bond. The energy barrier and reaction enthalpy for dehydrogenation of adsorbed pyridine into an adsorbed, upright bound α-pyridyl species are calculated to 0.71 eV and 0.18 eV, respectively (both zero-point energy corrected). The calculations are used to rationalize previous experimental observations from the literature for pyridine on Pt(111). *Published by AIP Publishing.* [http://dx.doi.org/10.1063/1.4947225]

I. INTRODUCTION

The binding of aromatic molecules to late transition metal surfaces is a key step in many industrial processes, including catalytic reforming in petroleum refining[1] and the production of fine chemicals in the pharmaceutical and agrochemical industry.[2] This has spurred interest in describing by both theoretical and experimental means the interaction of aromatic molecules with the prevailing facets of single crystalline surface of metals such as Rh, Pd, and Pt.[3–16] In particular, the adsorption on Pt(111) of the prototypical aromatic molecule benzene has been studied intensively and now serves as a benchmark for the assessment of theoretical methods.[17–23] In this paper, we complement this established literature by moving to a slightly more involved aromatic molecule: pyridine, C_5H_5N. Compared to benzene, pyridine has one CH group replaced by a secondary amine group, N. Pyridine is hence less symmetric than benzene and the lone pair on N adds new and interesting aspects to the energy balance established upon adsorption, diffusion, and reaction, since the molecule may interact through both the aromatic π-system and the lone pair.

Pyridine has many applications including acting as solvent for chemical reactions[24] and its variants are precursors in the synthesis of pharmaceuticals,[25] as well as a test subject for the development of surface-enhanced Raman scattering.[26] Additionally, pyridine can be used as a probe of heterogeneous sites of SiOH over silica[27] and to examine the number of Brønsted and Lewis acid sites on a zeolite-catalyst.[28] It has previously been shown using reflection-absorption infrared (IR) spectroscopy and surface-enhanced Raman scattering on several metal surfaces that the adsorption geometry of pyridine can be either flat, tilted, or upright. The upright phase comes in two forms: pyridine and its dehydrogenated derivative alpha-pyridyl.[4,29] Scanning tunnelling spectroscopy (STS) and scanning tunneling microscopy (STM),[30,31] temperature programmed desorption (TPD), low-energy electron diffraction (LEED), and electron stimulated desorption ion angular distribution (ESDIAD)[32] technique studies also confirm that the combination of different environments, including substrate, coverage, and temperature, shows different adsorption geometries, see Figure 1. However, the only clear trend is that as the coverage falls, pyridine tends to bend more towards the surface. This has been discussed in terms of the competition between the aromatic π to metal surface interaction in a flat-lying configuration parallel to the surface and the upright standing configuration dominated by the N lone pair interaction acting as a σ-donor.[31,33,34] On top of this, both favourable and unfavourable intermolecular interactions must also be considered.[35,36] It has been shown that pyridine on Pt(111) initially adsorbs either as flat-lying or as a somewhat tilted configuration at large coverages by investigation with electron energy loss spectroscopy (EELS) and infrared (IR) spectroscopy.[33] Extensive studies of pyridine by a range of experimental techniques including two-photon photoemission,[37] TPD,[32] IR,[4] STM[30] on Cu surfaces show a stronger tendency for pyridine to chemisorb with the N pointing towards the surface. Furthermore on silver surfaces there is evidence for a range of adsorption geometries supported by high resolution electron energy loss spectroscopy (HREELS) and UV photoemission spectroscopy.[38]

The complex nature of molecule-substrate interactions seems to be specific to each adsorbate-surface pair. As a result, a detailed analysis is needed for each case. So far it has been established that pyridine chemisorbs on the Pt(111) surfaces in different configurations and has the ability to transition into the α-pyridyl species at high temperature/coverage. We now

[a)]Electronic mail: hammer@phys.au.dk

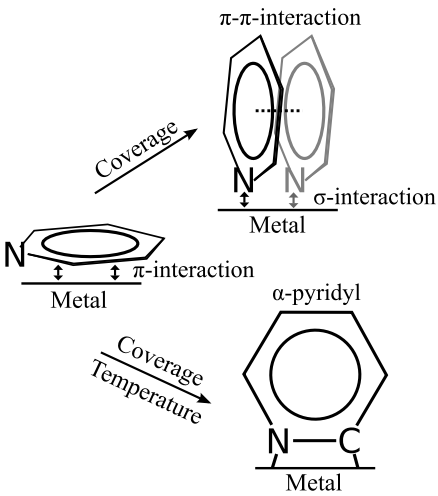

FIG. 1. Pyridine flat-lying with π metal surface interaction at low coverage. For higher coverage, a more upright configuration is present with both π-π interactions between adjacent molecules and a more σ like interaction with the surface. Finally at also high temperatures, the upright α-pyridyl shows two strong σ like bonds to the surface.

address the issue of how pyridine more specifically binds to the Pt(111) surface, and how it diffuses and transitions to the α-pyridyl species. A systematic approach is employed. The approach is not unique for pyridine but would be applicable to a large range of molecule-surface pairs as long as the molecules are relatively small and symmetric.

II. METHOD

Density functional theory (DFT) as implemented in the GPAW[39] code with the ASE[40] interface was used for the calculations. For the exchange-correlation effects, the optB88-vdW[42] functional is employed. Since we will describe the adsorption of an aromatic molecule on Pt(111), we use the optB88-vdW functional which has proven successful for describing similar systems, benzene/Pt(111)[18] and acetophenone-derivative/Pt(111).[41] The GPAW software uses the projector augmented wave method on a real-space grid.[43,44] All reported calculations are done with a grid spacing less than 0.1778 Å. If not stated otherwise the molecules are adsorbed on a $c(4 \times 8)$ slab represented by a 4×4 rectangular Pt(111) surface resulting in 16 Pt atoms in each of the four layers. We use the optimised lattice constants for the optB88-vdW[42] functional, $a = 4.02$ Å which is close to the experimental value of $a = 3.92$ Å. A convergence test with respect to the number of Pt layers shows that the adsorption energy is dependent on the number of layers. In a compromise between computational resources and accuracy, a four layer slab was picked, see the supplementary material, Fig. S1,[49] for a convergence test with respect to the number of layers. A 2×2 **k**-point mesh was used for all calculations to sample the Brillouin zone. All stable adsorption geometries have been recalculated with a denser **k**-point mesh (4×4) and can be seen in the supplementary material, Table S1.[49] The upper and lower changes in adsorption energy do not exceed +0.004 and −0.021 eV, and hence, in order to save on the computational effort, all reaction pathways and vibrational calculation were done with the 2×2 **k**-point grid. To stay consistent, all reported calculations in the paper are with the 2×2 mesh grid. Geometric optimisations were terminated when no force exerted on the atoms exceeded 0.025 eV/Å. The calculations were preformed in a 2D periodic cell with at least 8 Å between the atoms and the cell boundary perpendicular to the slab. At the non-periodic cell boundaries, a zero value condition was imposed on the wave function taking advantage of the GPAW code's capability.

Zero-point energy (ZPE) calculations were performed for all identified adsorption configurations and all located transition states (TSs).[45] The uncorrected energies from the tested structures can be found in Table S1.[49]

A systematic examination of the energy barriers between different configurations was handled with the Nudged Elastic Band (NEB) method.[46] The convergence criteria as well as calculational setup are the same for finding the highest lying energy points along the reaction pathway (TS) as for the geometric optimisations.

When searching for diffusion pathways, an intuitive approach would be to perform a NEB calculation for the pyridine moving from one occurrence of the preferred adsorption configuration to an adjacent occurrence, one lattice spacing away. Such a calculation would indeed provide a continuous pathway. However, owing to the nature of the NEB method, the calculation would not convincingly sample what meta-stable configurations the pyridine would pass through in the diffusion path. In order to introduce such a sampling, we performed the diffusion path search as a series of piece-wise NEB calculations connecting stable and meta-stable configurations with any nearby counterparts. With all piece-wise NEB pathways available, the full diffusion path was identified as the optimum collection of NEB pieces fulfilling the original objective of moving the pyridine one lattice spacing, where optimum means having the overall smallest energy barrier.

The handling and plotting of the meta-stable configurations and their NEB interconnections was done using the three coordinates, X, Y and θ, defining the lateral position of the pyridine and its in-plane rotation. In the searches for NEB pieces, the initial and final states were limited to subplanes, $X = 0$, $Y = 0$, or $\theta = 0$ or 180 as will be defined in the figures below. However, in the NEB runs, the images along the pathways were allowed to deviate from these subplanes in order for the system not to experience unnecessary constrains. In practice, most of the images between each stable minimum in many NEB calculations moved out of the plane when the path was relaxed.

III. RESULTS AND DISCUSSION

A. Pyridine adsorption on Pt(111)

The study of pyridine on Pt(111) starts from an identification of the possible adsorption configurations. Because of pyridines resemblance to benzene, we considered

the same flat-lying, high symmetry, adsorption configurations that have been found for benzene.[12]

The presence of nitrogen (N) in pyridine however lowers the symmetry of this adsorbate in the high symmetry sites and we hence adopt a new naming scheme. The configurations are named after the types of bonds the N is making with the surface. Examples of the σ- and π-bond can be seen in Figures 2(a) and 2(b), respectively. With the C–C bonds at a 30° angle to the Pt–Pt lattice, we find four configurations: two pairs named bri-N_σ and bri-N_π (Figures 3(a) and 3(c)) where the N, respectively, is σ-bonded and π-bonded to the Pt surface. When necessary we distinguish these paired configurations based on whether the N is in proximity to the hcp or the fcc hollow site underneath the molecule. However, the hcp/fcc distinction is inconsequential in terms of adsorption energy ($\Delta E(\text{bri-N}_{\sigma,(\text{hcp-fcc})}) = \sim 0.01$ eV) compared to if the N is σ- or π-bonded to the surface. Indeed, there is an immediate gain of about 0.30 eV when the N is σ-bonded to the surface and does not have to share a Pt atom. For pyridine (as is the case for benzene[12]) it turns out that bridge configurations with C–C bonds that are aligned with the Pt–Pt nearest neighbour directions in the surface are not stable, and they will not be considered more in this work. The remaining flat-lying configurations are centered over the three-fold sites, either fcc or hcp, and named according to the type of three-fold site and N-surface binding type (Figure 3(d)). Again, two directions of the C–C bonds with respect to the Pt–Pt directions are possible and consistent with the findings for benzene, only the aligned (0°) ones are of relevance. In addition to the flat-lying configurations, we considered three up-right configurations (Figures 3(b) and 3(e)). Upon adsorption all intermolecular bond lengths for flat-lying configurations are increased by 3%-5% while up-right configurations bond lengths remain almost unchanged. Depending on the configuration, as indicated in Figure 3, pyridine adsorbs at a distance of 1.88-2.11 Å above the slab. In summary Figure 3 illustrates the different stable adsorption configurations and Table I summarises the relative stability of the different configurations. A complete picture of all considered configurations is illustrated in Figure S2.[49]

It is clear from Table I that the most stable configuration for pyridine is the flat-lying bri-N_σ configuration. However, the most stable configuration calculated corresponds to α-pyridyl, which is the up-right dehydrogenated species of pyridine.

In Figure 4 the adsorption energy is plotted as a function of the coverage. The adsorption potential energies (APEs) are independent of coverage (within our calculational certainty) at the smallest coverages (1/25 and 1/16 ML) for all three adsorption configurations. As the coverage increases, the bri-$N_{\sigma,\text{fcc}}$ configuration becomes much less stable relative to the other configurations. In general, the various structures contained in Figure 4 are calculated in p($N \times N$) surface cells (N = 2-5), but in some cases the surface cell is changed into a cell allowing for more favourable packing. This is the case for the α-pyridyl species when going above the 1/16 coverage to accommodate the decrease in surface area. The molecules can be spaced out more evenly across the surface and hence increase the overall stability. A significantly more favourable

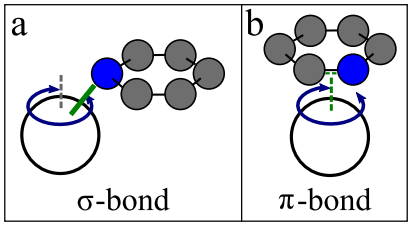

FIG. 2. Illustration of (a) σ- and (b) π-bonds between pyridine (gray and blue circles) and the underlying Pt-atoms (big open circle). Blue arrows indicate rotation around Pt-atoms during diffusion.

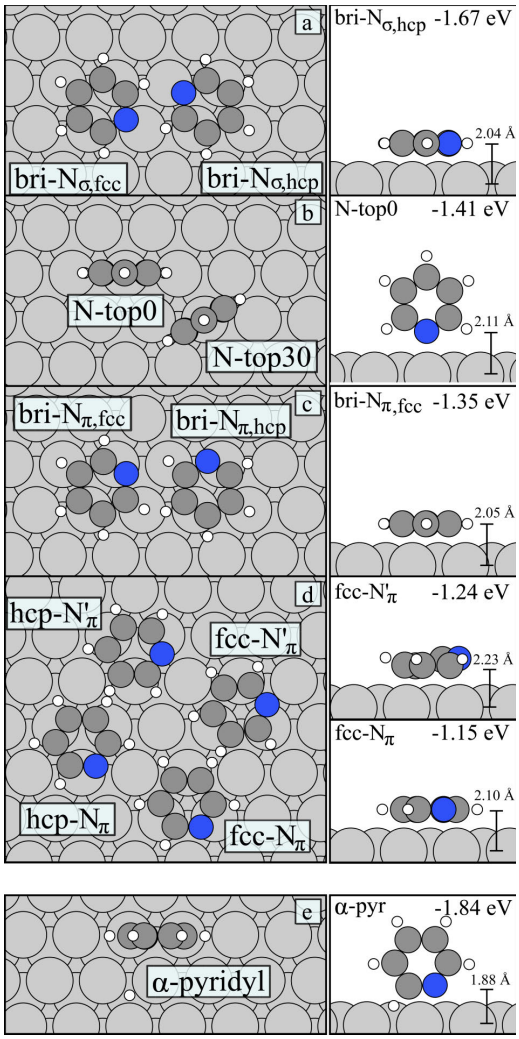

FIG. 3. Top and side views of all stable adsorption configurations for pyridine (Py) on Pt(111). The light gray spheres are the Pt atoms in the slab, while the dark gray, blue, and white spheres represent C, N, and H, respectively. The bri-$N_{\pi,(\text{hcp/fcc})}$, bri-$N_{\sigma,(\text{hcp/fcc})}$, fcc-$N_\sigma$, and hcp-$N_\sigma$ configurations are all flat, while the fcc-N'_σ and hcp-N'_σ configurations share a similar side profile with a slightly lifted N. Adsorption energies are quoted for a coverage of 1/16 ML. 1 ML is defined as 1 pyridine per surface Pt atom. The zero point reference is gas phase pyridine and an empty Pt slab.

TABLE I. Pyridine (Py) adsorption potential energies on Pt(111) (eV) for stable configurations at a coverage of 1/16 ML. All energies have been corrected for their respective ZPE.

	fcc	hcp		Flat	Tilted (')
bri-N_σ	−1.66	−1.67	fcc-N_π	−1.15	−1.24
bri-N_π	−1.35	−1.36	hcp-N_π	−1.20	−1.26
	0	30			
N-top	−1.41	−1.42	α-pyr	−1.84	

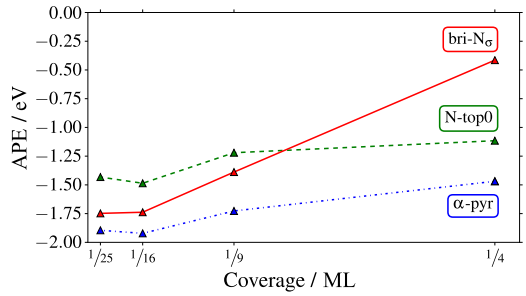

FIG. 4. Average adsorption potential energy (APE) in eV/molecule as a function of coverage for three different configurations. Green, red, and blue/yellow triangles represent the N-top0, bri-$N_{\sigma,\mathrm{fcc}}$, and α-pyridyl configurations, respectively. All calculations are done with rhombic unit cell so it is possible to consider the 3×3 and 5×5 cells.

surface structure is found for the 1/9 coverage in a $\begin{pmatrix} 0 & 3 \\ 3 & 2 \end{pmatrix}$ surface cell and for the 1/4 coverage a more stable packing is obtained in a c(2 × 4) cell. A range of different packings was tested and the most stable was picked. They can all be seen in the supplementary material, Figure S3.[49]

TPD experiments show a range of desorption peaks assigned by EELS to pyridine adsorbed in different configurations leaving the surface.[33] The order of the calculated adsorption energies follows the suggested order from the TPD/EELS experiment. The assignment following from the experiments at low temperatures as normal pyridine and at higher temperatures as α-pyridyl can be seen in Table II where they are paired with the respective calculated adsorption energies for the most stable configurations at a coverage of 1/9 ML.

The relative difference between the calculated binding configurations is in fairly good agreement with the experiments but the optB88-vdW functional seems to overbind pyridine to the surface. Having seen the same binding trends between theory and experiment, we now move to focus on the specific reasons for the most stable configurations at low coverage.

There is experimental evidence for the dependence of adsorption energy on the relative coverage of adsorbates.[4,33] As the temperature increases and/or the coverage increases, pyridine goes to a more upright adsorption configuration. This is exactly what the DFT data predict and we will later return to why α-pyridyl, the calculated most stable configuration, is only seen at high coverage/temperature. Figure 4 shows that by increasing the calculated coverage, the adsorption energy drops in all three cases and the difference between experiment and calculation decreases.

When the coverage increases and pyridine is pushed to an upright position, it can have severe implications on the reactivity of pyridine. An example of this consequence is seen in the exchange of H with D in pyridine on a Pt(110) surface.[47] Here pyridine stands upright at saturation coverage, but the exchange is seen to only occur when the molecules are orientated with the ring parallel to the surface. It is easy to speculate that this can influence many other types of reactions and substrates.

We can understand the difference between the bri-N_π and the bri-N_σ configurations by looking at the intramolecular bonding of the adsorbed pyridine molecule.[13,17] For the bri-N_π the N shares a Pt atom with a neighbouring C and forms a π-bond between the N–C p_z-orbitals and the appropriate Pt orbital. In Figure 5 we analyse the difference in electron density for the two configurations of pyridine — either in the bri-$N_{\pi,\mathrm{fcc}}$ or in the bri-$N_{\sigma,\mathrm{fcc}}$ configuration. The change in electron density arises from removing the molecule from the surface and looking at how the density is redistributed relative to both the slab and the molecule. From the plots, it is clear that the charge density rearrangements are smaller for the π-bond at the NC-shared Pt atom site than for the π-bond at the pure CC-shared Pt site. This is suggestive of the interaction strength being weaker at the NC-shared Pt atom site than at the pure C site for the bri-$N_{\pi,\mathrm{fcc}}$ configuration. The bri-$N_{\sigma,\mathrm{fcc}}$ configuration has two occurrences of the strong CC–Pt π-interaction and could be expected to be more strongly bound. However, in this configuration, one of the two C–Pt σ-bonds for C atoms not involved in π-bonding (so-called apical C atoms) has been traded for a N–Pt σ-bond. Judging from the charge density rearrangements, and confirmed by the calculated energetics, this bond is weaker and explains the preference for the bri-$N_{\pi,\mathrm{fcc}}$ configuration. Below, the charge density plots will be used to further rationalize the findings for the favoured diffusion pathway for adsorbed flat-lying pyridine.

Now comparing the bond strength between upright pyridine and its N pointing toward the surface to the flat-lying adsorption configurations where π-interactions dominate, it is

TABLE II. (1) Low coverage desorption temperatures from thermal desorption spectroscopy experiments,[33] and (2) the corresponding experimental adsorption energies calculated with an exponential factor of 10^{13} s^{-1} and heating rate of $\beta = 25$ K/s and (3) compared to the 1/9 ML configurations and (4) their relative calculated adsorption energies.

(1) Peak (K)	(2) Expt. E_{ad} (eV)	(3) Assignment	(4) Calculated E_{ad} (eV)
347	−0.95	N-top0/bri-N_σ	−1.41/−1.67
483	−1.23	α-pyr	−1.84

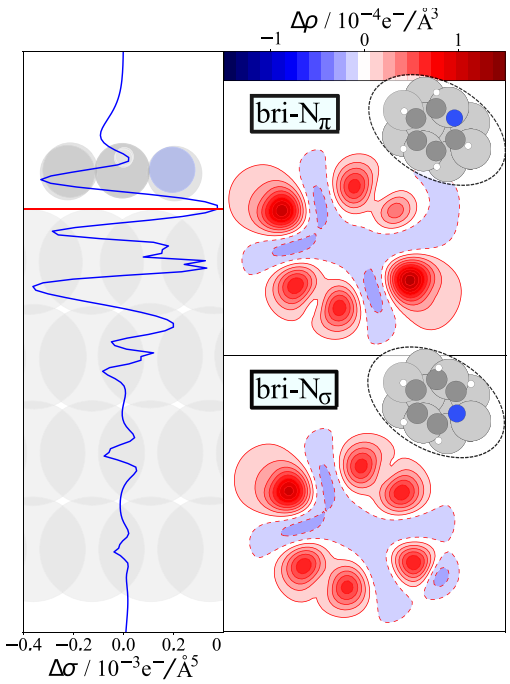

FIG. 5. Plot of the electron density difference between pyridine separated from the slab and the molecule adsorbed on the slab. To the left is the integrated electron density difference over the X-Y plane as a function of the Z coordinate (perpendicular to the surface) (for the bri-$N_{\pi,\mathrm{fcc}}$ configuration). To the right is the electron density difference at the interface between the slab and molecule plotted as a contour map. The top right shows the bri-$N_{\pi,\mathrm{fcc}}$ and the bottom left shows bri-$N_{\sigma,\mathrm{fcc}}$ configuration. The inset in both subfigures shows the adsorption configuration.

apparent that the N accounts for a large part of the adsorption energy. Indeed, the stability difference for bri-$N_{\sigma,\mathrm{hcp}}$ and N-top0 is 0.26 eV but the π system in flat pyridine accounts for a lot more of the inaction energy than only 0.26 eV. The dominance of the N–Pt-interaction is valid only if the lone pair is pointing directly towards the surface. It should be stated that the N is sp^2-hybridized which then leaves the remaining N lone pair pointing straight out of the molecular plane and hence not towards the underlying Pt-atom. Both the fcc-N_σ and hcp-N_σ configurations have two stable minima a flat and a more stable version when N is lifted off the surface where pyridine has a 7°–9° angle to the surface — hence a version marked (') exists for these two configurations.

B. Pyridine diffusion on Pt(111)

Having established the stable and meta-stable adsorption configurations of pyridine on Pt(111), we now move to the identification of the diffusion energy pathway. To do so, the pyridine is described by three coordinates, X, Y, and θ, as defined in the middle left of Figure 6. Next, four different 2D planes contained in the 3D space spanned by X, Y, and θ are considered as shown in the upper left of Figure 6. Within each of these planes, the pyridine diffuses under a constraint, e.g., with a constant rotational configuration in the X-Y-plane. The rest of Figure 6 presents the results of piece-wise NEB calculations connecting all stable bri-N_σ configurations and meta-stable bri-N_π, fcc-N_σ, hcp-N_σ configurations within the 2D planes. The neighbouring configurations are connected with an arrow whose color indicates the calculated energy difference with respect to the TS between the pair of minima and the bri-N_σ configuration. The combined path connecting two stable bri-$N_{\sigma,\mathrm{fcc}}$ configurations separated by one Pt–Pt spacing with the overall lowest barrier is highlighted with a green border in Figure 6 and is shown as an energy diagram in Figure 7.

A rotation around a C–C surface π-bond requires the fewest number of bonds with the surface to be broken when a molecule diffuses. Rotations around σ- and π-bonds are sketched in Figure 2. Steps like these are in Figure 6 plotted as oblique arrows in the X-θ plane and many of them have lower barriers than any single slide of the molecule. The lowest energy path has a transition state which is 0.53 eV less favourable than the bri-$N_{\sigma,\mathrm{fcc}}$ configuration and this path is exclusively in the X-θ dimension.

The reason why the highlighted path from Figure 6 is the most preferred can be understood as a combination of effects. First of all the pyridine seeks to minimise the number of bonds broken with the surface. This is achieved by rotating around a π-bond between two C atoms and a Pt atom. This movement preserves at least one bond to the surface. As discussed above for Figure 5, the charge density difference plots are suggestive that CN–Pt π interaction is weaker than the CC–Pt π interaction. In the highlighted path, the N either acts as "nose" or "tail" and the pyridine molecule does not, at any point, have to rotate around a CN–Pt π surface bond. Hence, it preserves a strong CC–Pt π surface bond all along the diffusion path. Additionally, as seen in Figure 6, this path also runs through the lowest lying minima and this will generally reduce surrounding barriers. See the supplementary material[49] for a video of the preferred forward pathway.

A logical question arising from the density difference in Figure 5 is whether a rotation around the apparently strong single C–Pt or maybe N–Pt bond is preferred over a CC–Pt rotation. This can quickly be excluded by taking a look at the two purple highlighted steps in the Y-θ plane in Figure 6. Both of these steps are not directly feasible and are associated with a high barriers. The same can be said about an overall translation in the X-Y plane which leaves no surface-adsorbate bonds intact. It would require the pyridine to slide across the surface which is significantly less favourable than a rotation around a C–C bond on top of a single Pt atom.[12,14]

The present results for pyridine diffusion can be compared to those of benzene diffusion. Rasmussen[12] calculated the diffusion barrier of benzene to 0.6 eV with the PBE functional. Comparing the present path for pyridine with that for benzene, it is realized that they are very similar. The critical part of the path is that of moving from a bridge site (bri-$N_{\sigma,\mathrm{fcc}}$ for pyridine, bri30 for benzene) to an fcc site (fcc-N_σ for pyridine, fcc0 for benzene). This is for pyridine the first part of Figure 7, which we further show with color in the blue scheme in Figure 8. Preforming the same calculation for benzene but with the optB88-vdW functional, we find the energy profile shown with grey color in the scheme of Figure 8. With this

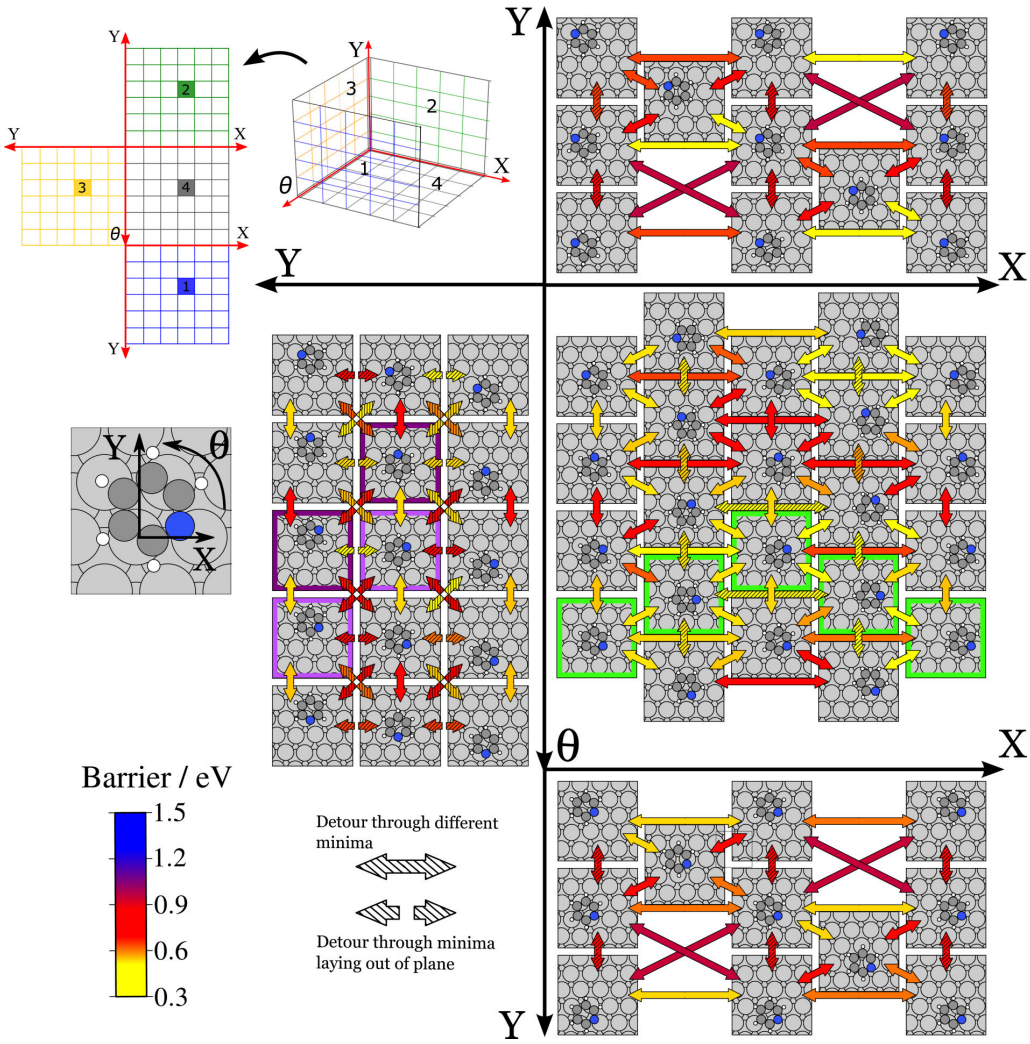

FIG. 6. Flat diffusion paths broken up into small steps for the three facets of the chosen coordinate system (X, Y, and θ). The color of the arrow indicates the relative stability of the transition state between each minimum relative to the bri-$N_{\sigma,\mathrm{fcc}}$ configuration. A hashed arrow indicates that a detour through different minima lying *in the indicated plane* is needed for the transition while a broken hashed arrow requires a detour through different minima lying *out of indicated plane*. The path connecting two global minima with the lowest barrier is highlighted with a green border. Both the bri-$N_{\sigma,\mathrm{fcc}}$ and bri-$N_{\sigma,\mathrm{hcp}}$ configurations for the X-Y facets have its own plot to cover the whole geometric space. The light/dark purple highlighted steps show examples of transition by rotation around a single N–Pt/C–Pt bond.

functional the benzene diffusion barrier becomes 0.46 eV (not ZPE corrected). This is very close to that of pyridine which is not surprising knowing that the anchoring part of benzene and pyridine during diffusion is a CC–Pt bond in both cases. Looking at the relative stability between the bridge and the fcc sites for pyridine the fcc site is 0.52 eV less stable than the bridge but for benzene the difference is only 0.26 eV. Lowering the product stability generally lowers the TS energy and rationalizes why the barrier for benzene diffusion is slightly less than that for pyridine. The smaller energy difference between the initial and final steps of the critical diffusion step for benzene relative to pyridine has consequence for the TS structure. According to Hammond's postulate,[48] the lowering of the reaction energy tends to make the TS less structurally similar to the final state. In the present case, this means that the diffusion TS of benzene should look less like the fcc configuration than the TS of pyridine looks like pyridine in the fcc configuration. Due to the similarities of the molecules, this can be illustrated in one plot as done in Figure 8. At the face of it a larger diffusion barrier for benzene could have been expected as benzene on Pt(111) binds with 1.91 eV (not ZPE corrected)[18] using the optB88-vdW functional compared to 1.58 eV (cf. Table S1[49]) for the non-ZPE corrected pyridine. However since benzene binds stronger also at intermediate sites that it passes during diffusion, the whole energy barrier is dragged down and hence the overall energy along the path is lower than that for pyridine.

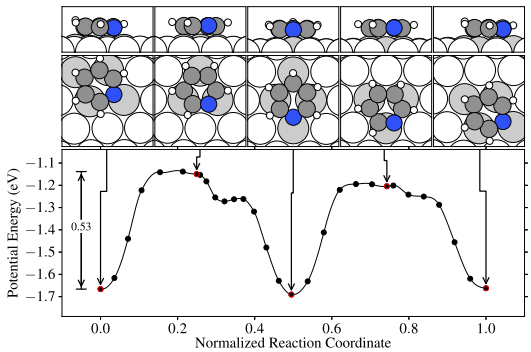

FIG. 7. Energy profile for the lowest barrier path through bri-$N_{\sigma,\mathrm{fcc}}$, fcc-N_{σ}, bri-$N_{\sigma,\mathrm{hcp}}$, hcp-N_{σ}, bri-$N_{\sigma,\mathrm{fcc}}$.

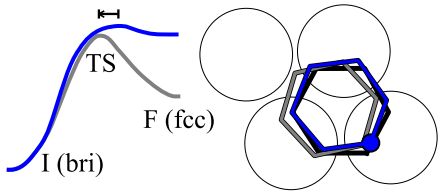

FIG. 8. To the left a schematic of the difference in the barrier for benzene (gray) and pyridine (blue). The gray curve is shifted down and the TS is consequently shifted to the left. Plotted to the right are the TS geometries for benzene (gray lines), pyridine (blue lines), and the fcc minimum (black) with TS for pyridine being closer to the fcc site.

To complement the above search for the diffusion path of pyridine in the flat-lying configuration, we performed searches in which the pathway included some upright minima. It could be the case that rotating up to an upright (N-top) configuration, hopping from one Pt row to the next, and finally rotating back down again, could have a lower barrier. Diffusion by hopping like this has been seen for pyridine on the Ag(110) surface.[31] We thus proceed exactly as before but just adding a fourth dimension ω representing the angle with respect to the plane of the surface. In this search pyridine only assumes two stable configurations in the upright configuration (N-top0 and N-top30).

The limited number of upright states reduces the complexity of the search for the pathway. We begin by first rotating around the N from the bri-N_{σ} configuration up to the N-top0/N-top30 configuration. A barrierless rotation around the N in the N-top position makes a hop to the next Pt row a possibility. This hop can proceed either as a straight on or a side hop. Both possibilities and the respective barriers (TS energy relative to the bri-N_{σ} configuration) can be seen in Figure 9. From the energy profiles it is apparent that the limiting step in these routes is the hop. Hence, only the bri-$N_{\sigma,\mathrm{fcc}}$ to N-top0 is considered (ignoring the bri-$N_{\sigma,\mathrm{hcp}}$ to N-top0 transition). The lowest energy transition state is found for the upper route (through N-top30 followed by a straight hop) with a destabilization of 0.84 eV relative to the bri-$N_{\sigma,\mathrm{fcc}}$ configuration. This is still far above the calculated barriers for flat diffusion and hence not a reasonable description for the preferred diffusion path for low coverage.

C. Pyridine to α-pyridyl

As stated earlier, pyridine is not stable at higher temperatures when adsorbed on a Pt(111) surface. Experiments show that it dehydrogenates into α-pyridyl, so we now focus on the transformation from pyridine to α-pyridyl. Again, employing a systematic approach there are at least two ways this could happen:

- First, a rotation from a bri-N_{σ} to an edge-on (N-top0/N-top30) configuration and then loss of an H to the Pt surface and finally a transition into the preferred α-pyridyl configuration.
- First, a rotation from a bri-N_{σ} to the flat hcp-N_{π}/fcc-N_{π} configuration and then loss of an H to the Pt surface to end up with a rotation up into the α-pyridyl configuration.

A selected representation of the possible paths is shown in Figure 10. A path starting from the bri-$N_{\sigma,\mathrm{hcp}}$ configuration and going through the fcc-N_{σ} configuration is equivalent to the bri-$N_{\sigma,\mathrm{fcc}}$ and hcp-N_{σ} route. Hence, we can focus on one

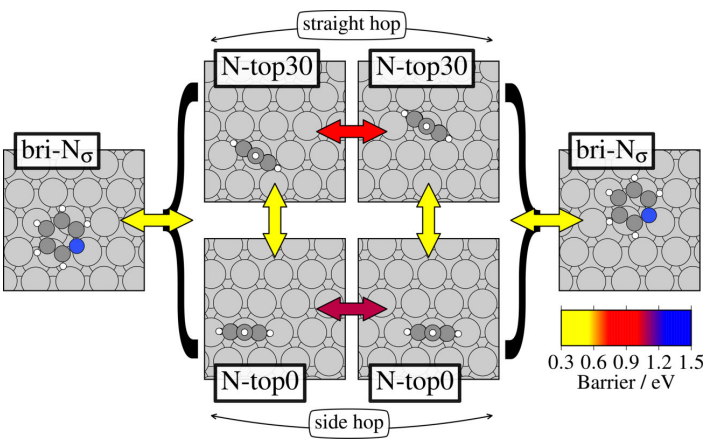

FIG. 9. The hopping inspired diffusion path. The transition state with the lowest barrier is found when following the upper route. No ZPE corrections have been applied.

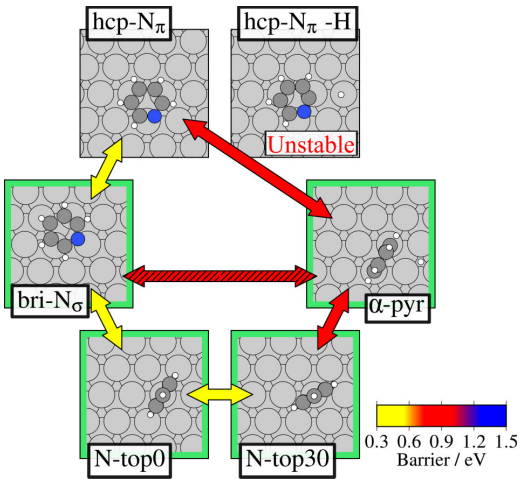

FIG. 10. Overview of the possible transitions into α-pyridyl. The color of the arrow indicates the relative stability of the transition state between each minimum. The path connecting two global minima with the lowest barrier is highlighted with a green border. As indicated the hcp-$N_{\sigma,\mathrm{fcc}}$ configuration with an H donated to the surface is not a stable minimum.

path. In this case there is a significant difference in the relative ZPE due to breaking the C–H bond.

As indicated in Figure 10, the flat-lying dehydrogenated species (hcp-N_π–H) is not a stable minimum, and therefore, the NEB transition proceeds only through stable minima but the structure is included for completeness. The direct path from bri-$N_{\sigma,\mathrm{fcc}}$ to α-pyridyl relaxes into a step-wise route. In this case, it becomes the lower route (highlighted with green) through the N-top0/N-top30 configurations. This route is the most favourable path for the reaction with a transition state 0.71 eV above the bri-$N_{\sigma,\mathrm{fcc}}$ configuration. Again, the total projected path onto the normalised reaction coordinate is plotted in Figure 11. Regardless of the path, the rate determining step is always to remove the H from the pyridine molecule.

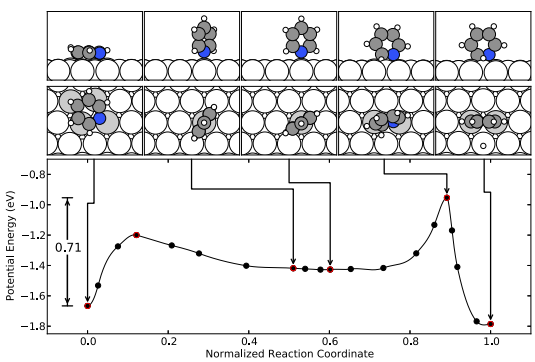

FIG. 11. Energy profile for the lowest barrier path for the conversion into α-pyridyl. ZPE for pyridine between TS and local minima are found by a linear interpolation between the surrounding TS/minima ZPE. The TS's were relaxed until only one imaginary frequency was found.

The larger energy barrier rationalizes why α-pyridyl does not populate the surfaces at low temperatures and explains why the IR experiments,[4] which are done at fixed temperatures, do not show peaks for α-pyridyl at low temperature and coverage. α-pyridyl first shows up at 265 K at saturation coverages, but not at lower temperature experiments (210 K, 140 K, 85 K). We can estimate the corresponding temperature to the calculated activation energy by an Arrhenius like expression ($N = N_0 e^{-[re^{-E_a/k_B T}]t}$). If we assume a low coverage and expect a sizeable conversion (10%) of pyridine to α-pyridyl with a reasonable attempt frequency of 10^{13} s^{-1}, the temperature needs to be 244 K in order for 10% of pyridines to be converted in a typical time scale of an experiment (1000 s) when the calculated activation energy (0.71 eV) is assumed. This calculated temperature of the forward transition lies exactly in between the temperatures in the two experiments where no α-pyridyl is measured (210 K) and α-pyridyl is measured (265 K).

IV. CONCLUSIONS

Pyridine adsorption, diffusion, and the transformation into α-pyridyl have been studied by vdW-corrected DFT calculations. The calculations show that pyridine is found to preferentially adsorb at all coverages in the dehydrogenated state, α-pyridyl. Both the flat (bri-N_σ) and the on-top (N-top0/N-top30) configurations are also very stable at low coverages; however, as the coverage increases, the bri-N_σ configuration becomes much less favourable which is in very good agreement with experiments. The importance of the position of the N and its interaction with the surface should be transferable to a general pyridyl-group or larger aromatic compounds with N atom(s) when adsorbed to a Pt(111) surface. The direct benefit of placing an N on top of a single Pt atom, like in pyridine, of course has to be compared to other potential gains/penalties another molecule may encounter.

Through an extended systematic search for the lowest barrier diffusion path, the pyridine diffusion is found to follow a flat stepwise walking like path with the N either leading (nose) or following (tail). The transition state energy for this path is found to be 0.53 eV above the global minimum configuration (bri-N_σ). Finally, the preferred path to dehydrogenate pyridine into α-pyridyl has a barrier of 0.71 eV.

ACKNOWLEDGMENTS

Grants from the Danish Research Councils (No. 0602-02566B) and The Lundbeck Foundation have supported this research.

[1]G. A. Somorjai, *Surface Chemistry and Catalysis* (John Wiley & Sons, 1994).
[2]H.-U. Blaser, A. Baiker, and R. Prins, *Heterogeneous Catalysis and Fine Chemicals IV* (Elsevier, 1997).
[3]S. D. Lin and M. A. Vannice, J. Catal. **143**, 539 (1993).
[4]S. Haq and D. A. King, J. Phys. Chem. **100**, 16957 (1996).
[5]H. Ihm and J. M. White, J. Phys. Chem. B **104**, 6202 (2000).
[6]C. Morin, D. Simon, and P. Sautet, J. Phys. Chem. B **108**, 5653 (2004).

[7]G. Hamm, T. Schmidt, J. Breitbach, D. Franke, C. Becker, and K. Wandelt, Surf. Sci. **562**, 170 (2004).
[8]C. Morin, D. Simon, and P. Sautet, J. Phys. Chem. B **108**, 12084 (2004).
[9]J. M. Gottfried, E. K. Vestergaard, P. Bera, and C. T. Campbell, J. Phys. Chem. B **110**, 17539 (2006).
[10]G.-K. Liu, B. Ren, D.-Y. Wu, S. Duan, J.-F. Li, J.-L. Yao, R.-A. Gu, and Z.-Q. Tian, J. Phys. Chem. B **110**, 17498 (2006).
[11]M. L. Honkela, J. Björk, and M. Persson, Phys. Chem. Chem. Phys. **14**, 5849 (2012).
[12]A. M. H. Rasmussen and B. Hammer, J. Chem. Phys. **136**, 174706 (2012).
[13]A. M. H. Rasmussen, M. N. Groves, and B. Hammer, ACS Catal. **4**, 1182 (2014).
[14]G. Goubert, A. M. H. Rasmussen, Y. Dong, M. N. Groves, P. H. McBreen, and B. Hammer, Surf. Sci. **629**, 123 (2014).
[15]D. Shi and J. M. Vohs, "Lignin-derived oxygenate reforming on a bimetallic surface: The reaction of benzaldehyde on Zn/Pt(111)," Sur. Sci. (published online).
[16]G. Li, J. Han, H. Wang, X. Zhu, and Q. Ge, ACS Catal. **5**, 2009 (2015).
[17]C. Morin, D. Simon, and P. Sautet, Surf. Sci. **600**, 1339 (2006).
[18]W. Liu, J. Carrasco, B. Santra, A. Michaelides, M. Scheffler, and A. Tkatchenko, Phys. Rev. B **600**, 245405 (2012).
[19]W. Liu, V. G. Ruiz, G.-X. Zhang, X. Ren, M. Scheffler, B. Santra, and A. Tkatchenko, New J. Phys. **15**, 53046 (2013).
[20]W. Liu, A. Tkatchenko, and M. Scheffler, Acc. Chem. Res. **47**, 3369 (2014).
[21]J. Wellendorff, T. L. Silbaugh, D. Garcia-Pintos, J. K. Nørskov, T. Bligaard, F. Studt, and C. T. Campbell, Surf. Sci. **640**, 36 (2015).
[22]S. Gautier, S. N. Steinmann, C. Michel, P. Fleurat-Lessard, and P. Sautet, Phys. Chem. Chem. Phys. **17**, 28921 (2015).
[23]P. K. Ayishabi, K. G. Lakshmikanth, and R. Chatanathodi, Chem. Phys. Lett. **637**, 182 (2015).
[24]A. P. Tanberg, J. Am. Chem. Soc. **36**, 335 (1914).
[25]J. Magano and R D. Joshua, Chem. Rev. **111**, 2177 (2011).
[26]M. Moskovits, Rev. Mod. Phys. **57**, 783 (1985).
[27]I. Gillis-D'Hamers, I. Cornelissens, K. C. Vrancken, P. Van Der Voort, E. F. Vansant, and F. Daelemans, J. Chem. Soc., Faraday Trans. **88**, 723 (1992).
[28]M. Karthik, C. J. Magesh, P. T. Perumal, M. Palanichamy, B. Arabindoo, and V. Murugesan, Appl. Catal., A **286**, 137 (2005).
[29]Z. Chen and P. W. Jagodzinski, J. Phys. Chem. **109**, 1788 (2005).
[30]D. B. Dougherty, J. Lee, and J. T. Yates, J. Phys. Chem. B **110**, 11991 (2006).
[31]J. R. Hahn and H. S. Kang, Surf. Sci. **604**, 258 (2010).
[32]J.-G. Lee, J. Ahner, and J. T. Yates, J. Chem. Phys. **114**, 1414 (2001).
[33]V. H. Grassian and E. L. Muetterties, J. Phys. Chem. **8**, 5900 (1986).
[34]Q.-X. Li, X.-K. Xue, Q.-J. Xu, and W.-B. Cai, Appl. Spectrosc. **61**, 1328 (2007).
[35]C. A. Hunter and J. K. M. Sanders, J. Am. Chem. Soc. **112**, 5525 (1990).
[36]S. Tsuzuki, K. Honda, T. Uchimaru, M. Mikami, and K. Tanabe, J. Am. Chem. Soc. **124**, 104 (2002).
[37]Q. Zhong, C. Gahl, and M. Wolf, Surf. Sci. **496**, 21 (2002).
[38]J. E. Demuth, K. Christmann, and P. N. Sanda, Chem. Phys. Lett. **76**, 201 (1980).
[39]J. Enkovaara, C. Rostgaard, J. J. Mortensen, J. Chen, M. Duak, L. Ferrighi, J. Gavnholt, C. Glinsvad, V. Haikola, H. A. Hansen, H. H. Kristoffersen, M. Kuisma, A. H. Larsen, L. Lehtovaara, M. Ljungberg, O. Lopez-Acevedo, P. G. Moses, J. Ojanen, T. Olsen, V. Petzold, N. A. Romero, J. Stausholm-Møller, M. Strange, G. A. Tritsaris, M. Vanin, M. Walter, B. Hammer, H. Häkkinen, G. K. H. Madsen, R. M. Nieminen, J. K. Nørskov, M. Puska, T. T. Rantala, J. Schiøtz, K. S. Thygesen, and K. W. Jacobsen, J. Phys.: Condens. Matter **22**, 253202 (2010).
[40]S. R. Bahn and K. W. Jacobsen, Comput. Sci. Eng. **4**, 56 (2002).
[41]M. N. Groves, G. Goubert, A. M. H. Rasmussen, Y. Dong, J.-C. Lemay, V. Demers-Carpentier, P. H. McBreen, and B. Hammer, Surf. Sci. **629**, 48 (2014).
[42]J. Klimeš, D. R. Bowler, and A. Michaelides, J. Phys.: Condens. Matter **22**, 022201 (2010).
[43]P. E. Blöchl, Phys. Rev. B **50**, 17953 (1994).
[44]J. J. Mortensen, L. B. Hansen, and K. W. Jacobsen, Phys. Rev. B **71**, 035109 (2005).
[45]D. Porezag and M. R. Pederson, Phys. Rev. B **54**, 7830 (1996).
[46]G. Henkelman, B. P. Uberuaga, and H. Jónsson, J. Chem. Phys. **113**, 9901 (2000).
[47]M. Surman, S. R. Bare, P. Hofmann, and D. A. King, Surf. Sci. **179**, 243 (1987).
[48]G. S. Hammond, J. Am. Chem. Soc. **77**, 334 (1955).
[49]See supplementary material at http://dx.doi.org/10.1063/1.4947225 for a convergence test with respect to the number of layers, all calculated configurations and adsorption energies with the PBE/optB88-vdW functionals, all the tested surface structures for coverage dependency of the adsorption energy, as well as a video of the preferred diffusion pathway.

Paper II

THE JOURNAL OF CHEMICAL PHYSICS **145**, 094107 (2016)

An automated nudged elastic band method

Esben L. Kolsbjerg, Michael N. Groves, and Bjørk Hammer[a)]
Interdisciplinary Nanoscience Center (iNANO), Department of Physics and Astronomy, Aarhus University, Aarhus C, Denmark

(Received 15 June 2016; accepted 9 August 2016; published online 2 September 2016)

A robust, efficient, dynamic, and automated nudged elastic band (AutoNEB) algorithm to effectively locate transition states is presented. The strength of the algorithm is its ability to use fewer resources than the nudged elastic band (NEB) method by focusing first on converging a rough path before improving upon the resolution around the transition state. To demonstrate its efficiency, it has been benchmarked using a simple diffusion problem and a dehydrogenation reaction. In both cases, the total number of force evaluations used by the AutoNEB method is significantly less than the NEB method. Furthermore, it is shown that for a fast and robust relaxation to the transition state, a climbing image elastic band method where the full spring force, rather than only the component parallel to the local tangent to the path, is preferred especially for pathways through energy landscapes with multiple local minima. The resulting corner cutting does not affect the accuracy of the transition state as long as this is located with the climbing image method. Finally, a number of pitfalls often encountered while locating the true transition state of a reaction are discussed in terms of systematically exploring the multidimensional energy landscape of a given process. *Published by AIP Publishing.* [http://dx.doi.org/10.1063/1.4961868]

I. INTRODUCTION

A reoccurring task in the theoretical study of catalytic surfaces and reactions is that of locating transition states (TS) in diffusion[1–6] and chemical reaction mechanisms.[7–25] This is not always a trivial problem and many different approaches have been formulated including different chain-of-state methods like the nudged elastic band (NEB) method,[26] Lanczos type schemes[27] such as the activation-relaxation technique nouveau (ARTn),[28] and the dimer method.[29] One advantage of the dimer and the ARTn methods is that no final state is necessary when searching for the transition state. They work by following the energy landscape uphill to the saddle point. The difference being that the dimer method uses only the first order derivative of the potential energy, while the ARTn method follows the eigenvector to the Hessian corresponding to the largest negative eigenvalue.

When the final state of a chemical process is available, it is much easier and more effective to use the NEB method since there is no guarantee that a method exclusively relying on local information, like the ARTn and dimer methods, will locate a transition state that directly links the initial and final states. The NEB works by converging an initial "guessed" path to the minimum energy path (MEP) in the immediate vicinity of the initial path. The minimization of all the intermediate images brings the path to the MEP where an image is a snapshot of the geometry of the progressed reaction. The images are moved according to a linear restoring spring force based on the distance between neighboring images and the local tangent of the path as well as the forces from the energy landscape perpendicular to the local tangent. The initial guess for the MEP is typically created by an interpolation of the atomic positions that is akin to a straight line connecting the initial and final images. In a very basic NEB, which we will refer to as an *all-image* NEB method, all the images are supplied at the beginning of a NEB calculation and are subsequently relaxed to the local MEP.

Regardless of Moore's law, which predicts continued exponential growth of computational power, it is still very important to efficiently deploy currently available resources. This is achieved by analysing modern procedures to determine suitable improvements. For instance, the *all-image* NEB approach relaxes all intermediate images to the minimum energy path (MEP) closest to the initial guessed pathway. Depending on the initial guess, this could mean that the path must be displaced very far in space as displayed in the top row of Figure 1. If the objective is to locate the TS with the fewest possible resources, an improved strategy would be to start with fewer images to define the reaction path, then add images only around the apparent peak thereby reducing the overall number of relaxation steps and focusing resources on the important regions. This method is illustrated in the bottom row of Figure 1. This is one example of a range of different suggested improvements to a regular NEB.[30–32]

Here we present an add-on for the NEB method which is based on the strategy proposed above and is available in the ASE[33] software package. The outline of the paper is as follows: first Sec. II contains the outline of the AutoNEB algorithm and the details of the computational setup. Next, we present the benchmarking results against an *all-image* NEB followed by a discussion of common pitfalls. Identifying problematic issues is especially relevant when developing an automated

[a)]Electronic mail: hammer@phys.au.dk.

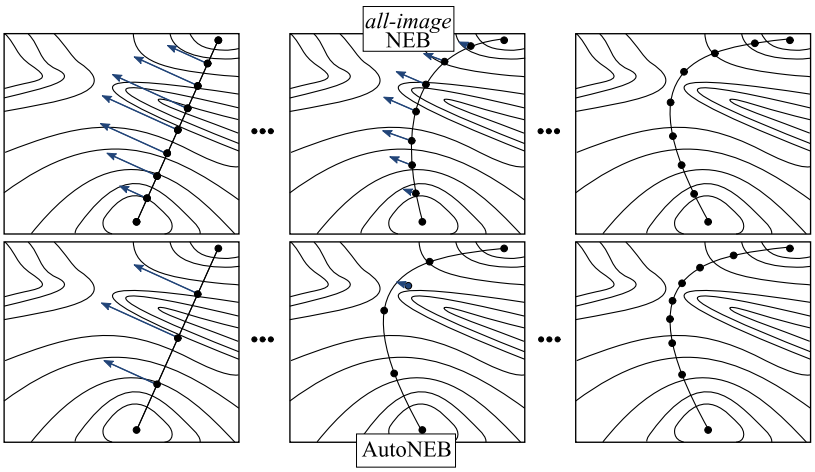

FIG. 1. Top row sketches snapshots of an *all-image* NEB strategy while the bottom row sketches snapshots of the AutoNEB strategy. In the latter, images are not added all at once, but instead dynamically so that new images are focused in the region of interest: the area around the peak.

implementation to locate TSs. We first deal with the possibility of finding the right saddle point in a complex energy landscape with multiple potential saddle points before finishing with an intrinsic instability of a regular NEB formulation that we have identified and discuss an alternative formulation where real springs are introduced.

II. METHOD

A. Algorithm

The AutoNEB algorithm employs the basic NEB method and acts as an add-on. The procedure is outlined in the flowchart in Figure 2. It has been clustered into two subgroups: an initialization phase and the main loop. An optional, final post-processing phase is described in the supplementary material. While running an AutoNEB optimization the algorithm handles N images, where N is a growing number starting from the number of user-supplied images (at least two, the initial and final image). The strategy is to perform the NEB only on a subset size: N_{sim}, of the N images. The N_{sim} images are always picked as sequential images centred on any images newly added by the algorithm. The strategy is to evaluate pieces of the path step by step to converge a rough path before adding more images. The size of individual pieces is specified by the user as a chosen number of images, N_{sim}. Typically, one chooses to focus on the area around the peak adding images here to improve the estimate of the TS.

All that is required are the two end points for which a NEB path is requested; however, a flexible number of intermediate images can also be supplied as a user inputted guess of the MEP when the AutoNEB is initialized. The AutoNEB algorithm executes the following procedure:

- The first step is to supplement any user-supplied images. If the number of user-supplied images is less than N_{sim}, new images are added in the biggest geometrical gap as an image on the *image dependent pair potential* (IDPP) surface[34] or if requested as a linear interpolation of the atoms of the surrounding images.
- The main loop of the algorithm then proceeds with a normal NEB calculation focussing on the N_{sim} images centred on any newly added images until either of the convergence criteria specified below are reached.
- Then a new image is added either to increase the resolution in areas of rapid change in the potential energy surface or to improve the geometric resolution. The algorithm will put images in the biggest geometric gap if the inequality, defined in Eq. (4), is true. Otherwise, a new image will be added in a gap to strengthen the energy resolution,

$$\frac{f(\{\mathbf{R}_i\})}{g(\{E_i\})} > r_{se}, \tag{1}$$

$$f(\{\mathbf{R}_i\}) = \frac{\max(|\mathbf{R}_{i+1} - \mathbf{R}_i|)}{|\mathbf{R}_N - \mathbf{R}_1|}, \tag{2}$$

$$g(\{E_i\}) = \frac{\max(\overline{\Delta E}_i)}{E_{norm}}. \tag{3}$$

With the energy difference, ΔE_i, the scaled energy difference, $\overline{\Delta E}_i$, and the average energy, $E_{avg,i}$, between two images at image i, and the norm of the energy, E_{norm}, are defined as

$$\overline{\Delta E}_i = \Delta E_i \; h(E_{avg,i}/E_{norm}), \tag{4}$$

$$h(x) = x, \tag{5}$$

$$E_{norm} = E_{max} - E_{min}, \tag{6}$$

$$E_{avg,i} = \frac{E_{i+1} + E_i - 2E_{min}}{2}, \tag{7}$$

$$\Delta E_i = |E_{i+1} - E_i|. \tag{8}$$

The value of r_{se} is a user specified ratio between 0 and 1, which balances geometric and energy resolution

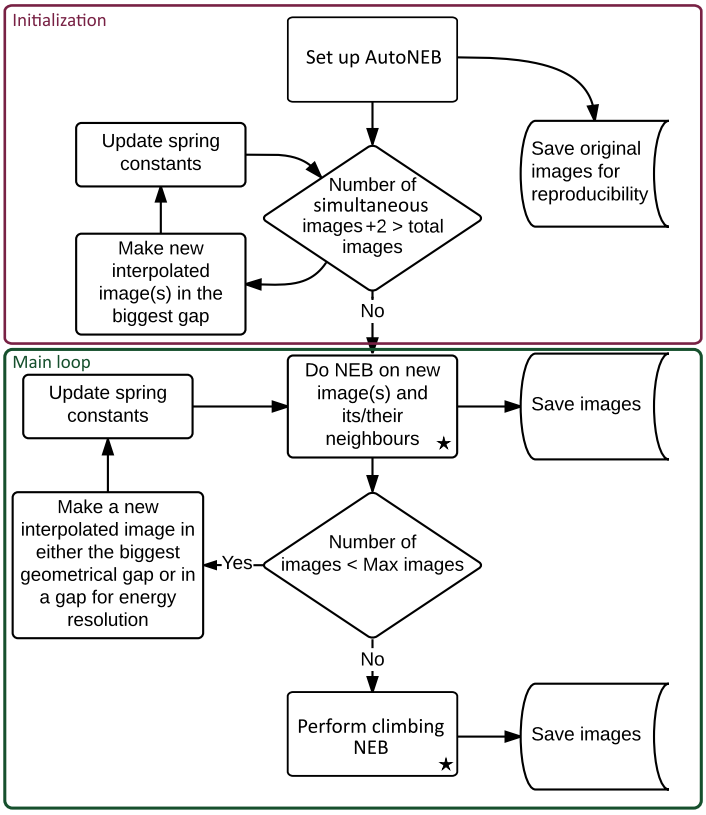

FIG. 2. The algorithm for the AutoNEB. In the two steps marked (★), the NEB is stopped either if the forces have converged or if the maximum number of allowed force evaluations is reached.

considerations when searching for the MEP. $h(x)$ is a linear scaling introduced to favour new images inserted near the peak. When $r_{se} = 1$, a new image is always added in the gap of the biggest distance between two images. When $r_{se} = 0$, a new image is added solely to improve energy resolution between i and $i+1$ where i is determined as the image where ΔE_i is the maximum. Figure 3 illustrates E_{norm}, $E_{avg,i}$, and ΔE_i used in Eq. (4) as well as the positions of image i and $i+1$ on the reaction path as $\mathbf{R}_i$ and $\mathbf{R}_{i+1}$.

By default, all images are added using the IDPP. The two new spring constants to the springs on either side of the new image are set so that they exactly replace the previous spring. This assures that adjacent images initially experience the same spring forces in the next iteration. In practice, the two new springs will have double the spring constant of the replaced spring.

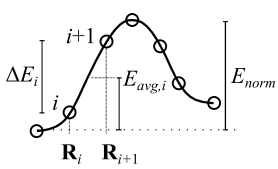

FIG. 3. A sketch of the assigned definitions of E_{norm}, $E_{avg,i}$, and ΔE_i.

- The above two steps are repeated as an iterative process until the maximum number of images, $N_{\max}$, is reached or, if specified, when a given resolution is obtained. Finally a climbing image NEB (CI-NEB)[35] is initialized with the highest energy image as the center of the NEB path.

The optional post-smoothing of the path that is outlined in the supplementary material can then be applied.

To converge an intermediate AutoNEB iteration either of the following two possible criteria should be met. The user specifies a maximum number of force evaluations per image per iteration after which the algorithm proceeds to the next step. If the maximum exerted force on any of the atoms is below a specified threshold before the maximum number of force evaluations is reached the algorithm is also considered converged and proceeds. For the last step where the TS is converged with the CI-NEB method (see below) only the maximum force exerted on any atom is relevant and as many force iterations as needed are used. To compare the effectiveness of the AutoNEB and the *all-image* NEB the total number of force evaluations is calculated by adding all relaxation steps for all images involved in creating the pathway. The

resulting number is referred to as the "total number of force evaluations."

B. Computational setup

ASE[33] was used to setup and optimize density functional theory (DFT) calculations as implemented in the GPAW[36] code as well for the calculations done with the Effective Medium Theory (EMT) potential.[37] In both computational setups, it is not important if parameters such as slab thickness, and for DFT the number of **k**-points or basis set size, are converged, given that we are only interested in how effective the TS path finding methods are. For this reason, the selection of these parameters is based on speed and parallelizability.

DFT Method: For the DFT calculations the Perdew-Burke-Ernzerhof exchange-correlation functional[38] was chosen in combination with a simple linear combination of atomic orbitals with a double zeta polarized (dzp) basis for the wave functions.[39] Geometric optimizations were terminated when no force exerted on the atoms exceeded 0.025 eV/Å. For the AutoNEB, geometric optimizations were also terminated when the maximum number of force evaluations was reached progressing the algorithm to the next step. The calculations were performed in a stepped Pt(211) surface decorated with Ag. The chosen super cell spans two small terraces four atoms wide. This results in a two layer slab where periodic boundary conditions are applied in the direction parallel to the surface with at least 6 Å to the boundary of the cell perpendicular to the slab. The surface is shown in the top half of Figure 4. The bottom layer of the slab was held fixed to mimic the bulk material. To model an oxygen diffusion process on top of the surface an oxygen atom was adsorbed, cf., Figure 4. It is experimentally and theoretically shown that on the stepped Pt(211), surface oxygen prefers to chemisorb at the bridge sites of what would have been the Pt edge.[40,41] The total number of atoms in each cell is 40, 8, and 1 of Pt, Ag, and O, respectively.

EMT Method: For the EMT potential,[37] a very similar surface cell was used and is displayed in the bottom half of Figure 4. The only difference is that one of the decorating Ag atoms has been exchanged with a Pt atom and that the atom diffusing on the surface is a Pt adatom. To calculate the adsorption potential energy (APE) for this Pt adatom as a function of the x and y coordinates, all but this Pt atom were constrained. A contour plot of the APE is displayed in the bottom of Figure 4 obtained by only relaxing the z coordinate of the Pt atom with 0.14 Å between grid points in the x-y-plane. EMT calculations were terminated when no force exerted on the atoms exceeded 0.025 eV/Å or if the maximum number of force evaluations was reached for the AutoNEB.

For the NEB implementation, a series of formulations are used and compared based on the total number of force evaluations used to converge to the TS, and to what degree the MEP follows the most direct pathway to and from a shared transition state. The regular NEB formulation[26] is used throughout the examples. For a number of examples, the regular NEB is further compared to what we consider a more robust method for finding transition states. This method relies on the combination of an elastic band (EB) and the climbing image method and will be referred to as CI-NEB.[42] This EB uses, unlike the regular NEB, the distance between the initial and final images divided by the number of springs to determine the equilibrium distance of each spring. For the purpose of this paper, the EB approach is used exclusively together with a climbing image since the purpose is to locate TSs and a real elastic band without a

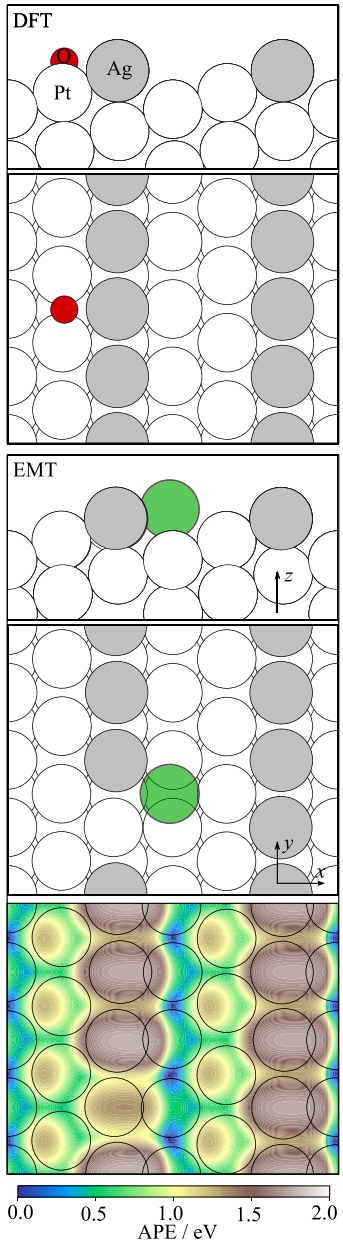

FIG. 4. The upper box displays the setup used for DFT calculations (O/Ag/stepped-Pt) while the bottom shows the setup for EMT calculations (Pt/Ag_3Pt/stepped-Pt) as well as the energy landscape for Pt adatom.

climbing image will cut corners[26] around the TS if the energy landscape is bending. The NEB and EB formulations used in the following examples can be found in Appendices B and C. The original NEB formulation, Appendix A, is also used for the following benchmarking example, but the results are left in the supplementary material Figure S2. CI-EB is one of a number of examples of adjustments that tries to improve upon the regular NEB method.[31,43,44] In the case of locating the TS, the climbing image NEB (CI-NEB) method[35] was utilized no matter the NEB/EB formulation.

III. RESULTS AND DISCUSSION

A. Benchmarking

Benchmarking the AutoNEB against an *all-image* NEB scheme is done for a simple diffusion process following the setup described by the *DFT Method*. Moving an oxygen atom across the Ag row is associated with a barrier and locating the transition state fast and reliably is desirable. In Figure 5, the converged path is shown as well as the total number of force evaluations as a function of the NEB procedure used to complete the task. The two chosen NEB formulations, see Appendices B and C, are used for both the AutoNEB (shown here using a maximum of 35 force evaluations per intermediate AutoNEB iteration) and for an *all-image* NEB. For an extended picture, see the supplementary material Figure S2, where the total number of force evaluations is plotted as a function of the allowed intermediate force evaluations.

The calculations, supported by supplementary material Figure S2, clearly show that no matter the chosen NEB formulation the AutoNEB outperforms an *all-image* NEB when solving the task at hand, i.e., locating the TS for O diffusion over the Ag decorated Pt step. As also reported earlier, the method by which images are kept equally spaced, in this case the definition of the spring force, does not have a considerable impact on computational demand[45] as does switching from a regular NEB to an AutoNEB scheme.

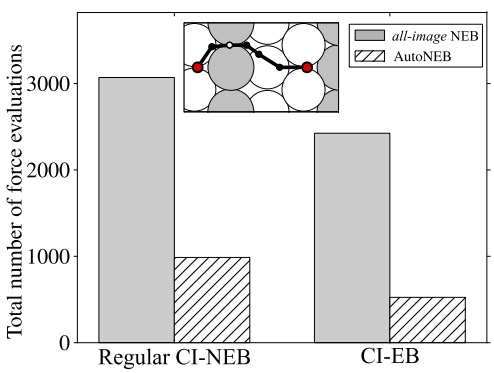

FIG. 5. Total number of force evaluations shown for an *all-image* NEB as the grey bars, while the hashed bars show the AutoNEB's performance using a maximum of 35 intermediate force evaluations.

We further tested the AutoNEB algorithm on a dehydrogenation reaction of pyridine on Pt(111) reported in the literature.[6] Here the AutoNEB algorithm performs very well locating the TS in half as many force evaluations compared to the required force evaluations for the *all-image* NEB both utilizing a climbing image (6507 and 13 220 force evaluations, respectively). This demonstrates that the algorithm works well for a variety of tasks. In the supplementary material the precise calculations preformed can be found as well as an image of the converged pathways.

B. Pitfalls

In this section, we discuss two issues often encountered when performing NEB calculations—regardless of using the *all-image* or AutoNEB scheme. The first issue is that of assuring that not just some local pathway is found, but that the optimum pathway having the globally lowest possible energy at the critical TS is found. The other issue is concerned with the behavior of the regular NEB in a flat energy landscape or energy landscapes with many local minima. We point out and illustrate that the regular NEB method may result in pathways with long detours. As a solution to this we introduce the CI-EB method.

1. Dealing with multiple transition states

NEB is a method used to locate the TS/MEP in the vicinity of an initial path. However, for a given initial and final image, the optimum pathway may not lie along a direct path between these two images. In order to be certain that a calculated TS is along the optimum pathway, alternative pathways must be probed. An example of a linearly interpolated initial path (whether formed by an *all-image* NEB or by an AutoNEB) is displayed in the top left of Figure 6. It does not converge to the desired TS. As the problems become more complicated so do the corresponding multidimensional energy landscapes, which reduces the certainty of locating the correct result. This can, for instance, be seen in the case of pyridine and 2,2,2-trifluoroacetophenone (TFAP) diffusion on Pt(111).[5,6] Taking the most direct path does not result in locating the correct TS and alternative pathways have to be considered. Different strategies can be utilized to explore other possible pathways between distant minima.[46–48] In Figure 6, two methods are examined for Pt diffusion on a fully constrained Pt(211) surface with the edge partially decorated with Ag and Pt atoms as described by the *EMT Method* in Section II B. The underlying energy landscape is shown as a colored contour map, and the NEB paths, revealing the routes discovered by the two algorithms, are shown as red curves. The extensive search is of course redundant for this specific case, where we know the energy landscape, but the simplicity only stems from the very simple test system and mapping all of a multidimensional energy landscape is of course impractical if not impossible for more complex problems.

The first suggested option ("minima hopping") is to locate all imaginable metastable configurations and interlinking the

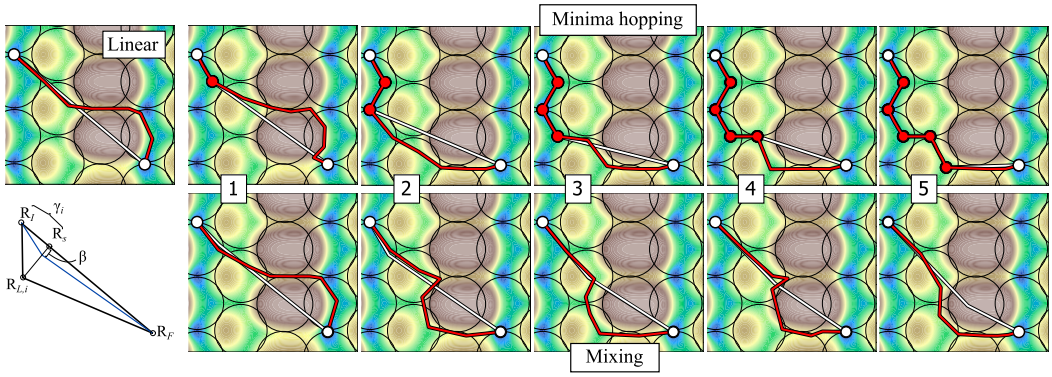

FIG. 6. The upper row shows the minima hopping strategy where neighboring minima (intermediate white and red circles) are connected in steps to complete the total path. The bottom row displays paths from mixing in minima in the neighborhood (same minima as for the minima hopping) and its progress towards the final reaction pathway.

neighboring minima and then proceed to calculate the barrier for each transition. The problem of finding the globally optimum path is then reduced to finding the route which takes you from the initial to the final image via local minima with the lowest critical TS as done in the upper panel of Figure 6.

Another option ("mixing") is to mix neighboring minima in the initial linearly interpolated path thereby diverting the path from a direct route. The principle is shown in the lower panel of Figure 6 with the present example resulting in an initial path following the white line. For this option we propose an algorithm that locates a "support" point of the mixing by projecting a neighboring minimum, $\mathbf{R}_{L,i}$, on to the linear path between the initial and final state. The size of the projection,

$$\gamma_i = \frac{(\mathbf{R}_{L,i} - \mathbf{R}_I) \cdot (\mathbf{R}_F - \mathbf{R}_I)}{|\mathbf{R}_F - \mathbf{R}_I|^2},$$

then decides the "support" image,

$$\mathbf{R}_s = \mathbf{R}_I + \gamma_i(\mathbf{R}_F - \mathbf{R}_I),$$

position. The interpolation between the initial, $\mathbf{R}_I$, and final, $\mathbf{R}_F$, images with a mixing of a neighboring image, $\mathbf{R}_{L,i}$, then becomes

$$\mathbf{R}_i(\alpha) = \mathbf{R}_I + \alpha(\mathbf{R}_F - \mathbf{R}_I) + f(\alpha, \gamma_i)\beta(\mathbf{R}_{L,i} - \mathbf{R}_s), \tag{9}$$

with the switching function, $f(\alpha, \gamma_i)$, that depends on γ_i as

$$f(\alpha, \gamma_i) = \begin{cases} \dfrac{\alpha}{\gamma_i} & \text{for} \quad \min(0, \gamma_i) \le \alpha \le \max(0, \gamma_i) \\ \dfrac{1-\alpha}{1-\gamma_i} & \text{for} \quad \min(1, \gamma_i) \le \alpha \le \max(1, \gamma_i) \end{cases}.$$

In this work, the mixing parameter β was chosen to be 0.25. As a side note, in the limit of $\beta = 1$ the mixing scheme approaches the minima hopping.

In Figure 6, both methods solve the problem and locate the globally optimum TS while only in this particular case, the minima hopping transmit the Pt through the lowest possible energy region resulting in a pathway that gives more insight into a more realistic diffusion mechanism. The individual NEB paths have been evaluated with the AutoNEB in combination with the regular NEB formulation found in Appendix B.

The minima hopping method was exploited for pyridine diffusion with great success.[6] The mixing of neighboring minima was found beneficial in the search for the lowest barrier for TFAP diffusion[5] in a slightly different implementation where γ was always set to 0.5.

2. Intrinsic instability of regular NEB

In the course of our work with the regular NEB method, we have often encountered that pathways deviate from the MEPs and that the overall path lengths may grow out of proportion. The problem is illustrated in Figures 7 and 8, where it is seen to persist even as the number of images is varied (Figure 7) or as spring constants are increased (Figure 8). The root cause for the instability can be traced to the formulation of the force-contribution from springs in the regular NEB formulation (see Appendix B for full details),

$$\mathbf{F}_i^s|_{\|} = (|\mathbf{R}_{i+1} - \mathbf{R}_i|k_i - |\mathbf{R}_i - \mathbf{R}_{i-1}|k_{i-1})\,\hat{\boldsymbol{\tau}}_i. \tag{10}$$

The magnitude of $\mathbf{F}_i^s|_{\|}$ is seen to vanish whenever two adjacent springs are equally long, which is a necessary condition to distribute images evenly along the path. However, the expression is formulated so that $\mathbf{F}_i^s|_{\|}$ vanishes irrespective of *how long* the springs are as long as they are of equal length. This allows the path to evolve into having very long segments that take the system on detours away from the direct MEP, visiting remote local minima. This can result in over-analyzing certain movements of the atoms allocating these as important steps in reaction mechanisms while just being an artifact of the relaxation process.

In the formulation of the regular NEB method,[26] the part of the spring force that is perpendicular to the local tangent is omitted. This is one of the cornerstones of the NEB since it assures that the spring forces do not drag the path up in the energy landscape where there is a bend in the curvature and hence eliminates the so-called *corner cutting* problem.[26] Using real springs instead is of course an issue if it results

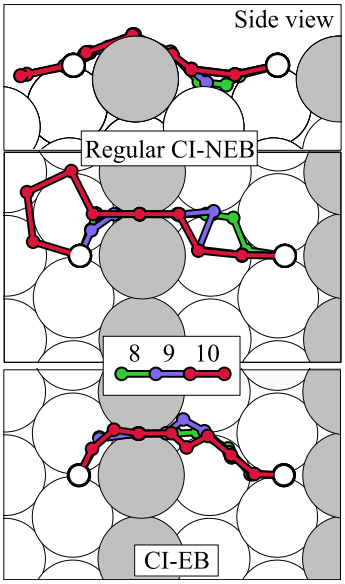

FIG. 7. Calculations with a spring force, $k = 1$, for the regular NEB formulation in the top two plots with the upper showing the side view and the middle image the top view for different number of images. At the bottom CI-EB is plotted for the same number of images as the regular NEB.

in corner cutting in the area of the energy landscape that is in the vicinity of the TS. This will result in an estimate of the barrier to be higher than what is actually true. However, the problem disappears if the TS is located with a CI-NEB, where the climbing image does not feel the spring forces. All that is required is a good guess for the two neighboring images to the CI-image that will then converge to the true TS. However, the penalty is that the images along the path will not necessarily converge to the true MEP except for the climbing image when the full spring force is used (see also supplementary material Figure S3 where this is apparent). Another approach would be to return to the original NEB implementation, see Appendix A, dealing with the possible kinks in the pathway by adding a switching function that penalizes kinks directly.[48,49]

The difference between an elastic band as described in Appendix C and the regular NEB method in Appendix B where both are used with a climbing image NEB scheme is plotted in Figure 7. The problem is highlighted in the top half of Figure 7, which uses the regular NEB formulation to resolve the oxygen diffusion on the Pt(211) surface with the *DFT Method*.

Increasing the number of images and hence in theory improving the resolution of the MEP does not cure the problem; it only makes the issue worse. By using the CI-EB as in the bottom of Figure 7, the path converges towards a much more direct and reasonable path between the initial and final state without taking huge detours visiting other irrelevant minima, and moving the path away from the desired direction. Two videos showing how the two ten image NEBs converge are available in the supplementary material.

The problem becomes even more evident if the initial guessed pathway lies very close to many local minima. In Figure 8 a case where an initial pathway (illustrated as a white line—most easily seen in the right hand plot) is constructed such that it includes many local minima. The initial path mimics what could have been a NEB in a complex energy landscape where many small less important local minima are located.

In Figure 8 the respective final paths (colored) are plotted depending on the NEB formulation and the choice of spring constant (calculated using the *EMT method*). The figure shows

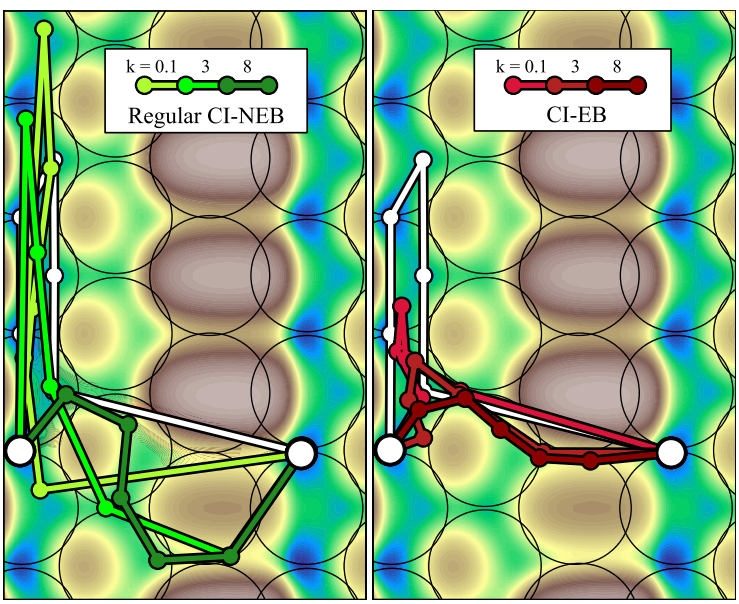

FIG. 8. For Pt diffusion on Ag decorated Pt(211) is the initial deliberately poorly "guessed" path plotted as white. To the left are shown three green relaxed paths for which a formulation of the spring force is given by the regular NEB while to the right three red curves using the CI-EB are depicted. The respective spring constants used to relax the paths are 0.1, 3, and 8 eV/Å^2.

that the individual images do not converge well to the MEP before both the spring force is high and CI-EB's real springs are introduced. The CI-EB method thus proves efficient in curing instability contained in the regular NEB as discussed in connection with Eq. (10). In Figure 8, the initial path was deliberately constructed so as to visit several local minima. Such a path seems unlikely to be chosen as an initial guess with the present problem, however working in a high-dimensional space one might inadvertently set up such an initial path based on knowledge of a number of local minima, and it is hence desirable that the method is robust enough to handle such a situation.

IV. CONCLUSIONS

The AutoNEB algorithm used to locate the barrier for oxygen diffusion on the Pt(211) surface decorated with Ag and for dehydrogenation of pyridine on a Pt(111) surface is shown to drastically reduce the number of steps needed to locate to the TS. It accomplishes this by first determining a rough outline of the MEP before increasing the resolution of the MEP at regions of highest interest to the user. In general, the lower number of force evaluations needed for the AutoNEB to locate the TS is especially pronounced for initial guessed paths that lie far away from the MEP. By introducing the autonomous AutoNEB, it becomes even more important to be aware of the different possible pitfalls when performing NEB calculations in order to recognise when results are anomalous. This includes exploring non-intuitive, alternative pathways with unique TSs. Here we have presented two successful methods to generate new images to include into the pathway: one that jumps between different minima and one of mixing in neighboring minima. If locating the TS is the objective, it is shown that resorting to an elastic band formulation, which includes a linear restoring force proportional to the distance between neighboring images, in combination with a climbing image appears to be a more robust and faster approach that yields a more direct pathway.

SUPPLEMENTARY MATERIAL

See the supplementary material for a smoothing extension to the AutoNEB algorithm and extensions to the benchmarking of the AutoNEB including two videos.

ACKNOWLEDGMENTS

We thank Hannes Jónsson for many fruitful discussions on the topic. Grants from the Danish Research Councils (Grant No. 0602-02566B) and The Lundbeck Foundation have supported this research.

APPENDIX A: ORIGINAL NEB

The original NEB formulation describes the local tangent as a bisection of the two neighboring normalized line segments,

$$\boldsymbol{\tau}_i = \frac{\mathbf{R}_i - \mathbf{R}_{i-1}}{|\mathbf{R}_i - \mathbf{R}_{i-1}|} + \frac{\mathbf{R}_{i+1} - \mathbf{R}_i}{|\mathbf{R}_{i+1} - \mathbf{R}_i|} \tag{A1}$$

and from that the spring force parallel to the band together with the perpendicular true force is described as

$$\mathbf{F}_i^s|_{\|} = [(\mathbf{R}_{i+1} - \mathbf{R}_i)k_i - (\mathbf{R}_i - \mathbf{R}_{i-1})k_{i-1}] \cdot \hat{\boldsymbol{\tau}}_i \hat{\boldsymbol{\tau}}_i, \tag{A2}$$

$$\mathbf{F}_i = \mathbf{F}_i^s|_{\|} - \nabla V(\mathbf{R}_i)|_{\perp}, \tag{A3}$$

$$\nabla V(\mathbf{R}_i)|_{\perp} = \nabla V(\mathbf{R}_i) - \nabla V(\mathbf{R}_i) \cdot \hat{\boldsymbol{\tau}}_i \hat{\boldsymbol{\tau}}_i, \tag{A4}$$

where $\hat{\boldsymbol{\tau}}_i = \boldsymbol{\tau}_i / |\boldsymbol{\tau}_i|$.

Initially, to deal with kinks appearing on the NEB path, a switching function not described here was introduced.[26]

APPENDIX B: REGULAR NEB

With the departure of the original NEB formulation the switching function was a new, simpler NEB formulation.[26] Here the definition of the tangent follows the relative energies of the images as

$$\boldsymbol{\tau}_i = \begin{cases} \boldsymbol{\tau}_i^+ & \text{if } V_{i+1} > V_i > V_{i-1} \\ \boldsymbol{\tau}_i^- & \text{if } V_{i+1} < V_i < V_{i-1} \\ \boldsymbol{\tau}_i^+ \Delta V_i^{max} + \boldsymbol{\tau}_i^- \Delta V_i^{min} & \text{if } V_{i+1} > V_{i-1} \\ \boldsymbol{\tau}_i^+ \Delta V_i^{min} + \boldsymbol{\tau}_i^- \Delta V_i^{max} & \text{if } V_{i+1} < V_{i-1} \end{cases}. \tag{B1}$$

The latter two only apply if i is at a minimum or a maximum. $\boldsymbol{\tau}_i^+ = \mathbf{R}_{i+1} - \mathbf{R}_i$ and $\boldsymbol{\tau}_i^- = \mathbf{R}_i - \mathbf{R}_{i-1}$ and

$$\Delta V_i^{max} = \max(|V_{i+1} - V_i|, |V_{i-1} - V_i|), \tag{B2}$$

$$\Delta V_i^{min} = \min(|V_{i+1} - V_i|, |V_{i-1} - V_i|). \tag{B3}$$

The spring force then becomes

$$\mathbf{F}_i^s|_{\|} = (|\mathbf{R}_{i+1} - \mathbf{R}_i| k_i - |\mathbf{R}_i - \mathbf{R}_{i-1}| k_{i-1})\, \hat{\boldsymbol{\tau}}_i, \tag{B4}$$

while the total force is calculated from the same expression as the original NEB,

$$\mathbf{F}_i = \mathbf{F}_i^s|_{\|} - \nabla V(\mathbf{R}_i)|_{\perp} \tag{B5}$$

$$\nabla V(\mathbf{R}_i)|_{\perp} = \nabla V(\mathbf{R}_i) - \nabla V(\mathbf{R}_i) \cdot \hat{\boldsymbol{\tau}}_i \hat{\boldsymbol{\tau}}_i, \tag{B6}$$

with $\hat{\boldsymbol{\tau}}_i = \boldsymbol{\tau}_i / |\boldsymbol{\tau}_i|$.

APPENDIX C: ELASTIC BAND (EB)

While the kinks discussed in Appendix A might have diminished with the reformulation of the tangent and the spring force in the regular NEB (Appendix B) other problems can now occur due to the reduced complexity of the spring force. Another solution for well-behaved paths is the simple idea that builds on the use of real springs as in a plain elastic band method but borrows the nudging of the true force from the NEB method.[26] Here we describe the spring force as

$$\mathbf{F}_i^s|_{\|} = (|\boldsymbol{\tau}_i^+| - L_{eq}) k_i \frac{\boldsymbol{\tau}_i^+}{|\boldsymbol{\tau}_i^+|} - (|\boldsymbol{\tau}_i^-| - L_{eq}) k_{i-1} \frac{\boldsymbol{\tau}_i^-}{|\boldsymbol{\tau}_i^-|}, \tag{C1}$$

where N is the number of images,

$$L_{eq} = \frac{|\mathbf{R}_N - \mathbf{R}_1|}{N-1}, \tag{C2}$$

$$\boldsymbol{\tau}_i^- = \mathbf{R}_i - \mathbf{R}_{i-1}, \text{ and} \tag{C3}$$

$$\boldsymbol{\tau}_i^+ = \mathbf{R}_{i+1} - \mathbf{R}_i. \tag{C4}$$

If i is a neighbor to i_{max}, it is non-static, and it is the climb NEB method whose formulation changes slightly,

$$\Delta V_i^{max} = \max(|V_{i+1} - V_i|, |V_{i-1} - V_i|), \tag{C5}$$

$$\Delta V_i^{min} = \min(|V_{i+1} - V_i|, |V_{i-1} - V_i|), \tag{C6}$$

$$\mathbf{F}_i^s|_{\parallel} = \left[(|\boldsymbol{\tau}_i^+| - L_{eq})k_i \frac{\boldsymbol{\tau}_i^+}{|\boldsymbol{\tau}_i^+|} - (|\boldsymbol{\tau}_i^-| - L_{eq})k_{i-1} \frac{\boldsymbol{\tau}_i^-}{|\boldsymbol{\tau}_i^-|}\right] \frac{\Delta V_i^{min}}{\Delta V_i^{max}}. \tag{C7}$$

Concerning the true force on the images it follows the idea from the original NEB method,

$$\boldsymbol{\tau}_i = \frac{\mathbf{R}_i - \mathbf{R}_{i-1}}{|\mathbf{R}_i - \mathbf{R}_{i-1}|} + \frac{\mathbf{R}_{i+1} - \mathbf{R}_i}{|\mathbf{R}_{i+1} - \mathbf{R}_i|}, \tag{C8}$$

$$\nabla V(\mathbf{R}_i)|_{\perp} = \nabla V(\mathbf{R}_i) - \nabla V(\mathbf{R}_i) \cdot \hat{\boldsymbol{\tau}}_i \hat{\boldsymbol{\tau}}_i, \tag{C9}$$

where $\hat{\boldsymbol{\tau}}_i = \boldsymbol{\tau}_i / |\boldsymbol{\tau}_i|$ and the total force is still given as

$$\mathbf{F}_i = \mathbf{F}_i^s|_{\parallel} - \nabla V(\mathbf{R}_i)|_{\perp}. \tag{C10}$$

[1]J. Greeley and M. Mavrikakis, Surf. Sci. **540**, 215 (2003).
[2]O. R. Inderwildi, D. Lebiedz, O. Deutschmann, and J. Warnatz, J. Chem. Phys. **122**, 34710 (2005).
[3]N. Capron, P. Broqvist, and A. Pasquarello, Appl. Phys. Lett. **91**, 192905 (2007).
[4]H. Cheng and A. Selloni, J. Chem. Phys. **131**, 54703 (2009).
[5]G. Goubert, A. M. H. Rasmussen, Y. Dong, M. N. Groves, P. H. McBreen, and B. Hammer, Surf. Sci. **629**, 123 (2014).
[6]E. L. Kolsbjerg, M. N. Groves, and B. Hammer, J. Chem. Phys. **144**, 164112 (2016).
[7]D. Loffreda, D. Simon, and P. Sautet, J. Chem. Phys. **108**, 6447 (1998).
[8]M. R. Sørensen, Y. Mishin, and A. F. Voter, Phys. Rev. B **62**, 3658 (2000).
[9]I. M. Ciobîcă, F. Frechard, R. A. Van Santen, A. W. Kleyn, and J. Hafner, J. Phys. Chem. B **104**, 3364 (2000).
[10]K. Honkala and K. Laasonen, Phys. Rev. Lett. **84**, 705 (2000).
[11]M.-L. Bocquet, A. Michaelides, D. Loffreda, P. Sautet, A. Alavi, and D. A. King, J. Am. Chem. Soc. **125**, 5620 (2003).
[12]D. E. Jiang and E. A. Carter, Surf. Sci. **570**, 167 (2004).
[13]J. Greeley and M. Mavrikakis, Nat. Mater. **3**, 810 (2004).
[14]S. Sakong and A. Groß, J. Catal. **231**, 420 (2005).
[15]D. Loffreda, F. Delbecq, F. Vigné, and P. Sautet, J. Am. Chem. Soc. **128**, 1316 (2006).
[16]C. Dupont, Y. Jugnet, and D. Loffreda, J. Am. Chem. Soc. **128**, 9129 (2006).
[17]H. Fu, Z.-P. Liu, Z.-H. Li, W.-N. Wang, and K.-N. Fan, J. Am. Chem. Soc. **128**, 11114 (2006).
[18]D. Torres, N. Lopez, F. Illas, and R. M. Lambert, Angew. Chem., Int. Ed. **46**, 2055 (2007).
[19]D. Borthwick, V. Fiorin, S. J. Jenkins, and D. A. King, Surf. Sci. **602**, 2325 (2008).
[20]O. R. Inderwildi and S. J. Jenkins, Chem. Soc. Rev. **37**, 2274 (2008).
[21]O. R. Inderwildi, S. J. Jenkins, and D. A. King, J. Phys. Chem. C **112**, 1305 (2008).
[22]Y. Pan, C. Liu, and Q. Ge, J. Catal. **272**, 227 (2010).
[23]R. B. Getman and W. F. Schneider, ChemCatChem **2**, 1450 (2010).
[24]F. Auneau, L. S. Arani, M. Besson, L. Djakovitch, C. Michel, F. Delbecq, P. Sautet, and C. Pinel, Top. Catal. **55**, 474 (2012).
[25]B. T. Loveless, C. Buda, M. Neurock, and E. Iglesia, J. Am. Chem. Soc. **135**, 6107 (2013).
[26]G. Henkelman and H. Jónsson, J. Chem. Phys. **113**, 9978 (2000).
[27]L. J. Munro and D. J. Wales, Phys. Rev. B **59**, 3969 (1999).
[28]R. Malek and N. Mousseau, Phys. Rev. E **62**, 7723 (2000).
[29]G. Henkelman and H. Jónsson, J. Chem. Phys. **111**, 7010 (1999).
[30]J.-W. Chu, B. L. Trout, and B. R. Brooks, J. Chem. Phys. **119**, 12708 (2003).
[31]S. A. Trygubenko and D. J. Wales, J. Chem. Phys. **120**, 2082 (2004).
[32]L. Xie, H. Liu, and W. Yang, J. Chem. Phys. **120**, 8039 (2004).
[33]S. R. Bahn and K. W. Jacobsen, Comput. Sci. Eng. **4**, 56 (2002).
[34]S. Smidstrup, A. Pedersen, K. Stokbro, and H. Jónsson, J. Chem. Phys. **140**, 214106 (2014).
[35]G. Henkelman, B. P. Uberuaga, and H. Jónsson, J. Chem. Phys. **113**, 9901 (2000).
[36]J. Enkovaara, C. Rostgaard, J. J. Mortensen, J. Chen, M. Duak, L. Ferrighi, J. Gavnholt, C. Glinsvad, V. Haikola, H. A. Hansen, H. H. Kristoffersen, M. Kuisma, A. H. Larsen, L. Lehtovaara, M. Ljungberg, O. Lopez-Acevedo, P. G. Moses, J. Ojanen, T. Olsen, V. Petzold, N. A. Romero, J. Stausholm-Møller, M. Strange, G. A. Tritsaris, M. Vanin, M. Walter, B. Hammer, H. Häkkinen, G. K. H. Madsen, R. M. Nieminen, J. K. Nørskov, M. Puska, T. T. Rantala, J. Schiøtz, K. S. Thygesen, and K. W. Jacobsen, J. Phys.: Condens. Matter **22**, 253202 (2010).
[37]K. W. Jacobsen, P. Stoltze, and J. K. Nørskov, Surf. Sci. **366**, 394 (1996).
[38]J. P. Perdew, K. Burke, and M. Ernzerhof, Phys. Rev. Lett. **77**, 3865 (1996).
[39]A. H. Larsen, M. Vanin, J. J. Mortensen, K. S. Thygesen, and K. W. Jacobsen, Phys. Rev. B **80**, 195112 (2009).
[40]P. Gambardella, Ž. Šljivančanin, B. Hammer, M. Blanc, K. Kuhnke, and K. Kern, Phys. Rev. Lett. **87**, 056103 (2001).
[41]Ž. Šljivančanin and B. Hammer, Surf. Sci. **515**, 235 (2002).
[42]H. Jónsson, private communication (2016).
[43]P. Maragakis, S. A. Andreev, Y. Brumer, D. R. Reichman, and E. Kaxiras, J. Chem. Phys. **117**, 4651 (2002).
[44]M. Melander, K. Laasonen, and H. Jónsson, J. Chem. Theory Comput. **11**, 1055 (2015).
[45]D. Sheppard, R. Terrell, and G. Henkelman, J. Chem. Phys. **128**, 134106 (2008).
[46]D. J. Wales, Mol. Phys. **100**, 3285 (2002).
[47]J. M. Carr, S. A. Trygubenko, and D. J. Wales, J. Chem. Phys. **122**, 234903 (2005).
[48]E. Maras, O. Trushin, A. Stukowski, T. Ala-Nissila, and H. Jónsson, Comput. Phys. Commun. **205**, 13 (2016).
[49]H. Jónsson, G. Mills, and K. W. Jacobsen, "Nudged elastic band method for finding minimum energy paths of transitions," in Classical and Quantum Dynamics in Condensed Phase Simulations, edited by B. J. Berne, G. Ciccotti and D. F. Coker, **385** (World Scientific, 1998).

Paper III

ACSNANO
www.acsnano.org
ARTICLE

Supramolecular Corrals on Surfaces Resulting from Aromatic Interactions of Nonplanar Triazoles

Siddharth J. Jethwa,[†] Esben L. Kolsbjerg,[†] Sundar R. Vadapoo,[†] Jacob L. Cramer,[‡] Lutz Lammich,[†] Kurt V. Gothelf,[‡] Bjørk Hammer,*[,†] and Trolle R. Linderoth*[,†]

[†]Department of Physics and Astronomy and [‡]Department of Chemistry, Interdisciplinary Nanoscience Center (iNANO), Aarhus University, 8000 Aarhus, Denmark

Supporting Information

ABSTRACT: **Interaction forces between aromatic moieties, often referred to as $\pi-\pi$ interactions, are an important element in stabilizing complex supramolecular structures. For supramolecular self-assembly occurring on surfaces, where aromatic moieties are typically forced to adsorb coplanar with the surface, the possible role of intermolecular aromatic interactions is much less explored. Here, we report on unusual, ring-shaped supramolecular corral surface structures resulting from adsorption of a molecule with nonplanar structure, allowing for intermolecular aromatic interactions. The discrete corral structures are observed using high-resolution scanning tunneling microscopy, and the energetic driving forces for their formation are elucidated using density functional theory calculations and Monte Carlo simulations. The individual corrals involve between 11 and 18 molecules bound through triazole moieties to a ring-shaped ensemble of bridge site positions on (111) surfaces of copper, silver, or gold. The curvature required to form the corrals is identified to result from the angle dependence of aromatic interactions between molecular phenanthrene moieties. The study provides detailed quantitative insights into triazole−surface and aromatic interactions and illustrates how they may be used to drive surface supramolecular self-assembly.**

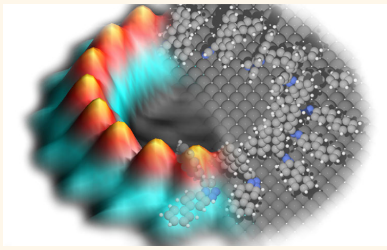

KEYWORDS: *scanning tunneling microscopy, molecular corrals, self-assembly, aromatic interactions, triazole, Monte Carlo simulations, density functional theory*

The 1,2,3-triazole ring is the product of the Huisgen azide−alkyne 1,3-dipolar cycloaddition, of which the copper-catalyzed and the strained cyclic alkyne version have been widely used in organic chemistry, bioconjugation, and for surface functionalization.[1] The functional group consists of a five-membered ring containing two double bonds, with three nitrogen atoms located adjacent to one another. It has been shown to chemisorb to well-defined binding sites[2] on metal surfaces, making direct triazole−metal coupling an interesting type of interaction akin to that of other functional groups such as thiols.[3] However, apart from the corrosion inhibitor benzotriazole,[4] which has been shown to adopt a range of upright and flat-lying hydrogen-bonded supramolecular structures,[5,6] the adsorption of triazole-containing molecules has been explored very little in the context of surface supramolecular self-assembly.

In this study, we report on unusual ring-shaped supramolecular surface structures formed from molecules in which a triazole group links two distinct aromatic substituents. The structures are observed on metal surfaces under ultrahigh vacuum (UHV) conditions using high-resolution scanning tunneling microscopy (STM). To understand the energetic driving forces behind the formation of the ring structures, we have performed van der Waals (vdW) density functional theory (DFT) calculations to determine the energetics of the triazole−metal coupling and the angle-dependent intermolecular aromatic interactions, enabling the entire structures to be energetically optimized in Monte Carlo (MC) simulations. The corrals are shown to result from the nonplanar molecular structure, which allows the two distinct aromatic groups to play very different roles: interacting with the substrate and to other molecules in the ring structure. The curvature of the molecular assembly results from optimizing the intermolecular aromatic interactions.

Aromatic interactions are noncovalent interactions between aromatic moieties, comprised primarily of van der Waals,

Received: May 18, 2017
Accepted: July 18, 2017
Published: August 1, 2017

ACS Publications © 2017 American Chemical Society

DOI: 10.1021/acsnano.7b03484
ACS Nano 2017, 11, 8302−8310

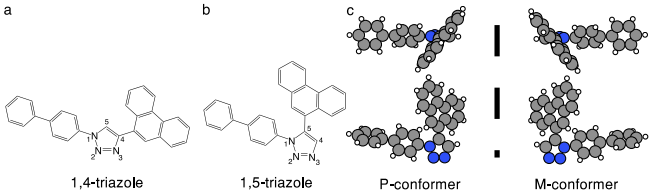

Figure 1. (a) Chemical structure of 1,4-triazole. (b) Chemical structure of 1,5-triazole. (c) Two distinct conformers of 1,5-triazole, labeled as *P* and *M*, result from the sterical hindrance between the phenanthrene and biphenyl groups.

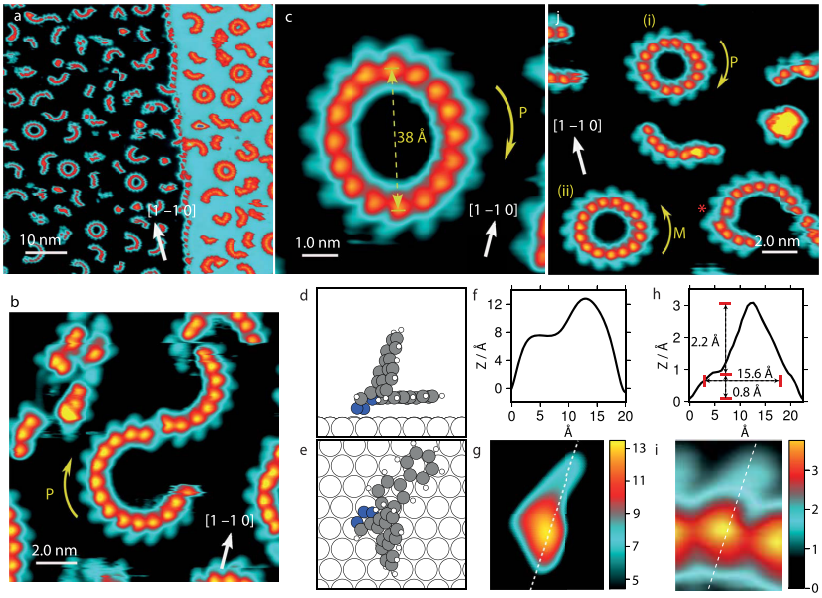

Figure 2. STM images of corrals and chain structures formed by 1,5-triazole on Cu(111), including DFT configuration of 1,5-triazole and simulated/experimental STM images. (a) Overview image of terraces showing a mixture of chain structures and supramolecular corrals (660 × 660 Å^2). (b) Curved chain (120 × 120 Å^2). (c) 16-monomer corral formed by *P*-conformer (80 × 80 Å^2). (d,e) Energetically favored adsorption configuration of the *P*-conformer (side and top view, respectively). (f,g) Tersoff−Hamann simulated STM image and line scan. (h,i) Experimental line scan and corresponding image including the color scale bar used for the images. (j) Corrals composed of different numbers (i) 14 and (ii) 15 of monomers of opposite chirality (160 × 160 Å^2), where * denotes clash between opposite conformers.

electrostatic, and inductive components. Whereas such interactions are believed to be involved in stabilizing many complex supramolecular structures such as dipeptide nanotubes,[7] helical dendrimers,[8] and molecular tweezers,[9] the detailed nature of aromatic interactions has been contentious,[10−12] and aromatic interactions have only been studied to a limited extent in surface supramolecular assembly[13−15] where aromatic moieties typically adsorb coplanar with the surface. Furthermore, observations of discrete supramolecular molecular ring structures are very rare.[16,17] An important element in stabilizing the observed discrete ring structures is identified to be the binding of the molecular triazole moieties to an ensemble of non-equivalent bridge binding sites of the (111) metal surfaces. Subtle differences in the triazole−metal interaction allow observed variations in sizes of the ring-shaped structures between surfaces of Cu, Ag, and Au to be explained. Overall, the insights gained through the study provide perspectives for the generation of functional molecular architectures through triazole−metal coupling and aromatic interactions.

The investigated molecule, 1,5-triazole, is shown in Figure 1b and consists of a triazole ring linking biphenyl and phenanthrene aromatic moieties at the 1- and 5-positions, respectively. The molecule is closely related to the 1,4-triazole shown in Figure 1a, which was investigated recently in our groups[18] in the context of demonstrating that the Cu-catalyzed azide−alkyne 1,3-dipolar cycloaddition can be performed in an on-surface synthesis scheme by reaction of azides and alkynes adsorbed at metallic substrates under UHV conditions.[19] Whether synthesized *in situ* on the surface or *ex situ* in solution, the 1,4-triazole molecule was observed to lie in a planar configuration with all three aromatic components adsorbed parallel to the Cu(111) plane to maximize molecule−substrate interactions, and apart from a propensity to form dimer pairs, no extended supramolecular structures were observed. In the 1,5-triazole molecule studied here, the three aromatic components are unable to arrange in a coplanar

DOI: 10.1021/acsnano.7b03484
ACS Nano 2017, 11, 8302−8310

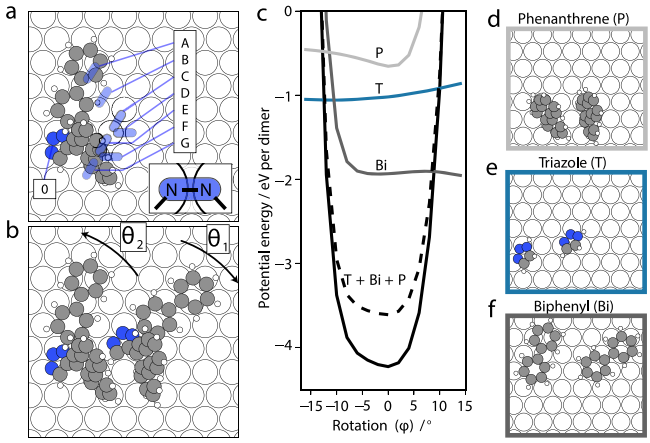

Figure 3. Calculated dimer configurations and analysis of energy contributions. (a) Seven identified dimer configurations. The blue rounded rectangular shapes represent the footprint of the nitrogen atoms binding to the underlying substrate as shown in the inset. (b) Global minimum for a single dimer (configuration 0C). Rotation angles, θ_1 and θ_2, are used for mapping the potential energy surface. (c) DFT potential energy variation (solid black line) for configuration 0C as a function of the angle $\varphi = \theta_1 - \theta_1^{opt} = \theta_2 - \theta_2^{opt}$ and decomposition into contributions from the interactions of the molecular fragments phenanthrene (P), triazole (T), and biphenyl (Bi). (d−f) Individual molecular fragments resulting from splitting configuration 0C.

fashion due to their close proximity on adjacent sites of the triazole ring. The copper-catalyzed reaction exclusively provides the 1,4-substituted triazole, whereas the thermal reaction can provide a mixture of the 1,4- and 1,5-isomers. However, for the current combination of reactants, the arrangement of the substituents in the transition state during the click reaction is so sterically unfavorable that the thermal reaction exclusively provides the 1,4-product. Instead, we applied an alternative reaction to obtain the investigated 1,5-triazole (see Supporting Information).

The *ex situ* synthesized 1,5-triazole is deposited using thermal sublimation at ∼388 K under UHV conditions onto a Cu(111) surface held at 300 K, subsequently cooled to 90−115 K for STM measurements. Figure 2a depicts an overview STM image of 1,5-triazole on Cu(111) at medium coverage. Immediately evident is the presence of curved chains and complete ring structures, henceforth referred to as *supramolecular corrals* on the surface.

Their appearance is independent of surface coverage apart from when approaching monolayer saturation coverage, where only the curved chain structures are observed, in order to maximize packing. The partial chains are presumably less energetically stable due to the absence of nearest neighbors for the terminating molecules, and the coexistence of partial chains with the corrals at intermediate coverages is ascribed to kinetic trapping during the quenching of the sample from the deposition temperature (room temperature) to the STM imaging temperature (90−115 K), preventing the chains from being completed into full corrals. A high-resolution image of a curved chain is shown in Figure 2b, where distinct protrusions (orange) are visible on the inner perimeter, each with an outer halo of "cog-tooth" (light blue) features. The combination of an inner/outer feature is attributed to a single molecule of 1,5-triazole. A complete corral composed of 16 monomers of 1,5-triazole with a pore size of approximately 38 Å is shown in Figure 2c.

To correctly assign the features in the STM images, it is insightful to understand the adsorption configuration of a single molecule of 1,5-triazole on the Cu(111) surface. Using DFT calculations, multiple possible adsorption geometries of the molecule on different surface sites were systematically surveyed, as summarized in Supporting Information Figure S6. The minimum energy adsorption configuration identified (Figure 2d,e) is bound *via* the N_2 and N_3 atoms of the triazole moiety along the bridge site of the (111) lattice. The molecule clearly retains the three-dimensional nonplanar conformation it adopts in the gas phase. Interestingly, it is the smaller biphenyl ring system that lies parallel to the surface, rather than the larger phenanthrene ring that is arranged almost orthogonally at 80° to the surface plane. The overall calculated adsorption energy for 1,5-triazole is −2.04 eV, indicative of strong chemisorption. The individual contributions from each component of 1,5-triazole toward the overall binding energy are shown in Supporting Information Figure S7. The triazole contribution (−0.76 eV) toward the adsorption energy arises from metal insertion into the nitrogen double bond between the N_2 and N_3 nitrogens. This energy contribution is similar to the calculated adsorption energy of benzotriazole (−0.60 eV) on Cu(111).[2] The two phenyl rings of the biphenyl system contribute a combined binding energy of −0.90 eV, stabilizing the nonplanar adsorption geometry.

A calculated STM image for the energetically minimized adsorption structure is shown in Figure 2g, which agrees qualitatively very well with the experimental STM footprint of an individual 1,5-triazole monomer, shown in a zoomed-in image of the corral structure in Figure 2i. We therefore confidently assign the inner (orange) features to the phenanthrene units and the outer cog-tooth features (light blue) to the biphenyl units. The slight difference in the shape of the phenanthrene unit is ascribed to electronic contributions from neighboring molecules, which are not included in the simulated image, whereas the increased shoulder intensity of the biphenyl unit is ascribed to the simulation being overly

DOI: 10.1021/acsnano.7b03484
ACS Nano 2017, 11, 8302−8310

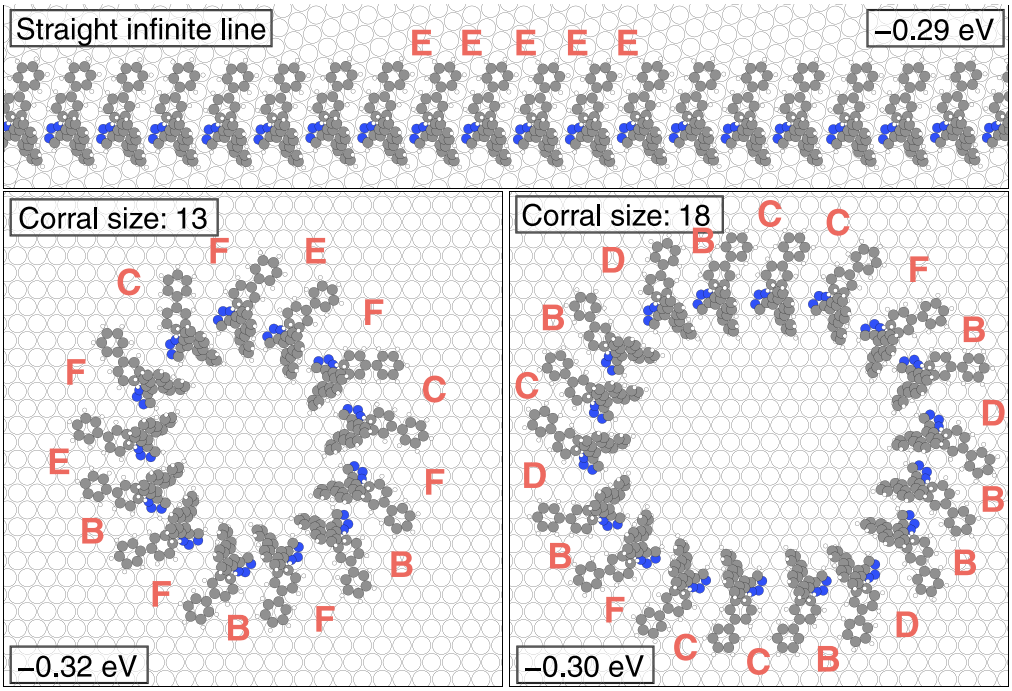

Figure 4. MC simulation results for the minimization of corrals of size 13 (left) and 18 (right) and of 1,5-triazole aligned in a straight line (top). The letters A, B, ... G correspond to the respective dimers (0A, 0B, ... 0G) for the neighboring molecules as defined in Figure 3a. The stabilization energy gain of the structures is given in eV per molecule.

dominated by topographical rather than electronic effects, which is also reflected in the larger apparent heights of the simulated image.

Further confirmation of the assigned adsorption configuration arises from the arrangement of the outer cog-teeth in the corral structures, which are angled to form either clockwise or counterclockwise helical arrangements. A mixture of corrals with clockwise and counterclockwise arrangements are seen to coexist in Figure 2j. The sterical hindrance between the bulky phenanthrene and biphenyl moieties due to their close proximity in the 1- and 5- positions results in restricted rotation about the C_5−C single bond, leading to the existence of two distinct conformers of equal population, labeled as *P* and *M* in Figure 1c, known as *atropisomers* that exhibit axial chirality.[20] The helical arrangements occur because the biphenyl moiety arranges on either side of the phenanthrene moiety when the 1,5-triazole adopts either the *P*- or the *M*-isomeric forms. Each of the molecular corrals or curved chain structures therefore represent homochiral arrangements of triazole molecules.

Interestingly, the corral sizes observed are not homogeneous but vary in diameter between 30 and 39 Å (Supporting Information Figure S4), due to the corrals comprising different numbers of triazole molecules; for example, the two corrals labeled (i) and (ii) in Figure 2c are formed from 14 and 15 units, respectively (see Supporting Information Figure S1 for further corral examples). The observation of different corral sizes suggests flexibility in the formation of the corrals, and it is immediately clear that the corrals do not constitute a commensurate overlayer structure with all molecules in identical adsorption geometries. The question thus arises how the corrals form through intermolecular interactions of the 1,5-triazole molecules and to what extent they are templated by molecule−surface interactions.

To understand the energetic driving forces leading to the formation of the molecular corrals, we focus on the interactions that take place within a pair of 1,5-triazole molecules. The strong binding of the triazole ring along the bridge site allows for a discrete determination of the dimer interaction strength. Guided by the experimentally determined separation of ∼5−7 Å between individual molecules in the corrals, we find only seven possible ways in which two bridge sites support a dimer. Naming one bridge site 0 and the other A−G (cf. Figure 3a), the dimer configurations can be referred to as 0A, 0B, ... 0G. The optimal adsorption configuration for a dimer arrangement determined using DFT calculations is found for configuration 0C shown in Figure 3b. The preferred alignment of the 1,5-triazole molecules occurs for a nonparallel stacking arrangement with an angle of θ_{opt} = 35° between the two molecules. The overall potential energy gain relative to isolated molecules in the gas phase is −4.23 eV per dimer adsorbed on the Cu(111) surface. When referenced to adsorbed molecules located far apart (9 Å) on the surface, the intermolecular interaction in the dimer is −0.27 eV per molecule. Rotating the molecules away from their ideal binding configuration will affect the binding energy of the molecules to the surface as well as their intermolecular interaction. The energetic variation is illustrated in Figure 3c, where the solid black curve shows the

DOI: 10.1021/acsnano.7b03484
ACS Nano 2017, 11, 8302−8310

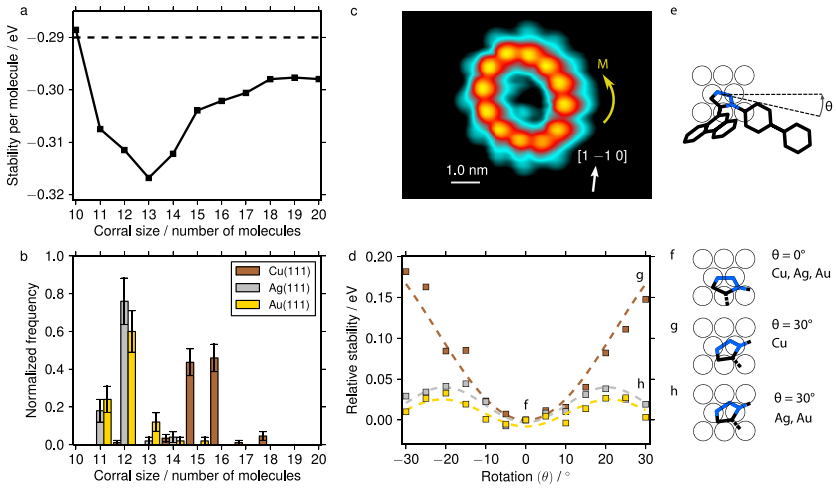

Figure 5. Size distribution for simulated and experimental corrals. (a) Stabilization energy as a function of corral size from MC simulations of corrals on Cu(111). The dashed line represents molecules aligning in straight lines (Figure 4) instead of corrals. (b) Experimental size distribution (normalized) for corrals on Ag(111), Au(111), and Cu(111). Total number of counted corrals are 93 (Cu), 50 (Ag), and 50 (Au). (c) Example of the preferred corral size 12 on Ag(111). (d) Energetic penalty for rotating a single 1,5-triazole away from the optimal alignment with the substrate on Cu, Ag, and Au (same color scheme as in (b)). (e) Definition of the rotation angle of the triazole away from the optimum bridge position. Schematic representations of the triazole adsorption configuration on the optimal bridge site (f) and at θ = 30° on Cu (g) and Ag/Au (h).

potential energy of the dimer when the two 1,5-triazoles are symmetrically rotated away from their optimal alignment through the angles θ_1 and θ_2 as defined in Figure 3b. To determine the contribution from each molecular component to the variation in the overall dimer energy, the phenanthrene, the triazole, and the biphenyl groups (Figure 3d–f) are considered in isolation and fixed on the surface at the positions they would assume if still in the intact molecules (the dangling bonds created when removing the rest of the molecule are saturated by hydrogen atoms). Interestingly, when rotating the phenanthrene units (Figure 3d), the light gray curve shows a distinct minimum at $\varphi \sim 1.4°$, corresponding to an angle of ~30° between the planes of the phenanthrene groups, where it allows for a particularly attractive interaction between the neighboring phenanthrenes. The blue curve in Figure 3c, representing the triazole interaction, is slightly sloped, thereby favoring rotation away from the preferred phenanthrene configuration. This energy contribution brings the overall minimum in binding energy to $\varphi = 0°$. The edge-on interaction between the biphenyl subunits (Figure 3f, dark gray curve) turns out to be of less importance: The dimer stabilization is severely penalized at close distances (negative φ), but within the range of angles relevant for the molecular corrals, the biphenyl units are not in immediate proximity of each other and hence do not interact significantly, as is seen by the dark gray curve plateauing at small negative angles. Adding up the three individual contributions, we arrive at the dashed line in Figure 3c. The offset of this line from the full DFT result (solid line) illustrates the limits of subdividing the interactions. However, the relatively constant magnitude of the offset for intermediate rotation angles gives credit to the approach and allows us to state that the angle dependence of the interaction between the 1,5-triazoles is primarily governed by aromatic interactions between the phenanthrene groups.

To address the formation of the full molecular corrals, including a possible variation in the intermolecular arrangements along the corral perimeter, we analyzed all of the seven possible dimer configurations 0A–0G and created pair potentials by calculating the dimer interactions as a function of the relative orientations (θ_1 and θ_2) for the 1,5-triazoles in each dimer pair. (The most stable arrangement for each dimer pair is shown in Supporting Information Figure S8.) Using the pair potentials, it is computationally inexpensive to build full corrals containing different numbers of 1,5-triazole molecules on the Cu(111) surface, evaluate their stability, and minimize their energy using MC simulations. Details of the MC simulations are given in the Supporting Information as well as in a video of the optimization occurring during a MC run. Two optimized corrals containing 13 and 18 molecules are depicted in Figure 4. (Corrals for 10–20 molecules are shown in Supporting Information Figure S9.) The relative molecular positions are indicated for the dimers formed along the corral perimeter, showing that the optimized corral arrangement is not completely regular but involves an ensemble of different bridge site pairs. Careful perusal of the STM images indeed shows a slight variation in intermolecular spacing along the corral perimeters. In the corrals, the triazole moieties are in many cases rotated significantly away from the ideal binding site along the bridge sites, indicating that any loss of the molecule–substrate coordination is compensated by enhanced molecule–molecule interactions. (In the optimized corral composed of 13 molecules, the rotation of the triazole moiety ranges between 0 and 25°.) The top panel of Figure 4a shows for reference a hypothetical infinite line of molecules composed

DOI: 10.1021/acsnano.7b03484
ACS Nano 2017, 11, 8302–8310

of molecules oriented parallel to each other and formed from the 0E dimer, which is the most stable parallel dimer from Figure 3a. The potential energy per molecule relative to isolated molecules on the surface is indicated for each structure and may be compared to the energy gain of −0.27 eV per molecule for the isolated optimum dimer of Figure 3b. The analysis thus shows a significant stabilization energy gain for molecules arranged in the condensed structures, where all participants have two neighbors, albeit not in the optimum dimer arrangements. The energy gain varies with the nature of the structure and according to the corral size; in the 13-molecule corral, the formation of a curved molecular arrangement thus results in a stabilization energy which is ∼30 meV per molecule more favorable than for the hypothetical infinite line of molecules.

The calculated stabilization energy per molecule is plotted in Figure 5a as a function of corral size. The energetically most favored corrals on the Cu(111) surface contain 13 molecules of 1,5-triazole, and for larger corrals, the stabilization energy converges toward the value for the infinite chain. The experimental size distribution for corrals observed on the Cu(111) surface is shown in Figure 5b. The most abundant corrals observed experimentally consist of 15−16 triazole monomers. The MC simulations thus somewhat underestimate the preferred corral size, although the formation of stable corral structures using MC simulations demonstrates that the modeling based on the pair potentials is sufficiently accurate to explain the formation of the self-assembled structures. However, the pair potentials do not include any extended interactions, and hence, the advantageous angles formed in a dimer, where only two molecules have to optimize their mutual interaction, are not necessarily the same as if a third or fourth molecule is added. It is believed that this effect will decrease the average favorable relative angle, thereby increasing the optimal theoretical corral size to lead to a better fit with the experimental results. Nevertheless, this detail does not alter the insight obtained concerning the driving force behind the corral formation; that following adsorption, the molecule adopts a conformation allowing for a strong binding to the surface but also sets up the possibility for an interaction between the phenanthrene groups of neighboring molecules that drive the nonaligned coordination resulting in the curved corral shape.

To understand the templating effect of the surface upon corral formation, 1,5-triazole was deposited upon the surfaces of Au(111) and Ag(111). Here, corral formation was also observed, as illustrated by the 12-membered *M*-corral on Ag(111) in Figure 5c. Strikingly, however, the corrals on both of these surfaces typically consist of fewer monomers (12) than found on the Cu(111) surface (15−16), as demonstrated by the normalized size distribution in Figure 5b. To rationalize this effect, DFT calculations were performed that model the relative energy of a single molecule of 1,5-triazole as a function of rotation angle away from the ideal bridge site ($\theta = 0°$) for the three different surfaces as shown in Figure 5d. It is evident that 1,5-triazole is far less energetically penalized for large rotations away from the ideal bridge site on Ag/Au than it is on Cu. This is primarily due to a lower interaction energy of the triazole moiety on Ag/Au (E_{ads} = −0.58 eV/−0.52 eV) than on Cu (E_{ads} = −0.76 eV), as displayed in Table 1. Additionally, it is noted that a second energetic minimum is present on silver/gold at $\theta = \pm 30°$. This qualitative difference is illustrated in Figure 5f−h, where at $\theta = 30°$, the triazole moiety on Ag(111)/Au(111) adopts a different adsorption configuration not possible on Cu(111). On Cu, the triazole stays centered over the Cu−Cu bridge for $\theta = 30°$ (Figure 5g), whereas on Ag/Au, the triazole slides to a three-fold site and becomes almost as stable as for $\theta = 0°$ (Figure 5h). The increased complexity for the molecular substrate interaction leads to far more local minima for Ag/Au than for Cu and in practice hinders the MC corral optimization scheme to be used for Ag/Au. The smaller energy penalty with rotation angle calculated over Ag/Au (Figure 5d) suggests that larger relative rotations between neighboring molecules are allowed, which leads to the formation of smaller corrals on these surfaces. We further emphasize that the possibility on Ag/Au to alternate between minima separated by 30° coincides with the average rotation of 30° of the molecules in the experimentally most abundant 12-membered corrals on these surfaces.

Table 1. DFT Bond Lengths for N Bound to the Substrate and to the Neighboring N for the Ideal Bridge Site[a]

	Cu	Ag	Au
M−N/Å	2.169/2.158	2.607/2.650	2.616/2.658
N−N/Å	1.328	1.319	1.318
triazole E_{ads}/eV	−0.76	−0.58	−0.52

[a]Adsorption energy E_{ads} for triazole moiety on the (111) surfaces of copper, silver, and gold.

DISCUSSION

While many examples exist for the formation of molecular corrals within extended 2D porous supramolecular networks[21−24] or molecular clusters,[25−27] the observation of *discrete* supramolecular corrals arising through the noncovalent interactions of large numbers of molecules is rare. A comparable study concerns the adsorption of rubrene on Cu(111),[16] resulting in complex, discrete ring structures through a *hierarchical* self-assembly mechanism rather than the direct successive addition of a large number of molecular building blocks to generate discrete corrals as observed here. Concentric supramolecular rings and spirals have also been observed from a TTF derivative deposited from octanoic acid solution on graphite. The mechanism of their formation is speculated to directly involve solvent molecules.[17]

The prevalent approach to attain desired supramolecular surface architectures has been to judiciously design molecular building blocks to exploit directional intermolecular interactions within the surface plane, in particular, hydrogen bonds. Examples where aromatic interactions direct the self-assembly are much rarer.[14−16] From the analysis of interaction energies performed for the individual components of 1,5-triazole (Figure 3), we find that the driving force for rotation between neighboring molecules is indeed the aromatic interaction between the neighboring phenanthrene rings, which hence direct the corral formation. The crystal structure of phenanthrene[28] shows an alternating stacking arrangement of the rings rotated ∼65° about the long axis, with the closest point of contact (C−H···C) distance of 2.9 Å. This stacking arrangement is qualitatively similar to the situation for the phenanthrene rings in the corral structures, which from our calculations show a maximum interaction when the rings are angled ∼30° to each other (Figure 3), enabling favorable $\sigma-\pi$ interactions between the C−H bonds and the aromatic rings at the point of closest contact (3.2 Å in case of the dimer pair shown in Figure 3b). Both arrangements can be interpreted as a

DOI: 10.1021/acsnano.7b03484
ACS Nano 2017, 11, 8302−8310

balance between maximizing the dispersive forces between the aromatic rings in a cofacial arrangement,[10] while minimizing electrostatic repulsion arising between neighboring π-electron clouds,[11] resulting in a rotation of the molecules.

Recently, there have been a number of studies on the 2D quantum confinement of metal surface electrons within nanoporous organic networks.[29−32] Echoing the seminal work on iron adatom corrals formed by STM manipulation,[33] these studies have investigated the role of surface electronic states in stabilizing the formation of molecular nanoporous structures. In particular, the porous network of anthroquinone on Cu(111) was found to be partially stabilized by the confinement of surface electrons within the pores that adopt a filled noble gas atom electronic configuration.[31] Interestingly, the hexagonal pore diameter of ∼40 Å observed in the anthroquinone networks is comparable to the diameter (∼34 ± 4 Å) of the most prevalent 16-membered corrals formed by 1,5-triazole on Cu(111). Whereas a coupling to the surface electronic states thus cannot be ruled out for the current system, the observation of multiple short, yet curved *partially* formed corral structures (Figure 2a,j) clearly points to intermolecular interactions and molecule−surface coupling as the primary driving force behind the observed corral formation.

A final point of interest is the chirality of the molecular corrals, expressed as the clockwise/counterclockwise arrangement of the cog-wheel blue halo ascribed to the peripheral biphenyl moieties. The chirality is ascribed to the corrals being formed from mirror image conformers of 1,5-triazole. Using climbing image elastic-band DFT calculations,[34] the barrier for rotation of the phenanthrene unit to allow switching between the two conformers is calculated as 0.41 eV (see Supporting Information Figure S5). At the surface temperature of 300 K, where the 1,5-triazole molecules are deposited, this energy barrier allows rapid interconversion between the two conformers ($t_{1/2} = 3.62 \times 10^{-6}$ s). However, at lower temperatures, the two conformers (enantiomers) become stable on the surface ($t_{1/2} > 1000$ s when $T < 132$ K). Although it could not be directly observed with STM due to rapid surface diffusion of the molecules above ∼115 K, we therefore ascribe the dynamic formation of homochiral corrals to chiral accommodation[35,36] of incoming triazole molecules to match the chiral conformation of neighboring molecules as the corral structures grow.

CONCLUSIONS

We have reported on the self-assembly of 1,5-triazole molecules into unusual supramolecular corral structures on three metallic substrates. The unusual corral formation is explained by the careful balance between the triazole−metal interaction and the intermolecular aromatic interactions that arise from the nonplanar adsorption geometry of the 1,5-triazole. The site-specific binding of the triazole moiety acts as a pivot between the biphenyl and phenanthrene aromatic systems, causing the former to bind to the surface and stabilize the adsorption configuration, forcing the phenanthrene ring to orientate almost orthogonally to the surface, allowing for angle-dependent aromatic interactions. The triazole−metal coupling acts as a template for the molecules to bind on a ring-shaped ensemble of inequivalent bridge site pairs of the (111) surface. Rotations away from the optimum orientation at the bridge site result in an energy penalty that is compensated by more favorable aromatic interactions driving the formation of the curved corral shape. Variations of the triazole−metal interaction are responsible for the distinct corral size distributions on Ag/Au and on Cu. We suggest that the design protocol introduced here for the formation of isolated corral structures, using triazoles and sterically hindered aromatic systems, could be of interest in the quantum confinement of surface states[37] in cases where coupling between neighboring pores may not be desirable or for the synthesis of reaction pockets.[21]

METHODS

UHV-STM. To investigate the formation of molecular corrals on surfaces, sub-monolayer coverages of 1,5-triazole were deposited on crystals of Cu(111), Ag(111), and Au(111). All STM experiments were conducted under UHV conditions where the base pressure is $\leq 1.5 \times 10^{-10}$ mbar. Following a lengthy degassing period, 1,5-triazole was deposited onto the metal surfaces using a Knudsen cell, with thermal sublimation occurring at ∼388 K. During deposition, the cleaned substrate was held at room temperature, subsequently being cooled in the STM block to 90 K and scanned in the temperature range of 90−110 K. The crystal surfaces were prepared by repeated sputter−anneal cycles (sputtering the surfaces with 1.5 kV Ar^+ ions, followed by annealing to 750 K), until large terraces separated by monatomic steps were observed using STM.

Simulations. For the theoretical modeling, the ASE[38] software package was used to setup, handle, and optimize the DFT and MC calculations. The GPAW[39] software was used to perform the DFT calculations. The code utilizes a real-space grid for the projector-augmented wave method to represent the wave functions and electron density.[40,41] Geometric optimizations were terminated when no force exerted on the atoms exceeded 0.025 eV/Å regardless of the setup. For the exchange-correlation functional, the optB88-vdW[42] was picked. This functional uses a nonlocal van der Waals scheme that performs very well for aromatic molecules like 1,5-triazole, where a large part of interactions are governed by vdW interactions. A range of 2D periodic Cu(111) surfaces with a lattice constant of $a = 3.632$ Å, optimized for the used functional,[43] and a minimum of 6 Å of vacuum between the atoms and the cell boundary perpendicular to the slab, were used for the calculations. It is unfeasible to use the largest needed surface for all of the calculations, and hence, a range of tests of the importance of the number of layers, cell size, and the sampled K-points was carried out to ensure that no important information was missed. By going from a two-layer 6 × 6 to a four-layer 6 × 6 orthorhombic cell sampling, the Γ point (the largest energy difference of all sampled adsorption configurations) is 0.05 eV. A 2 × 2 × 1 K-point sampling changes the four-layer Cu adsorption energy by a maximum of 0.07 eV with no reordering of the relative stability. Moving from the two-layer 6 × 6 orthorhombic cell to a two-layer 8 × 12 hexagonal cell changes the binding energy by only 0.09 eV. Observing only small relative changes, all the reported energies are with a sampling of the Γ point. Adsorption energies are reported for 6 × 6 × 4 orthorhombic cells, whereas dimer energies are calculated in an 8 × 8 × 2 hexagonal cell except for when the reference energy of the parallel dimer in Figure 3b was determined. For this, an 8 × 12 × 2 hexagonal cell was utilized to secure that the individual 1,5-triazoles were not interacting (at least 9 Å between nearest atoms). For mapping the angle dependencies, single-point energies for different dimers with an increment of 5° for both θ_1 and θ_2 were used with a quadratic interpolation between the points on the grid of angles. For the Ag/Au(111) surfaces, a unit cell constant of $a = 4.101/4.093$ Å[43] was used with the gold lattice constant compressed 4% to mimic the herringbone reconstruction. The adsorption energy as a function of the angle was also calculated in the 6 × 6 × 4 orthorhombic cell as previously done for Cu.

ASSOCIATED CONTENT

Supporting Information

The Supporting Information is available free of charge on the ACS Publications website at DOI: 10.1021/acsnano.7b03484.

DOI: 10.1021/acsnano.7b03484
ACS Nano 2017, 11, 8302−8310

Additional STM data, further DFT and MC calculations, synthetic details, and associated spectra (PDF)
MC simulation run (AVI)

AUTHOR INFORMATION

Corresponding Authors

*E-mail: hammer@phys.au.dk.
*E-mail: trolle@inano.au.dk.

ORCID

Kurt V. Gothelf: 0000-0003-2399-3757
Bjørk Hammer: 0000-0002-7849-6347
Trolle R. Linderoth: 0000-0001-9008-7581

Notes

The authors declare no competing financial interest.

ACKNOWLEDGMENTS

We acknowledge financial support from the Danish National Research Foundation, The Danish Council for Independent Research | Natural Sciences, and the Lundbeck Foundation. We thank C. Bombis and F. Bebensee for their assistance toward initial experiments in this project.

REFERENCES

(1) Moses, J. E.; Moorhouse, A. D. The Growing Applications of Click Chemistry. *Chem. Soc. Rev.* **2007**, *36*, 1249−1262.
(2) Peljhan, S.; Kokalj, A. DFT Study of Gas-phase Adsorption of Benzotriazole on Cu(111), Cu(100), Cu(110), and Low Coordinated Defects Thereon. *Phys. Chem. Chem. Phys.* **2011**, *13*, 20408−20417.
(3) Vericat, C.; Vela, M. E.; Corthey, G.; Pensa, E.; Cortes, E.; Fonticelli, M. H.; Ibanez, F.; Benitez, G. E.; Carro, P.; Salvarezza, R. C. Self-assembled Monolayers of Thiolates on Metals: a Review Article on Sulfur-metal Chemistry and Surface Structures. *RSC Adv.* **2014**, *4*, 27730−27754.
(4) Finšgar, M.; Milošev, I. Inhibition of Copper Corrosion by 1,2,3-benzotriazole: A Review. *Corros. Sci.* **2010**, *52*, 2737−2749.
(5) Grillo, F.; Garrido Torres, J. A.; Treanor, M. J.; Larrea, C. R.; Gotze, J. P.; Lacovig, P.; Fruchtl, H. A.; Schaub, R.; Richardson, N. V. Two-dimensional Self-assembly of Benzotriazole on an Inert Substrate. *Nanoscale* **2016**, *8*, 9167−9177.
(6) Grillo, F.; Tee, D. W.; Francis, S. M.; Fruchtl, H. A.; Richardson, N. V. Passivation of Copper: Benzotriazole Films on Cu(111). *J. Phys. Chem. C* **2014**, *118*, 8667−8675.
(7) Gorbitz, C. H. The Structure of Nanotubes Formed by Diphenylalanine, the Core Recognition Motif of Alzheimer's Beta-amyloid Polypeptide. *Chem. Commun.* **2006**, *22*, 2332−2334.
(8) Percec, V.; Glodde, M.; Bera, T. K.; Miura, Y.; Shiyanovskaya, I.; Singer, K. D.; Balagurusamy, V. S. K.; Heiney, P. A.; Schnell, I.; Rapp, A.; Spiess, H. W.; Hudson, S. D.; Duan, H. Self-organization of Supramolecular Helical Dendrimers into Complex Electronic Materials. *Nature* **2002**, *417*, 384−387.
(9) Klärner, F.-G.; Kahlert, B. Molecular Tweezers and Clips as Synthetic Receptors. Molecular Recognition and Dynamics in Receptor−Substrate Complexes. *Acc. Chem. Res.* **2003**, *36*, 919−932.
(10) Grimme, S. Do Special Noncovalent $\pi-\pi$ Stacking Interactions Really Exist? *Angew. Chem., Int. Ed.* **2008**, *47*, 3430−3434.
(11) Hunter, C. A.; Sanders, J. K. The Nature of π-π Interactions. *J. Am. Chem. Soc.* **1990**, *112*, 5525−5534.
(12) Martinez, C. R.; Iverson, B. L. Rethinking the Term "Pi-stacking". *Chem. Sci.* **2012**, *3*, 2191−2201.
(13) Beniwal, S.; Chen, S.; Kunkel, D. A.; Hooper, J.; Simpson, S.; Zurek, E.; Zeng, X. C.; Enders, A. Kagome-like Lattice of π-π stacked 3-hydroxyphenalenone on Cu(111). *Chem. Commun.* **2014**, *50*, 8659−8662.
(14) Langlais, V. A.; Gauthier, Y.; Belkhir, H.; Maresca, O. Self-organized calix[4]arenes on Au(110)−(1 × 2): A Combined Low-energy Electron Diffraction and Scanning Tunneling Microscopy Experimental Study with Molecular Mechanics Calculations. *Phys. Rev. B: Condens. Matter Mater. Phys.* **2005**, *72*, 085444.
(15) Treier, M.; Ruffieux, P.; Groning, P.; Xiao, S.; Nuckolls, C.; Fasel, R. An Aromatic Coupling Motif for Two-dimensional Supramolecular Architectures. *Chem. Commun.* **2008**, 4555−4557.
(16) Blum, M. C.; Cavar, E.; Pivetta, M.; Patthey, F.; Schneider, W. D. Conservation of Chirality in a Hierarchical Supramolecular Self-assembled Structure with Pentagonal Symmetry. *Angew. Chem., Int. Ed.* **2005**, *44*, 5334−5337.
(17) Li, B.; Puigmarti-Luis, J.; Jonas, A. M.; Amabilino, D. B.; De Feyter, S. Hierarchical Growth of Curved Organic Nanowires Upon Evaporation Induced Self-assembly. *Chem. Commun.* **2014**, *50*, 13216−13219.
(18) Bebensee, F.; Bombis, C.; Vadapoo, S. R.; Cramer, J. R.; Besenbacher, F.; Gothelf, K. V.; Linderoth, T. R. On-Surface Azide-Alkyne Cycloaddition on Cu(111): Does It "Click" in Ultrahigh Vacuum? *J. Am. Chem. Soc.* **2013**, *135*, 2136−2139.
(19) Díaz Arado, O.; Mönig, H.; Wagner, H.; Franke, J.-H.; Langewisch, G.; Held, P. A.; Studer, A.; Fuchs, H. On-Surface Azide−Alkyne Cycloaddition on Au(111). *ACS Nano* **2013**, *7*, 8509−8515.
(20) Oki, M. Recent Advances in Atropisomerism. *Topics in Stereochemistry*; John Wiley & Sons, Inc.: Hoboken, NJ, 1983; Vol. *14*, pp 1−81.
(21) Bonifazi, D.; Mohnani, S.; Llanes-Pallas, A. Supramolecular Chemistry at Interfaces: Molecular Recognition on Nanopatterned Porous Surfaces. *Chem. - Eur. J.* **2009**, *15*, 7004−7025.
(22) Dobrin, S.; Harikumar, K. R.; Jones, R. V.; Li, N.; McNab, I. R.; Polanyi, J. C.; Sloan, P. A.; Waqar, Z.; Yang, J.; Ayissi, S.; Hofer, W. A. Self-assembled Molecular Corrals on a Semiconductor Surface. *Surf. Sci.* **2006**, *600*, 43−47.
(23) Klappenberger, F.; Kühne, D.; Krenner, W.; Silanes, I.; Arnau, A.; García de Abajo, F. J.; Klyatskaya, S.; Ruben, M.; Barth, J. V. Dichotomous Array of Chiral Quantum Corrals by a Self-Assembled Nanoporous Kagomé Network. *Nano Lett.* **2009**, *9*, 3509−3514.
(24) Yitamben, E. N.; Niebergall, L.; Rankin, R. B.; Iski, E. V.; Rosenberg, R. A.; Greeley, J. P.; Stepanyuk, V. S.; Guisinger, N. P. Tracking Amino Acids in Chiral Quantum Corrals. *J. Phys. Chem. C* **2013**, *117*, 11757−11763.
(25) Karan, S.; Wang, Y.; Robles, R.; Lorente, N.; Berndt, R. Surface-Supported Supramolecular Pentamers. *J. Am. Chem. Soc.* **2013**, *135*, 14004−14007.
(26) Yokoyama, T.; Yokoyama, S.; Kamikado, T.; Okuno, Y.; Mashiko, S. Selective Assembly on a Surface of Supramolecular Aggregates with Controlled Size and Shape. *Nature* **2001**, *413*, 619−621.
(27) Selvanathan, S.; Peters, M. V.; Schwarz, J.; Hecht, S.; Grill, L. Formation and Manipulation of Discrete Supramolecular Azobenzene Assemblies. *Appl. Phys. A: Mater. Sci. Process.* **2008**, *93*, 247−252.
(28) Kay, M. I.; Okaya, Y.; Cox, D. E. Refinement of Structure of Room Temperature Phase of Phenanthrene, $C_{14}H_{10}$, from X-Ray and Neutron Diffraction Data. *Acta Crystallogr., Sect. B: Struct. Crystallogr. Cryst. Chem.* **1971**, *27*, 26−33.
(29) Chen, M.; Shang, J.; Wang, Y. F.; Wu, K.; Kuttner, J.; Hilt, G.; Hieringer, W.; Gottfried, J. M. On-Surface Synthesis and Characterization of Honeycombene Oligophenylene Macrocycles. *ACS Nano* **2017**, *11*, 134−143.
(30) Lobo-Checa, J.; Matena, M.; Muller, K.; Dil, J. H.; Meier, F.; Gade, L. H.; Jung, T. A.; Stohr, M. Band Formation from Coupled Quantum Dots Formed by a Nanoporous Network on a Copper Surface. *Science* **2009**, *325*, 300−303.
(31) Wyrick, J.; Kim, D. H.; Sun, D. Z.; Cheng, Z. H.; Lu, W. H.; Zhu, Y. M.; Berland, K.; Kim, Y. S.; Rotenberg, E.; Luo, M. M.; Hyldgaard, P.; Einstein, T. L.; Bartels, L. Do Two-Dimensional "Noble Gas Atoms" Produce Molecular Honeycombs at a Metal Surface? *Nano Lett.* **2011**, *11*, 2944−2948.
(32) Schouteden, K.; Ivanova, T.; Li, Z.; Iancu, V.; Tahara, K.; Tobe, Y.; Adisoejoso, J.; De Feyter, S.; Van Haesendonck, C.; Janssens, E.

DOI: 10.1021/acsnano.7b03484
ACS Nano 2017, 11, 8302−8310

Alkoxylated dehydrobenzo[12]annulene on Au(111): From Single Molecules to Quantum Dot Molecular Networks. *Chem. Commun.* **2015**, *51*, 10917−10920.
(33) Crommie, M. F.; Lutz, C. P.; Eigler, D. M. Confinement of Electrons to Quantum Corrals on a Metal-Surface. *Science* **1993**, *262*, 218−220.
(34) Kolsbjerg, E. L.; Groves, M. N.; Hammer, B. An Automated Nudged Elastic Band Method. *J. Chem. Phys.* **2016**, *145*, 094107.
(35) Weigelt, S.; Busse, C.; Petersen, L.; Rauls, E.; Hammer, B.; Gothelf, K. V.; Besenbacher, F.; Linderoth, T. R. Chiral Switching by Spontaneous Conformational Change in Adsorbed Organic Molecules. *Nat. Mater.* **2006**, *5*, 112−117.
(36) Demers-Carpentier, V.; Goubert, G.; Masini, F.; Lafleur-Lambert, R.; Dong, Y.; Lavoie, S.; Mahieu, G.; Boukouvalas, J.; Gao, H.; Rasmussen, A. M. H.; Ferrighi, L.; Pan, Y.; Hammer, B.; McBreen, P. H. Direct Observation of Molecular Preorganization for Chirality Transfer on a Catalyst Surface. *Science* **2011**, *334*, 776−780.
(37) Muller, K.; Enache, M.; Stohr, M. Confinement Properties of 2D Porous Molecular Networks on Metal Surfaces. *J. Phys.: Condens. Matter* **2016**, *28*, 153003.
(38) Larsen, A. H.; Mortensen, J. J.; Blomqvist, J.; Castelli, I. E.; Christensen, R.; Dułak, M.; Friis, J.; Groves, M. N.; Hammer, B.; Hargus, C.; Hermes, E. D.; Jennings, P. C.; Jensen, P. B.; Kermode, J.; Kitchin, J. R.; Kolsbjerg, E. L.; Kubal, J.; Kaasbjerg, K.; Lysgaard, S.; Maronsson, J. B.; et al. The Atomic Simulation Environment − a Python Library for Working with Atoms. *J. Phys.: Condens. Matter* **2017**, *29*, 273002.
(39) Enkovaara, J.; Rostgaard, C.; Mortensen, J. J.; Chen, J.; Dułak, M.; Ferrighi, L.; Gavnholt, J.; Glinsvad, C.; Haikola, V.; Hansen, H. A.; Kristoffersen, H. H.; Kuisma, M.; Larsen, A. H.; Lehtovaara, L.; Ljungberg, M.; Lopez-Acevedo, O.; Moses, P. G.; Ojanen, J.; Olsen, T.; Petzold, V.; et al. Electronic Structure Calculations with GPAW: a Real-space Implementation of the Projector Augmented-wave Method. *J. Phys.: Condens. Matter* **2010**, *22*, 253202.
(40) Blöchl, P. E. Projector Augmented-wave Method. *Phys. Rev. B: Condens. Matter Mater. Phys.* **1994**, *50*, 17953−17979.
(41) Mortensen, J. J.; Hansen, L. B.; Jacobsen, K. W. Real-space Grid Implementation of the Projector Augmented Wave Method. *Phys. Rev. B: Condens. Matter Mater. Phys.* **2005**, *71*, 035109.
(42) Klimeš, J.; Bowler, D. R.; Michaelides, A. Chemical Accuracy for the van der Waals Density Functional. *J. Phys.: Condens. Matter* **2010**, *22*, 022201.
(43) Klimeš, J.; Bowler, D. R.; Michaelides, A. Van der Waals Density Functionals Applied to Solids. *Phys. Rev. B: Condens. Matter Mater. Phys.* **2011**, *83*, 195131.

DOI: 10.1021/acsnano.7b03484
ACS Nano 2017, 11, 8302−8310

Paper IV

ACS NANO
Cite This: ACS Nano 2018, 12, 513−520
www.acsnano.org
ARTICLE

Exciting H_2 Molecules for Graphene Functionalization

Line Kyhl,[†] Régis Bisson,[‡] Richard Balog,[§] Michael N. Groves,[§] Esben Leonhard Kolsbjerg,[†] Andrew Martin Cassidy,[§] Jakob Holm Jørgensen,[†] Susanne Halkjær,[§] Jill A. Miwa,[†,§] Antonija Grubišić Čabo,[†] Thierry Angot,[‡] Philip Hofmann,[§] Mohammad Alif Arman,[∥] Samuli Urpelainen,[∥] Paolo Lacovig,[⊥] Luca Bignardi,[⊥] Hendrik Bluhm,[#] Jan Knudsen,[∥,∇] Bjørk Hammer,[†,§] and Liv Hornekaer*[,†,§]

[†]iNANO, Aarhus University, DK-8000 Aarhus C, Denmark
[‡]Aix-Marseille University, CNRS, PIIM, 13007 Marseille, France
[§]Department of Physics and Astronomy, Aarhus University, DK-8000 Aarhus C, Denmark
[∥]The MAX IV Laboratory, Lund University, 221 00 Lund, Sweden
[⊥]Elettra-Sincrotrone Trieste S.C.p.A., S. S. 14 km 163.5, 34012 Trieste, Italy
[#]Chemical Sciences Division and Advanced Light Source, Lawrence Berkeley National Laboratory, Berkeley, California 94720, United States
[∇]Division of Synchrotron Radiation Research, Lund University, 221 00 Lund, Sweden

Supporting Information

ABSTRACT: Hydrogen functionalization of graphene by exposure to vibrationally excited H_2 molecules is investigated by combined scanning tunneling microscopy, high-resolution electron energy loss spectroscopy, X-ray photoelectron spectroscopy measurements, and density functional theory calculations. The measurements reveal that vibrationally excited H_2 molecules dissociatively adsorb on graphene on Ir(111) resulting in nanopatterned hydrogen functionalization structures. Calculations demonstrate that the presence of the Ir surface below the graphene lowers the H_2 dissociative adsorption barrier and allows for the adsorption reaction at energies well below the dissociation threshold of the H−H bond. The first reacting H_2 molecule must contain considerable vibrational energy to overcome the dissociative adsorption barrier. However, this initial adsorption further activates the surface resulting in reduced barriers for dissociative adsorption of subsequent H_2 molecules. This enables functionalization by H_2 molecules with lower vibrational energy, yielding an avalanche effect for the hydrogenation reaction. These results provide an example of a catalytically active graphene-coated surface and additionally set the stage for a re-interpretation of previous experimental work involving elevated H_2 background gas pressures in the presence of hot filaments.

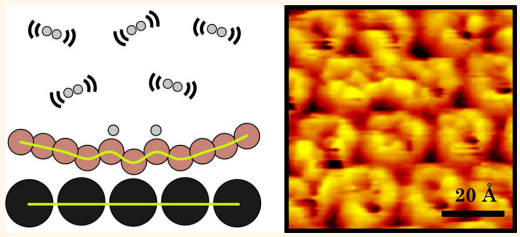

KEYWORDS: *graphene, vibrational excitation, nanostructured functionalization, band gap engineering, molecular hydrogen, catalysis*

The controlled chemical functionalization of graphene is of broad interest for modifying its chemical, optical, mechanical, and electronic properties. The adsorption of a single H atom onto the graphene lattice induces magnetic moments in the sheet[1] enabling the development of spintronic devices. At a higher hydrogen coverage, manipulation of the global electronic structure is possible, and in some systems a tunable band gap can be obtained, which is of interest for the use of graphene in electronic applications.[2,3] A complete hydrogenation of graphene by H atoms yields the two-dimensional electronically insulating sp^3 structure called graphane,[4] which has been proposed as a hydrogen storage material.[5,6] The interaction between graphene and its substrate is a crucial factor for the reactivity of graphene and thus for its chemical functionalization.[7] Several experimental and theoretical studies have shown that hot atomic hydrogen can chemisorb onto the basal plane of graphite, free-standing graphene, and graphene on metal and semiconductor substrates.[2−4,8−16] For

Received: October 6, 2017
Accepted: December 18, 2017
Published: December 18, 2017

 © 2017 American Chemical Society
DOI: 10.1021/acsnano.7b07079
ACS Nano 2018, 12, 513−520

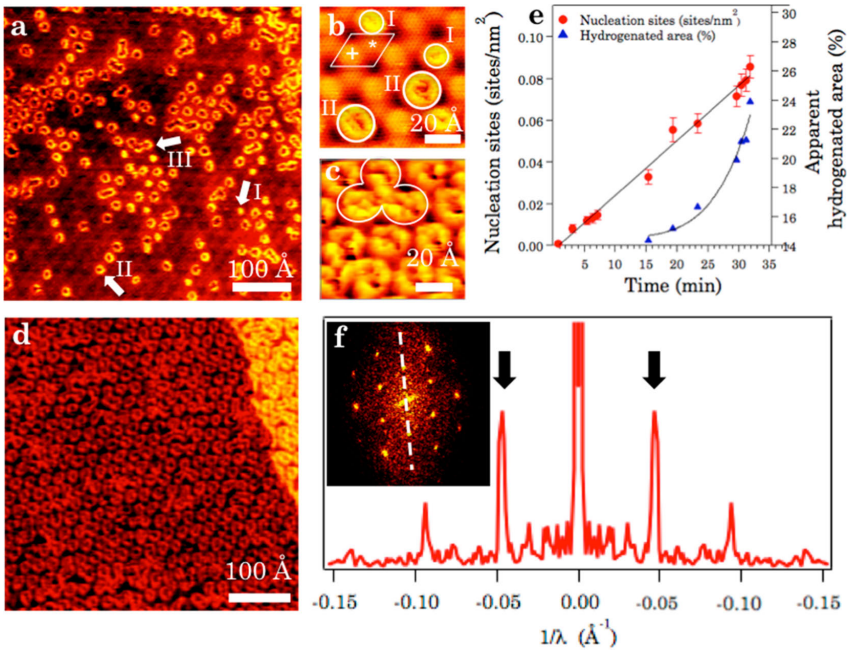

Figure 1. (a–d) STM images of gr/Ir(111) exposed to vibrationally excited H_2 or D_2: (a) H_2 with method (i) at $P = 2 \times 10^{-5}$ mbar for 32 min. (b) D_2 with method (ii) at $P = 5 \times 10^{-7}$ mbar for 20 min, $T_W > 2000$ K. Features of types I and II are indicated with circles. The rhombus outlines a moiré unit cell, the "*" and the "+" denote the FCC and HCP areas, respectively, and the corners of the rhombus mark the atop regions. (c) D_2 with method (ii) at $P = 5 \times 10^{-7}$ mbar for 60 min, $T_W > 2000$ K. A type III feature is outlined. (d) D_2 with method (ii) at $P = 5 \times 10^{-7}$ mbar for 60 min, $T_W > 2000$ K. (e) Time evolution of hydrogenation structures during exposure to vibrationally excited H_2, using method (i), at $P = 1 \times 10^{-5}$ mbar. Red dots: Total number of nucleation sites, normalized to the imaged area, plotted against time. Error bars represent the intrinsic error assuming a Poisson distribution. Blue triangles: Apparent hydrogenated area, in % of total image area, plotted against time. (f) A line profile through the Fourier transform shown in the inset, along the line indicated. The Fourier transform is performed on a larger scale STM image (see Supporting Information, S2) in the same area as shown in the STM image in (d). The Fourier transform illustrates a high degree of order on the surface after the exposure to vibrationally excited H_2. The separation of the peaks indicated by arrows in the line profile corresponds to a real space separation of ~21.5 Å which equals ~25 Å × cos(30°), confirming a global hydrogen-induced patterning with moiré superlattice periodicity. Imaging parameters for (a–d): (a) $V_t = 478.2$ mV, $I_t = 0.790$ nA. (b) $V_t = 67.1$ mV, $I_t = 1.090$ nA. (c) $V_t = -351.9$ mV, $I_t = -0.310$ nA. (d) $V_t = -351.9$ mV, $I_t = -0.320$ nA.

graphene on Ir(111) (gr/Ir(111)), the reactivity varies over the surface, since the graphene-Ir interaction is modulated with a ~25 Å periodicity, reflecting the moiré pattern that originates from the ~10% lattice mismatch between graphene and Ir(111).[17,18] In so-called HCP and FCC areas of the moiré structure, the position of every second carbon atom coincides with the position of an Ir atom below.[2,3] In these HCP and FCC areas, the graphene lattice can distort upon hydrogen functionalization and form a configuration where every second C atom binds to the underlying Ir, while neighboring C atoms bind to H atoms on top.[3,10] This configuration becomes thermodynamically stable at a certain H cluster size, and adsorption at the HCP site is found to be slightly more favorable than the FCC site.[2] A selective functionalization of HCP areas by hot H atoms has been achieved by elevating the sample temperature during the atomic exposure. Such selective functionalization leads to highly ordered hydrogenation structures, including the opening of a gap in the electronic band structure.[2]

While functionalization of graphene with atomic H is well established, functionalization using H_2 molecules is less explored[19−21] and is in general energetically unfavorable due to the high stability of the H_2 molecule. For free-standing graphene, the barrier for dissociative adsorption is estimated to be 3.1−3.4 eV.[8,22−25] It has been predicted, however, that the barrier can be lowered in the presence of a perpendicular electric field[26,27] or at defects and edges.[24,28,29] For nonfree-standing graphene, the barrier can be substantially lower as shown in this report. A few experimental studies report partial hydrogenation of graphene at high-pressure H_2 ($P_{H_2} > 1$ bar).[19−21] Additionally, it has been proposed that nanoparticles can dissociate H_2 and transfer the resulting hydrogen atoms to the graphene through spillover effects.[30−32] The validity of this spillover phenomenon was however questioned in a recent theoretical study.[33] The H_2 adsorption energy and activation barrier are consistently reported to depend on the graphene curvature.[9,34,35]

Here we present combined scanning tunneling microscopy (STM), high-resolution electron energy loss spectroscopy (HREELS), and X-ray photoemission spectroscopy (XPS) data to demonstrate that highly vibrationally excited H_2 molecules can functionalize gr/Ir(111), yielding highly ordered nanopatterned graphene, *via* dissociative adsorption reactions.

DOI: 10.1021/acsnano.7b07079
ACS Nano 2018, 12, 513−520

Ambient pressure XPS (APXPS) excludes the possibility of graphene hydrogenation through direct dissociation of H_2 molecules on the Ir(111) surface. The experimental observations are supported by density functional theory (DFT) calculations showing that the dissociation barrier is lowered substantially by the graphene-mediated catalytic effect of the Ir substrate. Moreover, the barrier to adsorption continues to decrease for further addition of H_2 at sites adjacent to adsorbed molecules due to local distortion effects. Consequently, an avalanche of H_2 dissociation and H-addition reactions becomes possible, providing an efficient route toward hydrogenation.

RESULTS AND DISCUSSION

Highly vibrationally excited H_2 is produced *via* Eley−Rideal abstraction reactions between gas-phase H atoms and H atoms adsorbed on metal surfaces. Such reactions have been shown to yield vibrationally excited H_2 molecules exhibiting superthermal vibrational energy level populations up to at least $\nu = 9$.[36,37] The exact population distribution depends on the metal surface on which the recombination occurs.[36] While gaseous H atoms are expected to either adsorb or undergo abstraction reactions upon collision with metal surfaces, the vibrationally excited H_2 molecules are found to survive hundreds of collisions before thermalizing.[36] A high yield of highly vibrationally excited molecules was obtained by letting H_2 or D_2 gas pass through a ∼2300 K ThO_2·Ir filament (method (i)) or a hot W capillary with temperature T_W (method (ii)). The filament and W capillary are both sources of hot atomic H. Thus, to avoid the influence of these hot H atoms in our experiments, the sample was always placed out of the line of sight and far from any atomic H source. This yields a complicated trajectory for hot H atoms between the source and the sample surface. In their trajectory, the gas-phase H atoms will inevitably collide with metallic elements. During such collisions, they have a high probability to recombine with adsorbed H atoms on the metallic surfaces to yield gas-phase vibrationally excited H_2.[36] To exclude the possibility that any hot H atoms reach the sample surface in our experiments, a highly oriented pyrolytic graphite (HOPG) sample was exposed to vibrationally excited H_2 as described above. Graphite becomes hydrogen functionalized when exposed to hot H atoms.[8] In our experiments with vibrationally excited H_2, the graphite was, however, completely inert, as shown by HREELS and STM measurements (see Supporting Information), even for exposure times up to ∼12 h, and the influence of hot H atoms can thus be excluded.

STM Results. Figure 1a−d displays STM images of gr/Ir(111) following exposure to vibrationally excited H_2 or D_2 molecules. Figure 1a depicts gr/Ir(111) after a ∼32 min exposure (method (i)) at a background pressure of 2×10^{-5} mbar H_2. Three types of bright features related to the H_2 exposure are identified and indicated by arrows: Disc shaped (type I), donut shaped (type II), and merged (type III). Type I and II features are outlined in Figure 1b, and a type III feature is outlined in Figure 1c. Type III features are represented by the merging of neighboring type I and/or II features. It is observed (not shown here) that during a continuous exposure to vibrationally excited H_2, type I features evolve into type II, which may merge at higher exposure into type III. Type II and III features sometimes appear instantaneously, which we ascribe to the limited time resolution of the STM imaging. The image in Figure 1a is the last in a series of STM images (see Supporting Information, S1) obtained during a continuous exposure to vibrationally excited H_2. The accumulated number of nucleation sites was obtained from these images at different exposure times and plotted in Figure 1e (red dots). The plot shows a linear trend. The fractional apparent functionalized area *vs* time is plotted in Figure 1e (blue triangles) displaying a square dependency on the fluence. These findings indicate that the dissociative adsorption of excited H_2 is more likely to lead to an expansion of existing clusters rather than the initiation of new ones. The absolute values in this plot are not a direct measure of the hydrogen coverage since the appearance of features in STM varies with the bias voltage applied. From the STM data in Figure 1 it is evident that features of types I and II appear almost exclusively on one area of the moiré structure. In Figure 1b this area is seen to be the brightest part of the moiré unit cell, which is identified as the HCP site.[2,18,38] When other moiré areas are occupied, it is observed to almost exclusively occur in a type III structure where type II features have grown together to occupy neighboring moiré areas. Inspection of Figure 1a reveals a strong tendency for H-functionalized areas to cluster in neighboring moiré unit cells. In the inset of Figure 1f, a Fourier transform of a larger scale STM image (see Supporting Information, S2), obtained on the same area as the image presented in Figure 1d, is shown. The hexagonal pattern observed in the Fourier transform underlines that hydrogen functionalization structures appear preferentially on one site in the moiré unit cell conferring a high degree of order to the functionalized surface. A line profile along the line indicated on the Fourier transform is presented. The separation between the spots in the Fourier transform, indicated by arrows on the line profile, corresponds to a real space distance of ∼21.5 Å. This equals ∼25 Å × cos(30°) and thus demonstrates the preferred occupancy of one site in the moiré super lattice, identified in the STM images as the HCP site. The exposure to vibrationally excited H_2 thus leads to a highly ordered global patterning of the graphene, with moiré periodicity. No obvious isotopic dependence was observed in the STM experiments. An entirely clean gr/Ir(111) surface can be regained by annealing the sample above ∼720 K.

HREELS Results. Figure 2 depicts HREEL spectra of functionalized graphene after exposure to D atoms (red crosses) and after exposure to vibrationally excited D_2

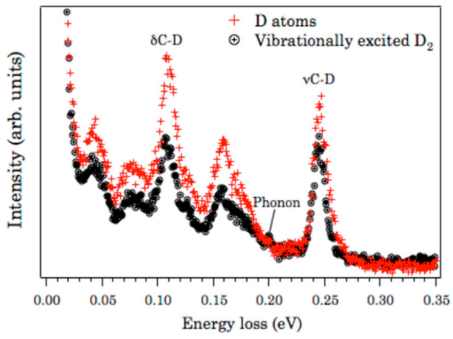

Figure 2. HREEL spectra of gr/Ir(111) exposed to D atoms (flux 3.5×10^{13} D/cm^2 s, fluence 1.0×10^{16} D/cm^2) (red), and to vibrationally excited D_2 using method (i) at 2×10^{-4} mbar for 45 min (black), both up to saturation. Incident energy E_0 = 5 eV and momentum transfer of 0.07−0.1 Å^{-1} over the presented energy range.

DOI: 10.1021/acsnano.7b07079
ACS Nano 2018, 12, 513−520

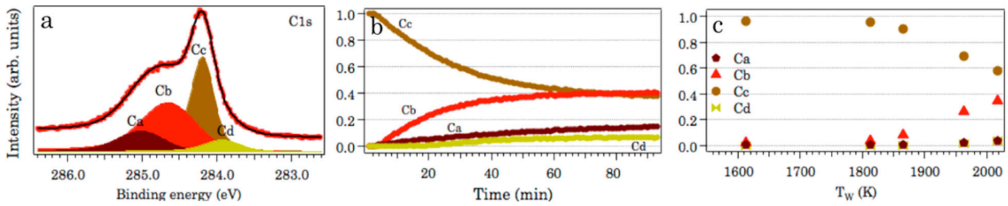

Figure 3. (a) XPS ($h\nu$ = 400 eV) C 1s core level spectrum of gr/Ir(111) after ~1.5 h exposure to vibrationally excited H_2 at $P = 4.5 \times 10^{-8}$ mbar, produced by method (ii), T_W = ~2018 K (saturation coverage). The spectrum is the last spectrum from the uptake series shown in (b). (b) Uptake of vibrationally excited H_2 shown as the relative intensities of components Ca, Cb, Cc, and Cd over time during exposure at same parameters as in (a). (c) The relative intensities of components Ca, Cb, Cc, and Cd in the XPS ($h\nu$ = 390 eV) C 1s core level spectrum for a series of experiments where gr/Ir(111) was exposed for 20 min to $P = 5 \times 10^{-7}$ mbar of H_2, method (ii), with a variable temperature T_W.

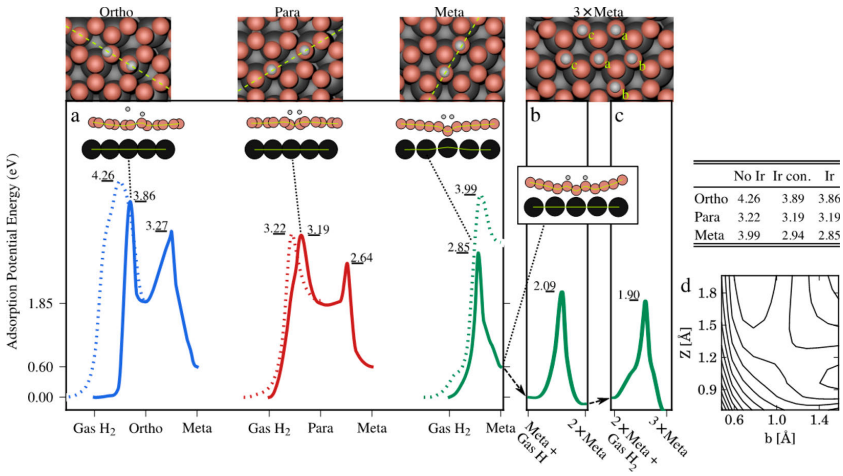

Figure 4. (a) Reaction pathways for one H_2 molecule to adsorb onto *ortho*-, *meta*-, and *para*-sites of an HCP region of graphene over an Ir(111) surface. Solid lines refer to when the graphene sheet and Ir (except for the bottom layer) are allowed to fully relax. Dashed lines reflect the calculations for free-standing graphene. Calculated transition states are plotted (side-view) as well as the final adsorption into the *ortho*-, *para*-, and *meta*-configuration (top-view). The pathway for the *ortho*-site is for a semiconstrained reaction. (b) The reaction pathway for a second H_2 molecule adsorbing in the vicinity of an adsorbed *meta*-dimer. (c) The reaction pathway for a third H_2 molecule adsorbing in the vicinity of the first two *meta*-adsorbed H_2 molecules with a top-view of the final configuration. (d) The potential energy surface around the transition state into the *meta*-configuration expanded in the H_2 height, *Z*, above the graphene and the internal H−H bond length, *b*. The table gives the calculated barrier heights for the three dimer configurations for: free-standing graphene (no Ir); in the case where the Ir atoms are not allowed to move (Ir con); and for the fully relaxed system (Ir) displayed in the figure.

molecules (black circles), both at saturation coverage. The HREEL spectrum obtained after exposure to highly excited D_2 molecules depicts all characteristic features found for gr/Ir(111) functionalized with atomic D.[10] The two most intense vibrational features in the spectra are positioned at 108 and 245 meV corresponding to the C−D bending (δC−D) and stretching (νC−D) modes, respectively.[10] The presence of these features in both spectra proves that regardless of deuterium precursor, atomic D or vibrationally excited D_2, the formation of C−D covalent bonds takes place yielding chemically functionalized gr/Ir(111). The two spectra differ only in intensity (reflecting different saturation coverages) and by the peak at 195 meV, corresponding to the clean graphene TO/LO phonon, which is stronger in the spectrum for the D_2 exposed sample. The persistence of this phonon after vibrationally excited D_2 saturation exposure indicates that larger graphene areas are unfunctionalized, consistent with the lower intensity of the C−D vibrational features.[10]

XPS Results. XPS measurements were performed on gr/Ir(111) as a function of the exposure time to vibrationally excited H_2 produced by method (ii) at a background pressure of 4.5×10^{-8} mbar. A spectrum at saturation coverage is shown in Figure 3a. The spectrum was fit following the procedure used to analyze gr/Ir(111) exposed to hot H atoms[11] and is composed of an sp^2 carbon component (Cc) and three C−H related components at positions +0.81 eV (Ca), +0.44 eV (Cb), and −0.27 eV (Cd) relative to the position of Cc. The C−H related components have been suggested[11] to originate from H clusters in FCC and/or HCP regions (Cb), vacancies in the clusters as well as C atoms neighboring C−H bonds (Cd), and finally C−H in atop regions (Ca). Figure 3b shows the evolution of the relative intensities of the four components during the continuous exposure of gr/Ir(111) to vibrationally excited H_2. The spectra shift to higher binding energy as the degree of functionalization increases, which we attribute to doping, and only the relative positions of the components were

DOI: 10.1021/acsnano.7b07079
ACS Nano 2018, 12, 513−520

fixed during the fitting procedure (see Methods). At saturation coverage, the loss of sp^2 carbon (Cc component) was ~62%, which is lower than what has been reported for functionalization using atomic H, where a ~70% loss in the Cc component was observed.[11] This is consistent with HREELS in Figure 2. Besides the lower saturation coverage, the main difference for vibrationally excited H_2 compared to H atom functionalization is a relatively lower contribution from the Ca component in the case of the former.

To verify the described mechanism for production of vibrationally excited H_2, the temperature of the W capillary (T_W) was varied, keeping a constant hydrogen pressure of 5×10^{-7} mbar and exposure time of 20 min. The sample was flashed to $T = 900$ K between different exposures. The relative component intensities plotted against T_W are shown in Figure 3c. It can be seen that functionalization is initiated at an onset of $T_W > 1800$ K, which corresponds to the onset of atomic H production,[39] in agreement with the proposed mechanism for the generation of highly vibrationally excited H_2 described above.

DFT Results. Figure 4a displays calculated reaction pathways for the dissociative adsorption of H_2 on the HCP areas of the moiré unit cell for dissociation and adsorption into *ortho*- (blue), *para*- (red) and *meta*- (green) configurations. Full lines represent calculations where the graphene and the Ir (except the bottom Ir layer) are allowed to fully relax. The dashed lines represent the same calculations for free-standing graphene with no underlying Ir substrate. All energies are referenced to the relaxed graphene and gas-phase H_2 molecules. Consistent with previous reports, the H_2 adsorption configuration with the lowest barrier, on free-standing graphene, is found to be the *para*-configuration (3.22 eV, dashed red line). This barrier, as well as the transition and final state, is unchanged in the presence of an underlying Ir surface (3.19 eV, full red line). However, for the adsorption into an *ortho*- or *meta*-configuration, when Ir is present, the barriers are lowered by 0.40 to 3.86 eV and by 1.14 to 2.85 eV, respectively (compare dashed to full lines). The presence of the Ir substrate thus changes the most likely adsorption configuration (lowest barrier) from the *para*- to the *meta*-position. Additionally, *meta*-adsorption gives the most thermodynamically stable product due to the possibility for the center C atom to bind down to the Ir surface, leading to a local sp^2 to sp^3 rehybridization of the graphene lattice. The internal energy needed for a gas-phase H_2 molecule to overcome the 2.85 eV barrier for adsorption into the *meta*-configuration requires vibrational excitation to the $\nu \geq 7$ level (~3.0 eV).[36]

The barrier for adsorption into the *para*-configuration would require the population of the $\nu \geq 8$ level (~3.3 eV).[36] If an H_2 molecule adsorbs into the *para*-configuration on gr/Ir(111) (red full line), it is thermodynamically favorable for it to diffuse (~0.8 eV diffusion barrier) to the more stable *meta*-configuration. No H atom diffusion is expected to occur once dissociation into the stable *meta*-configuration is established. Adsorption into the *ortho*-configuration is unlikely since an excitation to the $\nu \geq 11$ level is required to overcome the ~4 eV barrier.[36]

While exhibiting different adsorption barriers, the reaction coordinates for adsorption into the *para*- or *meta*-configurations also undergo very different transition states, see insets in Figure 4. For adsorption in the *para*-configuration, two C atoms in the graphene lattice move slightly upward to accommodate H_2 adsorption in a *para*-dimer configuration. In the case of *meta*-adsorption, an Ir atom moves slightly out of the Ir(111) plane toward the graphene lattice and several C atoms move toward the Ir surface simultaneously as the H_2 approaches. After binding to a C atom, the Ir atom relaxes back into the Ir(111) plane, while the adjacent C atoms bind to the H atoms from the dissociated H_2. Thus, a stabilized sp^3 hybridized state is produced locally in the graphene sheet. The rearrangement of atoms in the described transition state for *meta*-site adsorption, especially the movement of the Ir atom in and out of the plane, happens on a time scale much slower than the vibrational time scale of the excited H_2 molecule. Hence it is unclear whether the incoming excited H_2 molecule will experience the fully relaxed potential energy surface. The potential energy barriers for hydrogen adsorption were explored, by keeping the Ir lattice constrained in its undisturbed state ("Ir con." in the table in Figure 4), since the movement of only the graphene sheet is more likely to match the relevant time scales. The barrier is unchanged for *ortho*- and *para*-adsorption, as expected, and increases only by 0.09 eV for *meta*-adsorption. With such a small increase it seems that the movement of the Ir atom is not the determining factor for the reaction mechanism, while the mere presence of the Ir surface has a huge impact on the barriers, through stabilization of the final state.

The DFT calculations, see Figure 4b–c, also reveal that the adsorption of a subsequent impinging H_2 molecule, into the vicinity of an H_2 molecule that has already dissociated and adsorbed into a *meta*-configuration on gr/Ir(111), has a barrier that is 0.76 eV lower and the reaction is exothermic. Furthermore, the barrier is lowered by an additional 0.19 eV for the third impinging H_2 molecule, which then only needs vibrational excitation to the $\nu \geq 4$ level to overcome a 1.90 eV adsorption barrier. This is consistent with our STM observations in Figure 1e, which show a faster increase of the total area of adsorbed hydrogen (triangles in Figure 1e) compared to the increase in number of nucleation sites (circles in Figure 1e). The barriers are expected to further decrease for subsequent H_2 adsorption until the H–C–Ir cluster becomes thermodynamically stable at a critical size.[2] Thus, the adsorption of the first H_2 molecule triggers an avalanche reaction for the formation of clusters mainly in HCP sites as observed by STM. These clusters may extend to include adsorption into FCC sites *via* the perimeter of the HCP-site cluster, as the distortion of the graphene makes more sites energetically available for dissociation of the highly excited molecules. This is consistent with the STM observations for higher coverages (Figure 1c–f).

Figure 4d shows an elbow plot of the potential energy surface (PES) in the vicinity of the transition state for adsorbing H_2 into the *meta*-site obtained by moving the H atoms only. The transition state is located in the curved region of the PES. Such energy landscapes have been reported to lead to strong vibrational coupling.[40]

The adsorption scheme for hydrogen at the atop areas of the gr/Ir(111) moiré unit cell should be similar to free-standing graphene and graphite. The dissociation of H_2 on graphite predominantly occurs in a *para*-adsorption configuration.[8] The related adsorption barrier is expected to be similar to that for free-standing graphene and is significantly higher than the barriers found for dissociative adsorption of hydrogen on gr/Ir(111). Hence, only hot H atoms can adsorb onto graphite as well as on the atop regions of gr/Ir(111), which is consistent with HREELS (Figure 2) and XPS measurements (Figure 3), showing that saturation coverage for exposure to vibrationally

DOI: 10.1021/acsnano.7b07079
ACS Nano 2018, 12, 513–520

excited H_2 is lower than for exposure to atomic H. However, even though the barrier for *para*-site adsorption is higher, vibrationally excited H_2 in $\nu = 8$ or $\nu = 9$, should have enough energy to overcome it. This contradicts our observations, indicating that the energy loss to the surface, needed to stabilize the reaction products in the dissociative adsorption process, is less efficient for free-standing graphene.

To corroborate the presented interpretation of our results, the viability of an alternative scenario involving H_2 dissociation on bare patches of Ir and subsequent reaction with the overlying graphene in a spillover-like scheme[30−32] was investigated by APXPS. The APXPS measurements (see Supporting Information, S4) show that nonvibrationally excited H_2 molecules, even at high-pressure exposures above 0.01 mbar, do not lead to chemisorption of H onto gr/Ir(111). The experiments yield identical negative results for the monolayer as well as submonolayer (Ir exposed) gr/Ir(111) samples.

CONCLUSIONS

To conclude, we have demonstrated a route to graphene functionalization using vibrationally excited H_2 molecules. The functionalization occurs in a highly ordered manner and is therefore a viable tool for band gap engineering of graphene. The functionalization route exploits the finding that graphene can mediate the catalytic activity of an underlying metal substrate resulting in reduced dissociative adsorption barriers for molecular hydrogen on graphene. Furthermore, the described mechanism exhibits an avalanche effect where the first dissociative adsorption event leads to reduced barriers for subsequent dissociative adsorption. This study is not only an important proof of concept, but the essential insight provided by the mechanism, where nucleation is the most energetically expensive step for the graphene hydrogenation, provides an approach toward the detailed control of graphene and its properties, through chemical functionalization. The presented results further demonstrate that at high chamber pressures of H_2 an atomic source, like an ion gauge filament, may produce vibrationally excited H_2 molecules, with potential influence on the outcome of the experiment. In the absence of a source of atomic hydrogen, vibrationally excited H_2 molecules may be produced *via* VUV or UV excitation processes.[41]

METHODS

Experimental Details. A high-quality gr/Ir(111) sample was prepared by chemical vapor deposition procedures and/or temperature-programmed growth.[17] STM was performed using home-built Aarhus-type STMs[42] at Aarhus University, Aarhus, Denmark. HREELS was performed at Aix-Marseille Université, Marseille, France in a setup described elsewhere.[10] APXPS was performed at beamline 11.0.2 at the Advanced Light Source, Berkeley, California and at SPECIES[43−45] at the MAX II storage ring of MaxIV (formerly Max lab), Lund, Sweden. Time-resolved XPS was performed at the SuperESCA beamline at Elettra, Trieste, Italy. Conventional high-resolution XPS was performed at beamline I311 at the MAX II storage ring of MaxIV (formerly Max lab), Lund, Sweden. All experiments were performed under ultrahigh-vacuum (UHV) conditions, unless stated otherwise.

Hydrogen background pressures used in the experiments varied from 1×10^{-6} to 2×10^{-4} mbar (method (i)) and 4.5×10^{-8} to 7×10^{-7} mbar (method (ii)). The mean free path of H_2 molecules at 300 K at these pressures corresponds to 0.5−2400 m, exceeding the geometry of the chamber setups.

Computational Methods. DFT was used to calculate adsorption potential energies and reaction barriers for H_2 on graphene supported by Ir(111). The real-space, grid-based, projector augmented wave method GPAW[46,47] was employed and supported by the Atomic Simulation Environment (ASE).[48] In order to include the dispersion related effects which govern the interaction between graphene and the Ir surface, the vdW enabled functional optB88-vdW was used.[49] The parameters used for the presented calculations, which reproduce experimental observations,[2] are as follows: an 8 × 8 graphene lattice over a 7 × 7 Ir(111) surface simulated the surface for the adsorption of H_2. The Ir slab was composed of three layers, where the bottom layer was held fixed. The dimensions of the cell parallel to the surface are defined by the optB88-vdW calculated lattice constant for graphene ($a_{\text{graphene,optB88-vdW}}$ = 2.465). This functional uses the vdW-DF framework proposed by Dion *et al.*[50] with a reparameterized version of B88 exchange[51] fitted to the S22 data set.[52] It expands the Ir lattice by 1.6% relative to the optB88-vdW calculated value of 3.921 Å. At least 7.5 Å separates any atom from the top or bottom of the cell. A grid spacing of 0.1779 Å defines the length of each grid point. Finally, a 2 × 2 *k*-point mesh was sampled, and all forces were relaxed until they were below 0.02 eV/Å. Reaction pathways are determined using the AutoNEB code found in ASE with the CI-EB method.[53] As it is not possible to make the direct hydrogenation of the *ortho*-configuration, we have used a constraint CI-EB relaxation for completeness to ensure that a direct barrier was found. A free CI-EB relaxation forces the atoms first into the *meta*-configuration before moving into the *ortho*-configuration. In the constrained case, the transition state has been allowed to only move in the plane crossing the right of the two attacked atoms in the inset in Figure 4 with a normal vector pointing in the direction of the left attacked atom.

Data Analysis. STM images were lightly filtered from noise and flattened to compensate for piezo creep.

HREELS spectra were normalized and calibrated to the intensities and positions respectively of their elastic peak. No further data handling was performed for the presented spectra.

XPS data (obtained from SuperESCA, Elettra, Trieste (Figure 3a,b), from I311 Maxlab, Lund (Figures 3c and S3) and beamline 11.0.2 at the Advanced Light Source, Berkeley, California (Figure S4) were fitted using Doniach−Sunjic profiles convoluted with a Gaussian profile (DS°G). Clean gr/Ir were fit using a Lorentzian full width at half-maximum (LFWHM) of 0.135 eV and a Gaussian full width at half-maximum (GFWHM) of 0.177 eV for data obtained at SuperESCA and LFWHM = 0.158 eV and GFWHM = 0.129 eV for data obtained at I311. The GFWHM was allowed to broaden slightly during the vibrationally excited H_2 exposure, yielding a maximum of GFWHM = 0.279 eV for the last spectrum in the uptake series presented in Figure 3a,b. For the T_W = 2018 K exposure, presented in Figure S3, the Cc component has GFWHM = 0.217 eV. The C 1s core levels change in binding energy upon formation of C−H bonds due to doping effects.[11] The component related to clean sp^2 graphene (Cc) was therefore allowed to shift its binding energy position when fitting spectra that represent vibrationally excited H_2 exposed samples, and the positions of the C−H related components (Ca, Cb and Cd) were fixed relative to the position of Cc by +0.81, +0.44, and −0.27 eV respectively. This procedure is equivalent to the fitting scheme for the data presented by Balog *et al.*[11] for gr/Ir(111) exposed to hot H atoms. Peak assignment was also done according to this previous work. APXPS data (obtained at beamline 11.0.2 at the Advanced Light Source, Berkeley) shown in Figure S4 (left inset) were fit with a LFWHM = 0.135 and GFWHM = 0.35 eV. The binding energy scale for all XPS data was calibrated to the Fermi edge. Linear backgrounds were used for the fits.

ASSOCIATED CONTENT

Supporting Information

The Supporting Information is available free of charge on the ACS Publications website at DOI: 10.1021/acsnano.7b07079.

Supplemental STM, HREELS, and XPS data (PDF)

AUTHOR INFORMATION

Corresponding Author

*E-mail: liv@phys.au.dk.

DOI: 10.1021/acsnano.7b07079
ACS Nano 2018, 12, 513−520

ORCID

Andrew Martin Cassidy: 0000-0001-8352-8721
Paolo Lacovig: 0000-0001-7001-7930
Luca Bignardi: 0000-0002-9846-9100
Hendrik Bluhm: 0000-0001-9381-3155
Bjørk Hammer: 0000-0002-7849-6347
Liv Hornekaer: 0000-0003-0828-3642

Author Contributions

L.K., R. Bisson, R. Balog, and L.H. designed the experiments. L.K., S.H., and J.M., performed STM experiments. L.K., R. Bisson, R. Balog, and T.A. performed HREELS experiments. L.K., A.C, J.J., R. Balog, A.G.Č., M.A., J.K., P.L,. and L.B. performed XPS measurements. L.K., H.B., S.U., and J.K. performed APXPS measurements. M.G., E.K., and B.H. performed DFT calculations. A.G.Č. helped prepare samples. L.K., R. Bisson, R. Balog, and L.H. analyzed the data and wrote the manuscript. All authors contributed to discussions.

Notes

The authors declare no competing financial interest.

ACKNOWLEDGMENTS

We acknowledge financial support from The Danish Council for Independent Research (grant no. 0602-02566B and grant no. 0602-02265B), Innovation Fund Denmark (NIAGRA), The European Research Council (CoG GRANN), Villum Foundation via Villum Centre of Excellence for Dirac Materials (Grant no. 11744). H.B. acknowledges support by the Director, Office of Science, Office of Basic Energy Sciences, and by the Division of Chemical Sciences, Geosciences and Biosciences of the U.S. Department of Energy at LBNL under contract no. DE-AC02-05CH11231. The Advanced Light Source is supported by the Director, Office of Science, Office of Basic Energy Sciences of the U.S. Department of Energy at LBNL under contract no. DE-AC02-05CH11231.

REFERENCES

(1) González-Herrero, H.; Gómez-Rodríguez, J. M.; Mallet, P.; Moaied, M.; Palacios, J. J.; Salgado, C.; Ugeda, M. M.; Veuillen, J.-Y.; Yndurain, F.; Brihuega, I. Atomic-Scale Control of Graphene Magnetism by Using Hydrogen Atoms. *Science* **2016**, *352*, 437−441.

(2) Jørgensen, J. H.; Čabo, A. G. i.; Balog, R.; Kyhl, L.; Groves, M. N.; Cassidy, A. M.; Bruix, A.; Bianchi, M.; Dendzik, M.; Arman, M. A.; et al. Symmetry-Driven Band Gap Engineering in Hydrogen Functionalized Graphene. *ACS Nano* **2016**, *10*, 10798−10807.

(3) Balog, R.; Jorgensen, B.; Nilsson, L.; Andersen, M.; Rienks, E.; Bianchi, M.; Fanetti, M.; Laegsgaard, E.; Baraldi, A.; Lizzit, S.; Sljivancanin, Z.; Besenbacher, F.; Hammer, B.; Pedersen, T. G.; Hofmann, P.; Hornekaer, L. Bandgap Opening in Graphene Induced by Patterned Hydrogen Adsorption. *Nat. Mater.* **2010**, *9*, 315−319.

(4) Elias, D.; Nair, R.; Mohiuddin, T.; Morozov, S.; Blake, P.; Halsall, M.; Ferrari, A.; Boukhvalov, D.; Katsnelson, M.; Geim, A. Control of Graphene's Properties by Reversible Hydrogenation: Evidence for Graphane. *Science* **2009**, *323*, 610−613.

(5) Tozzini, V.; Pellegrini, V. Prospects for Hydrogen Storage in Graphene. *Phys. Chem. Chem. Phys.* **2013**, *15*, 80−89.

(6) Camiola, V. D.; Farchioni, R.; Cavallucci, T.; Rossi, A.; Pellegrini, V.; Tozzini, V. Hydrogen Storage in Rippled Graphene: Perspectives from Multi-Scale Simulations. *Front. Mater.* **2015**, *2*, 3.

(7) Trotochaud, L.; Head, A. R.; Karslıoğlu, O.; Kyhl, L.; Bluhm, H. Ambient Pressure Photoelectron Spectroscopy: Practical Considerations and Experimental Frontiers. *J. Phys.: Condens. Matter* **2017**, *29*, 053002.

(8) Hornekaer, L.; Sljivancanin, Z.; Xu, W.; Otero, R.; Rauls, E.; Stensgaard, I.; Laegsgaard, E.; Hammer, B.; Besenbacher, F. Metastable Structures and Recombination Pathways for Atomic Hydrogen on the Graphite (0001) Surface. *Phys. Rev. Lett.* **2006**, *96*, 156104.

(9) Balog, R.; Jørgensen, B.; Wells, J.; Lægsgaard, E.; Hofmann, P.; Besenbacher, F.; Hornekær, L. Atomic Hydrogen Adsorbate Structures on Graphene. *J. Am. Chem. Soc.* **2009**, *131*, 8744−8745.

(10) Kyhl, L.; Balog, R.; Angot, T.; Hornekaer, L.; Bisson, R. Hydrogenated Graphene on Ir (111): A High-Resolution Electron Energy Loss Spectroscopy Study of the Vibrational Spectrum. *Phys. Rev. B: Condens. Matter Mater. Phys.* **2016**, *93*, 115403.

(11) Balog, R.; Andersen, M.; Jorgensen, B.; Sljivancanin, Z.; Hammer, B.; Baraldi, A.; Larciprete, R.; Hofmann, P.; Hornekaer, L.; Lizzit, S. Controlling Hydrogenation of Graphene on Ir(111). *ACS Nano* **2013**, *7*, 3823−3832.

(12) Bocquet, F. C.; Bisson, R.; Themlin, J. M.; Layet, J. M.; Angot, T. Deuterium Adsorption on (and Desorption from) Sic(0001)-(3 × 3), (Root 3 X Root 3) R30 Degrees, (6 Root 3 × 6 Root 3) R30 Degrees and Quasi-Free-Standing Graphene Obtained by Hydrogen Intercalation. *J. Phys. D: Appl. Phys.* **2014**, *47*, 094014.

(13) Kim, H.; Balgar, T.; Hasselbrink, E. Is There Sp 3-Bound H on Epitaxial Graphene? Evidence for Adsorption on Both Sides of the Sheet. *Chem. Phys. Lett.* **2012**, *546*, 12−17.

(14) Kim, H.; Balgar, T.; Hasselbrink, E. The Stretching Vibration of Hydrogen Adsorbed on Epitaxial Graphene Studied by Sum-Frequency Generation Spectroscopy. *Chem. Phys. Lett.* **2011**, *508*, 1−5.

(15) Luo, Z.; Yu, T.; Kim, K.-j.; Ni, Z.; You, Y.; Lim, S.; Shen, Z.; Wang, S.; Lin, J. Thickness-Dependent Reversible Hydrogenation of Graphene Layers. *ACS Nano* **2009**, *3*, 1781−1788.

(16) Zhao, W.; Gebhardt, J.; Späth, F.; Gotterbarm, K.; Gleichweit, C.; Steinrück, H. P.; Görling, A.; Papp, C. Reversible Hydrogenation of Graphene on Ni (111)—Synthesis of "Graphone. *Chem. - Eur. J.* **2015**, *21*, 3347−3358.

(17) Coraux, J.; N'Diaye, A. T.; Engler, M.; Busse, C.; Wall, D.; Buckanie, N.; Heringdorf, F.; van Gastel, R.; Poelsema, B.; Michely, T. Growth of Graphene on Ir(111). *New J. Phys.* **2009**, *11*, 023006.

(18) N'Diaye, A. T.; Coraux, J.; Plasa, T. N.; Busse, C.; Michely, T. Structure of Epitaxial Graphene on Ir(111). *New J. Phys.* **2008**, *10*, 043033.

(19) Kim, B. H.; Hong, S. J.; Baek, S. J.; Jeong, H. Y.; Park, N.; Lee, M.; Lee, S. W.; Park, M.; Chu, S. W.; Shin, H. S.; Lim, J.; Lee, J. C.; Jun, Y.; Park, Y. W. N-Type Graphene Induced by Dissociative H_2 Adsorption at Room Temperature. *Sci. Rep.* **2012**, *2*, 690.

(20) Smith, D.; Howie, R. T.; Crowe, I. F.; Simionescu, C. L.; Muryn, C.; Vishnyakov, V.; Novoselov, K. S.; Kim, Y.-J.; Halsall, M. P.; Gregoryanz, E.; Proctor, J. E. Hydrogenation of Graphene by Reaction at High Pressure and High Temperature. *ACS Nano* **2015**, *9*, 8279−8283.

(21) Shin, D. S.; Kim, Y. B.; Kim, D. Y.; Choi, T. H.; Kim, B. H. Direct Measurement of the Amount of Dissociated Hydrogen Atoms Attached on Graphene. *Synth. Met.* **2015**, *200*, 80−84.

(22) Miura, Y.; Kasai, H.; Dino, W.; Nakanishi, H.; Sugimoto, T. First Principles Studies for the Dissociative Adsorption of H_2 on Graphene. *J. Appl. Phys.* **2003**, *93*, 3395−3400.

(23) McKay, H.; Wales, D. J.; Jenkins, S. J.; Verges, J. A.; deAndres, P. L. Hydrogen on Graphene under Stress: Molecular Dissociation and Gap Opening. *Phys. Rev. B: Condens. Matter Mater. Phys.* **2010**, *81*, 075425.

(24) Wang, N.; Wang, L.; Tan, Q.; Pan, Y.-X. Effects of Hydroxyl Group on H 2 Dissociation on Graphene: A Density Functional Theory Study. *J. Energy Chem.* **2013**, *22*, 493−497.

(25) Doi, K.; Onishi, I.; Kawano, S. Dissociative Adsorption of H_2 Molecules on Steric Graphene Surface: Ab Initio MD Study Based on DFT. *Comput. Theor. Chem.* **2012**, *994*, 54−64.

(26) Ao, Z.; Peeters, F. Electric Field Activated Hydrogen Dissociative Adsorption to Nitrogen-Doped Graphene. *J. Phys. Chem. C* **2010**, *114*, 14503−14509.

(27) Ao, Z.; Peeters, F. Electric Field: A Catalyst for Hydrogenation of Graphene. *Appl. Phys. Lett.* **2010**, *96*, 253106.

DOI: 10.1021/acsnano.7b07079
ACS Nano 2018, 12, 513−520

(28) Allouche, A.; Ferro, Y. Dissociative Adsorption of Small Molecules at Vacancies on the Graphite (0001). *Carbon* **2006**, *44*, 3320−3327.
(29) Diño, W. A.; Nakanishi, H.; Kasai, H.; Sugimoto, T.; Kondo, T. H_2 Dissociative Adsorption at the Zigzag Edges of Graphite. *e-J. Surf. Sci. Nanotechnol.* **2004**, *2*, 77−80.
(30) Divya, P.; Ramaprabhu, S. Hydrogen Storage in Platinum Decorated Hydrogen Exfoliated Graphene Sheets by Spillover Mechanism. *Phys. Chem. Chem. Phys.* **2014**, *16*, 26725−26729.
(31) Parambhath, V. B.; Nagar, R.; Sethupathi, K.; Ramaprabhu, S. Investigation of Spillover Mechanism in Palladium Decorated Hydrogen Exfoliated Functionalized Graphene. *J. Phys. Chem. C* **2011**, *115*, 15679−15685.
(32) Gao, Y.; Zhao, N.; Li, J.; Liu, E.; He, C.; Shi, C. Hydrogen Spillover Storage on Ca-Decorated Graphene. *Int. J. Hydrogen Energy* **2012**, *37*, 11835−11841.
(33) Blanco-Rey, M.; Juaristi, J. I. a.; Alducin, M.; Lopez, M. J.; Alonso, J. A. Is Spillover Relevant for Hydrogen Adsorption and Storage in Porous Carbons Doped with Palladium Nanoparticles? *J. Phys. Chem. C* **2016**, *120*, 17357−17364.
(34) Tozzini, V.; Pellegrini, V. Reversible Hydrogen Storage by Controlled Buckling of Graphene Layers. *J. Phys. Chem. C* **2011**, *115*, 25523−25528.
(35) Goler, S.; Coletti, C.; Tozzini, V.; Piazza, V.; Mashoff, T.; Beltram, F.; Pellegrini, V.; Heun, S. Influence of Graphene Curvature on Hydrogen Adsorption: Toward Hydrogen Storage Devices. *J. Phys. Chem. C* **2013**, *117*, 11506−11513.
(36) Hall, R. I.; Cadez, I.; Landau, M.; Pichou, F.; Schermann, C. Vibrational Excitation of Hydrogen *via* Recombinative Desorption of Atomic Hydrogen Gas on a Metal Surface. *Phys. Rev. Lett.* **1988**, *60*, 337.
(37) Eenshuistra, P. J.; Bonnie, J. H. M.; Los, J.; Hopman, H. J. Observation of Exceptionally High Vibrational Excitation of Hydrogen Molecules Formed by Wall Recombination. *Phys. Rev. Lett.* **1988**, *60*, 341.
(38) N'Diaye, A. T.; Gerber, T.; Busse, C.; Mysliveček, J.; Coraux, J.; Michely, T. A Versatile Fabrication Method for Cluster Superlattices. *New J. Phys.* **2009**, *11*, 103045.
(39) Tschersich, K. Intensity of a Source of Atomic Hydrogen Based on a Hot Capillary. *J. Appl. Phys.* **2000**, *87*, 2565−2573.
(40) Gross, A. *Theoretical Surface Science*. Springer-Verlag: Berlin, Germany, 2014; Vol. *1*.
(41) Chelkowski, S.; Bandrauk, A. Raman Chirped Adiabatic Passage: A New Method for Selective Excitation of High Vibrational States. *J. Raman Spectrosc.* **1997**, *28*, 459−466.
(42) Laegsgaard, E.; Besenbacher, F.; Mortensen, K.; Stensgaard, I. A Fully Automated, Thimble-Size Scanning Tunnelling Microscope. *J. Microsc. (Oxford, U. K.)* **1988**, *152*, 663−669.
(43) Knudsen, J.; Andersen, J. N.; Schnadt, J. A Versatile Instrument for Ambient Pressure X-Ray Photoelectron Spectroscopy: The Lund Cell Approach. *Surf. Sci.* **2016**, *646*, 160−169.
(44) Schnadt, J.; Knudsen, J.; Andersen, J. N.; Siegbahn, H.; Pietzsch, A.; Hennies, F.; Johansson, N.; MÅrtensson, N.; Öhrwall, G.; Bahr, S.; et al. The New Ambient-Pressure X-Ray Photoelectron Spectroscopy Instrument at Max-Lab. *J. Synchrotron Radiat.* **2012**, *19*, 701−704.
(45) Urpelainen, S.; SÅthe, C.; Grizolli, W.; AgÅker, M.; Head, A. R.; Andersson, M.; Huang, S.-W.; Jensen, B. N.; Wallén, E.; Tarawneh, H.; et al. The Species Beamline at the Max Iv Laboratory: A Facility for Soft X-Ray Rixs and Apxps. *J. Synchrotron Radiat.* **2017**, *24*, 344−353.
(46) Mortensen, J. J.; Hansen, L. B.; Jacobsen, K. W. Real-Space Grid Implementation of the Projector Augmented Wave Method. *Phys. Rev. B: Condens. Matter Mater. Phys.* **2005**, *71*, 035109.
(47) Enkovaara, J.; Rostgaard, C.; Mortensen, J. J.; Chen, J.; Dułak, M.; Ferrighi, L.; Gavnholt, J.; Glinsvad, C.; Haikola, V.; Hansen, H.; et al. Electronic Structure Calculations with Gpaw: A Real-Space Implementation of the Projector Augmented-Wave Method. *J. Phys.: Condens. Matter* **2010**, *22*, 253202.
(48) Larsen, A.; Mortensen, J.; Blomqvist, J.; Castelli, I.; Christensen, R.; Dulak, M.; Friis, J.; Groves, M.; Hammer, B.; Hargus, C.; et al. The Atomic Simulation Environment—a Python Library for Working with Atoms. *J. Phys.: Condens. Matter* **2017**, *29*, 273002.
(49) Klimeš, J.; Bowler, D. R.; Michaelides, A. A Critical Assessment of Theoretical Methods for Finding Reaction Pathways and Transition States of Surface Processes. *J. Phys.: Condens. Matter* **2010**, *22*, 074203.
(50) Dion, M.; Rydberg, H.; Schröder, E.; Langreth, D. C.; Lundqvist, B. I. Van Der Waals Density Functional for General Geometries. *Phys. Rev. Lett.* **2004**, *92*, 246401.
(51) Becke, A. D. Density-Functional Exchange-Energy Approximation with Correct Asymptotic Behavior. *Phys. Rev. A: At., Mol., Opt. Phys.* **1988**, *38*, 3098.
(52) Jurečka, P.; Šponer, J.; Černý, J.; Hobza, P. Benchmark Database of Accurate (Mp2 and Ccsd (T) Complete Basis Set Limit) Interaction Energies of Small Model Complexes, DNA Base Pairs, and Amino Acid Pairs. *Phys. Chem. Chem. Phys.* **2006**, *8*, 1985−1993.
(53) Kolsbjerg, E. L.; Groves, M. N.; Hammer, B. An Automated Nudged Elastic Band Method. *J. Chem. Phys.* **2016**, *145*, 094107.

DOI: 10.1021/acsnano.7b07079
ACS Nano 2018, 12, 513−520

Paper V

THE JOURNAL OF CHEMICAL PHYSICS **148**, 124703 (2018)

Rotation and diffusion of naphthalene on Pt(111)

E. L. Kolsbjerg,[1] G. Goubert,[2] P. H. McBreen,[3] and B. Hammer[1,a)]
[1]*Interdisciplinary Nanoscience Center (iNANO), Department of Physics and Astronomy, Aarhus University, Aarhus, Denmark*
[2]*Department of Chemistry and Applied Biosciences, ETH Zurich, 8093 Zurich, Switzerland*
[3]*Department of Chemistry, Laval University, Quebec, Quebec G1V 0A6, Canada*

(Received 28 November 2017; accepted 23 January 2018; published online 23 March 2018)

The behavior of naphthalene on Pt(111) surfaces is studied by combining insight from scanning tunneling microscopy (STM) and van der Waals enabled density functional theory. Adsorption, diffusion, and rotation are investigated by a series of variable temperature STM experiments revealing naphthalene ability to rotate on-site with ease with a rotational barrier of 0.69 eV. Diffusion to neighbouring sites is found to be more difficult. The experimental results are in good agreement with the theoretical investigations which confirm that the barrier for diffusion is slightly higher than the one for rotation. The theoretical barriers for rotation and translation are found to be 0.75 and 0.78 eV, respectively. An automatic mapping of the possible diffusion pathways reveals very detailed diffusion paths with many small local minima that would have been practically impossible to find manually. This automated procedure provides detailed insight into the preferred diffusion pathways that are important for our understanding of molecule–substrate interactions. *Published by AIP Publishing.*
https://doi.org/10.1063/1.5017581

I. INTRODUCTION

Heterogeneous catalysis using metal catalysts is a cornerstone in the development of tomorrow's fine chemicals as an ever increasing demand for green and energy efficient chemical processes proceeds. A recurring motive in many of these interesting organic compounds is an aromatic carbon ring. Molecule-metal interactions are critically important for our understanding of catalytic processes, and benzene on Pt(111) has developed into a prototypical system for the study of chemisorbed organic molecules on catalysts. Our understanding of aromatic interactions with transition metal surfaces is steadily improving with models of this benchmark case.[1–7] Advancing from benzene, an obvious next step toward more complex yet abundant organic molecules would be naphthalene.[8,9] With more carbon atoms and a lower symmetry, naphthalene presents more varied interactions with the surface, allowing us to probe more complex processes on the way to larger and more complex systems. Much theoretical and experimental effort has already been devoted to understanding the heat of adsorption[6,10–12] and the packing structure[13–19] of naphthalene on Pt(111) but key aspects like site to site diffusion are still lacking. We present a combined scanning tunneling microscopy (STM) and density functional theory (DFT) study of single naphthalene molecules on Pt(111) and show that they experience both on-site rotation and translation to neighbouring sites. The same area can be repeatedly scanned to acquire a time-lapsed series of STM images, allowing one to construct the so-called STM videos. From the comparison of successive images, dynamic processes such as the diffusion of molecules can be followed. The time resolution of the microscope is on the scale of tens of seconds to minutes, which is too slow for many processes. However, under ultra high vacuum (UHV) conditions, the temperatures can be widely varied to slow down surface processes and find a window where the scanning speed of the STM is appropriate for the particular system under study. Assuming Arrhenius behavior, it is possible to estimate energy barriers, the most important parameter when studying kinetic processes on surfaces, from temperature dependent rate measurements.

From a theoretical point of view, studying any likely diffusion, rotation, or reaction paths in a multi-dimensional coordinate space can be formulated as finding the paths with the lowest energy transition barrier from one atomic configuration to another. Mapping the whole ~3N atomistic space is completely impossible for systems of even moderate size.[20–22] Reasonable limits or approximations must be applied so that results can be obtained—e.g., movement constraints on the considered reaction participants. Approximations need to be justified from an experimental or a theoretical point of view and still allow for a systematic examination of the problem to improve the precision of the simulation. Rational reduction of complexity has been successfully achieved when studying diffusion of smaller symmetric and asymmetric aromatic molecules on transition metal surfaces for benzene,[23] pyridine,[24] and 2,2,2-trifluoroacetophenone[25] on a Pt(111) surface as well as for chemical reactions, for instance, for CO oxidation over nanoporous gold[26] and for acetylene selective hydrogenation on Pd-doped Cu(111).[27] The complexity of the problem grows with the size of the molecules and more severe constraints must be put in place above a certain molecule size. More sophisticated strategies to minimize the required number of full *ab initio* evaluations include the use of scaling relations with machine learning algorithms to

a)Electronic mail: hammer@phys.au.dk.

estimate the energy barriers in complex reaction networks. The speedup is achieved by only evaluating potential relevant barriers based on predictions from a cheaper computational method with DFT.[28] The gradual increase of the level of theory has also been successfully employed in related topics such as a cascade genetic algorithm approach, where each successful step allows for an increasingly accurate level of theory starting from a simple reactive force-field.[29] Recent advances in the field of machine learning have also made it possible to locate reaction barriers with iteratively trained ML potentials reducing the time spent on expensive *ab initio* calculations.[30,31]

The paper is organized as follows: Sec. II covers the STM and DFT setup together with a description of how the reaction network is modeled. This is followed by the STM experimental results and the analysis of the observed rotation events. We then compare the experimental findings with adsorption, rotation, and diffusion barriers calculated within DFT. The calculations are made possible by setting up a systematic and detailed reaction network formed from hierarchical improvements of the theoretical approach. Finally, we compare our findings with other estimations of barriers and Arrhenius prefactors in the literature.

II. METHOD

A. Experimental setup

Naphthalene (Sigma-Aldrich) was introduced into the UHV chamber (base pressure 2×10^{-10} Torr) using a gate valve, without purification. It was left to evaporate onto the Pt(111) single crystal without heating. The surface was imaged using a SPECS Aarhus 150 STM at various temperatures. The temperature was held constant during each acquisition. The tunneling current was held at a constant value during imaging, between 170 pA and 280 pA depending on the experiment. The bias voltage between the tip and the sample was between 1.16 V and 1.25 V in all acquisitions, resulting in a tunneling junction resistance of about 6 GΩ. At each temperature, sequences of images were acquired at a rate between 15 and 47 s per 512×512 pixel image. The position and orientation of each naphthalene molecule in a sequence of images were measured to determine its movement on the surface. The Pt(111) crystal was cleaned by cycles of argon (10^{-5} Torr) sputtering at 600 K, flash annealing at 1000 K, annealing under an oxygen atmosphere (10^{-7} Torr) at 900 K, and flash annealing at 1000 K.

B. Computational setup

DFT as implemented in the GPAW[32] code with the atomic simulation environment (ASE)[33] interface was used for the present calculations. The GPAW software uses the projector augmented wave method on a real grid space.[34,35] All published calculations are done with a grid spacing of less than 0.175 Å. If not stated otherwise, the molecules are adsorbed on a $c(12 \times 6)$ slab represented by a 6×6 rectangular Pt(111) surface. The resulting slab consists of 36 Pt atoms in each of the four layers using the optimized lattice constants for the optB88-vdW[36] functional, $a = 4.02$ Å. (The experimental value is $a = 3.92$ Å.) A 2×2 **k**-point mesh was used throughout the calculation to sample the Brillouin zone. Geometric optimizations were terminated when no force exerted on any atom exceeded 0.025 eV/Å. The calculations were performed in a 2d periodic cell with at least 6 Å of vacuum between the atoms and the cell boundary perpendicular to the slab.

The automated climbing-image elastic band (CI-EB) method[37] and the AutoNEB algorithm utilizing the EB method were extensively used to locate all pathways with the highest energy (climbing) image as the corresponding transition state (TS). Only the TS and the images in the immediate vicinity were fully converged with the previously described geometric optimizations (0.025 eV/Å), as is the nature of the AutoNEB method.

C. Reaction network construction

To locate the lowest energy path for the diffusion of naphthalene, we employ a systematic strategy to attack the problem of mapping the diffusion network. The procedure follows a three-step approach: (1) scan the surface for local minima, (2) build a reaction network, and (3) calculate the reaction barriers. While it would be very resource intensive to perform the searching, scanning, and analysis with the final calculational setup, all the pre-steps before the final calculation have been done at cost efficient levels.

The first step involves screening the surface for any local minima. This has been done by moving a naphthalene molecule on a predefined grid on top of the surface. The grid chosen for this specific case is 2 Å × 2 Å × 6° and the details and choice of the coordinate system can be seen in Fig. 1 together with examples of contour plots of the energy landscape at fixed rotation angles with accompanying minima. In Fig. 1(a), the two center atoms have been marked and at each grid point, the x and y coordinates of the center of mass (COM) for these two atoms have been constrained while relaxing the

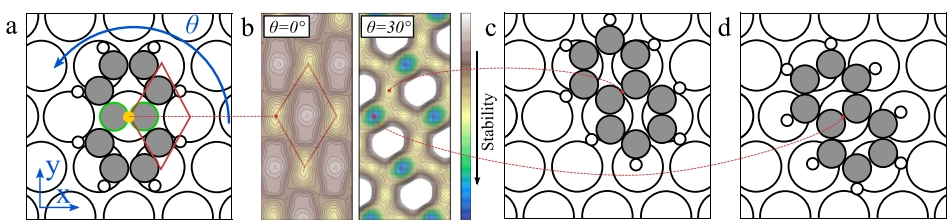

FIG. 1. (a) shows the chosen coordinate system for the grid that the adsorption potential energy of naphthalene has been mapped onto, while (b) shows contour plots of the energy landscape for fixed angles of $\theta = 0°$ and $\theta = 30°$. (c) and (d) show examples of two minima that exist in the $\theta = 30°$ energy landscape.

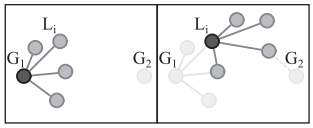

FIG. 2. Schematic of how the reaction network is created. To the left, the first initial images have been connected to the four nearest minima, and for one of the four, it is shown how it connects to the next four images in the right frame.

structure with the Perdew–Burke–Ernzerhof (PBE) functional on a 4 × 4 × 2 slab. Subsequently all the potential local minima were found by relaxing without constraints (to remove any false minima) and then the structures were moved to the 6 × 6 cell and reoptimized with the optB88-vdW functional.

Next the networks were created by connecting two global minima to complete a potential diffusion pathway. The start for each path begins at the global minimum and then proceeds to move toward the next global minimum in a neighboring unit cell. For a minimum, $\mathbf{R}_{L_i}$, to be considered a possible stop on the path, its COM, $\overline{\mathbf{R}}_{L_i}$, has to be located in between the first, $\overline{\mathbf{R}}_{G_1}$, and second, $\overline{\mathbf{R}}_{G_2}$, global minima COM, hence, fulfilling $||\overline{\mathbf{R}}_{G_2}-\overline{\mathbf{R}}_{G_1}|| > ||\overline{\mathbf{R}}_{G_2}-\overline{\mathbf{R}}_{L_i}||$. The distance between two given minima, $\mathbf{R}_{L_a}$ and $\mathbf{R}_{L_b}$, is defined as the normalized length between the same index atoms ($||\mathbf{R}_{L_b}-\mathbf{R}_{L_a}||$). The minima have then been connected by a simple recipe: initializing from the global minimum, the network moves toward the end global minimum as a spider web connecting up to the four nearest minima and the process keeps propagating until the network reaches the end.

A schematic of the initial connections is shown in Fig. 2, where the first minima are connected with the four nearest on the left side and one of the four images has been connected to the next four images on the right side.

Each of these pathways has been evaluated with the CI-EB adopting the image dependent pair potential (IDPP)[38] procedure for the initial guesses for the paths with the PBE functional on a 4 × 4 × 2 slab. The TSs within a window of 0.1 eV of the immediate lowest energy path have been tested for alternative routes by mixing in other local minima in the initial guesses following the same procedure as used for 2,2,2-trifluoroacetophenone[25] and pyridine[37] diffusion on Pt(111). In this case, the two nearest minima have been mixed in with $\beta = 0.25$. All paths in the same 0.1 eV window and their barriers have been reoptimized in a large 6 × 6 super cell with the optB88-vdW functional as stated above.

III. DISCUSSION

A. Imaging naphthalene rotation

Naphthalene was evaporated on Pt(111) and a coverage between 0.01 and 0.14 molecules/nm^2 was achieved. All but two series of images were acquired at a naphthalene coverage below 0.04 molecules/nm^2, a typical example is shown in Fig. 3. Omitting the two higher coverage measurements from the study does not change the resulting activation barrier value; significantly, hence, all the measurements were retained for the Arrhenius analysis.

Sequences of STM images were acquired at temperatures between 263 and 301 K. The comparison of the position and orientation of each naphthalene molecule from frame to frame in the sequence of images demonstrates the presence of translational and rotational movement. An example of a series of STM images used to resolve the kinetics is shown in Fig. 3. In the bottom panel of images, naphthalene molecules are seen rotating over a total span of ∼1 min. In each series of images, the position and orientation of each naphthalene were followed. The distribution of wait times between diffusion events (rotation or translation) was determined. Under the assumption that the rotation process is well described by a Poisson distribution, the distribution of wait times follows an exponential law. Fitting this exponential time decay provides an estimation of the rate constant. This process is shown for a room temperature measurement in Fig. 4(a). By repeating this measurement at various temperatures, we perform an Arrhenius analysis as shown in Fig. 4(b) and extract an estimation of the activation barrier. The rotation barrier found from the STM experiments was based on the assumption that jumps only happened between nearest neighbor sites of the global minimum, i.e., they represent a simple 60° rotation. One should be aware

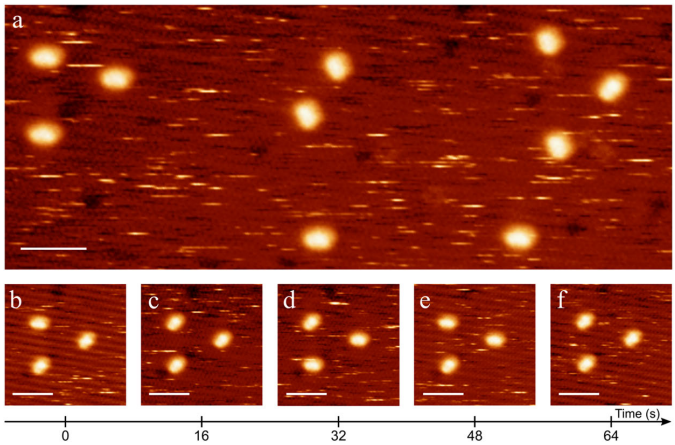

FIG. 3. The top panel (a) shows a STM image of a larger area (20 nm × 8 nm) while (b)–(f) show a zoom in on the top left three naphthalenes as monitored over roughly 1 min (16 s between each image). Scale bars represent 2 nm in all images.

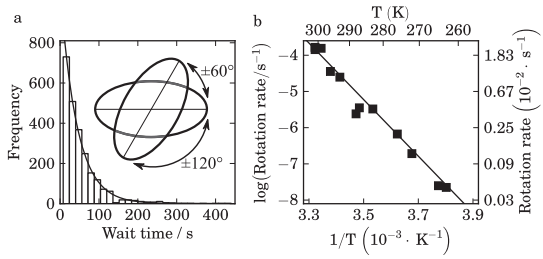

FIG. 4. (a) The distribution of wait times for the on-site rotation of naphthalene on Pt(111) for a series of STM images taken at room temperature. The solid line is the best single exponential fit. We call an event on-site rotation where the center of the naphthalene molecule does not move but the orientation of the molecule changes by ±60°, as shown in the inset. For each measurement, the intervals between consecutive rotations were measured and their distribution fitted to an exponential function revealing rate constants. (b) The Arrhenius analysis of the measured rate constant for on-site naphthalene rotation at temperatures between 263 and 301 K. Determination of the activation barrier is highly dependent on the prefactor, the best fit is shown on a semi-log scale in the plot as the full line.

that this simple analysis can overestimate the energy barrier since it, for instance, neglects any combination of rotations that would leave the molecule at the same place or any combination of rotations, whose total angle is 0/180°. Due to the high symmetry of naphthalene, it is also not possible to differentiate between a rotation of ±60° and a rotation of ∓120°. We use mild tunneling condition (6 GΩ junction resistance) but we cannot completely rule out an increase of the diffusion rate caused by tip-molecule interactions. It should materialize as a large number of hopping/rotation observations while the tip is hovering over the molecule, meaning that naphthalene moves while it is imaged by the STM. However, these are rare cases and the vast majority of hopping/rotation events happen while the tip is not hovering over the moving molecule. We believe that this indicates that the effect of the tip on the diffusion rate is small in our case. The best estimation for the activation barrier is found to be 0.67 ± 0.07 eV and the best estimation for the prefactor is found to be $4 \cdot 10^9$ s^{-1}, as shown in Fig. 4(b). It is noteworthy that the prefactor is difficult to estimate based on an Arrhenius analysis. Given the linear dependence of the rate on the prefactor, it has a much smaller impact than the activation energy. Even though the prefactor seems low, it fits well in the range of prefactors (from 10^6 to 10^{12} s^{-1}) for similar rotational systems.[39–42]

One can get a feeling for the sensitivity of the measured energy barrier to the prefactor by varying it in the range from 10^9 to 10^{12} s^{-1}. Doing so, we find that the activation barrier varies from 0.64 to 0.82 eV, which thus gives a rough estimate of the uncertainty.

Translations were found to be rare and it was not possible to accumulate enough events to evaluate the associated activation barrier or attempt frequency. This indicates that the barrier for translation is higher than the barrier for rotation and/or the attempt frequency is much lower.

B. Adsorption

As described in Sec. II, a thorough scan for adsorption configurations has been carried out resulting in the identification of a large number of stable adsorption configurations which are shown in Fig. 5. Analyzing the different adsorption configurations reveals that maximizing the footprint is desirable as the global minimum is the only one in which the naphthalene carbon atoms truly bind to seven surface atoms (highlighted by the gray Pt atoms). The remaining minima are all relatively stable and many are of almost equal stability (the ten most stable are within ∼1 eV). For the eight mainly flat configurations, the average adsorption height (Pt–C distance) of each configuration lies in the range of 2.08–2.25 Å. Two stable buckled configurations are also present with the most stable configuration having half the molecule bending 22.2° away from the surface.

A previous study[10] of the preferred adsorption of naphthalene on Pt(111) found the same preferred configuration, Fig. 5(a), but the use of a smaller unit cell (hence increased coverage) and the use of a different exchange-correlation functional (PW 91) make the adsorption energies non-transferable as the adsorption potential energy (APE) of the global minimum for Morin *et al.*'s study is –1.37 eV while the present work results in –2.81 eV. A more recent study with an almost identical unit cell as in the current work but utilizing the PBE

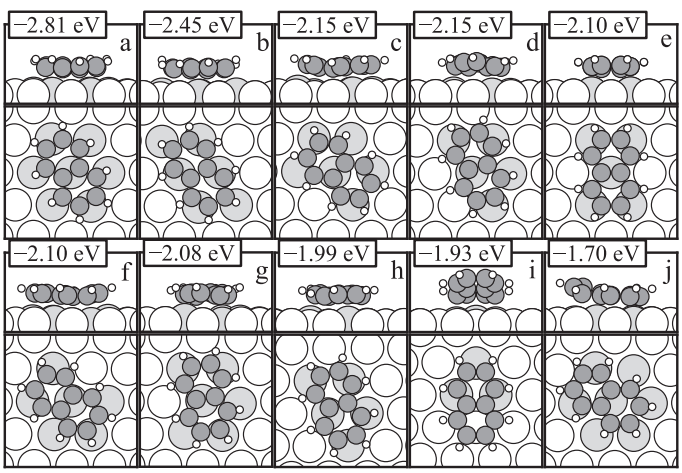

FIG. 5. The ten most stable adsorption geometries found for naphthalene on the Pt(111) surface. Light gray atoms represent the footprint onto the Pt atoms from the respective configurations (defined as within 2.5 Å of any carbon atom).

functional [which does not include any explicit van der Waals (vdW)] also underestimates the APE (−1.31 eV) compared to the present work.[12]

The following relation for the heat of adsorption for naphthalene, $(300 - 34\theta - 199\theta)$kJ/mol, which has been deduced for a defect free Pt(111) surface from adsorption calorimetry experiments, also support a stronger binding energy.[11] The current calculations performed in a 6×6 unit cell correspond to a ∼1/3 monolayer (θ) adopting Gottfried *et al.*'s definition ($\theta = 1.557 \cdot 10^{14}$ molecules/cm^2). Plugging that into the formula results in a heat of adsorption of −2.82 eV, which is in excellent agreement with our DFT calculations. This further strengthens the credibility of optB88-vdW functional as the benchmark functional when describing aromatic molecules on transition metal surfaces as it outperforms other vdW functionals tested on the same system.[6] However, other more general vdW functionals like the recent vdW-DF-cx seem to also describe aromatic carbon metal surfaces well.[43]

C. Diffusion

Following the strategy described in Sec. II, the reaction network for naphthalene diffusion is constructed and presented in Fig. 6. The network shows a large multiple of small steps between the two end points.

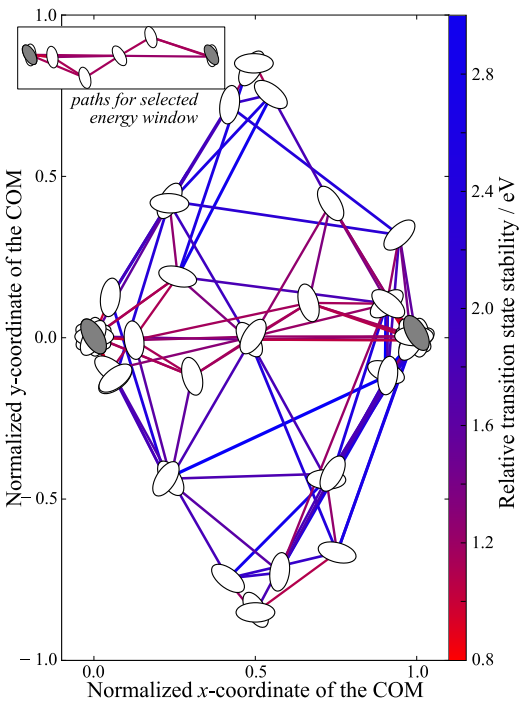

FIG. 6. The connected minima that make up the total network of tested pathways. The ovals' position and orientation serve to indicate the location of the COM and the molecular orientation of the naphthalene minimum they represent. The start and the end minima are colored dark gray. The minima that have their connections explored have a linking colored line. The color represents the relative stability of the TS for the transition. The inset in the top left shows the paths within the 0.1 eV window of the lowest path that is presented in Fig. 7.

The pathways with the lowest energy TS within a window of 0.1 eV of the immediate lowest energy path were reevaluated as described in Sec. II and their respective barriers are shown on the left side of Fig. 7. The same paths are shown in the inset of Fig. 6 and in the middle panel of Fig. 7 revealing the relevant relatively confined geometric area. From the different paths explored, the critical TS energy for naphthalene translation is found to be 0.78 eV. Analyzing the paths, it is evident that three of them are very competitive and with the current precision of the DFT calculations, we are not able to distinguish which one is the lowest energy path. What is evident is that all reasonable pathways involve a local minimum that lies in the middle of the path, which is shown in the 3rd image in the upper panel of Fig. 7. We recognize this configuration as the second most stable configuration, Fig. 5(b). Taking a closer look at the critical TS, most of them are very diverse in the precise geometries, highlighting the complexity of the system.

As visible from the simple curvature of the yellow path, it is the least complex of the four but clearly also the least favored. This path is directly the result of a linear interpolation between the two global minima. This exactly highlights the need to explore more than one initial guess as the yellow path exactly would be the most obvious initial human guess for a diffusion path. Without the current comprehensive search the estimated barrier would be 0.07 eV higher than the present best estimate, but more importantly we would gain erroneous insight into the mechanism which could impede further understanding of how aromatic molecules interact with surfaces.

Interestingly there is a relevant discrepancy between the first and second half of the pathway because of the ABC stacking nature of the Pt FCC-111 layers. It is evident that diffusion over the first half requires less energy than over the second half. The importance of the "hinging" of C–C double bonds on top of a Pt atoms under diffusion, as seen for the diffusion of other aromatic molecules,[23–25] is also noticeable for naphthalene on Pt(111). The same trend can most easily be seen in a video of the lowest energy path which is accessible online in the supplementary material. It is evident that while diffusing, naphthalene proceeds to maximize the surface interaction by keeping intact as many bonds to the surface as possible. It proceeds by naphthalene pushing the surface atoms as it slides and rotates across the surface while at least one C–C double bond interacts with a single Pt atom at any time.

The barrier for naphthalene on-site rotation when positioned in the global minimum can also be extracted from the right side of Fig. 7. Because of the six-fold symmetry of the system, naphthalene only needs to rotate 30° to map the entire unique path for rotation—a transition from configuration (a) to configuration (e), cf. Fig. 5. The relevant TS for rotation also lies on the first part of the red path in Fig. 7 and with a barrier of 0.75 eV it is slightly easier than a complete diffusion step. The barrier can be compared directly to the experimentally determined value of 0.67 ± 0.07 eV found in the STM experiments reported above. Given the uncertainties both from the experimental and theoretical sides, the barriers found for the rotation are in good agreement. If we consider

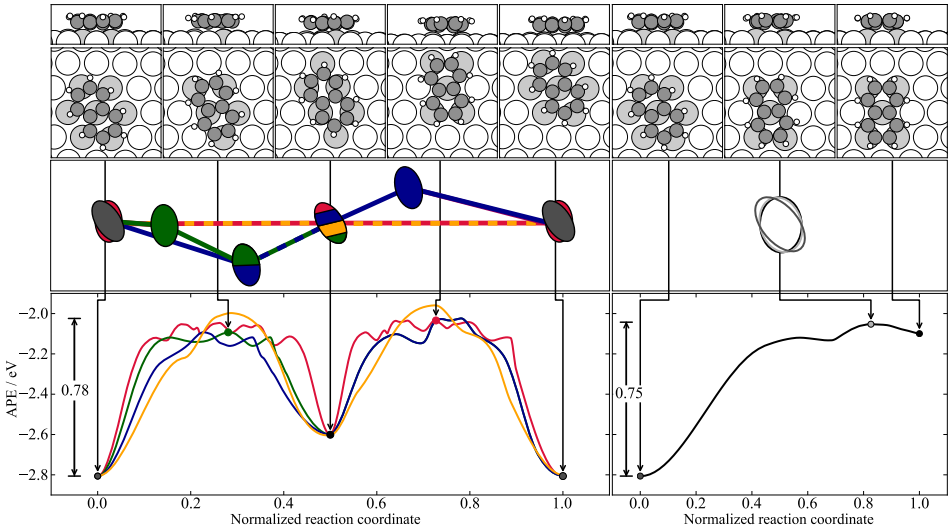

FIG. 7. (Left) Color coded pathways that are transferred from the preliminary scan. Above the paths are the same colored paths between the major minima. (Right) The first 30° of the rotation path is shown. (Top) Panel shows the major TS geometries for the green, red, and black rotation paths as well as start, middle, and endpoint of all of the paths, respectively.

a reasonable range of prefactor to fit the experimental data, we find that the theoretical value is toward the middle of the possible range of activation barriers derived from the STM experiment.

In agreement with the experiment, the barrier for translation is higher than the barrier for rotation, although the difference in the barriers is not tremendous for rotation versus translation. A successful "jump" is dependent on the exponential of the barrier height (and the temperature) and hence very sensitive to the exact energy. With the current energy difference at a temperature of 275 K (assuming the same jump frequency), it would correspond to more than three times as many rotation as translation events. A very different jump frequency could actual be the key to why we do not see many diffusion events as the translation mechanism is significantly more complicated and hence more vibrational inaccessible.

Campbell and Sellers have recently, within the harmonic transition state theory (HTST), discussed how to calculate prefactors for surface reactions.[44] From a comprehensive analysis of an extensive data set of experimental entropies for desorption they concluded, among other things, how the reaction rate can be calculated with, e.g., DFT. Using the HTST, the rate for diffusion can be written as

$$k_{\text{diff}} = \nu_{\text{diff}} \exp\left(\frac{-\Delta E^0_{TS}}{k_B T}\right) \tag{1}$$

with

$$\nu_{\text{diff}} = \frac{k_B T}{h} \exp\left(\frac{S^0_{TS,diff} - S^0_{ad}}{R}\right), \tag{2}$$

where both entropies are evaluated about the zero point energy at the relevant temperature and calculated as the sum over all N vibrational modes as

$$S = R \sum_i^N \left\{ \frac{\frac{h\nu_i}{k_B T}}{\exp\left(\frac{h\nu_i}{k_B T}\right) - 1} - \ln\left[1 - \exp\left(\frac{h\nu_i}{k_B T}\right)\right] \right\}. \tag{3}$$

The vibrational frequencies used are calculated for the adsorption and the TS configurations within the harmonic approximation using a finite difference approximation of the dynamical matrix.[45]

Applying Eqs. (2) and (3), we have calculated the pre-exponential factor for rotations to be $1.04 \cdot 10^{13}$ s^{-1}, which is orders of magnitude larger than the experimental value. However, this is not surprising as the HTST theory is dominated by the $k_B T/h$ front factor and only extremely large entropy changes between the adsorbed state and TS can make significant changes to the attempt frequency. At 280 K, ΔS is calculated to be 4.84 J/(mol K) and an entropy change of $\Delta S \approx -60$ J/(mol K) is needed to bring the attempt frequency down to the experimental value of $4 \cdot 10^9$ s^{-1}. Moreover, the $k_B T/h$ front factor in HTST is derived for the system of N vibrational degrees of freedom, where any rotational mode is totally neglected—modes which of course are very important for TSs within a rotational motion. This means that the HTST does not describe the current problem very accurately as would be seen from attempting to fit the data in Fig. 4(b) with an attempt frequency of 10^{13} s^{-1}. A more sophisticated theoretical approach has been conducted by Shea and Kreuzer[46] who described diffusion of a large organic molecule by a stochastic model based on DFT calculations. The model that is derived from the Langevin equation leads to a prefactor that is smaller by approximately an order of magnitude compared to the HTST equivalent. The change predominately results from frictional dampening and the anharmonic nature at bottom of the potential surface well. The new theoretical prefactor

is still two orders of magnitude too large when compared to the experimental results, but nevertheless a step in the right direction.[46] We anticipate that the use of such more advanced methods would have a similar effect of reducing the theoretical diffusional prefactor for the system considered in this work, naphthalene on Pt.

IV. CONCLUSION

Detailed STM experiments and theoretical analysis show how naphthalene adsorbs predominantly flat at a relatively low coverage on the surface of Pt(111) and is able to both diffuse and rotate around itself while still maintaining a strong surface interaction—the TS still has an adsorption potential energy of ~2 eV. The barrier for rotation is experimentally found to be 0.67 ± 0.07 eV, which is in good agreement with the theoretically found rotation barrier of 0.75 eV. Likewise, both experiments and theory predict that diffusion of naphthalene requires more energy than rotation. The exhaustive examinations of naphthalene adsorbed on Pt(111) revealed that a range of possible naphthalene configurations exist on the Pt(111) surface with high symmetry configurations that maximize the footprint as the most favored. The high number of configurations leads to a detailed diffusion network with many small pathway pieces which must be explored to reveal a realistic path. The network showcased that more than one diffusion route is competitive with a common stable midpoint and the easiest route has a barrier of around 0.78 eV. Examining the details of the sub-paths reveals that, similar to other aromatic molecules, naphthalene "walks" across the surface with one or more anchored C–C double bonds positioned on top of a Pt atom.

SUPPLEMENTARY MATERIAL

See supplementary material for a video of the lowest energy diffusion path found for naphthalene moving across a Pt(111) surface.

ACKNOWLEDGMENTS

Grants from VILLUM FONDEN (Investigator grant, Project No. 16562) and the Danish Research Council (No. 0602-02566B) have supported this research.

[1] C. Morin, D. Simon, and P. Sautet, Surf. Sci. **600**, 1339 (2006).
[2] W. Liu, J. Carrasco, B. Santra, A. Michaelides, M. Scheffler, and A. Tkatchenko, Phys. Rev. B **86**, 245405 (2012).
[3] W. Liu, V. G. Ruiz, G.-X. Zhang, X. Ren, M. Scheffler, B. Santra, and A. Tkatchenko, New J. Phys. **15**, 53046 (2013).
[4] W. Liu, A. Tkatchenko, and M. Scheffler, Acc. Chem. Res. **47**, 3369 (2014).
[5] J. Wellendorff, T. L. Silbaugh, D. Garcia-Pintos, J. K. Nørskov, T. Bligaard, F. Studt, and C. T. Campbell, Surf. Sci. **640**, 36 (2015).
[6] S. Gautier, S. N. Steinmann, C. Michel, P. Fleurat-Lessard, and P. Sautet, Phys. Chem. Chem. Phys. **17**, 28921 (2015).
[7] P. K. Ayishabi, K. G. Lakshmikanth, and R. Chatanathodi, Chem. Phys. Lett. **637**, 182 (2015).
[8] R. Forker, J. Peuker, M. Meissner, F. Sojka, T. Ueba, T. Yamada, H. S. Kato, T. Munakata, and T. Fritz, Langmuir **30**, 14163 (2014).
[9] M. G. Yazdi, P. H. Moud, K. Marks, W. Piskorz, H. Öström, T. Hansson, A. Kotarba, K. Engvall, and M. Göthelid, J. Phys. Chem. C **121**, 22199 (2017).
[10] C. Morin, D. Simon, and P. Sautet, J. Phys. Chem. B **108**, 12084 (2004).
[11] J. M. Gottfried, E. K. Vestergaard, P. Bera, and C. T. Campbell, J. Phys. Chem. B **110**, 17539 (2006).
[12] G. Santarossa, M. Iannuzzi, A. Vargas, and A. Baiker, ChemPhysChem **9**, 401 (2008).
[13] J. L. Gland and G. A. Somorjai, Surf. Sci. **38**, 157 (1973).
[14] D. Dahlgren and J. C. Hemminger, Surf. Sci. **109**, L513 (1981).
[15] D. Dahlgren and J. C. Hemminger, Surf. Sci. **114**, 459 (1982).
[16] A. Gavezzotti and M. Simonetta, Surf. Sci. Lett. **116**, L207 (1982).
[17] D. Dahlgren and J. C. Hemminger, Surf. Sci. **134**, 836 (1983).
[18] V. M. Hallmark, S. Chiang, and Ch. Wöll. J. Vac. Sci. Technol., B: Microelectron. Nanometer Struct. **9**, 1111 (1991).
[19] V. M. Hallmark, S. Chiang, J. K. Brown, and Ch. Wöll. Phys. Rev. Lett. **66**, 48 (1991).
[20] F. H. Stillinger and T. A. Weber, Science **225**, 983 (1984).
[21] S. S. E. H. Elnashaie and S. S. Elshishini, *Modelling, Simulation and Optimization of Industrial Fixed Bed Catalytic Reactors* (CRC Press, 1993).
[22] D. J. Wales, Int. Rev. Phys. Chem. **25**, 237 (2006).
[23] A. M. H. Rasmussen and B. Hammer, J. Chem. Phys. **136**, 174706 (2012).
[24] E. L. Kolsbjerg, M. N. Groves, and B. Hammer, J. Chem. Phys. **144**, 164112 (2016).
[25] G. Goubert, A. M. H. Rasmussen, Y. Dong, M. N. Groves, P. H. McBreen, and B. Hammer, Surf. Sci. **629**, 123 (2014).
[26] P. Wang, X. Tang, J. Tang, and Y. Pei, J. Phys. Chem. C **119**, 10345 (2015).
[27] L.-L. Ma, C.-Q. Lv, and G.-C. Wang, Appl. Surf. Sci. **410**, 154 (2017).
[28] Z. W. Ulissi, A. J. Medford, T. Bligaard, and J. K. Nørskov, Nat. Commun. **8**, 14621 (2017).
[29] S. Bhattacharya, B. H. Sonin, C. J. Jumonville, L. M. Ghiringhelli, and N. Marom, Phys. Rev. B **91**, 241115 (2015).
[30] A. A. Peterson, J. Chem. Phys. **145**, 074106 (2016).
[31] O.-P. Koistinen, E. Maras, A. Vehtari, and H. Jónsson, J. Chem. Phys. **147**, 152720 (2017).
[32] J. Enkovaara, C. Rostgaard, J. J. Mortensen, J. Chen, M. Dułak, L. Ferrighi, J. Gavnholt, C. Glinsvad, V. Haikola, H. A. Hansen, H. H. Kristoffersen, M. Kuisma, A. H. Larsen, L. Lehtovaara, M. Ljungberg, O. Lopez-Acevedo, P. G. Moses, J. Ojanen, T. Olsen, V. Petzold, N. A. Romero, J. Stausholm-Møller, M. Strange, G. A. Tritsaris, M. Vanin, M. Walter, B. Hammer, H. Häkkinen, G. K. H. Madsen, R. M. Nieminen, J. K. Nørskov, M. Puska, T. T. Rantala, J. Schiøtz, K. S. Thygesen, and K. W. Jacobsen, J. Phys.: Condens. Matter **22**, 253202 (2010).
[33] A. H. Larsen, J. J. Mortensen, J. Blomqvist, I. E. Castelli, R. Christensen, M. Dułak, J. Friis, M. N. Groves, B. Hammer, C. Hargus, E. D. Hermes, P. C. Jennings, P. B. Jensen, J. Kermode, J. R. Kitchin, E. L. Kolsbjerg, J. Kubal, K. Kaasbjerg, S. Lysgaard, J. B. Maronsson, T. Maxson, T. Olsen, L. Pastewka, A. A. Peterson, C. Rostgaard, J. Schiøtz, O. Schütt, M. Strange, K. S. Thygesen, T. Vegge, L. Vilhelmsen, M. Walter, Z. Zeng, and K. W. Jacobsen, J. Phys.: Condens. Matter **29**, 273002 (2017).
[34] P. E. Blöchl, Phys. Rev. B **50**, 17953 (1994).
[35] J. J. Mortensen, L. B. Hansen, and K. W. Jacobsen, Phys. Rev. B **71**, 035109 (2005).
[36] J. Klimeš, D. R. Bowler, and M. Angelos, Phys. Rev. B **83**, 195131 (2011).
[37] E. L. Kolsbjerg, M. N. Groves, and B. Hammer, J. Chem. Phys. **145**, 094107 (2016).
[38] S. Smidstrup, A. Pedersen, K. Stokbro, and H. Jónsson, J. Chem. Phys. **140**, 214106 (2014).
[39] M. Wahl, M. Stöhr, H. Spillmann, T. A. Jung, and L. H. Gade, Chem. Commun. **2007**(13), 1349.
[40] A. E. Baber, H. L. Tierney, and E. C. H. Sykes, ACS Nano **2**, 2385 (2008).
[41] A. D. Jewell, H. L. Tierney, A. E. Baber, E. V. Iski, M. M. Laha, and E. C. H. Sykes, J. Phys.: Condens. Matter **22**, 264006 (2010).
[42] H. L. Tierney, J. W. Han, A. D. Jewell, E. V. Iski, A. E. Baber, D. S. Sholl, and E. C. H. Sykes, J. Phys. Chem. C **115**, 897 (2011).
[43] K. Berland, C. A. Arter, V. R. Cooper, K. Lee, B. I. Lundqvist, E. Schröder, T. Thonhauser, and P. Hyldgaard, J. Chem. Phys. **140**, 18A539 (2014).
[44] C. T. Campbell and J. R. V. Sellers, J. Am. Chem. Soc. **134**, 18109 (2012).
[45] D. Porezag and M. R. Pederson, Phys. Rev. B **54**, 7830 (1996).
[46] P. Shea and H. J. Kreuzer, J. Chem. Phys. **142**, 154105 (2015).

Paper VI

THE JOURNAL OF CHEMICAL PHYSICS **148**, 124704 (2018)

NH_3 adsorption on anatase-TiO_2(101)

Stig Koust,[1] Kræn C. Adamsen,[1] Esben Leonhard Kolsbjerg,[1,2] Zheshen Li,[2] Bjørk Hammer,[1,2] Stefan Wendt,[1] and Jeppe V. Lauritsen[1,a)]
[1]*Interdisciplinary Nanoscience Center (iNANO) , Aarhus University, DK-8000 Aarhus C, Denmark*
[2]*Department of Physics and Astronomy, Aarhus University, DK-8000 Aarhus C, Denmark*

(Received 4 January 2018; accepted 16 February 2018; published online 23 March 2018)

The adsorption of ammonia on anatase TiO_2 is of fundamental importance for several catalytic applications of TiO_2 and for probing acid-base interactions. Utilizing high-resolution scanning tunneling microscopy (STM), synchrotron X-ray photoelectron spectroscopy, temperature-programmed desorption (TPD), and density functional theory (DFT), we identify the adsorption mode and quantify the adsorption strength on the anatase TiO_2(101) surface. It was found that ammonia adsorbs non-dissociatively as NH_3 on regular five-fold coordinated titanium surface sites (5f-Ti) with an estimated exothermic adsorption energy of 1.2 eV for an isolated ammonia molecule. For higher adsorbate coverages, the adsorption energy progressively shifts to smaller values, due to repulsive intermolecular interactions. The repulsive adsorbate-adsorbate interactions are quantified using DFT and autocorrelation analysis of STM images, which both showed a repulsive energy of ~50 meV for nearest neighbor sites and a lowering in binding energy for an ammonia molecule in a full monolayer of 0.28 eV, which is in agreement with TPD spectra. *Published by AIP Publishing.* https://doi.org/10.1063/1.5021407

I. INTRODUCTION

Titanium dioxide (TiO_2) is used in many applications such as Grätzel solar cells,[1] heterogeneous catalysis,[2–5] and photocatalysis.[6,7] Among the main polymorphs of TiO_2, rutile, anatase, and brookite, only the former two are used in technical applications.[2,7] Whereas rutile has traditionally been the most studied polymorph in the surface science literature,[7] anatase has bulk and surface properties that make this polymorph the most relevant for, e.g., photocatalytic and heterogeneously catalysed reactions.

For this reason, the most stable of the anatase facets, the TiO_2(101) surface [a-TiO_2(101)], has been the subject of numerous studies addressing the adsorption of small molecules, such as CO,[8,9] H_2O,[10–12] O_2,[13] and acetic acid.[14] These studies have shown a rather complex behavior of these simple molecules, although their adsorption seems to be less dominated by bulk and surface defects than for rutile TiO_2. Here we focus on the fundamental interaction of NH_3 with a-TiO_2(101). The NH_3 adsorption on a-TiO_2(101) is highly important, insofar as adsorption studies of NH_3 with a-TiO_2 have been used to probe Lewis acid-base interactions with anatase powders.[15] In addition, the NH_3/anatase TiO_2 system is of importance in the selective catalytic reduction (SCR) of NO with NH_3 using submonolayer vanadium oxides on a-TiO_2[2,16] or for titania-based catalysts for the removal of NH_3 pollution from air and water.[17,18]

Studies addressing the NH_3 adsorption on the rutile polymorph, r-TiO_2(110), have employed scanning tunneling microscopy (STM),[19] temperature programmed desorption (TPD),[20,21] X-ray photoemission spectroscopy (XPS),[21–23] and theoretical calculations[15,24,25] to conclude that ammonia adsorbs molecularly on five-fold coordinated titanium (5f-Ti) surface sites and desorbs again without dissociation. The desorption energy was found to be coverage-dependent and decrease from ~1.0-1.3 eV[20,21] at low NH_3 coverage to ~0.6 eV at full monolayer coverage. This is reasoned by repulsive NH_3–NH_3 interactions which cause the ammonia to occupy every second 5f-Ti surface site.[19,22,23,26] On r-TiO_2(110), a full monolayer is therefore considered in some studies to be achieved by the occupation of half the available 5f-Ti sites.[19,22] However, Kim *et al.*[20] reported by using TPD that a full NH_3 monolayer on rutile TiO_2 (110) corresponds to occupation of all 5f-Ti sites.

The present study combines STM, XPS, TPD, and density functional theory (DFT) to reveal the adsorption mode, intermolecular interactions, and desorption of NH_3 on a-TiO_2(101). Our STM and DFT results reveal the preferential adsorption site to be on 5f-Ti surface sites of a-TiO_2(101). We conclude that NH_3 adsorbs and desorbs molecularly based on XPS and TPD. In line with comparable studies of NH_3 monolayers on r-TiO_2(110), we find that repulsive interactions between neighboring NH_3 molecules influence binding energies, reflected by an observed intermediate (2 × 1) superstructure. However a full NH_3 monolayer is considered as occupation of all 5f-Ti-sites.

II. EXPERIMENTAL

The STM and TPD experiments were performed in an ultra-high vacuum chamber (SPECS) with a base pressure below 1×10^{-10} mbar, equipped with a commercial Aarhus-type STM (Aarhus-150, SPECS) that allows for cooling to liquid nitrogen temperatures. Tungsten (W) STM tips prepared

a)Electronic mail: jvang@inano.au.dk

by electrochemical etching were used for imaging. Typical scanning parameters were 1000-1400 mV and 0.1-0.2 nA. All TPD spectra were acquired using a quadrapole mass spectrometer (HIDEN). The XPS experiments were carried out at the ASTRID2 synchrotron source at the Institute for Storage Ring Facilities (ISA) at Aarhus University on the AU-MatLine beamline.[27] The beamline is equipped with a SX-700 monochromator and SCIENTA SES200 electron energy analyzer running with a pass energy of 75 eV, curved analyzer slit of 0.8 mm, and a beamline monochromator slit width of 60 μm. The base pressure was around 5×10^{-10} mbar. The N1s core level was collected using a photon energy of 480 eV.

Natural anatase single crystals (SurfaceNet) were prepared by preparation cycles of sputtering (Ar^+, 1.5 kV, 298 K), O_2 annealing (1×10^{-8} mbar, 820-950 K), and subsequent sputtering and vacuum-annealing (820-950 K). The temperature of the sample is measured by a K-type thermocouple spot-welded onto the sample holder close to the sample. NH_3 was dosed on to the anatase TiO_2(101) surface through a leak valve by means of a directional doser. This was done to minimize ammonia contaminants in the residual gas and thereby minimize re-adsorption onto the surface after the initial exposure. Typical exposures for submonolayer coverage of NH_3 were 5×10^{-10} mbar for 1-2 s. The coverage is given in ML, with 1 ML defined as one NH_3 molecule per Ti surface atom in the a-TiO_2(101) surface, i.e., 9.7×10^{14} NH_3 molecules per cm^2.

For constructing, manipulating, and optimizing the atomistic systems, the ASE[28] package was used in combination with the GPAW[29] density functional theory (DFT) code. We use the grid-based mode of GPAW with a spacing of at least 0.1771 Å sampling $4 \times 4 \times 1$ K-points of the Brillouin zone. To mimic the experimental crystal, we employ a 4-layer TiO_2 (101) anatase slab spanning 1×2 surface unit cells, resulting in a total stoichiometry of $Ti_{24}O_{48}$. We use the optB88-vdW functional with optimized lattice parameters of a = b = 3.82 Å and c = 9.61 Å with periodic boundary conditions parallel to the slab surface with at least 6 Å of vacuum from any atom to the non-periodic cell boundaries. The bottom layer was held frozen, and systems were considered converged when no force on any atom exceeded 0.025 eV/Å.

III. RESULTS AND DISCUSSION

Figure 1 shows STM images following NH_3 exposure at room temperature (RT). The a-TiO_2(101) surface exhibits large trapezoidal islands separated by monoatomic steps typical for this surface.[30] As we expose the clean a-TiO_2(101) surface to 0.05 ML ammonia, bright protrusions appear in the STM image reflecting adsorption at room temperature. The ammonia-related protrusions reside homogeneously across the terraces [Fig. 1(a)]. The protrusions appear to have little affinity for binding at step edges, and no apparent agglomeration of molecules was observed. In order to illustrate local structural information of the adsorbed ammonia, we present a high-resolution (6 nm × 6 nm) STM image in Fig. 1(b). The superimposed lattice points (red circles) are attributed to protruding two-fold coordinated O atoms (2f-O) on a-TiO_2(101). The bright features associated with ammonia (blue circles) are observed to bind in between the surface lattice rows running in the [010] direction in a position which is slightly displaced toward one of the rows. The fivefold coordinated Ti atoms (5f-Ti) terminating the a-TiO_2(101) surface (gray) are also illustrated in the STM image, and their position coincides with the adsorption site of ammonia. Thus, the STM data suggest that ammonia binds to the a-TiO_2(101) surface on top of the 5f-Ti surface sites. In agreement, we find from DFT that ammonia is predicted to adsorb molecularly without dissociation with an exothermic adsorption energy of 1.20 eV. The DFT-calculated adsorption site of isolated NH_3 molecules on a stoichiometric a-TiO_2(101) is indeed found to be on 5f-Ti, as illustrated in Fig. 1(c). The ammonia is found off-centered between 2f-O rows running in the [010] direction.

XPS data were collected in order to verify the non-dissociative binding of molecular ammonia to a-TiO_2(101). XPS allows for easy distinction between various amines as the shift in N1s binding energy between NH_2, NH_3, and NH_4 is in the order of 1.5 eV.[31] We exposed the a-TiO_2 (101) surface to more than a monolayer of ammonia at 118 K and collected the N1s core level spectra (Fig. 2). This was followed by stepwise heating at elevated temperatures for 5 min until the N1s signal vanished. The XPS data were collected at ~120 K throughout the series. The N1s peak position is found at 400.9 eV for all temperatures and can be fitted with a

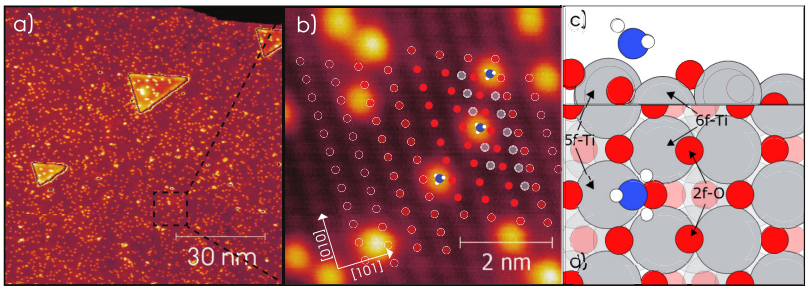

FIG. 1. (a) STM image (120 nm × 120 nm) of 0.05 ML NH_3 adsorbed on anatase-TiO_2(101), imaged at RT. (b) Atom-resolved STM (6 nm × 6 nm) image at room temperature, showing the NH_3 adsorption site. Rows of surface lattice points [2f-O (red) and 5f-Ti(gray)] are superimposed. NH_3 (blue/white) molecules reside between rows, on top of the 5f-Ti sublattice. [(c) and (d)] DFT-predicted NH_3 adsorption site on 5f-Ti. (c) shows a side view of adsorbed ammonia and (d) shows a top view.

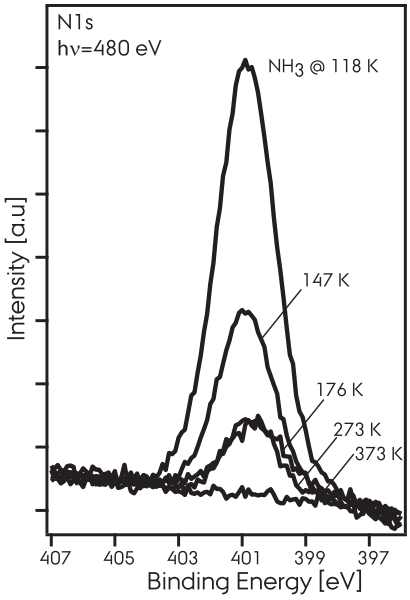

FIG. 2. N1s XPS spectra (hν = 480 eV, data collection at 110 K) of NH_3 adsorbed on anatase TiO_2 (101) (at 110 K) after heating in the range 118 K–373 K.

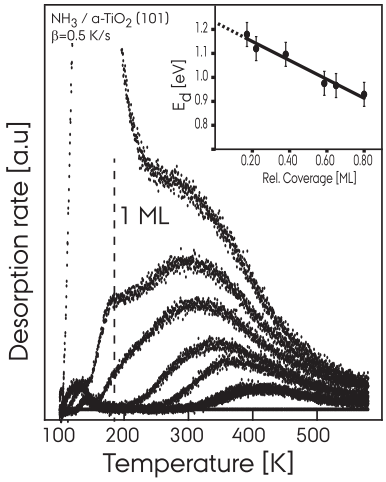

FIG. 3. TPD spectra of NH_3 (m/z = 17) adsorbed on anatase-TiO_2(101) for various coverages (0.2–1.8 ML). Inset shows redhead analysis of TPD spectra, i.e., showing the change in binding energy as a function of coverage (peak area).

single peak with FWHM of 1.8 eV, indicating that only a single nitrogen species is present on the surface at all temperatures. This binding energy for nitrogen corresponds to molecularly adsorbed NH_3 bound to a Lewis acid center, thus a NH_3–Ti bond.[21,22,31,32] A dative bond with a Lewis acid center is formed by donation of a free electron pair from nitrogen.[31] The N1s intensity decreases upon heating to 147 K and further at 176 K but then stays constant up to 273 K. Complete desorption of NH_3 was found after heating up to 373 K. This evolution of the N1s intensity suggests that multilayers of NH_3 accommodate the surface at the lowest temperature. The multilayer desorbs for temperatures around 176 K, where a stable monolayer is left on the surface, which is stable up to temperatures at 373 K. This is corroborated by TPD studies of ammonia desorption, which furthermore indicates considerable adsorbate-adsorbate interactions. In the TPD experiment, NH_3 was adsorbed on the a-TiO_2 (101) surface at ~100 K in various coverages, followed by a linear temperature ramp rate (β) of 0.5 K s^{-1} to 600 K. The corresponding desorption spectra (m/z = 17) are presented in Fig. 3. The coverage is estimated by relating the integrated areas for the different spectra to the spectrum where multilayers start forming. At the lowest coverage, a single high temperature desorption peak around 410 K is observed. For higher coverages, the leading edge shifts progressively toward lower temperature, whereas the trailing edge stays constant, resulting in a broadening of the desorption peak. The desorption peak maximum shifts from 410 K (lowest coverage) to 327 K (full monolayer) in the submonolayer regime. For coverages above a monolayer, we observe a multilayer desorption peak forming around 180 K. The decrease in temperature of desorption peak maximum (T_m) for increasing NH_3 coverage indicates a strongly coverage-dependent desorption energy (E_d), which can be calculated on the basis of T_m. We note that this method is valid strictly for first-order desorption.[33] This is fulfilled for non-dissociative adsorption,[20] despite the shift of maximum desorption to lower temperature with increasing coverages, which is otherwise typically related to second-order desorption.[34] E_d is calculated iteratively from the following equation:

$$E_d = k_b T_m \ln\left[\frac{k_b T_m^2 \nu}{E_d \beta}\right], \tag{1}$$

where the pre-exponential factor (ν) is calculated as in Ref. 34 to be 1.8×10^{13} s^{-1}, which coincides with previously published values.[20,33,34] E_d as a function of coverage in the submonolayer regime is presented in the inset in Fig. 3. We observed a shift from 1.18 eV to 0.93 eV for increasing coverage. Extrapolating to the zero coverage limit yields E_d of a single ammonia molecule on a-TiO_2(101) to be 1.23 ± 0.1 eV, which is in excellent agreement with theory (1.2 eV). In this limit NH_3–NH_3 interactions can be neglected; thus only the NH_3–TiO_2 interaction is determining E_d for an isolated NH_3 molecule.

The TPD spectra are also in accordance with the desorption trend observed in the XPS spectra (Fig. 2), as multilayer coverages were seen to desorb in the temperature range below 176 K, whereas a complete desorption occurred at temperatures higher than 276 K. The strong coverage-dependent desorption energy is attributed to the repulsion between ammonia molecules.[20,21] A small tail is seen at the trailing edge at around 450 K; this is presumably caused by ammonia adsorption in vicinity of defects (subsurface donors), as only small affinity for adsorption at step edges is observed.

The repulsive interaction between NH_3 molecules was further quantified by analyzing the autocorrelation function of the ammonia positions (Fig. 4) from our STM data (Fig. 5) and comparing with DFT values for adsorption with a second NH_3

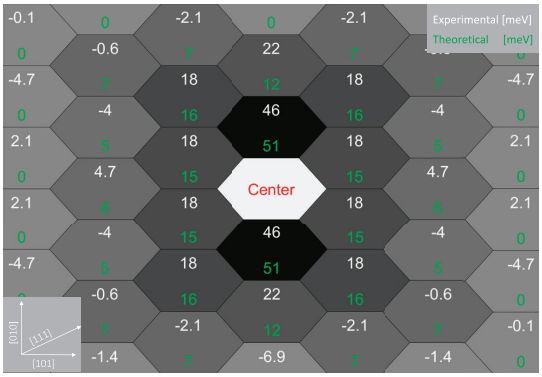

FIG. 4. Result of the autocorrelation function analysis, showing the obtained repulsion energies in meV. Experimental in white and theoretical in green. Each hexagon represents a neighboring Ti-5f site to the center. The gray color scale of each tile represents its likelihood of occupation (p_n). Black: less probable, i.e., high repulsion energy, white: very probable, gray: no effect.

molecule within the supercell modeling the a-TiO_2(101) surface. By marking the positions of adsorbed NH_3 molecules in an automated process and assigning them to an adsorption site, the probabilities of occupations are calculated. This is visualized in Fig. 4, by the gray scale colormap. The experimental repulsion energy (E_{rep}) is extracted by[8]

$$E_{rep} = -kT \ln\left(\frac{p_n}{p_{av}}\right), \tag{2}$$

where p_n denotes the probability for occupying neighboring site obtained directly from our autocorrelation analysis and p_{av} denotes the average probability for a random 5f-Ti site (coverage). Assuming the occupation of sites follow a Boltzmann distribution, the repulsion energy can be extracted. The experimentally extracted repulsion energies are displayed in Fig. 4 in white, on a grid reflecting the lattice of NH_3 adsorption sites. The values are shown together with the change in theoretical (DFT) adsorption energy with NH_3 on the neighboring sites in green. Very good agreement between theory and experimental acquired values are observed. In general, the nearest neighbor sites along the [010] are considerably less favorable than next-nearest neighbor adsorption sites and other sites further away. The nearest neighbor sites show repulsion energies of ~50 meV, next-nearest neighbor sites show ~20 meV, and sites further away show repulsion energy close to zero which reflects randomly distributed molecules. These results are also in good qualitative agreement with the observed NH_3 positions observed in Fig. 5 as nearest neighbor adsorption

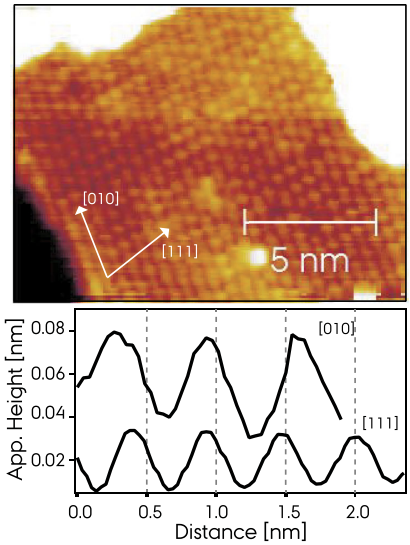

FIG. 6. STM (15 nm × 11 nm) image of NH_3 adsorbed on anatase-TiO_2(101) at 110 K. Inset: Linescan along the [111] and [010] directions, respectively.

sites are rarely observed. By increasing the ammonia coverage (Fig. 5), the STM images show local patterns of double lattice distance along the [010] directions (Fig. 5). Patterns along [111] direction are also observed (Fig. 5). We found that at even higher coverages, STM imaging becomes troublesome at room temperature, because of rapidly diffusing ammonia molecules. This can be circumvented at lower imaging temperatures (~100 K), where a static ordered overlayer structure can be imaged (Fig. 6). The overlayer consists of patches of adsorbed ammonia separated by ~5.5 Å formed in the [111] direction upon dosage and a longer distance of 7.8 Å along [010] directions. The intermolecular distances in the ordered areas (7.8 Å × 5.6 Å) coincide with a (2 × 1) symmetry with the underlying 5f-Ti surface atoms, i.e., a NH_3-(2 × 1)-TiO_2 overlayer. No STM images were obtained when further increasing the NH_3 coverage; thus, only TPD and XPS measurements are present for full monolayer coverages.

By adding all the obtained experimental or theoretical repulsion energies (Fig. 4), the adsorption energy per ammonia molecule for a full monolayer (all 5f-Ti sites occupied) is estimated to be 0.28 eV less than for the low coverage situation. The shift in energy between the low coverage adsorption and a full monolayer is in agreement with desorption features in the

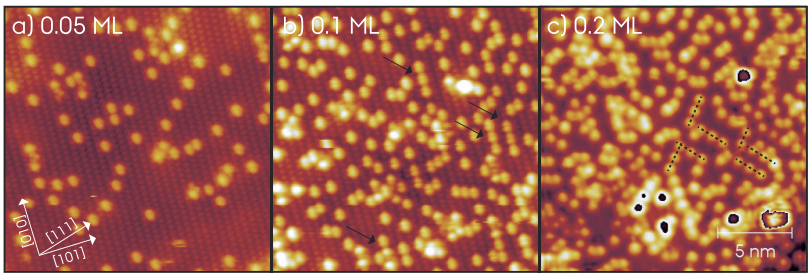

FIG. 5. STM (18 nm × 18 nm) image of NH_3 adsorbed on anatase-TiO_2(101) at RT at various coverages. (a) 0.05 ML, (b) 0.1 ML, (c) 0.2 ML.

TPD, where a shift of 0.28 eV is seen in Fig. 3, inset, i.e., NH_3 in a full monolayer is destabilized by this energy compared to a single NH_3. Compared with the NH_3/rutile-TiO_2(110) system,[20,21] the adsorption of NH_3 on TiO_2(101) is very similar. The NH_3 adsorption sites are on 5f-Ti atoms on both surfaces. For a-TiO_2(101), we detect a significant NH_3–NH_3 repulsion reflected by a coverage-dependent desorption energy, but the effect is weaker than on rutile-TiO_2(110), which can be explained by a larger 5f-Ti spacing in anatase (101) compared to rutile (110) TiO_2 (3.78 Å and 2.96 Å, respectively).

IV. CONCLUSION

In summary, by high-resolution STM combined with XPS, TPD, and DFT, we find that NH_3 adsorbs molecularly on anatase TiO_2 (101). Specifically, when NH_3 was deposited at sub-monolayer coverage at room temperature, we found an affinity for NH_3 to reside at 5f-Ti atom sites. The theoretical adsorption energy (DFT) was calculated to be 1.20 eV and measured by TPD analysis to be 1.23 eV. Our XPS and TPD data indicated that NH_3 did not undergo dissociation at elevated temperatures and desorbed molecularly. Upon increasing the coverage, the NH_3 adsorption energy was significantly lowered by 0.28 eV because of dipole-dipole repulsive interactions, confirmed by TPD and autocorrelation analysis of STM images. In addition, the strong interaction between NH_3 resulted in a preference for occupying next-nearest 5f-Ti neighbor sites along the [010] direction, whereas NH_3 molecules occupying adjacent nearest neighbor sites in the [101] direction was seldom, and a repulsion energy of ~50 meV was found for this site from DFT and autocorrelation analysis of low NH_3 coverage STM images. Furthermore, an intermediate (2×1) overlay NH_3 adsorbate structure was observed at low temperature as a result of the intermolecular interaction.

ACKNOWLEDGMENTS

This work was partly funded by the Innovation Fund Denmark (IFD) under File Nos. 12-132681 (Cat-C) and 6151-00008B (ProNOx), VILLUM FONDEN (Investigator grant, Project No. 16562), and Danish Research Councils (No. 0602-02566B). We gratefully acknowledge support from Haldor Topsøe A/S. We acknowledge beamtime received at ASTRID2 on the MatLine beamline.

[1] M. Grätzel, J. Photochem. Photobiol., C **4**, 145 (2003).
[2] G. Busca, L. Lietti, G. Ramis, and F. Berti, Appl. Catal., B **18**, 1 (1998).
[3] I. E. Wachs, Dalton Trans. **42**, 11762 (2013).
[4] L. Artiglia, S. Agnoli, and G. Granozzi, Coord. Chem. Rev. **301**, 106 (2015).
[5] N. Y. Topsøe, H. Topsøe, and J. Dumesic, J. Catal. **151**, 226 (1995).
[6] B. M. Weckhuysen and D. E. Keller, Catal. Today **78**, 25 (2003).
[7] U. Diebold, Surf. Sci. Rep. **48**, 53 (2003).
[8] M. Setvin, M. Buchholz, W. Hou, C. Zhang, B. Stöger, J. Hulva, T. Simschitz, X. Shi, J. Pavelec, G. S. Parkinson, M. Xu, Y. Wang, M. Schmid, C. Wöll, A. Selloni, and U. Diebold, J. Phys. Chem. C **119**, 21044 (2015).
[9] M. Setvin, B. Daniel, U. Aschauer, W. Hou, Y.-F. Li, M. Schmid, A. Selloni, and U. Diebold, Phys. Chem. Chem. Phys. **16**, 21524 (2014).
[10] C. Dette, M. A. Pérez-Osorio, S. Mangel, F. Giustino, S. J. Jung, and K. Kern, J. Phys. Chem. C **121**, 1182 (2017).
[11] Y. He, A. Tilocca, O. Dulub, A. Selloni, and U. Diebold, Nat. Mater. **8**, 585 (2009).
[12] G. S. Herman, Z. Dohnalek, N. Ruzycki, and U. Diebold, J. Phys. Chem. B **107**, 2788 (2003).
[13] M. Setvín, M. Wagner, M. Schmid, G. S. Parkinsona, and U. Diebold, Chem. Soc. Rev. **46**, 1772 (2017).
[14] D. C. Grinter, M. Nicotra, and G. Thornton, J. Phys. Chem. C **116**, 11643 (2012).
[15] A. Markovits, J. Ahdjoudj, and C. Minot, Surf. Sci. **365**, 649 (1996).
[16] I. E. Wachs, G. Deo, B. M. Weckhuysen, A. Andreini, M. Vuurman, M. de Boer, and M. D. Amiridis, J. Catal. **161**, 211–221 (1996).
[17] J. Lee, H. Park, and W. Choi, Environ. Sci. Technol. **36**, 5462 (2002).
[18] S. Yamazoe, T. Okumura, Y. Hitomi, T. Shishido, and T. Tanaka, J. Phys. Chem. C **111**, 11077 (2007).
[19] C. L. Pang, A. Sasahara, and H. Onishi, Nanotechnology **18**, 44003 (2007).
[20] B. Kim, Z. Li, B. D. Kay, Z. Dohnalek, and Y. K. Kim, Phys. Chem. Chem. Phys. **14**, 15060 (2012).
[21] E. Farfan-Arribas and R. J. Madix, J. Phys. Chem. B **107**, 3225 (2003).
[22] U. Diebold and T. E. Madey, J. Vac. Sci. Technol., A **10**, 2327 (1992).
[23] W. K. Siu, R. A. Bartynski, and S. L. Hulbert, J. Chem. Phys. **113**, 10697 (2000).
[24] D. Cheng, J. Lan, D. Cao, and W. Wang, Appl. Catal., B **106**, 510 (2011).
[25] J. G. Chang, S. P. Ju, C. S. Chang, and H. T. Chen, J. Phys. Chem. C **113**, 6663 (2009).
[26] J. N. Wilson and H. Idriss, Langmuir **20**, 10956 (2004).
[27] Z. Li, http://www.isa.au.dk/facilities/astrid2/beamlines/AU-Matline/AU-Matline.asp.
[28] A. Larsen, J. Mortensen, J. Blomqvist, I. Castelli, R. Christensen, M. Dulak, J. Friis, M. Groves, B. Hammer, C. Hargus, E. Hermes, P. Jennings, P. B. Jensen, J. Kermode, J. Kitchin, E. L. Kolsbjerg, J. Kubal, K. Kaasbjerg, S. Lysgaard, J. B. Maronsson, T. Maxson, T. Olsen, L. Pastewka, A. Peterson, C. Rostgaard, J. Schiøtz, O. Schütt, M. Strange, K. S. Thygesen, T. Vegge, L. Wilhelmsen, M. Walter, Z. Zeng, and K. W. Jacobsen, J. Phys.: Condens. Matter **29**, 273002 (2017).
[29] J. Enkovaara, C. Rostgaard, J. J. Mortensen, J. Chen, M. Dułak, L. Ferrighi, J. Gavnholt, C. Glinsvad, V. Haikola, H. A. Hansen, H. H. Kristoffersen, M. Kuisma, A. H. Larsen, L. Lehtovaara, M. Ljungberg, O. Lopez-Acevedo, P. G. Moses, J. Ojanen, T. Olsen, V. Petzold, N. A. Romero, J. Stausholm-Møller, M. Strange, G. A. Tritsaris, M. Vanin, M. Walter, B. Hammer, H. Häkkinen, G. K. H. Madsen, R. M. Nieminen, J. K. Nørskov, M. Puska, T. T. Rantala, J. Schiøtz, K. S. Thygesen, and K. W. Jacobsen, J. Phys.: Condens. Matter **22**, 253202 (2010).
[30] W. Hebenstreit, N. Ruzycki, G. S. Herman, Y. Gao, and U. Diebold, Phys. Rev. B **62**, R16334 (2000).
[31] C. Guimon, A. Gervasini, and A. Auroux, J. Phys. Chem. B **105**, 10316 (2001).
[32] J. Keränen, C. Guimon, E. Iiskola, A. Auroux, and L. Niinistö, Catal. Today **78**, 149 (2003).
[33] A. M. de Jong and J. W. Niemantsverdriet, Surf. Sci. **233**, 355 (1990).
[34] I. Chorkendorff and J. W. Niemantsverdriet, *Concepts of Modern Catalysis and Kinetics* (Wiley, 2003).

Paper VII

Neural-network-enhanced evolutionary algorithm applied to supported metal nanoparticles

E. L. Kolsbjerg,[1] A. A. Peterson,[2] and B. Hammer[1,*]
[1]*Interdisciplinary Nanoscience Center (iNANO), Department of Physics and Astronomy, Aarhus University, Denmark*
[2]*School of Engineering, Brown University, Providence, Rhode Island, 02912, USA*

(Received 10 November 2017; revised manuscript received 26 April 2018; published 16 May 2018)

We show that approximate structural relaxation with a neural network enables orders of magnitude faster global optimization with an evolutionary algorithm in a density functional theory framework. The increased speed facilitates reliable identification of global minimum energy structures, as exemplified by our finding of a hollow Pt_{13} nanoparticle on an MgO support. We highlight the importance of knowing the correct structure when studying the catalytic reactivity of the different particle shapes. The computational speedup further enables screening of hundreds of different pathways in the search for optimum kinetic transitions between low-energy conformers and hence pushes the limits of the insight into thermal ensembles that can be obtained from theory.

DOI: 10.1103/PhysRevB.97.195424

I. INTRODUCTION

The field of automated structure determination [1,2] and high-throughput computational studies in condensed matter physics and materials science [3] is seeing great advances in capabilities following developments in first-principles computational methods and the advancements in computing power available. The buildup of databases of structure-property relations [4,5] enables efficient prediction of promising new materials that are not yet experimentally characterized, or even synthesized [6,7]. Such computational studies rely on accurate identification of possible ground-state and metastable structures of matter across variations in stoichiometries, symmetries, and, for extended system, also lattice parameters.

The same scenario plays out in the field of heterogeneous catalysis which has a strong record of providing insight and guidance for both computational and experimental investigations [8,9]. Coordination models have proven useful in rationalizing the catalytic activity of solid surfaces with and without imperfections [10], and descriptor-based models have led to predictions of new catalytic materials [11]. As an example, the study of oxide-supported size-selected nanoparticles of reactive metals has revealed that "each atom counts"[12]. That is, the nanoparticles are showing pronounced variations in their catalytic activity with particle size and shape [13–16], and theoreticians have sought to use computational means to unravel the underlying mechanisms [17–19].

In the search for realistic atomistic models for such systems [20–23], it has become obvious that unbiased structure search algorithms such as evolutionary algorithms [24,25] (EA), basin hopping [1,26], or minima hopping [27] algorithms are required whether it is to locate realistic geometries of nanoparticles, to identify representative catalytic sites, or to create an ensemble of different configurations. As system sizes grow and become more realistic, so does the complexity of the models needed and hence more structures must be considered before a good representation of candidates can be obtained. Any measure to reduce the number of required *ab initio* calculations is hence much valued as it provides greater opportunity to explore relevant systems [28]. One way to achieve a great speedup but still be able to preserve the accuracy of first-principles calculations is to use well-trained machine-learning potentials [29] whether it is from support-vector machine methods [30], kernel methods [29,31–36], or artificial neural networks [20,22,28,37–41] (NN). With the introduction of machine-learning (ML) models that also include forces, either as derivatives of the learned energy potential [42] or by directly training the forces [34,43], it is now possible to bring a given configuration to its local minimum configuration with no prior assumption or analysis of the interaction mode as would otherwise be needed for inexpensive classical force fields. With the newly found opportunities, several successful attempts have been proposed to combine ML and global structure optimization as, e.g., a neural-network-biased genetic algorithm [44], a combination of a neural network potential and the basin-hopping method [45], the creation of hierarchical NN libraries for multicomponent systems by generating training data from EA runs [28], and particle swarm-intelligence based global optimization involving trained Gaussian approximation potentials [46]. Recently, Wu *et al.* showed that an adaptive evolutionary algorithm that reparametrizes classic interatomic potential parameters has the possibility to achieve large accelerations over purely *ab initio* evolutionary algorithm searches [47]. Similarly, Van den Bossche *et al.* have demonstrated comparable speedups for an EA by reparametrizing a tight-binding density functional model potential [48]. However, for complex or arbitrary multielement systems, the choice and reparametrization of such potentials can be cumbersome, thereby impeding and limiting the adaptive improvement of the potentials. Here, instead we suggest retraining agnostic machine-learned potentials as unbiased auxiliary energy expressions with no initiation mode assumed, which has the prospects of circumventing issues of choosing appropriate potential expressions. For this we chose an artificial neural network that eliminates relaxations at the first-principles level

*hammer@phys.au.dk

 ©2018 American Physical Society

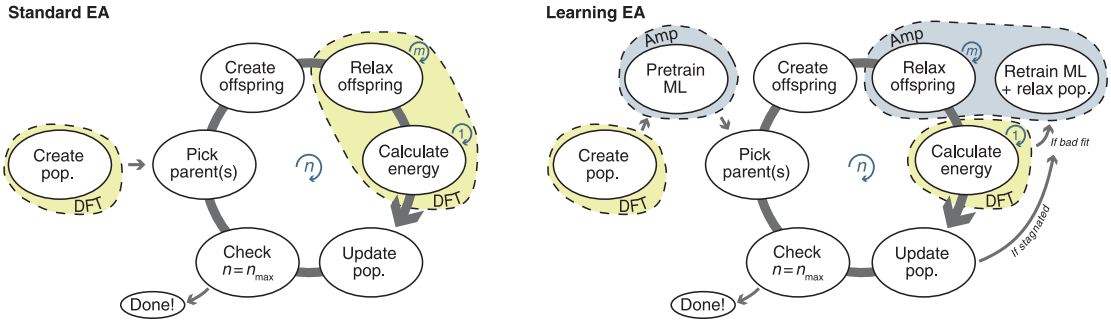

FIG. 1. Left: standard EA algorithm. Right: the proposed LEA algorithm in which new candidate structures are relaxed within the Amp model. The strategy is more conservative and hence more error tolerant than that of Ref. [47] as the model predicted energies are continuously monitored.

of theory. Following the above, we present a neural-network-enhanced evolutionary algorithm, a learning EA (LEA).

The paper is outlined as follows: We start by introducing the evolutionary algorithm, pointing out how an NN model can be trained initially and retrained on-the-fly on the steady production of new structure-energy candidates. Next, we present the details of the NN of the Behler-Parrinello [38,39] type as implemented in Amp [42] and the computational setup. We proceed by gauging the extent to which the method reduces the need for first-principles calculations. To achieve good statistics, we do this with a pseudoempirical energy expression, the effective medium theory (EMT) [49], applied to the model system of Ag_3Pt_3 nanoparticles on a Pt support. We then move to a full-scale density functional theory (DFT) investigation of MgO supported Pt particles where we apply the method showing that a combination of NN and EA enables us to unravel numerous unreported nanoparticle geometries that are considerably more stable than those previously reported. We finally investigate how the catalytic activity changes with the particle shape and effectively exploit the trained NN model to explore the transition barrier between relevant nanoparticles.

II. METHOD

The basic EA algorithm (available in the Atomic Simulation Environment (ASE) [50] and explained in details elsewhere [25]) is sketched in the left part of Fig. 1, which shows how the pool of candidates propagate towards the global minimum structure by creating a random initial population and from that picking parents to create new offsprings by pairing/mutation operations. The offsprings are relaxed to a local minimum before potentially entering the population, ideally improving the population fitness before a new loop is initiated. The expensive part of this type of global optimization algorithm is the local relaxation performed at the first-principles level. In our method, these calculations are hence circumvented by performing the relaxation in a ML model. To exclude the need for a large expensive precalculated data set for training, we chose to on-the-fly train a NN model, very much in line with NN accelerated saddle-point search proposed previously [51]. With the use of a NN model we further eliminate the need for cheaper inaccurate screening procedures like the use of classical potentials.

In this work, we chose a NN as the ML plug-in but any general ML model including force prediction is applicable and much more reliable than any classical force field [52]. To manage training, force calculation, etc., we utilize the open-source NN module of Amp, explained in detail elsewhere [42]. Amp has proven a powerful ML package with examples of its use spanning an acceleration of saddle-point searches with the nudged elastic band method [51], how dynamic Pd surfaces influence coverage-dependent oxygen interactions [53], exploring AuPd(111) slab properties [54], to predicting active CO/CO_2 sites on bimetallic nanoparticles [55]. For consistency, the construct of the NN is the same throughout this study with two hidden layers, each with five nodes to give the output atomistic energy, hence applying the atom-centered approach with the forces calculated for each atom by differentiating the energy with respect to the input parameters. The network architecture is kept simple to avoid overfitting as the variance in the data set is sparse especially for the initial training. The cosine cutoff function (radius of 7.0 Å) and the Gaussian (G2 and G4) descriptor used to describe the local structure in the region around the atoms both implemented in Amp follow the formalism suggested by Behler and Parrinello [38] with the chosen η, ζ, and γ values presented in Table I. The chosen parameters result in 40 and 72 symmetry functions per atom type for the two- and three-component systems, respectively.

The Amp structure optimization of each LEA candidate was in all cases terminated when no force exerted on any atom exceeded 0.1 eV/Å.

TABLE I. The chosen η, ζ, and γ values for the used G2 and G4 symmetry functions [39].

				G2				
η	0.01	0.05	1	4	10	20	40	80
				G4				
η	0.001	0.005						
ζ	1	4						
γ	−1	1						

The addition to the regular EA proposed in this work is illustrated in the right part of Fig. 1. First, a regular EA is initialized and the initial starting population is generated and relaxed with a total energy code of choice. We are presently resorting to two methods; the EMT [49] potential for statistical purposes and DFT for real scale systems (see details below). Before the next EA step, pairing/mutation, Amp is trained against the relaxation paths of the start population. When the training is satisfactorily converged (∼10 000 training iterations) the EA evolution proceeds but the structure relaxation is now performed at great speed with Amp instead of with the regular quantum mechanics (QM) based method. When converged to a local minimum within Amp, a single-point calculation is performed with the parent calculator and a new training point is added to the pool of training data. If there is significant discrepancy between the parent calculator and the Amp energy, $|E_{\mathrm{DFT}} - E_{\mathrm{Amp}}| > E_{\mathrm{tol}}$ (in this work chosen as 1 eV), the EA is paused and Amp is retrained based on all accumulated training data. Once the Amp energy prediction is sufficiently good, the EA proceeds as normal until it stagnates. Stagnation is here defined as $n_{\mathrm{stag}} = 40$ subsequent attempts with lower fitness than the fittest found so far. Amp is retrained (for an additional 1000 iterations) and the EA run is resumed using the optimized Amp potential. The algorithm, as any evolutionary algorithm, has no natural stopping point and is stopped once the progress is completely stagnated or after a set number of evolution steps n_{max}.

A. Effective medium theory with Ag_3Pt_3 nanoparticles

As a proof of concept, the EMT potential [49] has been employed to describe the energy of a Ag_3Pt_3 nanoparticle disposed on a Pt surface. The two-dimensional (2D) periodic model surface cell is an fcc(111) surface with the supercell spanning $4 \times 4 \times 2$ atoms with both layers held fixed. For all EMT calculations, the geometric convergence was considered achieved when no exerted force on any atom exceeded 0.025 eV/Å.

B. Density functional theory with Pt_x nanoparticles

To describe the MgO(100) supported Pt_x nanoparticle energies, we used the plane-wave method within the DFT framework of GPAW [56] with an energy cutoff of 340 and 400 eV for the parent calculator in the LEA search and final calculations, respectively. For comparability with previous studies [57,58], we used the Perdew-Burke-Ernzerhof exchange-correlation functional [59], sampling the gamma point of the Brillouin zone. The global minimum and other potential candidates were optimized in the final calculations until no forces on any atoms were above 0.025 eV/Å both with and without spin polarization. For spin-polarized calculations, the total magnetic moment was fixed at 1, 2, and 3 for each of the final structures to locate the most preferable spin configuration. Two slabs of bulk truncated MgO(100) with lattice constant 4.21 Å were used as substrate. For the LEA search, a (5×5) cell with two layers (both frozen) was utilized while a larger (7×6) cell consisting of four layers with only the bottom layer frozen was used for the post analysis. The parameters chosen for the post analysis thus conform fully with those used in Refs. [57,58].

III. RESULTS AND DISCUSSION

As NNs are interpolation methods, the performance is at best very suboptimal in regions outside the training data. The point of a global optimization algorithm such as an EA is exactly to quickly be able to search widely in parameter space in unexplored regions. This is prone to introduce structures that are not resembling those in the training data. So, why is it still possible to use a NN to optimize and evaluate the fitness of new candidates? The training data consist of a set of feature vectors centered on each atom, hence describing the local environment, and even though by the human eye a new structure might appear very different from any structure in the training set, its local feature vectors could very easily still be in the interpolated part of the training data. This is especially true as new candidates are often created by a pairing between two half-candidates (e.g., by the cut-and-splice operator). With that in mind, it is still possible, notably at the cutting plane, to create environments not possible to represent well with the current training data and hence the NN could perform unsatisfactorily. An unintended poor performance is caught as every new candidate is recalculated at the full level of accuracy, however, only as a single-point calculation with the parent calculator and added to the training data before a potential retraining is initialized.

A. Pt_3Ag_3 nanoparticles with EMT

To provide a relevant basis for a statistical analysis of the algorithm, a relative simple nanoparticle of three Pt and three Ag atoms is deposited on a Pt(111) surface. The global minimum model system is displayed in Fig. 2(a). Restarting the LEA and regular EA algorithms 100 times from scratch allows for a direct comparison between the number of candidates and parent (EMT in this case) calculations needed to locate the global minimum. In Fig. 2(b), we plot the fraction of the individual runs that have succeeded in finding the global minimum versus the improvement attempts made (or "generations") of the EA cycle (see Refs. [35,60] for a similar metric). Not surprisingly, the LEA runs are delayed in locating the global minimum before the same success rate is achieved. However, the cycle employing a neural network needs far fewer parent (*ab initio*/EMT) calculations per attempt, which is evident when we plot the same data versus the number of parent calculations [Fig. 2(c)]. Both methods need a proper starting point achieved by relaxing the initial random population 50 steps, hence, when analyzed we distinguish between the initial and the EA cycle calculations needed to propagate the search. Figure 2(b) reveals that to achieve finding the global minimum structure with 50% certainty the average number of attempts needed to make increases from ∼170 to ∼260. On the other hand, the amount of EA parent cycle calculations for the successful runs for the two strategies decreases from $\overline{n \times m} \approx 8900$ to $\overline{n} \approx 260$. The above is highlighted in Fig. 2(d). The average number of EA cycle parent calculations for the regular EA is shaded light red, where n and m introduced in Fig. 1 are the number of EA loops and parent relaxation steps, respectively. Correspondingly for the NN model, shaded light yellow, only the $\overline{n}$ EA cycle parent calculations are on average needed and if we consider the $\overline{m}$ model relaxations for basically free, which

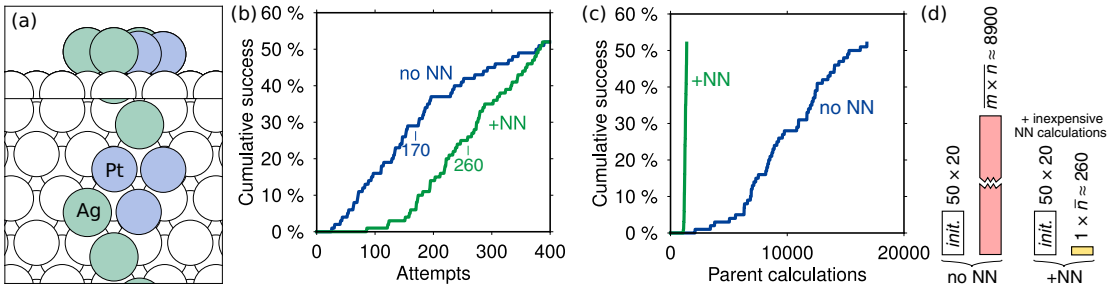

FIG. 2. (a) The atomistic model of the Pt_3Ag_3 nanoparticle supported on the Pt(111) with the Ag and Pt atoms colored green and blue, respectively, while the slab Pt atoms are white. (b), (c) The success rate of locating the global minimum as a function of the number of candidates evaluated and the number of needed parent calculations, respectively, while (d) highlights the significant reduction in the average parent calculations needed.

is a good approximation when compared to expensive DFT calculations, the difference in parent calculations is a very good representation of the amount of time on average gained when locating the global minimum. What is also evident is that a large amount of the needed parent calculations actually originate from the initial relaxation of the start population, the white bars, an amount that dominates the needed parent calculations for the LEA method. For this specific system, each LEA run requires ∼10 retraining steps, predominantly caused by stagnations.

B. Pt_x nanoparticles on MgO with DFT

Having established a robust algorithm, we apply it to a number of Pt nanoparticles on MgO which have been studied extensively for their catalytic properties both theoretically and experimentally [57,58,61–65]. A number of nanoparticle configurations of sizes 9, 10, and 13 have already been suggested from an extended search [57,58] and we employ the LEA algorithm for the exact same systems and computational setup. Running the NN accelerated EA for the three particle sizes reveals that the task of finding the right nanoparticles is indeed too complex to do by hand as several more stable configurations are located for all three sizes. For each size, we restarted the search three times and the evolution of all nine LEA runs are plotted in Fig. 3. The top 54 most stable candidates found during the LEA runs are plotted in the Supplemental Material [66], Fig. S1-3, for each particle size. The apparent global minimum is located by all three EA runs for the Pt_9 nanoparticle, and by $\frac{2}{3}$ of the runs for the Pt_{10} and Pt_{13} nanoparticles. The fact that we do not find the global minimum for every restart conforms with the findings in Fig. 2 for the Pt_3Ag_3 system, where Fig. 2(b), for instance, showed ∼50% hit rate after ∼400 attempts.

From the EA search, candidates within a ∼0.5 eV window from the top are transferred and rerelaxed in the same unit cell as used by Crampton *et al.* [57,58] Their best guess for each size is plotted in Figs. 4(c), 4(f), and 4(o). For the Pt_9 and Pt_{10} nanoparticles, the structures and the updated energies of our two best structures found are plotted in Figs. 4(a), 4(b), 4(d), and 4(e). Following Crampton *et al.,* the spin degree of freedom has been mapped and optimized for each of the structures resulting in both magnetic and nonmagnetic structures. A more extensive view of the explored structures is plotted for the Pt_{13} nanoparticles in Figs. 4(g)–4(o)which show the transition for LEA structures to the post-analyzed structures. In the top of Fig. 4(g), the density of states of uniquely found LEA candidates in the (5 × 5) cell is plotted, and just below is a zoom-in on a 0.6-eV window of the most stable candidates. Finally, at the bottom the final rerelaxed structures in the (7 × 6) cell are plotted on the same energy scale. The same analysis can be seen for the both the Pt_9 and Pt_{10} searches in the Supplemental Material [66], Figs. S4 and S5.

In general, some of the minima in the small unit cell are "false" minima and hence when transferred to the large

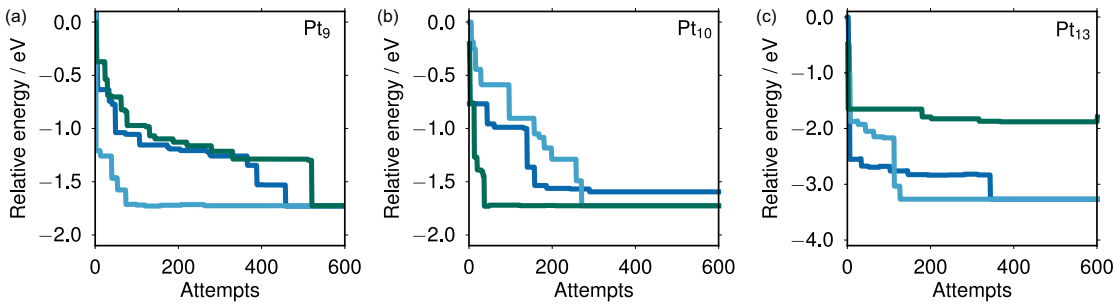

FIG. 3. The three individual LEA runs for each of the three nanoparticle sizes 9, 10, and 13 Pt atoms in (a), (b), and (c), respectively. The plots show the most stable candidate found as a function of the number of attempts.

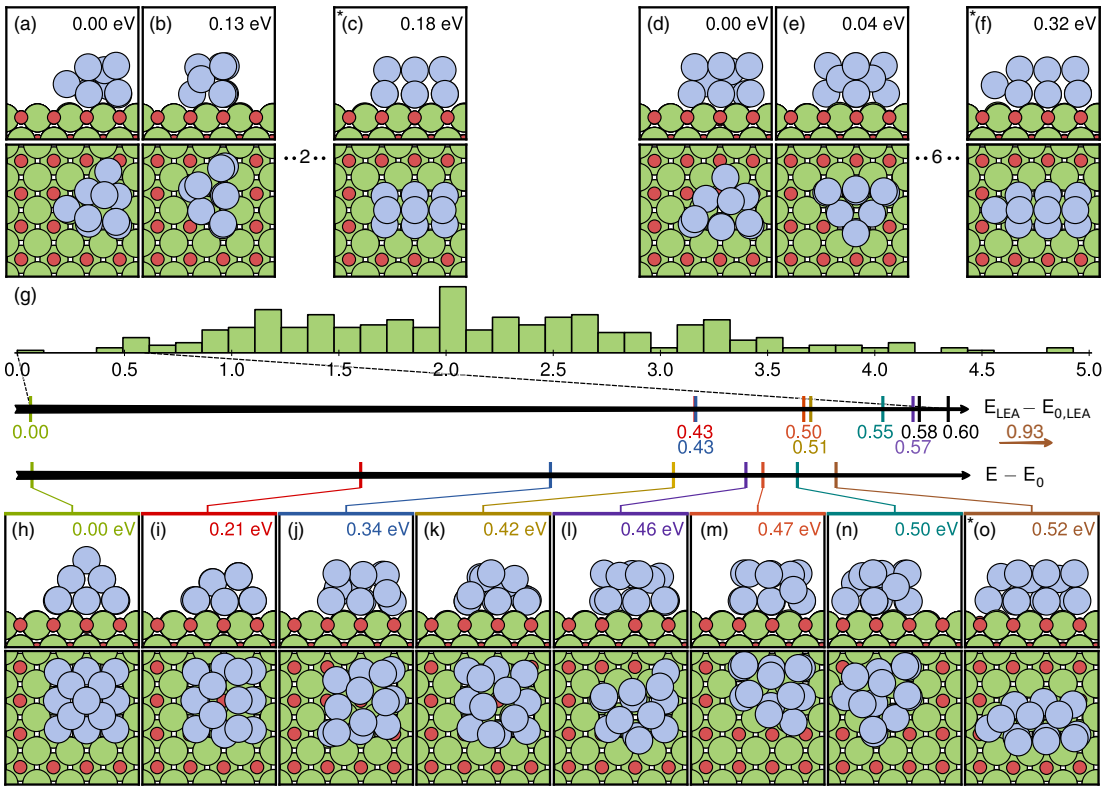

FIG. 4. Top and side views of the two most stable configurations and the previous reported (*) for the Pt_9 (a)–(c) and Pt_{10} (d)–(f). (g) From the top: the density of states for the 5-eV most stable Pt_{13} nanoparticles for all LEA runs, zoom-in on the window of the first 0.6-eV most stable particles, and the structures transferred to Crampton *et al.*'s (7×6) unit cell with the total magnetic moment optimized. (h)–(o) The eight best nanoparticles including Crampton *et al.*'s suggested (marked *) shown in a top view. (b), (c), (f) Have an optimized magnetic moment of 2 while (n) has a magnetic moment of 1; the remaining depicted structures are nonmagnetic. Green, red, and light blue spheres represent Mg, O, and Pt atoms, respectively.

unconstrained cell they relax into one of the other minima. The large change in energy seen for a couple of configurations is mostly due to a significant stability gain when allowed to possess a magnetic moment.

It is evident that a relevant proportion of the most stable Pt_9 structures are very asymmetric and hence even harder to guess. Out of the 10 best structures identified in our work, only three, including the previously suggested structure, have a high symmetry. The asymmetric trend is also observed for the Pt_{10} nanoparticles with the global minimum configuration showcasing four atoms twisted out of a high-symmetry configuration. A great example of a relevant peculiar deformation that a human would hardly imagine which could have relevant consequences for the catalytic property of the particle.

The situation is different for the larger Pt_{13} nanoparticles. Here, the most stable nanoparticle is very symmetric and formed like a hollow pyramid with a missing atom in the center. In hindsight, this is an obvious structure which is possible, at least in the case of Au_{13} supported on MgO(100) [67], for humans to guess but still overlooked for Pt_{13} in previous studies [57,58]. This is not a single incidence as a total of six highly symmetric structures are among the more stable geometries for the three particles sizes found in this work. In the next sections we will explore the consequences of not knowing the right particle geometry by comparing adsorption properties of the hollow pyramid [Fig. 4(h)] and the elongated structure [Fig. 4(o)] previously suggested.

C. Adsorption of CO and C_2H_4 on Pt_{13}

First, we examine the reactivity of the nanoparticles by calculating the adsorption energy, a classical catalytic descriptor. Both CO and ethylene have been adsorbed on the two different nanoparticles on any conceivable/reasonable site. All stable sites found are depicted in the top panel of Fig. 5. As the adsorption energy is site dependent, each site has been assigned a number and the corresponding adsorption potential energy can be found in Table II. For each nanoparticle, the most stable adsorption configuration has been depicted in the bottom panel of Fig. 5.

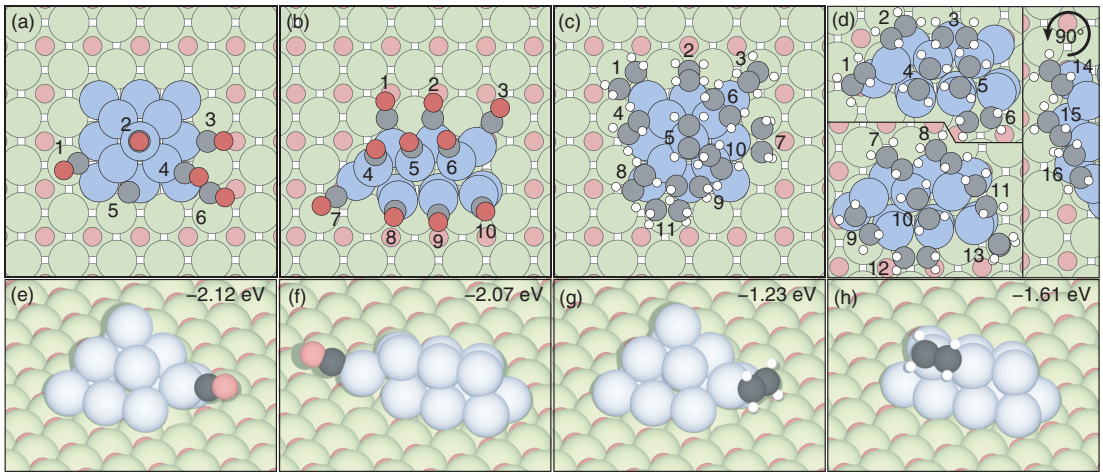

FIG. 5. The CO and C_2H_4 adsorption sites, respectively, on the hollow pyramid (a) and (c) and the elongated structure (b) and (d). The configurations pictured in (a)–(d) are of the relaxed clean structure with a schematic showing the added adsorbates. The favored adsorption configurations of CO and C_2H_4 imaged on the hollow pyramid [(e) and (g), respectively] and on the elongated structure [(f) and (h), respectively].

For the hollow pyramid, the same adsorption site is preferred whether the adsorbed molecule is a CO or an ethylene molecule. A middle interface atom is pulled slightly out and upward ∼1.23 Å from its resting position in both cases while solely bonding the adsorbate. For both molecules, there is a clear "best adsorption site" (CO: 0.22 eV and C_2H_4: 0.16 eV more stable than the second most stable). For ethylene, if we ignore the most favored adsorption, it seems that π bonding to a single Pt atom and σ bonding to two Pt atoms are relatively competitive as is seen for sites 2, 3, 5, and 6 (π bonded) versus 8, 9, 10, and 11 (σ bonded) in Fig. 5(c).

Adsorption on the elongated Pt_{13} nanoparticle is a bit more complicated as the low symmetry allows for many different adsorption sites as is seen when, e.g., comparing Figs. 5(c) and 5(d). Adsorbing CO at the most favorable site drags the immediate Pt atom ∼1.97 Å away from its resting position, a significant structural change. Ethylene on the elongated structure prefers to sit on one side of the nanoparticle bridging two Pt atoms making two σ-like bonds.

As adsorption of ethylene is significantly stronger on the elongated geometry, it is interesting to compare the relative stability of the two adsorption complexes and to consider if transforming the nanoparticle shape from the hollow pyramid to elongated is possible, perhaps during adsorption. The first is straightforward: the energy difference $E_{ad}(\text{hollow} + C_2H_4) - E_{ad}(\text{elongated} + C_2H_4) = -0.14$ eV shows that the pyramid complex is still slightly more stable; the latter is significantly more complex and is discussed in the next section.

D. Pt_{13} structure transformation

In order to determine for a given Pt nanoparticle size if the catalytic properties are governed by one particle shape or an ensemble of particle shapes, the transition barriers between particles must be known. The trained NN models lends themselves to a thorough investigation of such barriers. In Fig. 6 we consider the transition of the hollow Pt_{13} nanoparticle into the elongated Pt_{13} nanoparticle. If performed at the DFT level, only few guesses can be covered concerning which Pt atoms of the initial nanoparticle map onto which Pt atoms of the final nanoparticle. A natural choice would be the mapping that results from the Hungarian method in which the 2-norm distance of the two nanoparticles is minimized. This strategy is very similar to the approach Zhai *et al.* apply for exploring transitions between isomers of α-Al_2O_3 supported Pt_7 nanoparticles [68]. Using, however, the NN potential, a brute force strategy may be adopted to screen for the best

TABLE II. Adsorption potential energies in eV for the different adsorption sites on both the hollow pyramid and the elongated structure for both CO and C_2H_4. The bold numbers indicate the lowest energy adsorption sites of the four different nanoparticle adsorbate combinations. The corresponding structures are depicted in Fig. 5(e)–5(h).

		No.															
		1	2	3	4	5	6	7	8	9	10	11	12	13	14	15	16
CO	hPy	−1.90	−1.82	**−2.12**	−1.90	−1.73	−1.75										
	elong	−1.53	−1.91	−1.76	−1.97	−1.86	−1.48	**−2.07**	−1.94	−1.68	−1.80						
C_2H_4	hPy	−0.90	−1.05	−1.02	−0.88	−1.04	−1.07	**−1.23**	−0.99	−0.98	−1.02	−1.04					
	elong	−1.41	−1.28	−1.31	−0.55	−0.37	−1.15	−0.98	−1.05	−1.45	−0.33	−1.07	**−1.61**	−1.24	−1.23	−0.91	−1.14

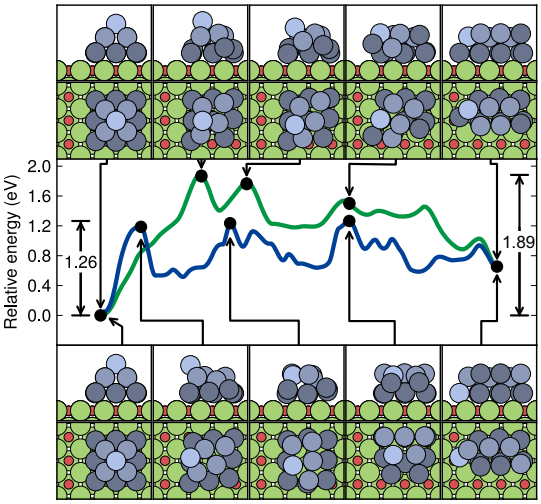

FIG. 6. The first axis shows the reaction coordinate for the transformation of the hollow pyramid to the elongated structure. The lowest-energy path is plotted in blue, while the pathway resulting from minimizing the 2-norm mapping is plotted as a reference in green. The top and bottom panels shows images of side and top views of the initial state, transition states, and final state of the two pathways. The Pt atoms are colored according to their relative height in the pyramid configuration: the lighter the blue, the higher the atoms are.

possible mapping. This is done adapting a parallel version of a machine-learning accelerated saddle-point search [51], but starting from the already trained Amp model. Collecting new training data (pathway points at the DFT level) and retraining is performed in parallel over all investigated paths using one common Amp model. Specifically, we have investigated the pathways for 600 different mappings resulting from freezing indices of five atoms, manually mapping three atoms in five different ways, and combining the remaining five Pt atoms in every conceivable way (see Supplemental Material [66], Fig. S6, for the different mappings). The rationale for fixing said indices is the like positions while the rationale for the manually shuffling of the three atoms is the desire to keep the number of pathway searches in the hundreds while still exploring any reasonable mapping.

The 600 NN-based searches were done using the AUTONEB [69] method adopting the IDPP [70] method for the initial guesses. The results showed several low-energy barrier pathways, six of which had estimated barriers less than 0.15 eV from the lowest-energy barrier. For reference, the Hungarian pathway emerged as the 71st lowest with a barrier 0.29 eV higher than the lowest. These seven pathways (including the Hungarian) were subsequently fully modeled at the DFT level and converged with very few iterations compared to what would have been required in the absence of the NN-based pathways. The mapping of the Hungarian method resulted in a barrier of 1.89 eV, while the best pathway of the six found with the systematic mapping showed a lower barrier of 1.26 eV. The corresponding energy profiles are depicted in Fig. 6 and movies of the two transitions are available in the

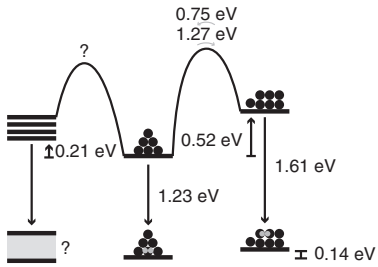

FIG. 7. Graphical representation of the two examined Pt_{13} nanoparticles with and without ethylene adsorbed. The left illustrates the possibility that one of the other stable configurations allows for an even stronger adsorption complex. The relative energy is plotted along the vertical axis and the unknown numbers are indicated with "?".

Supplemental Material [66]. The different barrier heights are crucial when preparing Pt_{13} particles for a catalytic experiment. If, at deposition of the Pt particles, elongated structures are formed they are easily converted into hollow pyramids as the barrier is "only" 0.75 eV which is manageable even at room temperature. This prediction would have been missed by only asserting the Hungarian mapping as it results in a 1.37-eV barrier which is not surpassable at room temperature. We note, however, that both the Hungarian and best systematic barrier estimates conform with the idea that as soon as hollow pyramids are formed they will be "trapped" in this state (at room temperature) as the barrier is simply too high to surmount, whether it is 1.26 or 1.89 eV does not matter.

The total stability of the most favorable elongated and pyramid ethylene complexes are almost equal but the barrier for transforming the nanoparticle from the hollow to the elongated is not expected to be dramatically reduced by adsorbing, e.g., ethylene; the exact effects though are at the moment unknown. Hence, not changing the fact that newly created particles will quickly convert to and be "trapped" as hollow pyramids even at elevated room temperature. A visual overview of the stability of the two nanoparticles (with and without adsorbed ethylene) is presented in Fig. 7. The very different adsorption configuration especially for ethylene (σ versus π bonded) and the energy difference between the two different configurations will very likely heavily influence the credibility of potential theoretical predictions of the catalytic reactivity of the real nanoparticles in practice, rendering them useless. In principle, there could be another combination of particle configuration and adsorption site that is even more stable as illustrated in the left part of Fig. 7. For the full picture situations involving different adsorbate chemical potential should also be considered. This would, however, require a detailed study and subsequent analysis and is outside the scope of this study.

Without exploring every stable nanoparticle conformation transformation barrier, we can get a feeling for how diverse the most stable conformations are and formulate qualified expectations on the distribution of experimentally found particles. This is achieved with the presumption that look-alike conformations are associated with a smaller transformation barrier and by grouping the conformations into clusters. All the unique Pt_{13}

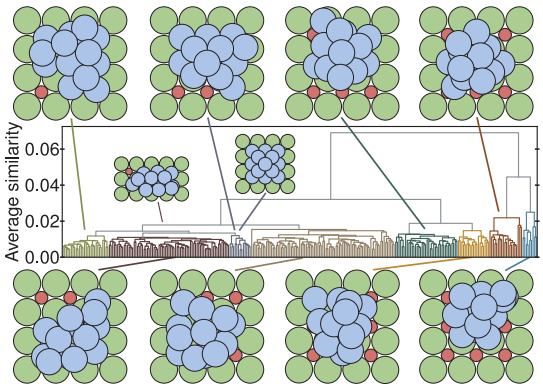

FIG. 8. A dendrogram including the eight clusters found by clustering the unique Pt_{13} structures (and the top MgO layer) following an agglomerative clustering algorithm with an average linkage and an inconsistent coefficient of 3.4 for separating clusters using the Bag of Bonds [71] fingerprint function following Ref. [60]. The hollow pyramid belongs to the purple cluster while the elongated structure belongs to the dark red cluster. For each cluster, the structure closest to the centroid has been plotted representing the geometry of the given cluster.

structures are clustered into eight clusters shown in Fig. 8 by measuring their relative similarity. For each cluster, the member closest to the centroid is visualized, as well as the cluster assignment of the hollow pyramid and the elongated structure. The five most stable structures are members of the first four clusters (from the left) with the hollow pyramid as the only member of the purple cluster. This indicates that it has no immediate very stable "relatives" suggesting, without performing the full search of every possible adsorption, mapping, and transformation, that experimentally prepared particles of 13 Pt atoms are expected to be found in this exact configuration at moderate temperatures.

IV. CONCLUSION

In summary, a neural-network-enhanced EA is outlined and applied to MgO supported Pt nanoparticles. The method proves highly CPU efficient and enables the identification of different particle shapes. This is, for instance, seen for the very stable Pt_{13} hollow pyramid. Our results highlight the need for efficient unbiased optimization methods, and the neural-network-enhanced EA described opens up for the study of, e.g., kinetic transitions between different particle shapes with the use of the on-the-fly trained neural networks. These transitions of rather diverse structures represent no easy task as is shown by investigating two Pt_{13} conformers and the "brute force" mapping allowed by our trained neural network brings the estimated barrier down by 0.62 eV compared to a mapping suggested by the Hungarian method. We show that indeed "every atom" counts and it is of utmost importance that we know every atomic position before statements on catalytic activity are made as, e.g., shown for the adsorption geometry and energy of CO and ethylene probe molecules on a Pt_{13} nanoparticle.

ACKNOWLEDGMENTS

Grants from VILLUM FONDEN (Investigator grant, Project No. 16562), Danish Council of Independent Research Natural Science (Grant No. 0602-02566B) have supported this research.

[1] D. J. Wales and J. P. K. Doye, J. Phys. Chem. A **101**, 5111 (1997).
[2] R. L. Johnston, Dalton Trans. **0**, 4193 (2003).
[3] S. Curtarolo, G. L. W. Hart, M. B. Nardelli, N. Mingo, S. Sanvito, and O. Levy, Nat. Mater. **12**, 191 (2013).
[4] J. E. Saal, S. Kirklin, M. Aykol, B. Meredig, and C. Wolverton, JOM **65**, 1501 (2013).
[5] B. R. Goldsmith, M. Boley, J. Vreeken, M. Scheffler, and L. M. Ghiringhelli, New J. Phys. **19**, 013031 (2017).
[6] J. Balluff, K. Diekmann, G. Reiss, and M. Meinert, Phys. Rev. Mater. **1**, 075502 (2017).
[7] F. A. Faber, A. Lindmaa, O. A. von Lilienfeld, and R. Armiento, Phys. Rev. Lett. **117**, 135502 (2016).
[8] M. Boudart, Adv. Cat. **20**, 153 (1969).
[9] M. Che and C. O. Bennett, Adv. Cat. **36**, 55 (1989).
[10] F. Besenbacher, I. Chorkendorff, B. S. Clausen, B. Hammer, A. M. Molenbroek, J. K. Nørskov, and I. Stensgaard, Science **279**, 1913 (1998).
[11] F. Studt, I. Sharafutdinov, F. Abild-Pedersen, C. F. Elkjær, J. S. Hummelshøj, S. Dahl, I. Chorkendorff, and J. K. Nørskov, Nat. Chem. **6**, 320 (2014).
[12] U. Heiz, A. Sanchez, S. Abbet, and W.-D. Schneider, J. Am. Chem. Soc. **121**, 3214 (1999).
[13] P. L. Hansen, J. B. Wagner, S. Helveg, J. R. Rostrup-Nielsen, B. S. Clausen, and H. Topsøe, Science **295**, 2053 (2002).
[14] Z.-P. Liu, S. J. Jenkins, and D. A. King, Phys. Rev. Lett. **94**, 196102 (2005).
[15] A. S. K. Hashmi and G. J. Hutchings, Angew. Chem. Int. Ed. **45**, 7896 (2006).
[16] T. Uchiyama, H. Yoshida, Y. Kuwauchi, S. Ichikawa, S. Shimada, M. Haruta, and S. Takeda, Angew. Chem. Int. Ed. **50**, 10157 (2011).
[17] J. K. Nørskov, T. Bligaard, J. Rossmeisl, and C. H. Christensen, Nat. Chem. **1**, 37 (2009).
[18] Y. Watanabe, Sci. Technol. Adv. Mater. **15**, 063501 (2014).
[19] A. Fernando, K. L. D. Weerawardene, N. V. Karimova, and C. M. Aikens, Chem. Rev. **115**, 6112 (2015).
[20] N. Artrith, B. Hiller, and J. Behler, Phys. Status Solidi B **250**, 1191 (2013).
[21] M. Hellström, D. Spångberg, K. Hermansson, and P. Broqvist, J. Phys. Chem. C **118**, 6480 (2014).
[22] N. Artrith and A. M. Kolpak, Comput. Mater. Sci. **110**, 20 (2015).
[23] S. Schauermann and H.-J. Freund, Acc. Chemi. Res. **48**, 2775 (2015).
[24] A. R. Oganov and C. W. Glass, J. Chem. Phys. **124**, 244704 (2006).
[25] L. B. Vilhelmsen and B. Hammer, J. Chem. Phys. **141**, 044711 (2014).
[26] D. J. Wales and H. A. Scheraga, Science **285**, 1368 (1999).

[27] S. Goedecker, J. Chem. Phys. **120**, 9911 (2004).
[28] S. Hajinazar, J. Shao, and A. N. Kolmogorov, Phys. Rev. B **95**, 014114 (2017).
[29] M. Rupp, A. Tkatchenko, K.-R. Müller, and O. A. von Lilienfeld, Phys. Rev. Lett. **108**, 058301 (2012).
[30] E. D. Cubuk, S. S. Schoenholz, J. M. Rieser, B. D. Malone, J. Rottler, D. J. Durian, E. Kaxiras, and A. J. Liu, Phys. Rev. Lett. **114**, 108001 (2015).
[31] A. P. Bartók, M. C. Payne, R. Kondor, and G. Csányi, Phys. Rev. Lett. **104**, 136403 (2010).
[32] A. P. Bartók and G. Csányi, Int. J. Quantum Chem. **115**, 1051 (2015).
[33] V. L. Deringer and G. Csányi, Phys. Rev. B **95**, 094203 (2017).
[34] S. Chmiela, A. Tkatchenko, H. E. Sauceda, I. Poltavsky, K. T. Schütt, and K.-R. Müller, Sci. Adv. **3**, e1603015 (2017).
[35] T. L. Jacobsen, M. S. Jørgensen, and B. Hammer, Phys. Rev. Lett. **120**, 026102 (2018).
[36] V. L. Deringer, C. J. Pickard, and G. Csányi, Phys. Rev. Lett. **120**, 156001 (2018).
[37] S. Lorenz, A. Groß, and M. Scheffler, Chem. Phys. Lett. **395**, 210 (2004).
[38] J. Behler and M. Parrinello, Phys. Rev. Lett. **98**, 146401 (2007).
[39] J. Behler, Phys. Chem. Chem. Phys. **13**, 17930 (2011).
[40] P. E. Dolgirev, I. A. Kruglov, and A. R. Oganov, AIP Advances **6**, 085318 (2016).
[41] H. Zhai and A. N. Alexandrova, J. Chem. Theory Comput. **12**, 6213 (2016).
[42] A. Khorshidi and A. A. Peterson, Comput. Phys. Commun. **207**, 310 (2016).
[43] Z. Li, J. R. Kermode, and A. De Vita, Phys. Rev. Lett. **114**, 096405 (2015).
[44] T. K. Patra, V. Meenakshisundaram, J.-H. Hung, and D. S. Simmons, ACS Comb. Sci. **19**, 96 (2017).
[45] R. Ouyang, Y. Xie, and D.-E. Jiang, Nanoscale **7**, 14817 (2015).
[46] Q. Tong, L. Xue, J. Lv, Y. Wang, M. Yanchao, and Y. Ma, Faraday Discuss (2018), doi:10.1039/C8FD00055G.
[47] S. Q. Wu, M. Ji, C. Z. Wang, M. C. Nguyen, X. Zhao, K. Umemoto, R. M. Wentzcovitch, and K. M. Ho, J. Phys.: Condens. Matter **26**, 035402 (2014).
[48] M. Van den Bossche, H. Grönbeck, and B. Hammer, J. Chem. Theory Comput. **14**, 2797 (2018).
[49] K. W. Jacobsen, P. Stoltze, and J. K. Nørskov, Surf. Sci. **366**, 394 (1996).
[50] A. Larsen, J. J. Mortensen, J. Blomqvist, I. E. Castelli, R. Christensen, M. Dułak, J. Friis, M. N. Groves, B. Hammer, C. Hargus *et al.*, J. Phys.: Condens. Matter **29**, 273002 (2017).
[51] A. A. Peterson, J. Chem. Phys. **145**, 074106 (2016).
[52] J. S. Smith, O. Isayev, and A. E. Roitberg, Chem. Sci. **8**, 3192 (2017).
[53] J. R. Boes and J. R. Kitchin, J. Phys. Chem. C **121**, 3479 (2017).
[54] J. R. Boes and J. R. Kitchin, Mol. Simul. **43**, 346 (2017).
[55] Z. W. Ulissi, M. T. Tang, J. Xiao, X. Liu, D. A. Torelli, M. Karamad, K. Cummins, C. Hahn, N. S. Lewis, T. F. Jaramillo, K. Chan, and J. K. Nørskov, ACS Catalysis **7**, 6600 (2017).
[56] J. Enkovaara, C. Rostgaard, J. J. Mortensen, J. Chen, M. Dułak, L. Ferrighi, J. Gavnholt, C. Glinsvad, V. Haikola, H. A. Hansen *et al.*, J. Phys.: Condens. Matter **22**, 253202 (2010).
[57] A. S. Crampton, M. D. Rötzer, C. J. Ridge, B. Yoon, F. F. Schweinberger, U. Landman, and U. Heiz, Surf. Sci. **652**, 7 (2016).
[58] A. S. Crampton, M. D. Rötzer, C. J. Ridge, F. F. Schweinberger, U. Heiz, B. Yoon, and U. Landman, Nat. Commun. **7**, 10389 (2016).
[59] J. P. Perdew, K. Burke, and M. Ernzerhof, Phys. Rev. Lett. **77**, 3865 (1996).
[60] M. S. Jørgensen, M. N. Groves, and B. Hammer, J. Chem. Theory Comput. **13**, 1486 (2017).
[61] S. E. Deutsch, J. T. Miller, K. Tomishige, Y. Iwasawa, W. A. Weber, and B. C. Gates, J. Phys. Chem. **100**, 13408 (1996).
[62] J. Goniakowski, A. Jelea, C. Mottet, G. Barcaro, A. Fortunelli, Z. Kuntová, F. Nita, A. C. Levi, G. Rossi, and R. Ferrando, J. Chem. Phys. **130**, 174703 (2009).
[63] J. Goniakowski and C. Mottet, Phys. Rev. B **81**, 155443 (2010).
[64] E. Florez, F. Mondragon, and F. Illas, Surf. Sci. **606**, 1010 (2012).
[65] K. Rossi, T. Ellaby, L. O. Paz-Borbón, I. Atanasov, L. Pavan, and F. Baletto, J. Phys.: Condens. Matter **29**, 145402 (2017).
[66] See Supplemental Material at http://link.aps.org/supplemental/10.1103/PhysRevB.97.195424 for an extensive view of the located Pt nanoparticles, the mapping procedure for the configuration transformation, and movies of the compared transformation paths.
[67] R. Ferrando, G. Barcaro, and A. Fortunelli, Phys. Rev. B **83**, 045418 (2011).
[68] H. Zhai and A. N. Alexandrova, J. Phys. Chem. Lett. **9**, 1696 (2018).
[69] E. L. Kolsbjerg, M. N. Groves, and B. Hammer, J. Chem. Phys. **145**, 094107 (2016).
[70] S. Smidstrup, A. Pedersen, K. Stokbro, and H. Jónsson, J. Chem. Phys. **140**, 214106 (2014).
[71] K. Hansen, F. Biegler, R. Ramakrishnan, W. Pronobis, O. A. von Lilienfeld, K.-R. Müller, and A. Tkatchenko, J. Phys. Chem. Lett. **6**, 2326 (2015).